Dynamics of the Min system in *Bacillus subtilis*

An analysis using fluorescence and single-molecule localization microscopy

Dissertation

zur Erlangung des Doktorgrades der Naturwissenschaften

(Dr. rer. nat.)

an der Fakultät für Biologie der

Ludwig-Maximilians-Universität München

Helge Feddersen

München, September 2020

Diese Dissertation wurde angefertigt
unter der Leitung von Prof. Dr. Marc Bramkamp
im Bereich der Mikrobiologie
an der Ludwig-Maximilians-Universität München

Erstgutachter/in:	Prof. Dr. Marc Bramkamp
Zweitgutachter/in:	Prof. Dr. Kirsten Jung

Tag der Abgabe:	18.09.2020
Tag der mündlichen Prüfung:	14.12.2020

ERKLÄRUNG:

Ich versichere hiermit an Eides statt, dass meine Dissertation selbständig und ohne unerlaubte Hilfsmittel angefertigt worden ist. Die vorliegende Dissertation wurde weder ganz, noch teilweise bei einer anderen Prüfungskommission vorgelegt. Ich habe noch zu keinem früheren Zeitpunkt versucht, eine Dissertation einzureichen oder an einer Doktorprüfung teilzunehmen.

Kiel, den 15.01.2021

Helge Feddersen

„Omnis cellula e cellula.“ - „Jede Zelle [entsteht] aus einer Zelle.“

- Rudolf Virchow, 1855

Contents:

I. Abstract

Cell division is an essential process and thus under tight spatio-temporal control, which includes identification of the divisional plane. In most bacterial cells, the divisional plane is positioned at the geometrical cell center and its localization is indicated by the tubulin homologue FtsZ. After polymerizing into a ring-like structure (Z-ring), FtsZ will eventually recruit a multi-enzyme complex responsible for cell division, termed “divisome”. Similar to *Escherichia coli*, the Min system of the Gram-positive soil bacterium *Bacillus subtilis* was thought to aid in confining FtsZ polymerization to midcell by inhibiting the process close to the poles. Consisting of MinCDJ and the curvature sensing protein DivIVA, the protein network was expected to form a stable, bipolar gradient, in contrast to the oscillating Min system in *E. coli*. Since the *B. subtilis* Min system was later also observed to dynamically relocalize to the divisional septum before cytokinesis, we set out to re-characterize the Min system and the dynamic behavior of the individual components MinD, MinJ and DivIVA.

In this work, we first constructed functional fluorescent fusions for the Min proteins, encoded in their native, genomic loci. Using fluorescence recovery after photobleaching (FRAP) studies, we show that all components of the Min system display fast protein recovery at divisional septa, and further affect each other in their dynamics. Moreover, individual protein copy numbers were determined through in-gel fluorescence. Using photoactivated localization microscopy (PALM), we found a majority of Min proteins associated in large protein clusters, occurring frequently along lateral cell membrane, besides the expected polar and septal regions. Based on these data, a minimal reaction-diffusion model was built, confirming the experimental observations during simulations. In conclusion, we propose a new model of the *B. subtilis* Min system as cell cycle regulator, where a majority of Min proteins resides in dynamic clusters that constantly probe the cell for curvature. Upon septum formation, they partially relocalize to the site of division to aid in disassembly of the divisome and the FtsZ-ring downstream of division.

Additionally, a single-particle tracking (SPT) PALM workflow was established for routine usage. This technique was then utilized to analyze and dissect dynamic subpopulations of MinD and DivIVA, where both exhibited an immobile, a slow- and a fast-diffusive subpopulation.

Finally, we present an optimized workflow for employing mNeonGreen in bacterial PALM. By controlled and stepwise enhancement of sample-preparation, imaging conditions and post-processing, we demonstrate that mNeonGreen can even be used to resolve dense structures with a localization precision of 25 nm, exemplified by use of DivIVA-mNeonGreen.

II. Zusammenfassung

Da Zellteilung einen für Bakterien lebensnotwendigen Prozess darstellt, wird dieser räumlich und zeitlich streng kontrolliert, was die Identifizierung der korrekten Zellteilungsebene miteinschließt. In Bakterien ist diese Teilungsebene für gewöhnlich in der geometrischen Zellmitte positioniert. Das bakterielle Tubulin-Homolog FtsZ lokalisiert als erstes Protein an dieser zukünftigen Teilungsebene. Dort bildet sie eine aus FtsZ-Filamenten bestehende, ringförmige Struktur (Z-Ring), die hauptverantwortlich für die Rekrutierung des Divisoms ist, ein Multienzymkomplex der die Zellteilung orchestriert. Ähnlich wie *Escherichia coli* verfügt das Gram-positive Bakterium *Bacillus subtilis* über Min Proteine. In *E. coli* verhindert das oszillierende Min System eine Polymerisierung von FtsZ-Filamenten in den polaren Regionen der Zelle und sorgt damit für die korrekte Positionierung des Z-Rings. In *B. subtilis* besteht das Min Netzwerk aus MinCDJ und DivIVA, einem Protein das in der Lage ist Membrankrümmung zu detektieren. Auch wenn das System in *B. subtilis* nicht oszilliert, sondern einen scheinbar stabilen, bipolaren Gradienten bildet, wurde dort eine ähnliche Funktion vermutet. Später wurde allerdings beobachtet, dass sich Min Proteine in *Bacillus* dynamisch zum Teilungsseptum bewegen, sobald sich dieses bildet, was die genannte Rolle in Frage stellte. Aus diesem Grund haben wir in dieser Studie die einzelnen Min Proteine und ihre Dynamik erneut beobachtet und charakterisiert.

Zu diesem Zweck wurden zuerst funktionale, fluoreszente Proteinfusionen konstruiert, welche im nativen Genlocus kodiert sind. Diese Fusionen wurden für „fluorescence recovery after photobleaching" (FRAP) Experimente genutzt. Dabei konnten wir zeigen, dass sich alle Min Proteine dynamisch verhalten und dabei gegenseitig beeinflussen. Weiterhin konnten wir durch in-Gel-Fluoreszenz Proteinmengen der einzelnen Min Protein bestimmen. Mithilfe von photoaktivierter Lokalisationsmikroskopie (PALM) konnten wir im nächsten Schritt erkennen, dass sich die Mehrheit der Min Proteine in dynamischen Proteinclustern befindet. Neben der erwarteten Lokalisation nahe der Pole und des Septums wurden diese auch vermehrt an der lateralen Zellwand und im Cytosol beobachtet. Basierend auf diesen Daten wurde ein mathematisches Modell erstellt, welches die experimentellen Beobachtungen simulierte und bestätigte. Aufgrund dieser Erkenntnisse vermuten wir, dass das Min System in *B. subtilis* die Aufgabe eines Zellzyklus Regulators hat, und eine Neuinitiation der Teilung neben der genutzten Teilungsebene verhindert. Dabei befindet sich die Mehrzahl der Min Proteine in dynamischen Clustern, welche die Zelle nach Membrankrümmung absuchen, und sich in entsprechenden Regionen stabilisieren. Nach der Bildung eines Septums verlagert sich eine

Mehrzahl dieser Cluster zur Mitte der Zelle, um nach erfolgter Teilung den Abbau des Zellteilungsapparates und des Z-Ringes zu unterstützen und voranzutreiben.

Darüber hinaus wurde ein Protokoll für die Routineanwendung von Einzelpartikelverfolgung (single-particle tracking, SPT) in PALM Experimenten entwickelt und optimiert. Dieses wurde dann zur Analyse und Unterscheidung der dynamischen Subpopulationen von MinD und DivIVA herangezogen. Diese konnten in jeweils drei Untergruppen unterteilt werden: immobile, langsam diffundierende und schnell diffundierende Proteine, wobei MinD das deutlich schnellere der beiden Proteine war.

Abschließend wurden im Rahmen dieser Arbeit ein Protokoll für den optimierten Einsatz des fluoreszenten Proteins mNeonGreen in der bakteriellen PAL Mikroskopie erarbeitet. Durch kontrollierte, schrittweise Verbesserung von Probenaufbereitung, Mikroskopie- und Belichtungsparametern sowie kontrolliertem Filtern der Bilddaten konnten wir demonstrieren, dass mNeonGreen sogar für die Rekonstruktion von dichten, zellulären Strukturen in Bakterien geeignet ist. Dabei erreichten wir bei Aufnahmen von DivIVA-mNeonGreen eine Lokalisationspräzision von 25 nm.

III. Abbreviations

Abbreviation	Definition
3D-SIM	Three dimensional structured illumination microscopy
AMR	Contractile actomyosin ring
ATPase	Adenosine triphosphatase
B2H	Bacterial two-hybrid
Ct	C-terminal domain
FOV	Field of view
FP	Fluorescent protein
FRAP	Fluorescent recovery after photobleaching
GFP	Green fluorescent protein
GlcNAc	*N*-acetylglucosamine
GTPase	Guanosine triphosphatase
JD	Jump distance
LAP	Linear assignment problem
mNG	mNeonGreen
MJD	Mean jump distance
MSD	Mean-squared displacement
MTS	Membrane targeting sequence
MurNAc	*N*-acetylmuramic acid
NA	Numerical aperture
Nt	N-terminal domain
NO	Nucleoid occlusion
oriC	Origin of replication of the chromosome
PA	Photoactivatable
PALM	Photoactivated localization microscopy
PBP	Penicillin-binding protein
PC	Photoconvertible
PDF	Probability density function
PG	Peptidoglycan (also known as Murein)
Plk1	Polo-like kinase 1
PS	Photoswitchable
PSF	Point-spread function
RhoGEF Ect-2	Guanine nucleotide exchange factor Ect-2
ROI	Region of interest
SIN	Septation initiation network
SNR	Signal-to-noise ratio

SPT	Single-particle tracking
STED	Stimulated emission depletion
STORM	Stochastic optical reconstruction microscopy
ter	Replication terminus
TM1	One transmembrane helix, TM2 -> two TM helices, etc.
WACA	Walker A cytomotive ATPase
YFP	Yellow fluorescent protein

1. Introduction

In this work, the Min system of the Gram-positive soil bacterium and model organism *Bacillus subtilis* was studied. Like most bacteria, *B. subtilis* divides in the geometric middle of the cell with relatively high precision. This process, termed binary fission, results in two genetically identical daughter cells and is performed and aided by a variety of proteins and mechanisms. Since cell division is such a fundamental and crucial process in virtually all pro- and eukaryotes, these mechanisms have to be performed under tight spatiotemporal control. The Min system in *B. subtilis* is involved in this control and has previously been thought to inhibit division at the poles of the cell, ensuring proper placement of the division site. To understand the function and implications of the Min system and its components in detail, it is important to first apprehend cell division itself. Therefore, I will first introduce the general mechanisms of bacterial cell division. Following, I will explain, how different bacteria tackle the challenge to ensure correct positioning of the division apparatus and then come back to *B. subtilis* and the Min system. Finally, recent advances in microscopy and super-resolution microscopy techniques will be introduced, as they were pivotal in studying the Min system.

1.1. Cell division in bacteria

The division of a parent cell into two healthy daughter cells is a central part of the life cycle in every living organism. Even though there is an estimated number of around 8.7 million different eukaryotic species found on earth and the oceans (Mora et al. 2011), cell division in all known species can be roughly summarized into only three different types of processes: binary fission, mitosis and meiosis. While most prokaryotes divide vegetatively via binary fission, mitosis and meiosis are the mechanism utilized by eukaryotes.

Bacteria are generally unicellular and do not store their genome in a membrane surrounded nucleus but in the cytosol. Consequently, cell division appears to be less complex when compared to the same process in eukaryotes. Simplified, most bacteria will grow in size, duplicate and segregate their chromosome(s) (and plasmid(s) if existent) and finally divide via binary fission, which indeed requires less steps and proteins when compared to eukaryotic mitosis and cytokinesis. However, since it is of highest importance for this process to be successful to produce viable daughter cells, even bacteria employ a diverse and complex set of mechanics and proteins that ensure tight spatio-temporal control, e.g. ensuring selection of the

correct division site, proper replication and segregation of genetic elements, but also functionality of cytokinesis and the division apparatus itself. Furthermore, a lower degree of complexity also means less tools and space to perform a task, which explains why some bacteria utilize exotic modes of division or control mechanisms during division that do not seem to have homologues in eukaryotes (Eswara and Ramamurthi 2017), of which some will be discussed later.

It is still under debate, how bacterial cells regulate their relative constant size and at what point a cell will initiate the process that leads to cytokinesis. For decades it was believed that most cells, including eukaryotes and bacteria, can sense when a critical cell size or mass threshold is reached, and will regulate their cell cycles or cell size accordingly (Turner et al. 2012; Campos et al. 2014). This mechanism had been observed in *S. cerevisiae* and *S. pombe* during G1-S transition and mitosis, respectively, and was henceforth called "sizer" (Fantes 1977; Johnston et al. 1977; Sveiczer et al. 1996). Contrary, the phrase "timer" was established for cells, which were assumed to use an alternative cell cycle control. In the timer model, division starts when a constant amount of time after a critical checkpoint (e.g. end of G1 phase or mitosis) has passed. The combination of these mechanisms (sizer and timer) was demonstrated in *Escherichia coli* and *Salmonella typhimurium* population level studies, where a link between DNA replication initiation and cell mass was described and believed to be transferable to single cell level, indicating an inherent relationship between division and replication (Donachie 1968). Even though these models were disputed (Wold et al. 1994; Boye and Nordstrom 2003; Bates and Kleckner 2005) and other mechanisms like a molecular clock, constant cell volumes or simple timers were proposed (Campos et al. 2014), the critical size paradigm became and remained a dogma in the field for decades. It was only recently that this paradigm was challenged by the Jacobs-Wagner's group, who utilized microfluidic chambers for single-cell microscopy combined with modelling to investigate cell size homeostasis of the evolutionary distant bacteria *E. coli* and *Caulobacter crescentus* (Campos et al. 2014). Surprisingly, they discovered that cells grow in average by an almost constant length increment between two divisions, which is why this growth mechanism was phrased "adders" henceforth. This mechanism is in agreement with different modes of division (symmetric & asymmetric) as well as different growth rates. It nevertheless remains puzzling, how bacteria can sense this and then trigger the steps that lead to division.

Even though it is unclear how or when division initiation is exactly triggered during growth, most bacteria indicate the onset of the process with the arrival of FtsZ at the medial future division site. FtsZ is a tubulin homologue that is almost universally conserved in bacteria and in a huge number of unicellular organisms that divide via binary fission (Lutkenhaus et al. 1980;

Bi and Lutkenhaus 1991; Mukherjee and Lutkenhaus 1994; Vaughan et al. 2004). This also includes *Bacillus subtilis* and *Escherichia coli*, the best characterized model organisms for Gram-positive and Gram-negative bacteria, respectively. In the next step, FtsZ polymerizes and forms a discontinued, ring-like structure (Holden et al. 2014; Jacq et al. 2015; Bisson-Filho et al. 2017) that is tethered to the plasma membrane by well conserved proteins FtsA (most bacteria) and ZipA (*E. coli*) or non-essential functional homologues (e.g. SepF in *Bacillus* and *Streptomyces* species). This ring formation is stabilized and promoted by ZapA and ZapB (Gueiros-Filho and Losick 2002; Buss et al. 2013). The name of this structure, the proto-ring, already indicates that it is an intermediate state (Aarsman et al. 2005; Gamba et al. 2009). Accordingly, one core function is the recruitment of a diverse set of ~20 - 30 different proteins to form the functional division apparatus, named "divisome". It is beyond the scope of this introduction to review all divisome components for every bacterium, but an overview about the core functions of the divisome and some of its proteins will be given in chapter 1.1.2. In addition, the next chapter will shed more light on FtsZ and its precise function and mechanism, while chapters 1.1.3 and 1.1.4 comprehend spatiotemporal control, i.e. the systems that help FtsZ and thus the division plane to localize correctly at the longitudinal cell center.

Briefly, FtsZ guides divisome components to gradually build up cell wall at midcell growing inwards (Weiss et al. 1997; Nguyen-Disteche et al. 1998), forming the division septa, that will eventually close and become the cell poles of the daughter cells. In this process, the divisome components and their functions cover all essential aspects, starting with septum growth in accordance with the maintenance of cell shape integrity, followed by constriction and eventually fission of the cell, recently reviewed by (den Blaauwen et al. 2017). Subsequently, the cell wall has to be hydrolyzed locally to separate the two daughter cells in concert with fusion of the respective membranes after separation.

To ensure cell viability and growth, cytokinesis and replication of genetic material need be concerted and are interdependent, ensuring a one-to-one ratio between cell division and chromosome replication as well as proper segregation of the genetic material (Bates and Kleckner 2005; Misra et al. 2018). While FtsZ first marks the future site of division, evidence from *B. subtilis* studies suggested a necessary, preceding step for its correct localization: chromosome replication initiation by the AAA+ ATPase DnaA binding to the origin of replication (*oriC*) at midcell (Harry et al. 1999; Moriya et al. 2010; den Blaauwen et al. 2017), followed by open complex formation. When replication initiation and open complex formation was blocked, FtsZ was aberrantly positioned, which was not the case when subsequent steps like replication fork elongation were blocked (Harry et al. 1999). This model was phrased "ready-set-go", as it proposes replication initiation as a prerequisite that primes and potentiates

midcell as position for FtsZ assembly (Moriya et al. 2010). Later however, the group around Elizabeth Harry corrected their own ready-set-go model, when they identified that FtsZ positioning at midcell is not potentiated by DNA replication initiation progression itself (Hajduk et al. 2019). Instead, absence of the two proteins Noc and Spo0J was sufficient to restore frequency of FtsZ-rings forming at midcell to wild-type levels during any stage of replication arrest (Hajduk et al. 2019). While Noc is a nucleoid occlusion protein that prevents Z-ring formation over the nucleoid (see chapter 1.1.4.1), Spo0J (ParB) is a chromosome-partitioning protein (Ireton et al. 1994; Lewis and Errington 1997; Autret et al. 2001) that has, amongst other things, been shown to recruit condensin to *oriC* regions in *B. subtilis*, promoting chromosome segregation (Gruber and Errington 2009). Both Spo0J and Noc appeared to be required for prevention of FtsZ-ring assembly over the nucleoid (Hajduk et al. 2019). Furthermore, the study demonstrated involvement of both proteins in fine-tuning the timing of Z ring formation (Hajduk et al. 2019), underlining the interdependence between chromosome replication and cytokinesis.

1.1.1. FtsZ and binary fission

The key orchestrator for synthesis of septal wall during division is FtsZ, a GTPase that guides and directly interacts with several components of the septal peptidoglycan (PG, also called Murein) synthesis machinery (Bi and Lutkenhaus 1991; Wang and Lutkenhaus 1993; Mukherjee and Lutkenhaus 1994), e.g. the division-associated transpeptidase PBP2B in *B. subtilis* (Bisson-Filho et al. 2017). FtsZ has been identified as a homologue of tubulin, displaying a weak sequence homology but relatively similar three-dimensional structure and biochemical properties (Löwe and Amos 1998). Like tubulin, it is a GTPase and can thus bind and hydrolyze GTP, a highly conserved feature that enables assembly and formation of filaments (de Boer et al. 1992; Mukherjee and Lutkenhaus 1994). This polymerization occurs in head-to-tail fashion, where a new subunit binds with the GTP-bound end to the opposite side of the next subunit, thereby forming single-stranded polymers (Mukherjee and Lutkenhaus 1998; Du and Lutkenhaus 2019). This self-activating process allows FtsZ to form the ring-like structure that had already been associated with division nearly two decades ago (Bi and Lutkenhaus 1991), illustrated in **Fig. 1.1 a** and **c**. The other core components of this ring are its membrane tethers, FtsA and ZipA (*E. coli*) / SepF (*B. subtilis*) (Pichoff and Lutkenhaus 2002; Duman et al. 2013). These tethers do not just scaffold FtsZ polymers, but also bundle these filaments and thus enable the more complex, ring-like structure (Conti et al. 2018; Krupka et al. 2018; Ramirez-Diaz et al. 2018).

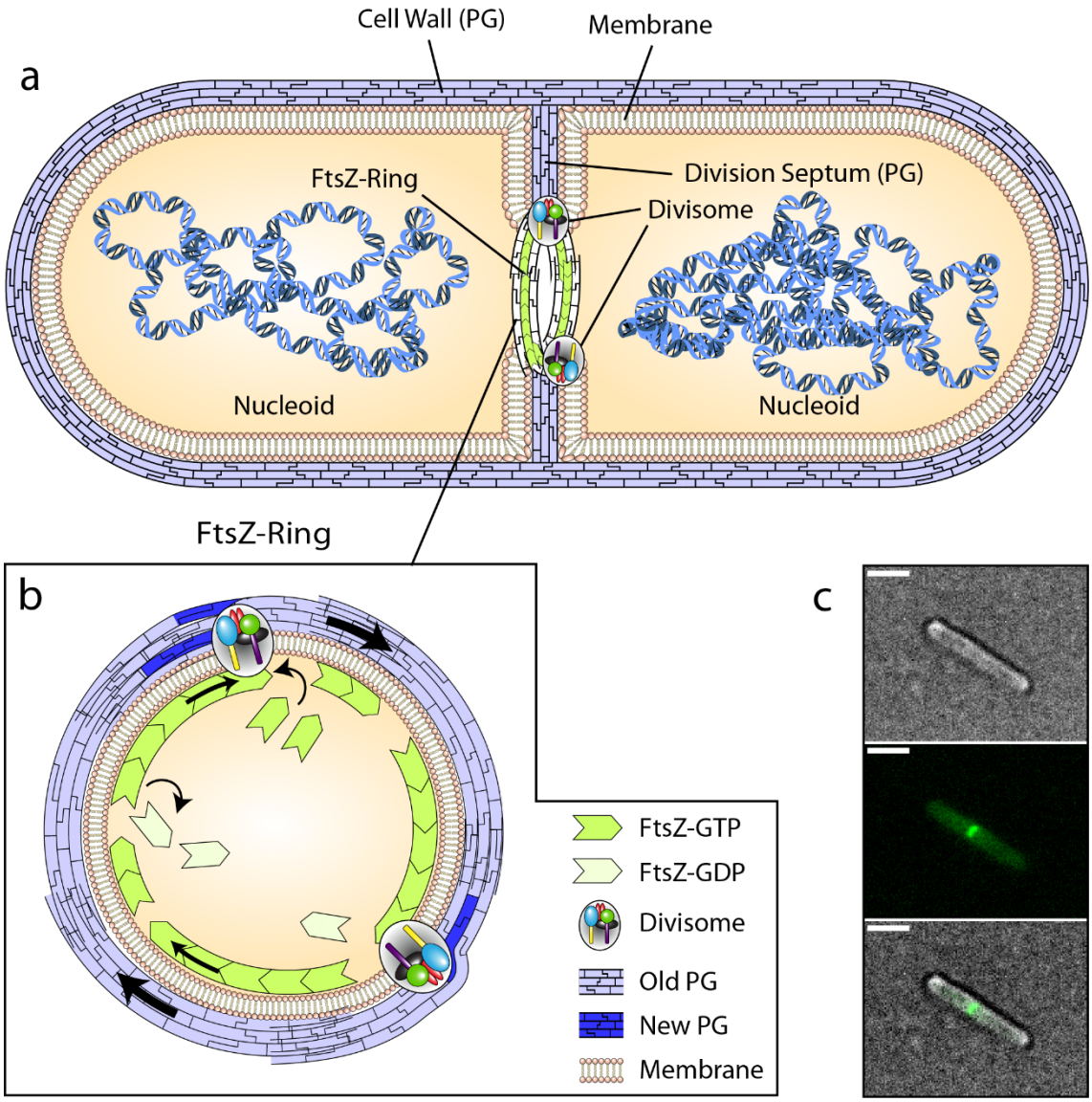

Fig. 1.1: Division and FtsZ in *B. subtilis*.

(a) Cartoon of a dividing *B. subtilis* cell, **(b)** the FtsZ-ring and **(c)** light microscopy images of *B. subtilis* expressing mNeonGreen-FtsZ. Scale bars 2 µm.

Even though the FtsZ-ring (from here on referred to as Z-ring) was envisioned as a closed ring, super-resolution microscopy revealed it to be discontinuous, displaying small, mobile clusters of FtsZ, connected via membrane tethers (Strauss et al. 2012; Holden et al. 2014; Lyu et al. 2016). Moreover, a *B. subtilis* study revealed multiple FtsZ filaments moving in both directions of a constrictive ring in a relatively wide area of the ring (600 to 1000 nm), colocalizing with FtsA (Bisson-Filho et al. 2017). Furthermore, PBP2B molecules were observed to co-localize and move with the Z-ring in different positions simultaneously, a direct indication of multiple simultaneous septal PG synthesis sites positioned through FtsZ (Bisson-Filho et al. 2017). The same study revealed that the observed motion is created via treadmilling, where GTP bound

FtsZ binds to the putative (+) end of a filament, while another monomer at the (-) end hydrolyzes GTP and detaches (see **Fig. 1.1 b**), a finding supported by another study (Yang et al. 2017). Noteworthy, septal wall in *E. coli* seems to be synthesized independently of FtsZ treadmilling, while the synthesis speed in *B. subtilis* appears to be coupled to treadmilling speed, in which case the cytokinesis rate scales with FtsZ treadmilling velocity (Bisson-Filho et al. 2017; Yang et al. 2017; Krupka and Margolin 2018).

It is still unclear and debated how the Z-ring generates enough force for the actual constriction of a cell. It has been proposed that sliding FtsZ filaments can exert enough force to bend membranes, opposed to the theory that localized PG synthesis and assembly is the rate-limiting step that deforms the membrane (Osawa et al. 2009; Osawa and Erickson 2013; Szwedziak et al. 2014). One reasonable theory is therefore a combination of both: each deformation by FtsZ filaments could be accompanied by FtsZ scaffolded reinforcement of local synthesis of PG, reducing the sufficient energy for constriction and stepwise construction of the invaginating septum (Bisson-Filho et al. 2017).

When the division septum closes, cells need to employ enzymes that locally remodel and hydrolyze the cell wall to split the two daughter cells, which is performed by cell well hydrolases, which can be classified as amidases, glycosidases and/or peptidases, depending on their catalytic domain(s), reviewed in (Vermassen et al. 2019). Thereby, amidases seem to have the most prominent role in cell separation of *E. coli*, where AmiA, AmiB and AmiC are mandatory to release daughter cells, with mainly AmiC being responsible for septum cleavage (Heidrich et al. 2001; Typas et al. 2012; Vermassen et al. 2019), whilst endopeptidases or the LytM family are also involved (Typas et al. 2012). In *B. subtilis*, the CwlO and LytE endopeptidase autolysins are important for cell growth and elongation (Bisicchia et al. 2007), and have also been shown to be regulated by FtsEX (Dominguez-Cuevas et al. 2013), two divisome proteins that activate septum splitting enzymes in *E. coli* (Uehara et al. 2010). It remains enigmatic, how membrane fusion after division is carried out exactly, or which factors are involved (den Blaauwen et al. 2017).

Even though the last steps of division have not nearly been investigated to the same extent as the initial steps, a recent study suggest that the divisome components are dissembled step-wise after cytokinesis, a process comprising roughly 15% of the total cell cycle in *E. coli* (Soderstrom et al. 2016).

On a closing note of this chapter, it should be mentioned that regardless of the high conservation of FtsZ throughout bacterial species, several fascinating exceptions to the rule of "one Z-ring that constricts a bacterial cell perpendicular to its long axis" have been identified, of which some can be found in this review: (Eswara and Ramamurthi 2017). A very exotic example of this is a

gamma-proteobacterium now referred to as *Candidatus Thiosymbion oneisti*, which lives in a symbiotic relationship with the marine nematode *Laxus oneistus*, on which it grows as a monolayer attached only via one pole of the cell. This bacterium divides through its long axis instead of perpendicular to it, but nevertheless via FtsZ, which forms an elliptical and discontinuous ring like structure (Leisch et al. 2012). The same group identified two other gamma-proteobacterial symbionts of marine nematodes, that are 45 µm and 120 µm long, respectively, and still divide quite precisely at midcell via FtsZ (Pende et al. 2014). Furthermore, plenty bacteria that divide without FtsZ or an homologue have been reported (Erickson and Osawa 2010; Eswara and Ramamurthi 2017).

1.1.2. Peptidoglycan and the divisome

One feature unique to bacteria and required for shape integrity is the composition of their cell wall, which is made of PG, a peptide-crosslinked sugar polymer. The building blocks for this are alternating N-acetylglucosamine (GlcNAc) and N-acetylmuramic acid (MurNAc), which are β-(1,4) linked and decorated with a short peptide of 4-5 amino acids. Crosslinking these peptides creates the mesh-like PG layer, which ranges from few nanometers (nm) in height in Gram-negative bacteria up to 30-100 nm in Gram-positive bacteria (Booth and Lewis 2019). The PG layer is essential for bacterial cells, as it maintains their structural integrity, a feature most vital for many cellular processes, as it has been shown very recently for DNA segregation in *B. subtilis* (Wu et al. 2020). Consequently and as mentioned above, this integrity has to be maintained throughout the cell cycle, including cytokinesis. Hence, all steps towards division need to be coordinated with PG synthesis and incorporation, e.g. in septal growth. This includes localized cell-wall hydrolysis, since new PG can only be incorporated into the mesh if a gap for insertion has been created previously. Synthesis of PG is carried out by the Penicillin-binding proteins (PBPs), which owe their name to their affinity for Penicillin.

Two proteins that are required and essential for septal PG synthesis and incorporation during division are enzymes that are recruited in the "late divisome": FtsW and FtsI (Pogliano et al. 1997; Mercer and Weiss 2002). While the exact function of FtsW is still somewhat unclear and debated (den Blaauwen et al. 2017), the groups around Bernhardt and Rudner hypothesized in 2016 that FtsW is a peptidoglycan glycosyltransferase due to specific homologies with RodA (Meeske et al. 2016). For decades, lipid II flipase activity of FtsW had been suspected (Holtje 1998), and could first be demonstrated in 2011, at least in vitro (Mohammadi et al. 2011), while the in vivo relevance is still unclear. In contrast, FtsI (PBP3) has been well characterized as transpeptidase that crosslinks the peptide moieties of GlcNAc and MurNAc (Spratt and Pardee

1975; Botta and Park 1981), and has therefore been identified as a key septal synthesis protein (Nguyen-Disteche et al. 1998). Thus, septal wall construction relies on FtsI and FtsW, but also utilizes other proteins like the non-essential bifunctional transpeptidase-transglycosylase PBP1b (Nakagawa and Matsuhashi 1982). Furthermore, the mature divisome includes proteins that bridge the interactions between the proto-ring and these PBPs, and others whose functions are still unknown (Haeusser and Margolin 2016).

1.1.3. Spatio-temporal control of division: Positive regulation

Just like eukaryotes, bacteria have evolved different control mechanisms ensuring cell division happens at the right "time and place", as it is not only a fundamental process in the bacterial life cycle, but also needs to be coordinated to ensure correct segregation of DNA. Due to the huge variety of shapes and lifestyles in the bacterial domain, it is even more impressive how similar but also different some of the mechanisms are that have been uncovered. Since not all control mechanisms can be covered in this section, it will be focused on a selection of rather well established ones. The majority of the well-understood spatio-temporal control systems revolve around controlling the almost universally conserved FtsZ, and timing and placement of the corresponding Z-ring, as it defines the divisional plane. Generally, these systems can be divided into two types of regulation, positive and negative. While negative regulation usually inhibits polymerization of FtsZ in positions different from the geometric center of the cell, positive regulation typically facilitates and reinforces Z-ring polymerization at the conventional divisional plane.

One example for positive regulation was identified in the Gram-positive actinobacterium *Streptomyces coelicolor* (**Fig. 1.2 a**). Even though FtsZ is dispensable in this organism, it is conserved, but apparently only utilized in sporulation (McCormick et al. 1994). During this process, the divisome component SsgB directly recruits FtsZ and promotes polymerization (Willemse et al. 2011). SsgB in turn is recruited to sporulation sites via SsgA, which can induce Z-ring formation directly when artificially overexpressed (Willemse et al. 2011).

Another fascinating form of positive regulation is exhibited by *Myxococcus xanthus*, a Gram-negative delta-proteobacterium (**Fig. 1.2 b**). Here, the PomXYZ system regulates positioning of Z-rings through interaction with the nucleoid (Treuner-Lange et al. 2013; Schumacher et al. 2017). PomZ, a ParA/MinD-type ATPase, binds the nucleus, forming a self-assembling complex with PomX and PomY that localizes to midcell, and stimulates division there (Schumacher et al. 2017). Positioning of this complex in the cell center is achieved by PomZ dependent translocation, which itself is positioned through a flux-based mechanism.

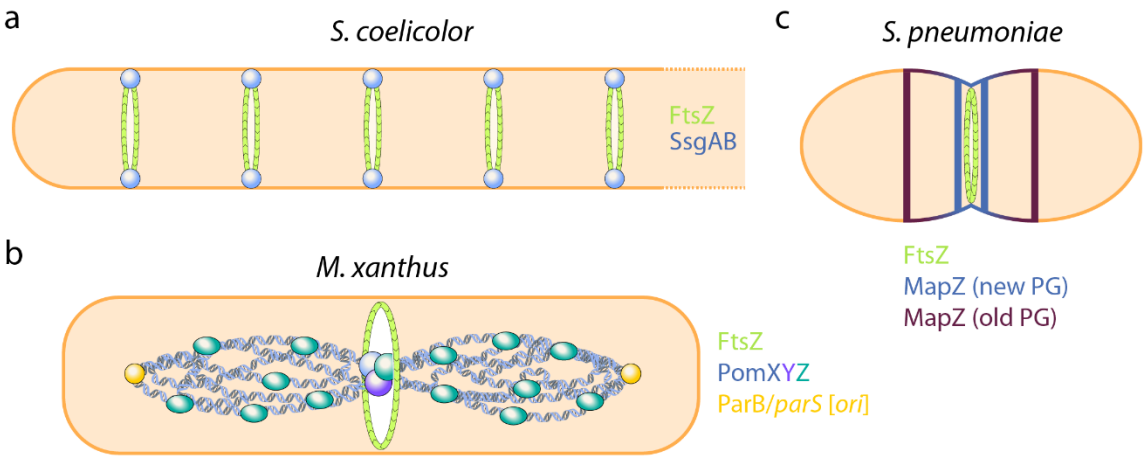

Fig. 1.2: Examples of positive regulation of division-site selection.

(a) *S. coelicolor* utilizes SsgAB during sporulation to recruit FtsZ and stimulate polymerization in sites of sporulation. **(b)** *M. xanthus* employs the PomXYZ system to place the division-site through interaction with the nucleoid. PomZ binds the nucleus and forms a self-assembling complex with PomX and PomY, which then moves toward midcell via a biased random walk, where it stimulates division. **(c)** In *S. pneumoniae*, the membrane protein MapZ is solely determining the division site. It localizes as a ring at the division-site where it facilitates FtsZ assembly. A subpopulation will bind PG at the division-site and move bidirectionally toward the cell centers of the future daughter cells, where it will aid the next division.

PomXYZ complexes diffuse on the nucleoid, exhibiting a biased random walk toward midcell. PomZ dimers also diffuse on the nucleoid, but significantly faster, and can attach to the PomXYZ complexes, but also detach and only re-attach to DNA after a delay, during which they freely diffuse until ATP is regenerated (Schumacher et al. 2017). This leads to a flux imbalance and consequently the intracellular asymmetry of PomXYZ is converted to a local PomZ concentration gradient. This gradient equalizes at midcell, as proteins diffuse from both sides of the nucleoid. This restrains motion in the center, leading to division precisely at midcell without involvement of a local spatial cue besides the nucleoid.

Another example of positive regulation concerns *Streptococcus pneumonia* (**Fig. 1.2 c**). These Gram-positive bacteria of ovoid shape rely on the membrane protein MapZ (LocZ) for placement of the division-site (Fleurie et al. 2014; Holeckova et al. 2014). MapZ appears to act independently of other proteins as all-in-one system, and is only conserved in the *Lactobacillales* families of *Enterococcaceae* and *Streptococcaceae* (Garcia et al. 2016). This transmembrane protein possesses an extracellular domain that can bind nascent peptidoglycan at the division-site (Manuse et al. 2016). It is found in a ring structure at the future division-site in the center of the cell, co-localizing with the later arriving FtsZ, where it recruits divisome proteins (Fleurie et al. 2014; Holeckova et al. 2014). When the cell elongates, the ring divides into two rings that move apart at the same rate as the cell elongates. Finally, a new, third ring forms at the constricting division-site and prevails until constriction is finished. Absence of MapZ in these studies produced aberrant division-site placement and anucleate minicells (Fleurie et al. 2014).

In a more recent study, this simple model of positive regulation through MapZ was however challenged, and instead, the group around Jan-Willem Veening demonstrated interdependence between DNA replication, chromosome segregation and division-site selection in *S. pneumoniae* (van Raaphorst et al. 2017). By in-depth analysis of chromosome segregation and DNA replication, the authors revealed a crucial link between proper segregation of the *oriC* and correct division-site selection. In contrast, MapZ is shown to be critical for placing the Z-ring in the correct angle, perpendicularly to the length axis of the cell, and is therefore suggested to rather identify but not select the site of division, whose position was not affected in the length axis in Δ*mapZ* cells (van Raaphorst et al. 2017). It should be noted that the study revealed a synthetic phenotype of *mapZ* mutants when combined with a FtsZ-mCherry fusion, that was formerly considered functional (Boersma et al. 2015) and might have perturbed previous analyses. Furthermore, *S. pneumoniae* strains with different genetic backgrounds have displayed dissimilar phenotypes in *mapZ* mutants (Fleurie et al. 2014; Holeckova et al. 2014; van Raaphorst et al. 2017), impeding the creation of a general model for division-site selection. This represents a general problem in bacteriology, as high mutation rates and repeated cultivation under laboratory conditions can lead to adaptation and thus a shift in the genotype (Clerc et al. 1998; Schloter et al. 2000), which, when undetected, can result in different experimental outcomes between strains.

1.1.4. Spatio-temporal control of division: Negative regulation

The most established systems of negative regulation are the Min system and nucleoid occlusion (NO), which will be discussed in detail later in this chapter. These systems keep Z-rings from forming at the poles (Min system, **Fig. 1.3 c** and **d**) and over the nucleoid (NO), respectively. Producing a similar outcome, another mechanism of negative regulation was observed in the Gram-negative alpha-proteobacterium *C. crescentus*, which lacks both NO and the Min system. Instead, the ParA-like ATPase MipZ is in charge of ensuring correct localization of the Z-ring. Similar to the Min system, it does so by inhibiting FtsZ polymerization close to the poles, in this case via direct interaction with FtsZ, displacing it (**Fig. 1.3 a**). MipZ itself forms a concentration gradient from poles towards midcell by directly interacting with ParB-*parS* complexes (Thanbichler and Shapiro 2006; Kiekebusch et al. 2012). These complexes are DNA-bound close to the *oriC* at the flagellated pole, and re-localize together with the newly replicated *oriC* to the nonflagellated pole (Thanbichler and Shapiro 2006; Eswara and Ramamurthi 2017). This mechanism allows FtsZ to polymerize only at the cell center, while MipZ depleted cells display aberrant division patters that produce anucleate minicells, miniswarmer cells and elongated stalked cells (Thanbichler and Shapiro 2006).

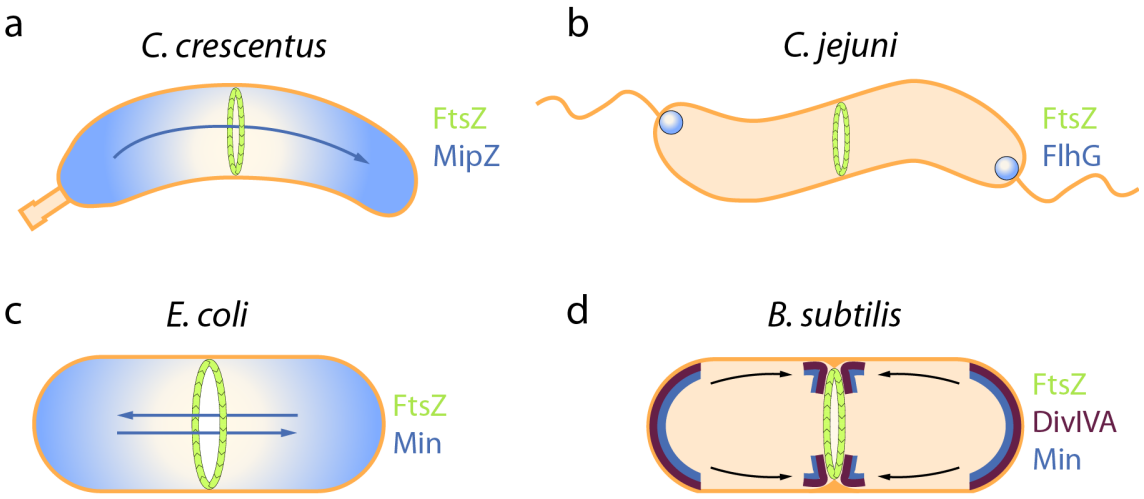

Fig. 1.3: Examples of negative regulation of division site placement.

(a) *C. crescentus* achieves central positioning of FtsZ due to a bipolar concentration gradient of the FtsZ-inhibitor protein MipZ, which directly interacts with ParB-*parS* complexes. **(b)** In *C. jejuni*, the regulator of flagellar number FlhG also inhibits FtsZ from polymerizing close to the poles. **(c)** FtsZ in *E. coli* can only polymerize at midcell due to the Min system, which oscillates from pole-to-pole, creating a time-resolved minimal concentration of the FtsZ-inhibitor MinC in the cell center. **(d)** *B. subtilis* also contains a Min system, which does not oscillate. Instead, it was reported to form a stable concentration gradient decreasing from poles and newly formed septa, held in place by the curvature sensing DivIVA. It is involved in prevention of re-initiation of division at new poles (old septa) and may be involved in divisome disassembly.

A different mechanism for negative division-site selection is used by the amphitrichous (bipolar) flagellated *Campylobacter jejuni*, a Gram-negative epsilon-proteobacterium (**Fig. 1.3 b**). It lacks a Min system, but the regulator of flagellar number (FlhG) in concert with components of the amphitrichous flagella inhibits FtsZ from initiating division at the poles (Balaban and Hendrixson 2011). In absence of FlhG, minicells are formed frequently, cells grow larger and more flagella per pole can be observed (Balaban and Hendrixson 2011; Gulbronson et al. 2016). FlhG is thereby another example of a MinD/ParA-type ATPase involved in regulating division-site selection. In the peritrichous (uniformely flagellated) *B. subtilis,* however, FlhG together with FlhF produce flagella in a grid-like pattern in the cell center absent from the poles, different from bacteria that possess polar flagella (Guttenplan et al. 2013), and are not involved in division-site selection.

1.1.4.1. Nucleoid occlusion

In *E. coli* and *B. subtilis,* the systems that were identified to influence Z-ring positioning are NO (Wu and Errington 2004; Bernhardt and de Boer 2005) and the Min system, both representing negative regulation, reviewed in (Tsang and Bernhardt 2015). NO prevents cytokinesis over the chromosome (Woldringh et al. 1991), but the precise mechanism appears to be different between

E. coli and *B. subtilis*. While the protein SlmA (*E. coli*) has been shown to directly inhibit FtsZ polymerization or promote disassembly of polymers (Tonthat et al. 2011; Cho and Bernhardt 2013), the direct target of Noc (*B. subtilis)*, a homologue to the chromosome segregation factor ParB, is unknown. Nevertheless, SmlA and Noc are considered functional homologues, as they do not share sequence homology, but exhibit comparable functions. Both proteins bind to specific DNA sequences that are dispersed all over the chromosome, except proximal to the replication terminus (ter) containing region (Wu et al. 2009; Tonthat et al. 2011). Furthermore, cells with deficiencies in the respective NO gene are almost indistinguishable from wild type cells when grown under normal conditions, but display synthetic lethality when the Min system is absent or not functional (Wu and Errington 2004; Bernhardt and de Boer 2005). Consequently, the NO system has been described as divisional "insurance policy" in *E. coli* and *B. subtilis* (den Blaauwen et al. 2017). It might play a more important role in other organisms like the Gram-negative *Vibrio cholera*, where it seems to be more heavily involved in positioning and timing of the Z-ring (Galli et al. 2016; den Blaauwen et al. 2017).

1.1.4.2. The Min system in *E. coli*

The second system known in *E. coli* and *B. subtilis* is the Min system, which is one major focus of this thesis, and will therefore be described in detail. The Min system was first identified in *E. coli* (Adler et al. 1967) and later in *B. subtilis* (Reeve et al. 1973) (**Fig. 1.3 c-d** and **Fig. 1.4)**. Mutations in the respective genes led to the production of elongated rods and "mini"-cells that do not contain genetic material (Jaffe et al. 1988; de Boer et al. 1989). The system suppresses the formation of division rings close to the poles (de Boer et al. 1989) and may aid in the disassembly of divisome components in *B. subtilis* (van Baarle and Bramkamp 2010). In *E. coli*, the Min system has been characterized extremely well both experimentally (Hu and Lutkenhaus 1999; Hu et al. 1999; Hu et al. 2002; Loose et al. 2008; Park et al. 2011) and theoretically (Huang et al. 2003; Fange and Elf 2006; Halatek and Frey 2012; Hoffmann and Schwarz 2014; Wu et al. 2016; Denk et al. 2018; Halatek and Frey 2018). It comprises three proteins: MinC, D and E. The active inhibitor of FtsZ polymerization and scaffolding in the Min system is MinC, which interacts directly with FtsZ (Hu et al. 1999; Dajkovic et al. 2008). Since MinC is unable to recruit or position itself to a specific locus, it can be described as "cargo" of MinD, a Walker-type AAA+ ATPase. MinD dimerises in its ATP-bound form, and binds the membrane upon dimerisation, recruiting MinC (de Boer et al. 1991; Hu and Lutkenhaus 2003). The ATPase activity of MinD is stimulated by the third protein, MinE, which forms a ring that moves along the longitudinal axis of the cell, thereby detaching MinCD complexes (Raskin and de Boer 1997; Hu et al. 2002). This interaction leads to a fascinating standing wave oscillation of MinCD traveling from pole

to pole, resulting in a time-resolved minimal concentration of MinC around midcell, where FtsZ is then allowed to polymerize into a ring (Hu and Lutkenhaus 1999; Raskin and de Boer 1999).

In vitro experiments and mathematical modelling of the Min system

Since the Min system is a prime example of an intracellular pattern-forming system, many in-vitro experiments have been performed to characterize the capabilities of reaction-diffusion systems. The Schwille Lab e.g. developed an expertise in producing standing wave oscillations on supported lipid membranes utilizing the Min proteins (Loose et al. 2008; Loose et al. 2011), also demonstrating their behavior in different settings of confinement (Schweizer et al. 2012). Combining in vivo/vitro experiments with theoretical modelling can help to reveal functional relevance of experimentally observed behaviors. Mathematical modelling demonstrated e.g. the importance of conversion of MinD-ADP to its ATP bound form for correct localization of FtsZ at midcell (Halatek and Frey 2012). Another example concerns MinE, which was observed biochemically to switch between conformations, dependent on MinD (Park et al. 2011). Thereby, the "latent" conformation describes a state where MinE is cytosolic and freely diffusive, while, in its "active" conformation, MinE is bound to MinD and the membrane (Park et al. 2011). In vitro experiments coupled to mathematic modelling later revealed this switch to be critical for the robustness of Min pattern against variations in protein concentrations (Denk et al. 2018), thereby determining the boundaries and robustness of this self-organizing protein system.

1.1.4.3. The Min system in *B. subtilis*

B. subtilis expresses MinCD but lacks MinE or an equivalent protein, and hence no oscillation of MinCD was observed. Instead, the coiled-coil protein DivIVA is the spatial determinant of the system. DivIVA does not directly interact with MinCD, but instead recruits the transmembrane scaffolding protein MinJ, which in turn recruits MinCD (see **Fig. 1.4, right**). Due to the lack of oscillation, the *Bacillus* Min system was classically categorized as a rather stable gradient when observed via conventional fluorescence microscopy (Haeusser and Margolin 2016). Before membrane invagination at the divisional septum, MinCDJ concentrations are highest at the poles and decrease towards midcell, allowing FtsZ to polymerize there. However, it was shown later that upon invagination of the membrane, DivIVA and therefore MinCDJ partially re-localize to the site of division, establishing a new polar gradient for the daughter cells when the septum closes (Bramkamp et al. 2008). Surprisingly, FtsZ rings still form in regular intervals in cells lacking DivIVA or MinJ, but rarely constrict (Bramkamp et al. 2008), suggesting a MinCDJ function downstream of division-site

selection. Furthermore, the Z-ring still positions precisely at midcell in the absence of both NO and the Min system in *B. subtilis* (Rodrigues and Harry 2012), suggesting that a yet unknown mechanism is responsible for division-site selection in *B. subtilis*.

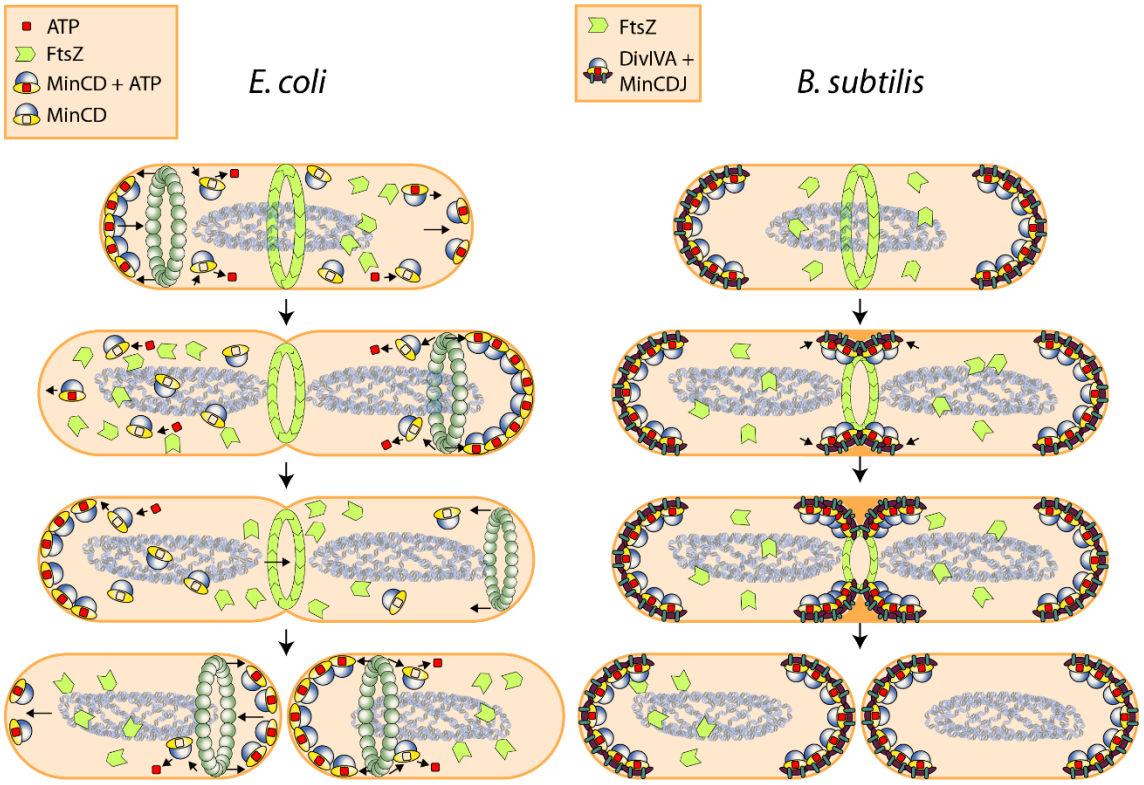

Fig. 1.4: Cartoon of the Min system in *E. coli* and *B. subtilis*.

(Left) In ***E. coli***, MinE laterally moves through the cell, stimulating MinD ATPase activity, thereby detaching MinCD complexes from the membrane. After ATP regeneration of MinD, these complexes will bind the membrane at the opposite pole, leading to a time-resolved oscillation of MinCD, allowing FtsZ only to polymerize at the cell center. Free FtsZ displays similar oscillation in response to MinC, lagging behind it. Close to cell division, oscillation will not surpass the septum (not shown), possibly to ensure equal distribution of Min proteins. Upon division, both daughter cells inherit an oscillating Min system. **(Right)** In ***B. subtilis***, DivIVA localizes to the negatively curved poles, where it recruits MinJ and in turn MinCD, leading to a bipolar gradient. Attracted by the strong negative curvature, a fraction of DivIVA localizes to midcell upon septum formation, recruiting MinCDJ. In daughter cells, both poles inherit a Min gradient, which inhibits re-initiation of division at the new pole.

DivIVA

DivIVA was first associated with cell division through mutational studies, where a point mutation in the *divIVA* locus produced a *ΔminCD* like phenotype, giving rise to the production of anucleate minicells (Reeve et al. 1973). While MinE in *E. coli* had already been characterized as the topological specificity factor of the Min system (de Boer et al. 1989), a corresponding homologue in *B. subtilis* could not be identified at the time. Later, in 1996, the *divIVA* minicell locus was first proposed to be involved in functional replacement of MinE in *B. subtilis*

(Rothfield and Zhao 1996). Around a year later, a study mapped and analyzed the coding region of *divIVA* and the respective *divIVA1* mutation, and also predicted it to encode a piloting protein that directs MinCD to polar septation sites (Cha and Stewart 1997). Localization of DivIVA was demonstrated shortly after in a study of the group around Jeff Errington, which first cloned the *divIVA* gene and utilized a DivIVA-GFP fusion that indeed targeted cell division-sites (Edwards and Errington 1997). After several more studies, the role and timing of DivIVA in sequestration of MinCD to the cell poles became clearer and confirmed previous predictions, as it appeared to recruit MinD to midcell directly before septal constriction, a late step during division (Marston et al. 1998; Marston and Errington 1999).

In succession to this work, a weak sequence similarity to many eukaryotic proteins like myosin, utrophin and especially tropomyosin was detected, all sharing a α-helical coiled-coil structure (Lupas et al. 1991; Edwards et al. 2000). Tropomyosin and its isoforms are cytoskeletal elements interacting with individual actin filaments in metazoan and fungi, thereby typically regulating the contraction of skeletal muscle, summarized in an excellent review by (Gunning et al. 2015). These coiled-coil proteins fold in a single α-helix, and dimerize in parallel when in solution (Gunning et al. 2015). Along the length of actin filaments, they form large polymers in a head-to-tail fashion (Gunning et al. 2015). When the structure of DivIVA was finally resolved, presence of a similar coiled-coil region could be confirmed (Oliva et al. 2010). Functionally, the protein can be divided in two domains, the N-terminal (Nt) and the C-terminal (Ct) domain, connected by a short, flexible linker (Lenarcic et al. 2009; Oliva et al. 2010), shown in **Fig. 1.5**. The Nt of DivIVA forms a paralleled coiled-coil, thereby exposing positively charged and hydrophobic residues at the loops that cap the protein and enable membrane binding (Oliva et al. 2010). The Ct on the other hand revealed a coiled-coil tetramer when crystalized (Oliva et al. 2010), involved in oligomerization of DivIVA into larger multimers, which however appeared to be tail-to-tail oriented.

DivIVA itself localizes to the division septum and polar regions of the cell, as these areas contain negative curvature (Lenarcic et al. 2009). At the division septum, this structure can be observed as a double-ring when highly resolved (Eswaramoorthy et al. 2011; Stockmar et al. 2018). The ability to "sense" curvature is most likely based on the elongated structure of DivIVA and its ability to self-interact and form multimers (Stahlberg et al. 2004; Lenarcic et al. 2009). These multimers favor molecular bridging of areas with specific, negative curvature, where the protein will bind the membrane and accumulate, according to the crystal structure and mathematical modelling (Stahlberg et al. 2004; Lenarcic et al. 2009; Oliva et al. 2010).

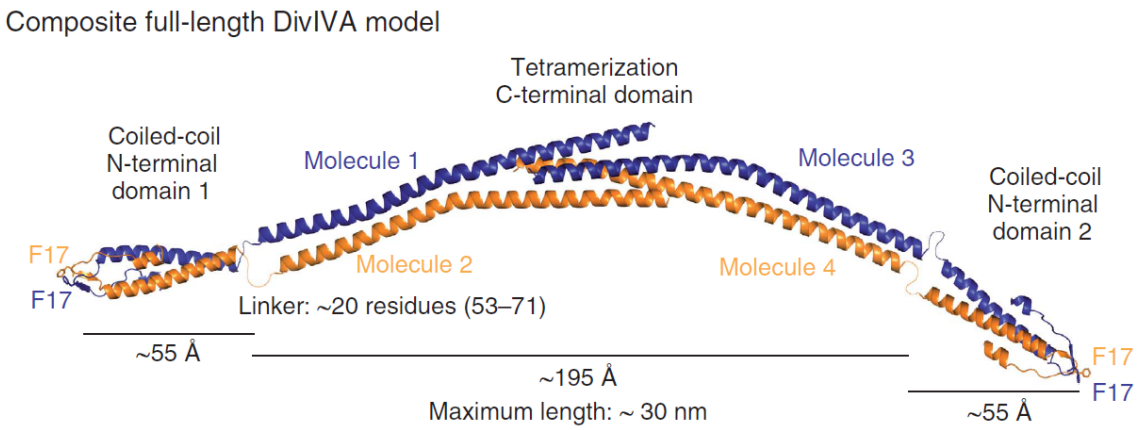

Fig. 1.5: Composite model of full-length *B. subtilis* DivIVA.

The N- and C-terminal domains of DivIVA, individually made from crystal structures, can be unambiguously joined because they are both parallel coiled-coils. The linker region (of about 20 residues) is likely flexible (as deduced from the NMR data). Overall length is ~30nm when fully extended but if the linkers are flexible, the N-terminal domains could swing around, producing kinked and shorter conformations. Note F17 and R18, important for membrane binding, which are exposed at the two tips of the molecule. This finding and the curvature are somewhat reminiscent of eukaryotic BAR domains, although it is possible that the curvature shown for DivIVA is in fact induced by crystal packing. Figure and figure description from Figure 6.A in (Oliva et al. 2010), used with permission from publisher.

DivIVA has a second, distinct function during sporulation, which will be discussed later. Interestingly, the Gram-positive cocci *Streptococcus pneumonia* and *Staphylococcus aureus* possess a conserved DivIVA homologue, despite lack of a Min system or the ability to sporulate. In the case of *S. pneumonia*, deletion of DivIVA results in severe growth inhibition and strong defects in cell division and chromosome segregation, and protein interaction studies revealed possible interactions with cell division proteins (Fadda et al. 2003). Furthermore, DivIVA plays an important role in the Gram-positive bacteria *Corynebacterium glutamicum* and *Streptomyces coelicolor*, where it is essential for polar growth and morphogenesis (Flardh 2003; Letek et al. 2008). DivIVA is however also found in Gram-negative organisms, e.g. some *Oligoflexia* and delta-proteobacteria (Akiyama et al. 2003), and its role in controlling progeny morphology in the predatory bacterium *Bdellovibrio bacteriovorus* was just demonstrated recently (Milner et al. 2020).

MinJ

For a long time, a direct interaction between DivIVA and MinD was proposed but could not be demonstrated, until MinJ was discovered as the “missing link”, bridging MinD and DivIVA (Bramkamp et al. 2008; Patrick and Kearns 2008). MinJ is conserved in *Bacillus, Listeria* and a few L*actobacillus* species, but has not yet been identified in other bacteria. It remains the most enigmatic protein of the Min system of *B. subtilis*, as no structural data could be obtained to

date, nor could another concrete function or mechanism besides scaffolding DivIVA and MinD be identified, even though it its very likely it plays a role in divisome disassembly (van Baarle and Bramkamp 2010). According to protein prediction databases, it is a transmembrane protein with 6-8 transmembrane helices and contains a PDZ domain near its C-terminus. When protoplasts expressing MinJ, either N- or C-terminally fused to green fluorescent protein (GFP), were exposed to proteolysis via Proteinase K, both fusion proteins retained fluorescence inside the cell (van Baarle and Bramkamp 2010). Loss of fluorescence would have indicated degradation of GFP, which should only occur for outward facing helices, thereby exposing GFP to the protease. Instead, this outcome favors a model with six transmembrane helices, with both termini pointing towards the inside of the cell. PDZ domains are often associated with protein-protein interactions between signaling and cytoskeletal proteins and frequently aid in ion channel signaling and other signal transduction systems (Jemth and Gianni 2007; Lee and Zheng 2010), but are also utilized for protein transport and even proteolysis (Ponting 1997).

In *ΔminJ* mutants, cells are extremely long, filamentous and produce a high number of minicells (Bramkamp et al. 2008; Patrick and Kearns 2008; van Baarle and Bramkamp 2010). Previous work from our lab characterized MinJ via truncation studies, where the presence of one or two transmembrane helices (TM1 or TM1+TM2) was sufficient to complement the *ΔminJ* cell-elongation phenotype, albeit their sole presence still led to a high number of minicells. Remarkably, the expression of the soluble PDZ domain alone already reduced the *ΔminJ* cell-elongation phenotype, although to a much smaller extent (van Baarle and Bramkamp 2010). Noteworthy, this soluble, GFP-fused construct lost its membrane association as expected. The same study suggests a role of MinJ in the localization and disassembly of divisome components: First, the FtsZ anchor FtsA, fused to GFP, frequently remained at previous division sites (new poles) in *ΔminJ* mutants, where it often could be observed as a double-ring. In contrast, it disappears from the septum after division in wild type cells, and usually only forms one ring around midcell (van Baarle and Bramkamp 2010). Second, the late division proteins PBP-2B and FtsL, both fused to GFP, failed to form rings at midcell in absence of MinJ, except for very rare septa (van Baarle and Bramkamp 2010). In wild type strains, these proteins are found at midcell during division and at the new poles only briefly after division, with only small amounts of protein at the poles. PBP-2B-GFP remained at these sites in *ΔminJ* mutants. To inhibit reassembly of the divisome, FtsZ was depleted in the same genetic background, leading to an even higher amount of PBP-2B-GFP at the poles, supporting the notion of a failure in divisome disassembly in cells lacking MinJ (van Baarle and Bramkamp 2010). These findings support the role of MinJ and the Min system downstream of cell division, but a distinct mechanism for this remains to be identified. However, these findings were supported very recently by a study which identified a role of the Min system in Z-ring disassembly (Yu et al. 2020). With

microfluidic devices, they could demonstrate involvement of the Min system in cell size maintenance through recycling of FtsZ. Furthermore, the study reports that the Min system inhibits PG turnover, mostly affecting the poles.

One puzzling finding regards the interaction between MinJ and MinD: The overexpression of MinD in a *ΔminJ* strain is lethal, and cells in which the overexpression has just been induced grow to an extreme length (average length 76.4 µm compared to 14.1 µm in *ΔminJ*) before dying (van Baarle and Bramkamp 2010). When overexpressing MinC instead of MinD in the same genetic background, no effect on the cell length can be observed. And even though MinD overexpression also produces filamentous cells in the wild type background (7.3 µm compared to 2.8 µm, (van Baarle and Bramkamp 2010)), this overexpression is not lethal. This apparent divisional block seems to be caused downstream of FtsZ assembly, as FtsA-YFP still localizes correctly in these cells (van Baarle and Bramkamp 2010), but the exact reason for this effect remains elusive.

MinC and MinD

The active Min component that inhibits FtsZ polymerization is MinC, which has been well characterized in *E. coli.* There, it has been shown to actively bind FtsZ and inhibit its bundling and scaffolding function (Hu et al. 1999; Dajkovic et al. 2008; Shen and Lutkenhaus 2010). Both Ct and Nt of MinC interact with FtsZ, while only the Ct interacts with MinD (Hu and Lutkenhaus 2000; Cordell et al. 2001). In vivo, this interaction has been shown to stimulate MinC activity and is required for the formation of MinC dimers (Hu and Lutkenhaus 2000, 2003; Johnson et al. 2004; Park et al. 2018). The well-conserved MinC from *B. subtilis* is attributed with the same functionality. As in *E. coli*, it is a cytosolic protein, which is only localized through interaction with MinD, which in turn recruited by MinJ and thus DivIVA in *B. subtilis*.

MinD belongs to the walker A cytomotive ATPase (WACA) family, which also comprises ParA-like proteins, typically involved in chromosome (or plasmid) segregation and sharing several biochemical features (Ebersbach and Gerdes 2005; Gitai 2006). Similar to MinC, most (in-vitro) experiments have been performed on *E. coli* MinD, while MinD in *B. subtilis* is well conserved and expected to behave similarly. Upon binding ATP, *E. coli* MinD dimerises, which in turn allows membrane binding through a conserved membrane-targeting sequence (MTS) located in the Ct (Szeto et al. 2002; Hu and Lutkenhaus 2003). With ATP available, MinC and MinD form alternating co-polymers that can assemble in cytomotive filaments in vitro, which inhibit FtsZ bundling locally (Ghosal et al. 2014; Conti et al. 2015). The importance of the ATPase domain for activity and localization of MinD has also been demonstrated in *B. subtilis*: When ATP

hydrolysis or nucleotide binding was impaired through specific point mutations in the ATPase domain (G12V and K16A, respectively), the specific localization of MinD and MinC to poles and septa was abolished (Karoui and Errington 2001).

While MinE in *E. coli* stimulates ATP hydrolysis of MinD and in consequence membrane detachment, a corresponding factor or stimulus has not yet been identified in *B. subtilis*. Another open question is hence, how exactly the Min system in *B. subtilis* is able to self-regulate. Upon septum formation, the proteins have to partially reposition and stabilize there, away from the poles, which likely includes membrane detachment of MinD. Therefore, it is likely that MinD ATPase activity in *B. subtilis* is stimulated by a yet unknown factor. Furthermore, the mechanistic difference between the oscillatory *E. coli* Min system and the rather stable *B. subtilis* Min system raises the question for the reason of these functional differences. This can at least be partially explained, as *B. subtilis* has the ability to sporulate. This alternative mode of division produces asymmetric daughter cells and hence requires a division septum in an asymmetric position. When the oscillating *E. coli* Min system is expressed in *Bacillus*, cells are unable to sporulate (Jamroskovic et al. 2012).

1.2. Sporulation of *Bacillus subtilis* as a second mode of division

B. subtilis is an almost ubiquitous bacterium, as it can adapt to various conditions in the environment. Amongst other things, these adaptations include the uptake of foreign DNA, motility, biofilm formation and sporulation (Rao et al. 2008; Burton and Dubnau 2010; Vlamakis et al. 2013; Tan and Ramamurthi 2014). When it encounters environmental or nutrient stress, it can thus switch to a second mode of division called sporulation, which produces one endospore instead of two daughter cells. These spores are highly resistant to external influences like heat or UV light, and can remain dormant for an extreme amount of time, until conditions that are more favorable are encountered, leading to germination and restoration of the vegetative cell cycle (Tan and Ramamurthi 2014). When sporulation is induced, division switches to an asymmetric mode, leading to the formation of a small, polar localized prespore/forespore and a larger mother cell. The mother cell later engulfs the prespore, which in turn differentiates and builds up several protective layers in a complex interaction between the two, reviewed in detail by (Tan and Ramamurthi 2014). In the final step, the mother cell lyses, releasing the endospore.

In the switch from vegetative to asymmetric division, the most important protein is the transcriptional master regulator Spo0A, which is also involved in biofilm formation (Hamon and Lazazzera 2001). Upon being activated through a phosphorelay system in response to e.g. starvation, Spo0A regulates the expression of around 121 genes, including sporulation genes

(Molle et al. 2003; Tan and Ramamurthi 2014). Different subsets of genes can thereby be activated, regulated by the level of Spo0A activation (Fujita et al. 2005). Contrary to vegetative division, the replicated chromosomes are not segregating to quarter positions. Instead, they form an elongated structure from pole-to-pole, the axial filament, where the *oriCs* are tethered to the poles (Ryter et al. 1966; Ben-Yehuda et al. 2003). An early indicator of asymmetric division is the following migration of increasingly produced FtsZ from midcell to both poles in a spiral trajectory, forming one ring close to each pole, respectively (Ben-Yehuda and Losick 2002). Only one of the two rings will be active and form a septum over one of the two chromosomes, which is then pumped into the prespore by DNA transporter protein SpoIIIE (Wu and Errington 1994), as asymmetric division proceeds.

DivIVA was shown to be involved in the process of alternative chromosome segregation during sporulation (Thomaides et al. 2001), where it sequesters and anchors the *oriC* to the pre-spore cell pole in cooperation with RacA and Soj-Spo0J (ParB) (Wu and Errington 2003). This model was extended later, when MinD and MinJ were also demonstrated to play a role in the Soj-Spo0J pathway during prespore chromosome segregation (Kloosterman et al. 2016). While MinJ likely just bridges between MinD and DivIVA, MinD was found to be essential for correct positioning and trapping of the *oriC* in the prespore (Kloosterman et al. 2016).

1.3. Super-resolution microscopy techniques

To understand organisms, their functioning principles and the underlying molecular mechanisms, it is essential to be able to observe them. However, biological specimens are generally very small. While eukaryotic cells have a typical size between 10-100 µm, bacteria are even smaller, with an average *B. subtilis* cell size of 2.8 µm in length and 0.8 µm in width. Therefore, microscopy is a very powerful and versatile tool in biological sciences, allowing magnification, visualization and consequently analysis of individual bacterial cells. Microscopy has come a long way: from the simplest form of magnification (magnifying lens, around 13th century) over the first documented records of microscopes (17th century) to the seemingly countless multitude of techniques that are available today. Here, the focus of the section lies on light and fluorescence microscopy, and the principle of single molecule localization microscopy (SMLM) as well as certain analysis techniques that utilize SMLM.

After the discovery of green fluorescent protein (GFP) in 1962, isolated from the jellyfish *Aequorea victoria* (Shimomura et al. 1962), over 30 years passed until it was first utilized as a marker for gene expression (Chalfie et al. 1994). This gave rise to an entirely new field of microscopy, termed fluorescence microscopy. For the first time, proteins could be visualized in-

and outside of cells, soon followed by the discovery and development of other fluorescent proteins (FPs) and colors. Nowadays, FPs and dyes are indispensable in the field of life sciences, and many techniques rely on them, even outside of microscopy. In combination with the development of improved optical systems, it became possible to determine e.g. dynamics, spatio-temporal localization, interaction, co-localization or quantities of protein.

Even though optical systems have improved significantly in the last decades, there is an absolute resolution limit in light microscopy, attributable to the physical properties and wave nature of light. Resolution can be generally defined as the shortest distance between two points that can still be distinguished from each other. The very first step towards identifying the physical parameters of resolution was made through an observation of George Biddell Airy in 1835. He described what is now called Airy pattern, a light diffraction pattern consisting of a central disk surrounded by (Airy) rings declining in intensity with increasing distance to the center. This pattern can be observed when uniform light travels through a circular aperture and hits a plane, being perfectly focused. Years later, Ernst von Abbe coined the phrase of numerical aperture (NA), which is defined as:

$$NA = n * \sin\alpha \qquad \textbf{Eq. 1.1}$$

where n is the refractive index of the surrounding medium and α is the half of the angle of the objectives aperture (Abbe 1873). Related to the observation of Airy pattern, Abbe could formulate the first definition of diffraction-limited resolution. He found that the possible resolution or distance d of an optical system is defined by the relationship between the wavelength of the light λ and the numerical aperture NA (Abbe 1873):

$$d = \frac{\lambda}{2NA} \qquad \textbf{Eq. 1.2}$$

This formula was later refined by Lord Rayleigh, who created a new formula considering Airy's observation and Abbe's formula, which is today known as the Rayleigh criterion or limit (Strutt 1879):

$$d = 0.61\frac{\lambda}{NA} \qquad \textbf{Eq. 1.3}$$

The Rayleigh criterion defines the distance between the center of an airy pattern and its first minimum as the highest achievable resolution in a perfectly aligned optical system, which is around 210 nm for a typical modern microscope set-up in thy x/y-axis and around 500 nm in the z-axis (505 nm green light, 1.45 NA objective).

To push these physical boundaries and achieve even higher resolution, several methods have been developed, most of them utilizing fluorescent protein or dyes. The most established techniques bypassing the diffraction limit of light are 3-dimensional structured illumination microscopy (3D-SIM), stimulated emission depletion (STED) microscopy and photoactivated localization microscopy/stochastic optical reconstruction microscopy (PALM/STORM), of which the latter techniques can be summed up under the term single molecule localization microscopy (SMLM). In 3D-SIM, a laser-based wide-field microscope is equipped with a movable diffraction grating located in the excitation beam path. During imaging, the grating moves (rotation and translation) between single-images, resulting in several different interference pattern on the focal plane. These interferences create Moiré effects, which can be Fourier-transformed to gain information about the total interference pattern (Heintzmann and Cremer 1999). From this, an image can be calculated and deconvolved, which can lead to an improved resolution of around ~100 nm in the x/y-axis and ~ 250 nm in the z-axis, a 2x improvement in spatial resolution (Heintzmann and Cremer 1999; Gustafsson et al. 2008). An advantage of this technique is the acquisition speed, which is considerably faster than SMLM or STED. Furthermore, this technique can be employed with most commonly used fluorophores, allowing the use of already existing strains. Unfortunately, this technique is also prone to artifacts due to the nature of image reconstruction, which includes e.g. pseudo-structures or artifically repeated features ("ghosting") (Demmerle et al. 2017). Moreover, the achievable resolutions are considerably lower when compared to SMLM or STED.

Contrary to 3D-SIM and SMLM, STED is performed on laser-scanning confocal microscopes that are additionally equipped with a donut-shaped depletion laser, which is spatially aligned with the excitation laser. The application of both lasers within a very short timeframe (usually in the picosecond range) will first excite all photon emitters in the range of the excitation laser, but will only allow regular photon emission in the narrow center of the depletion laser (Hell and Wichmann 1994; Klar and Hell 1999). Fluorophores in the range of the ring-shape of the depletion laser are quenched into a higher vibrational level of the ground-state, unable to emit photons (Hell and Wichmann 1994; Klar and Hell 1999). This leads to an effective resolution far beyond the diffraction limit of light (Klar and Hell 1999), down to 20 nm (Gottfert et al. 2013), without the need for image reconstruction. The laser-power thereby tunes the resolution, and there is no need for specialized fluorophores. The drawbacks of this method are however rather high laser-intensities for higher resolutions, which in turn lead to photobleaching (irreversible fluorophore damage) and phototoxicity (cell damage) (Strack 2015). The principle of SMLM, which was used for a variety of experiments in this thesis, will be explained in more detail in the next chapter.

1.3.1. Single molecule localization microscopy (SMLM)

When imaging a point shaped object in a wide-field microscope, the image will be projected as a Gaussian distribution rather than a point, due to previously discussed diffraction of light at the objective. This distribution can be described by the point-spread function (PSF). It is possible to determine the center of a PSF mathematically, if it does not overlap with another PSF, to determine its localization with sub-resolution precision (Betzig et al. 2006). To this end, special FPs are used, that will be described in detail in the next chapter. Roughly, these fluorophores can be switched between "on" or "off" states by a laser. The first photoswitching was discovered in GFP and yellow fluorescent protein (YFP) mutants (Dickson et al. 1997), creating the foundation for PALM (Betzig et al. 2006). STORM on the other hand makes use of organic dyes and their photophysical property of inducing blinking (Rust et al. 2006), which however requires specific conditions and buffers (Heilemann et al. 2008). By using a wide-field microscope equipped with tunable lasers, fluorophores are activated over time by an activation laser of low wavelength (typically 405 nm). Starting with low laser intensities that increase over time allows sequential activation of all fluorophores in the field of view. At the same time, an imaging laser excites and subsequently bleaches the activated fluorophores, eventually exhausting every available fluorophore, while a highly sensitive camera records the emission signals (exemplary shown in **Fig. 1.6**, left to right). Due to the stochastic chance of activation, it is unlikely that the imaged PSF of a fluorophore is overlapping with another, allowing very precise localization of the fluorophores center of emission (Betzig et al. 2006). Finally, all frames of the experiment are reconstructed into one image with very high localization precision (**Fig. 1.6**, **right**), which translates to around 10-times increased x/y-resolution compared to diffraction-limited microscopy, dependent on the fluorophore and the experimental set-up. The SMLM experiments presented in this work for instance reached a typical localization precision of around 25 nm (see **Fig. 2.11**).

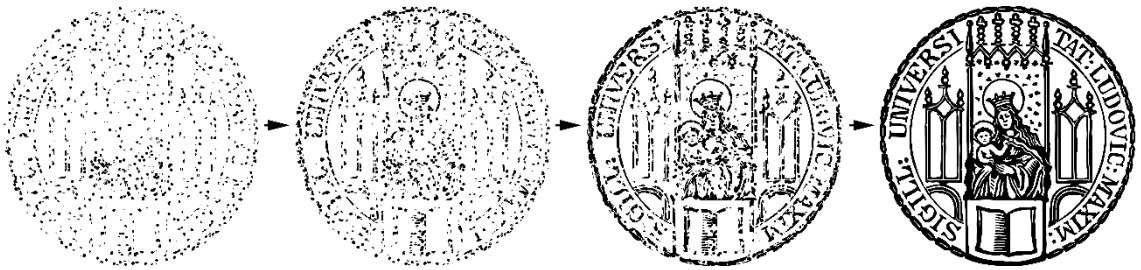

Fig. 1.6: Basic principle of PALM.

By sequentially activating and detecting fluorophores **(left to right)**, it is possible to reconstruct the underlying structure **(right)** with nanometer scale resolution.

In an optimal setting, the localization precision in SMLM only depends on the number of collected photons per event. Therefore, STORM images can generally be of higher localization precision compared to PALM due to increased quantum yields of organic dyes, but the technique does not allow for quantification and needs to be chemically buffered (Rust et al. 2006). PALM on the other hand allows quantitative studies, since FPs are expressed fused to the protein of interest (Annibale et al. 2011; Lee et al. 2012). Due to that, every recorded event theoretically corresponds to one molecule, which however requires careful analysis as well as characterization of the fluorophore for normalization of the data (Sengupta and Lippincott-Schwartz 2012).

One disadvantage of SMLM is the slow acquisition speed, which renders it unfeasible to image structures in live-cells. Due to relative low laser intensities and thus low phototoxicity, it is possible to image live-cells for a short amount of time, but this is rather used for single particle tracking (SPT, or more precisely sptPALM, from here on just referred to as SPT) than for structural analysis (Manley et al. 2008). As proteins in a cell are generally very mobile, live-cell imaging can lead to incomplete or false structures, which renders other super-resolution techniques more suitable (Godin et al. 2014). Hence, cells are often chemically fixed before imaging. Additionally, very dense structures can be problematic to image with high localization precision, as the chances for overlapping photon-emission increases, reducing the effective resolution (Kamiyama and Huang 2012). This can however be tackled by lowering the speed of increase of activation laser and increasing the total number of frames.

Since the final image in SMLM is entirely based on calculated values from recorded localizations, the raw data, a list of recorded events and their characteristics, can be utilized for a variety of point based analysis methods. This includes distance-based analysis like co-localization or cluster formation, but also tracking of single molecules over time in live-cells. Furthermore, since every event is recorded with characteristics like the number of photons collected, localization precision or the size of the PSF, data can be postprocessed to filter or subset the data. When done carefully, this can even be used to separate populations of simultaneously used fluorophores by their photocharacteristics (Rosenbloom et al. 2014), but is more commonly used to filter out artifacts, background signal or autofluorescence from other sources (Stockmar et al. 2018).

The development of STED (Stefan W. Hell) and PALM (Eric Betzig) and the discovery and characterization of photoactivatable fluorophores (William E. Moerner) were awarded with the Nobel Prize in Chemistry in 2014, underlining the importance of microscopy for life sciences.

1.3.1.1. Fluorescent proteins and fluorophores in PALM

The perhaps most important consideration in PALM experiments concerns the choice of the fluorophore(s). Most commonly used fluorophores, e.g. GFP or mCherry (Shaner et al. 2004), cannot be used in traditional PALM, as they do not require activation, and are therefore constantly active when excited via the excitation laser. Hence, PALM utilizes specific fluorophores that are either photoactivatable (PA), photoswitchable (PS) or photoconvertible (PC). These descriptions relate to the possible fluorescent states of the fluorophore. PA and PS fluorophores start in their inactive "off" state, until activated and switched "on", usually by a blue light laser (~405 nm). While PA fluorophores are irreversibly switched "on" before being bleached , PS fluorophores can further switch to a reversible "dark state", from which they can be re-activated a number of times (Dickson et al. 1997; Ando et al. 2004). PC fluorophores on the other hand come in an active form, but can be converted to a different color emission spectrum, usually green to red (Gurskaya et al. 2006; Zhang et al. 2012).

Many things have to be considered when choosing a fluorophore, as experimental conditions dictate which fluorophores can be used. This includes e.g. the characteristics of the organism of interest, the experiment type and aim, or the structure and localization of the tagged protein itself. There is rarely a perfect fit, so that compromises have to be made. **Table 1.1** displays a selection of fluorophores suited for PALM, including their most important characteristics.

Table 1.1: Selection of fluorophores suitable for PALM.

Typical fluorescent proteins used in PALM and their characteristics, displayed for the activated/converted state of the fluorophores. Ex λ = Excitation wavelength in nm; Em λ = Emission wavelength in nm. QY = Quantum yield.

Name	Type	Ex/Em λ	QY	Brightness	Maturation (min)	Monomer	Source(s)
Dendra2	PC	553/573	0.55	19.25	-	+	(Gurskaya et al. 2006)
Dreiklang	PS	511/529	0.41	34.03	120	+	(Brakemann et al. 2011)
Dronpa	PS	503/518	0.85	80.75	-	+	(Ando et al. 2004)
eYFP	?	513/527	0.67	44.89	9	-	(Ormo et al. 1996; Dickson et al. 1997; Miyawaki et al. 1997)
mEos3.2	PC	572/580	0.55	17.71	20	+	(Zhang et al. 2012)
mNeonGreen	?	506/517	0.8	92.8	10	+	(Shaner et al. 2013)
PA-GFP	PA	504/517	0.79	13.75	-	+	(Patterson and Lippincott-Schwartz 2002)
PAmCherry	PA	564/595	0.46	8.28	23	+	(Subach et al. 2009)

When choosing a FP, it should first be investigated or tested, if the fluorophore can be expressed and folded properly and in time (maturation time) in the organism of interest. If the generation time of an organism is shorter than the maturation time of the FP, the FP can hardly be utilized. The localization of the tag (Nt, Sandwich, Ct) thereby often influences functionality of the protein of interest, which needs to be tested. Furthermore, many bacteria display natural

autofluorescence in certain wavelengths (Yang et al. 2012), which can cause background in SMLM experiments. While there is a variety of FPs in different colors available to circumvent this problem for single-color imaging, multi-color SMLM is more challenging. This is aggravated by the fact that most FPs in PALM are activated by a laser of the same wavelength (405 nm), activating both FPs at the same time. These FPs cannot be imaged sequentially, and if the microscope is only equipped with one camera, simultaneous recording is limited by the equipped filter sets. Thus, the filters have to be switched between every frame, or the recorded signals have to be separated via their photocharacteristics during post-processing (Rosenbloom et al. 2014), which is both challenging and comes with downsides.

Next, the brightness and quantum yield, which represents the ratio of photons emitted to photons absorbed, should be considered. A brighter fluorophore can be localized more precisely due to the higher number of photons, which is generally favourable, if a choice can be made. The oligomerization state of FPs is another important factor, as naturally oligomerising or clustering proteins like YFP have led to false-assumptions based on artifacts in the past (Swulius and Jensen 2012). If the structure to be imaged is already known, this can be easily tested (Stockmar et al. 2018), but might turn out more difficult for novel proteins or those that are lowly expressed or do not form distinct, oligomeric structures. Also quantitative studies profit from the use of truly monomeric protein, as calibration and normalization data need to be reflected in the in-vivo situation (Sengupta and Lippincott-Schwartz 2012).When it comes to more advanced PALM techniques like SPT, the FP needs to be characterized even more detailed, as it is crucial to be informed about the specific photokinetics to be able to connect observed signals between consecutive frames in an educated manner. These include the blinking rates (rate and length of spontaneous on/off switching during imaging), the dark-times of FPs or the average time before an FP is irreversibly bleached. These characteristics help tuning the identification and connection of single-particles between recorded frames during the mostly automated analysis (Turkowyd et al. 2019).

On a finishing note, it should be said that some FPs display a very specific behavior that yet needs to be explained on the molecular level. This includes the photoswitching of eYFP (Dickson et al. 1997; Biteen et al. 2008) or mNeonGreen (mNG) (Shaner et al. 2013; Stockmar et al. 2018), which is difficult to control and only displayed by a fraction of the protein population. These proteins can however be utilized for special cases, since they do not need to be activated by a laser. Instead, most of the protein is bleached initially, leaving a small population where blinking is induced. This has been exploited in, which requires a low number of active FP (Rosch et al. 2018a) and can theoretically be used for dual-color imaging, as these proteins do not need an activation laser and thus allow sequential imaging of both fluorophores (Stockmar et al. 2018).

1.4. Aims

The Min system in *B. subtilis* aids in inhibiting cell division close to the poles. Furthermore, it seems to be essential for disassembly of the divisome after a successful round of division, while preventing re-initiation of division at former division sites (van Baarle and Bramkamp 2010). Compared to the highly dynamic, oscillating Min system in *E. coli,* it seems to form a more static and stable gradient in *B. subtilis*, mostly due to the lack of the oscillation inducing MinE, which is replaced by the spatial determinant DivIVA that can sense negative curvature. These functional differences are likely due to the second mode of division, as *Bacillus* initiates a highly asynchronous type of division during sporulation. It is however unclear, how the Min system can form a fixed gradient or stabilize itself, as it has to re-locate to the active site of division during septum formation. Additionally, our lab did observe dynamics in DivIVA (Bach et al. 2014), which prompted us to re-characterize the dynamics of the Min components.

Since most previous studies of the Min system in *B. subtilis* were performed in strains overexpressing ectopic protein, the first goal was to create functional fluorescent fusions of MinD, MinJ and DivIVA, expressed at native levels, to analyze them microscopically. These microscopic analyses include further characterization of the dynamics and localization of Min components with resolutions below the Abbe diffraction limit of light, with the aim to determine a model of Min protein localization and self-regulation.

To use the full potential of SMLM and obtain an independent proof for Min dynamics, I further decided to perform SPT analysis of the Min system as a second project. Since SPT is a very technical method that requires extreme care throughout the whole process of sample preparation, imaging and analysis, a reliable experimental routine had to be established first.

A third project was started, when we realized frequent limitations in the choice of fluorophores in our SMLM experiments. To that end, we wanted to optimize utilization of a rather unconventional fluorophore for SMLM, mNeonGreen, with its innate ability to blink. As mNeonGreen is frequently used in conventional microscopy due to its excellent photocharacteristics, short maturation time and folding efficiency, this might help other researchers to use existing strains for SMLM or help finding a compatible, second FP for dual-color SMLM experiments that are limited by fluorophore choice.

2. Results

2.1. Re-characterization of the Min system in *B. subtilis*

Here, the proteins of the Min system were re-characterized, specifically concerning their dynamics and intracellular localization. Due to the extended microscopy expertise in our group and suitable and strong methods in the field, dynamics of the Min proteins were primarily characterized microscopically, starting with analysis of protein dynamics through selective photoconversion and fluorescent recovery after photobleaching (FRAP). The Min system has been subject to extensive investigation before, both in *E. coli* and *B. subtilis*, reviewed by (Bramkamp and van Baarle 2009; Rowlett and Margolin 2013, 2015). Most of the data for *B. subtilis,* however, has been gathered from strains overexpressing Min proteins, e.g. (Marston et al. 1998; Marston and Errington 1999; Karoui and Errington 2001). Even small amounts of static protein can mask a dynamic population in FRAP (Gregory et al. 2008). The first steps in producing relevant microscopic data was therefore the construction of functional fluorescent fusions in their native genomic context, ensuring regular expression levels and utilization of a FRAP compatible fluorophore.

2.1.1. Construction of fluorescent fusions

B. subtilis is a naturally competent organism and has the ability to take up linear, foreign DNA, which it can insert via homologous recombination, a mechanism for horizontal gene transfer or curing DNA breaks, reviewed in (Lenhart et al. 2012). This natural competency can be taken advantage of to insert genetic material, e.g. the gene for expression of a FP, by flanking it with DNA homologous to the up- and downstream stretch of the position of interest on the chromosome of *B. subtilis*, with perfect precision down to the nucleotide. Exploiting this, we utilized Golden Gate cloning to combine fragments of homologous regions up- or downstream of either *minD*, *minJ* or *divIVA*, and the respective gene or part of it (illustrated in **Fig. 2.1**). These were combined with the genes for a FP and a resistance cassette, to create fluorescent fusions in the native locus, either N- or C-terminally. Due to the nature of Golden Gate cloning, a scar of four nucleotides between fragments cannot be avoided (Engler et al. 2008). This scar was extended by two nucleotides between the genes of the protein of interest and the FP to express a flexible linker of two glycines, to avoid a frameshift and allow proper folding and

maturation of the fusion-protein. In some constructs, this linker was changed into a flexible 15 amino acid linker according to (Bisson-Filho et al. 2017), indicated in **Table 2.1**.

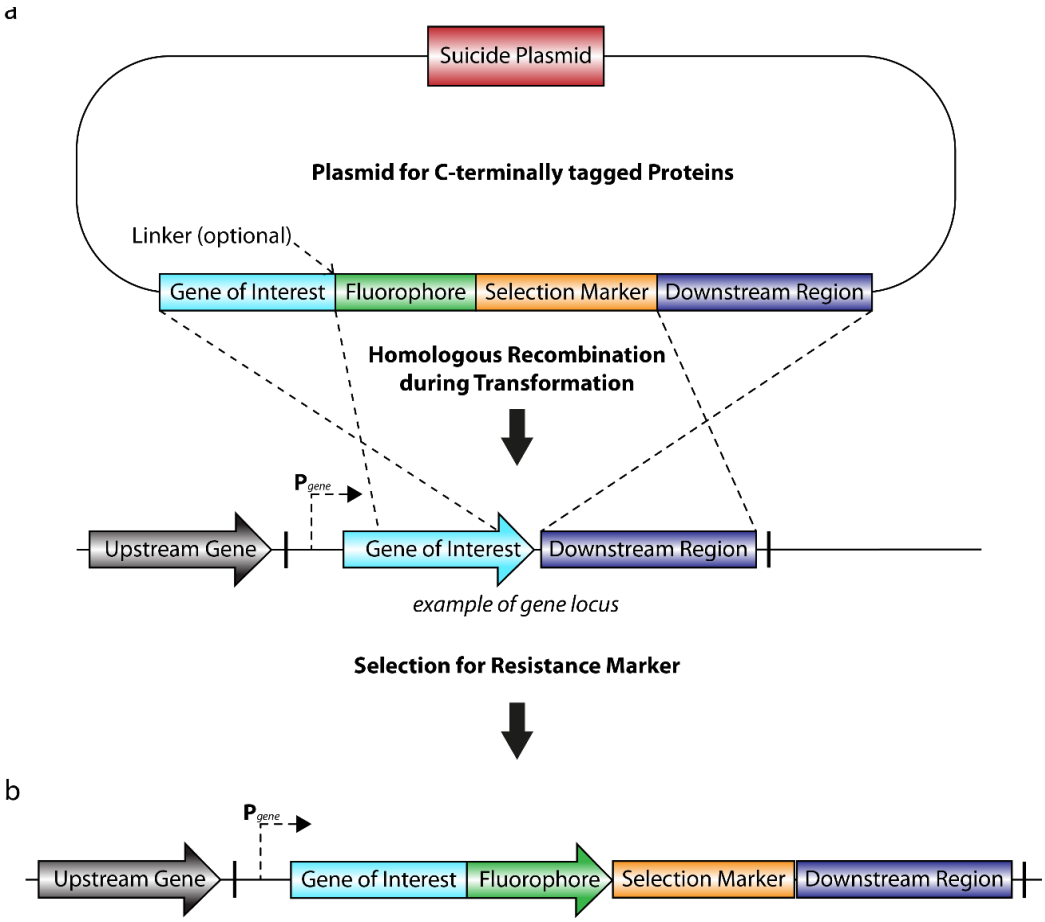

Fig. 2.1: Schematic of cloning strategy for *B. subtilis* genomic integration.

To create a C-terminal fluorescent fusion in the native genomic locus of *B. subtilis*, golden gate cloning was employed. **(a)** Illustration of a suicide plasmid containing the genes of the gene of interest, fluorophore, selection marker and the chromosomal downstream region of the gene of interest. **(b)** After transformation, clones that inserted genes for the fluorophore and selection marker via homologous recombination can be selected for through use of the respective antibiotic during outgrowth, while the toxin of the suicide plasmid kills clones with a single crossover.

The fragments were combined in a suicide plasmid (Bramkamp lab, not published) containing the inverted gene of a toxin that kills the cell upon single-crossover (i.e. inverting the toxin back to the correct orientation), ensuring only survival of those clones where double crossover was successful. MinC was excluded from this analysis because it can be seen as a passenger of MinD, as it is recruited and located by it (de Boer et al. 1991), and because it has been shown to be dynamic before (Gregory et al. 2008), which was one of the reasons we decided to re-investigate the Min system. Deletion or dysfunctionality of Min components manifests in a phenotype that is easily identified, as cells produce minicells and increase in length significantly (Adler et al. 1967; Reeve et al. 1973). Therefore, we tested clones microscopically for functionality by measuring cell length and amount of minicells.

Table 2.1: Phenotypic description of strains for microscopic analysis of the Min system.

Data was extracted from at least three independent, biological replicates; n per strain ≥ 200; averaged values include standard deviation.

Strain name	Description	Mean cell length [µm]	Mean growth rate [µ]	Minicells [%]
168	wild type	3.11 ± 0.77	0.53 ± 0.004	0.3
3309	*ΔminCD*	7.64 ± 2.70	0.45 ± 0.021	45.8
RD021	*ΔminJ*	6.65 ± 2.02	0.51 ± 0.049	13.8
4041	*ΔdivIVA*	8.13 ± 3.40	0.46 ± 0.020	29.6
BHF011	Dendra2-MinD	2.97 ± 0.68	0.49 ± 0.004	0.9
BHF016	mCherry2-MinD*	-	-	-
BHF059	mKate2-MinD*	-	-	-
BHF017	msfGFP-MinD	4.22 ± 1.04	0.55 ± 0.004	9.1
JB38	MinJ-Dendra2	3.84 ± 1.06	0.51 ± 0.006	0
JB40	MinJ-mNeonGreen	3.16 ± 0.67	0.57 ± 0.002	0
BHF007	MinJ-msfGFP	3.37 ± 0.75	0.57 ± 0.013	0.3
BHF029	MinJ-PSmOrange2**	-	-	-
JB36	DivIVA-Dendra2^{L}	4.33 ± 0.92	0.50 ± 0.007	8
BHF057	DivIVA-Dronpa$^{*, L}$	-	-	-
BHF058	DivIVA-mGeosM*	-	-	-
BHF004	DivIVA-mCherry2$^{*, L}$	-	-	-
BHF028	DivIVA-mNeonGreen^{L}	5.42 ± 1.35	0.54 ± 0.029	5.3
JB37	DivIVA-PAmCherry	4.35 ± 1.11	0.51 ± 0.019	3.3

* Strong phenotype, misslocalized fluorescent protein or artifacts, therefore not further characterized

** No detectable fluorescence due to very long maturation time (3.5 h) of PSmOrange2 (Subach et al. 2012)

^{L} tested with and without flexible-linker (15aa, LEGSGQGPGSGQGSG), from (Bisson-Filho et al. 2017)

Furthermore, we observed the localization of fluorophores attached to the respective protein to spot artificial localization. If the localization was strongly aberrant, no further experiments with these constructs were performed. Additionally, we measured the growth rate of strains to identify possible growth defects.

Several different constructs for the Min proteins were cloned and transformed successfully (**Table 2.1**, **Fig. 2.2**, **Table 4.2** and **Table 4.3**). The wild type (*B. subtilis* 168) and knockout mutants for *minCD*, *minJ* and d*ivIVA* were included as reference for the respective phenotype. Unfortunately, most of the strains constructed show a phenotype of a defective Min system, although to different extents. Some strains showed strongly aberrant positioning of the Min components, not only locating at poles and septa as expected, but also forming accumulations of fusion-protein (see **Fig. 2.3** and **Table 2.1**, indicated by asterisk). These strains were not characterized in detail, since initial inspection also revealed large numbers of minicells besides the obvious misslocalization of fusion-protein. We nevertheless found a number of strains expressing fusion-protein localizing in the expected regions of the cell, of which some are exemplary shown in **Fig. 2.2**.

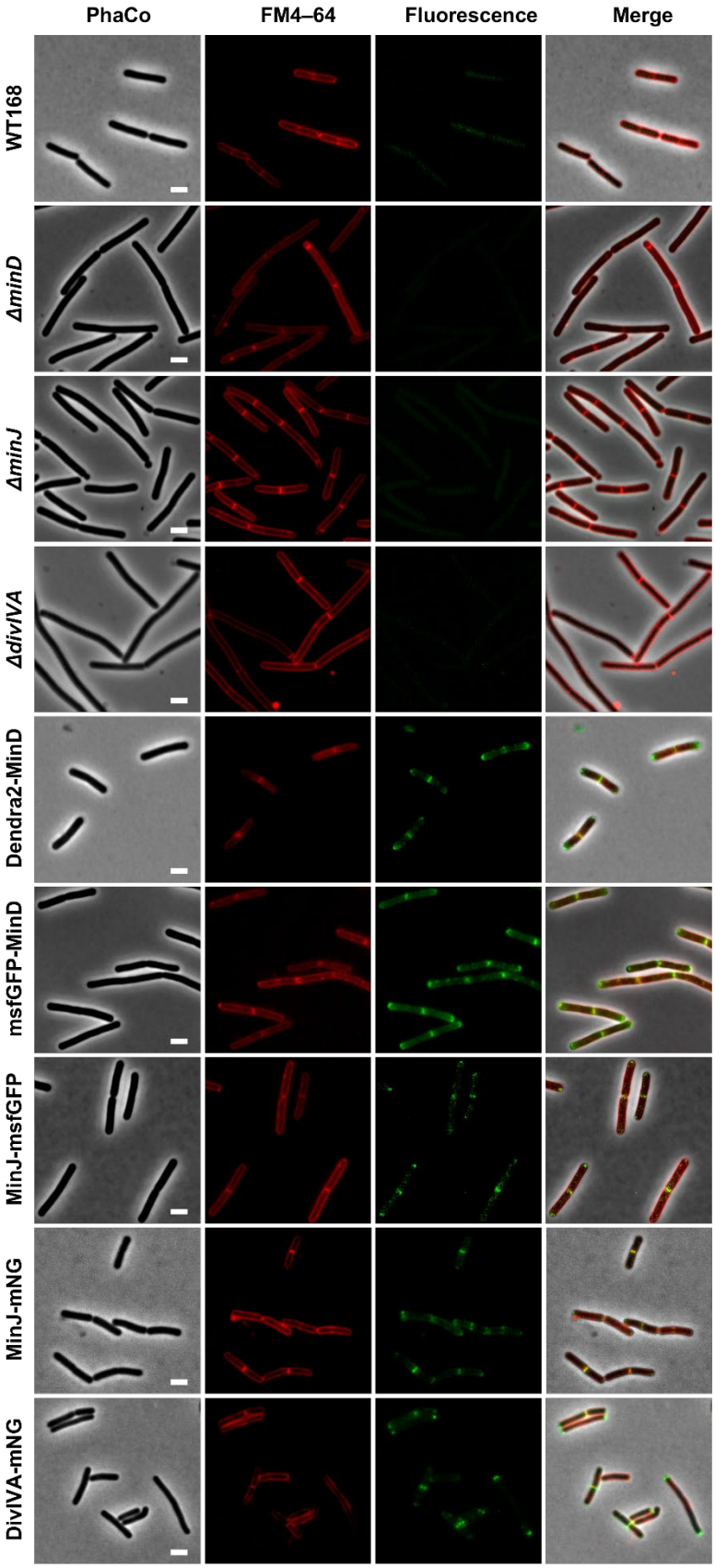

Fig. 2.2: Microscopic characterization of a selection of strains used in this study.

Columns from left to right: Phase contrast, red fluorescent channel using membrane dye (FM4-64), green fluorescent channel depicting the indicated fluorophore and composite of all three channels. Scale bars 2µm.

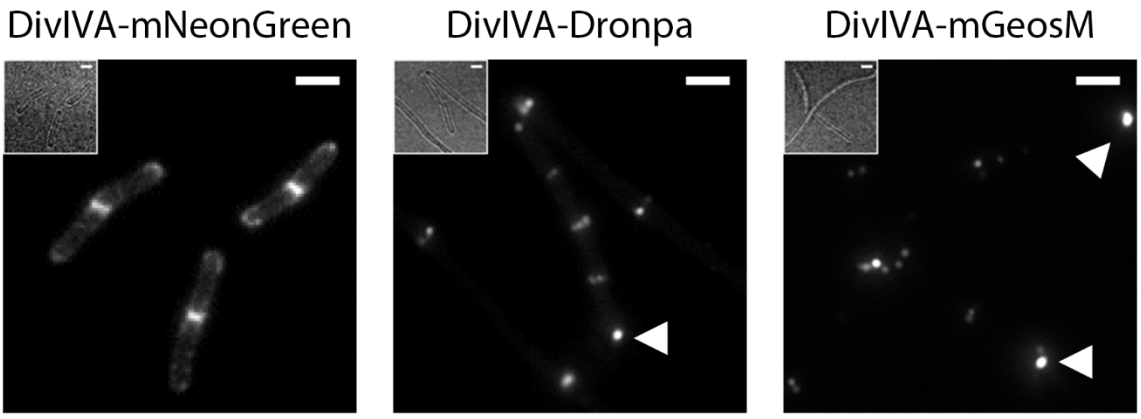

Fig. 2.3: Intracellular DivIVA localization is altered in some FP fusions.

Representative fluorescence microscopy images of *B. subtilis* expressing DivIVA fused to either mNeonGreen (BHF028), Dronpa (BHF057) or mGeosM (BHF058) from their native promoter. Top left inset displays the corresponding bright-field image, respectively. While DivIVA-mNeonGreen **(left)** localizes to poles, septa and lateral cell wall, DivIVA-Dronpa **(center)** and DivIVA-mGeosM **(right)** also exhibit accumulations of misslocalized fusion-protein indicated by white arrows. Scale bar 2nm, modified from (Stockmar et al. 2018).

Some of these strains did not show any significant phenotype when compared to wild type *B. subtilis*. This was true for Dendra2-MinD (BHF011), and virtually all tested MinJ constructs (Dendra2, JB38; mNeonGreen, JB40; msfGFP, BHF007). MinJ-Dendra2 however did not show any fluorescence when being imaged, even when using long exposure times (≥ 2 s), nor did the protein emit a detectable signal after photoconversion with a UV laser (405 nm, 15 ms). One reason for this could be the low native expression levels of MinJ (Nicolas et al. 2012) in combination with the rather dim fluorophore Dendra2 (Gurskaya et al. 2006). Furthermore, MinJ is a transmembrane protein, which can affect folding and maturation of fusion proteins.

Unfortunately, no fully functional fluorescent fusion of DivIVA could be obtained. Even strains displaying correct localization of fusion-protein (DivIVA-Dendra2, JB36; DivIVA-mNeonGreen, BHF028 and DivIVA-PAmCherry, JB37) were slightly elongated and produced minicells (**Table 2.1**). Therefore strain 1803 (Thomaides et al. 2001) was utilized for analysis of DivIVA dynamics. Besides the native *divIVA* gene, it carries an extra copy of *divIVA* fused to the gene for GFP, located in the ectopic *amyE* locus and controlled by the natural *divIVA* promoter to produce comparable protein levels. Additionally, protein dynamics were tested in the slightly elongated strain BHF028 expressing DivIVA-mNG and compared to strain 1803 (DivIVA-GFP), to account for the additional copy of *divIVA* in strain 1803. Fluorescence half-time recovery in strain BHF028 (DivIVA-mNG) thereby occurred in around half the time when compared to 1803 (DivIVA-GFP), likely due to the mixed population of GFP-tagged and native DivIVA protein in 1803 (**Table 2.2**).

2.1.2. Microscopic analysis reveals dynamics of all Min components

Besides its application in PALM, the fluorophore Dendra2 can be employed to visualize protein dynamics and migration (Gurskaya et al. 2006; Bach et al. 2014). It can be locally converted by a confined laser pulse to emit light in a higher wavelength, shifting its emission maximum from 507 nm (green) to 573 nm (red). By only monitoring the localization of previously converted fluorophores, it is possible to discriminate between newly synthesized and dynamically relocated fusion-protein. This was applied to analyze protein dynamics of Dendra2-MinD, which displayed a surprising intracellular migration of part of its population to midcell in a dividing cell (**Fig. 2.4**):

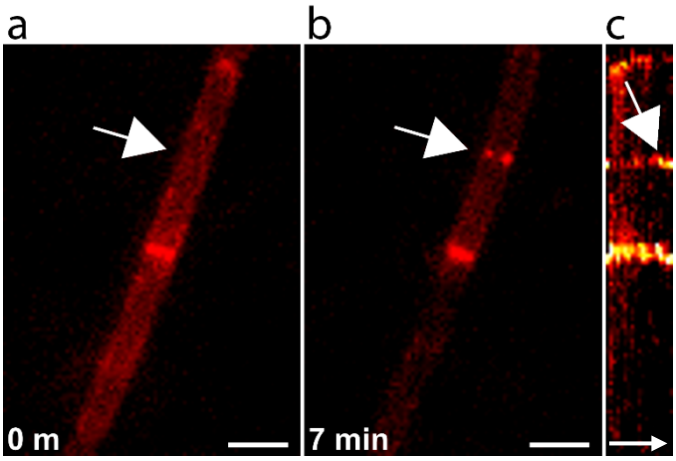

Fig. 2.4: Time-lapse analysis of photoconverted Dendra2 reveals MinD dynamics.

Strain BHF011 expressing Dendra2-MinD was grown in MD medium at 37°C and transferred to MD agarose slides during mid-exponential phase. Imaging was performed at 37°C and monitored microscopically every 30 s for 10 minutes. **(a)** After pre-bleaching and initial photoconversion of Dendra2 (405 nm laser pulse) with subsequent imaging, protein was quickly visible throughout the whole cell; the white arrow indicates absence of localization preference to midcell of the upper cell. **(b)** After 7 min, part of the Dendra2-MinD population re-localized to midcell of the upper-cell, indicated by the white arrow. **(c)** Kymograph of Dendra2-MinD localization **(from left to right)**; the white arrow indicates accumulation of Dendra2-MinD at mid-cell of the upper cell over time. Scale bar 2 µm.

Over time, a large fraction of the converted Dendra2-MinD population migrated to mid-cell (**Fig. 2.4 b** and **c**), likely recruited due to the formation of a septum at mid-cell. Since only converted protein is emitting red fluorescence, it can be excluded that newly synthesized protein was visualized. To confirm this finding, and to further characterize the observed dynamics, we set out to analyze the strains using FRAP. This technique makes use of the possibility to irreversibly inactivate (bleach) fluorophores in a defined area by applying a local, high intensity laser pulse. Subsequently, fluorescence recovery in the same area is measured, caused by non-bleached fluorescent fusion-proteins replacing the bleached protein population. Hence, the recovery rate correlates with mobility of the fluorescently tagged protein and can be used to calculate its diffusion rate. Unfortunately, Dendra2-MinD could not be used for FRAP studies, as it was converted from green to red via the excitation light (488 nm) over the cause

of the experiment (data not shown). When converting all protein prior the FRAP experiment with UV light (405 nm), the red fluorescent signal was insufficient for reliable quantification. Since FRAP analysis requires high imaging frequency scaling with the expected diffusion coefficient, a more stable fluorophore was required. Therefore, the largely functional msfGFP-MinD fusion (BHF17) was used instead.

To test for Min protein mobility via FRAP, bleaching was performed on apparent division septa. Surprisingly, all tested components of the Min system displayed relatively fast recovery (**Fig. 2.5**, **Table 2.2**). While bleaching was very effective (**Fig. 2.5 a**), cells kept growing and dividing throughout the experiments, indicating intact fitness and low phototoxicity in the experimental set-up. To confirm that florescent recovery was based on protein diffusion and not due to newly synthesized protein, FRAP was also performed in cells growing in the presence of kanamycin. While these cells stopped growing, recovery was not affected (data not shown).

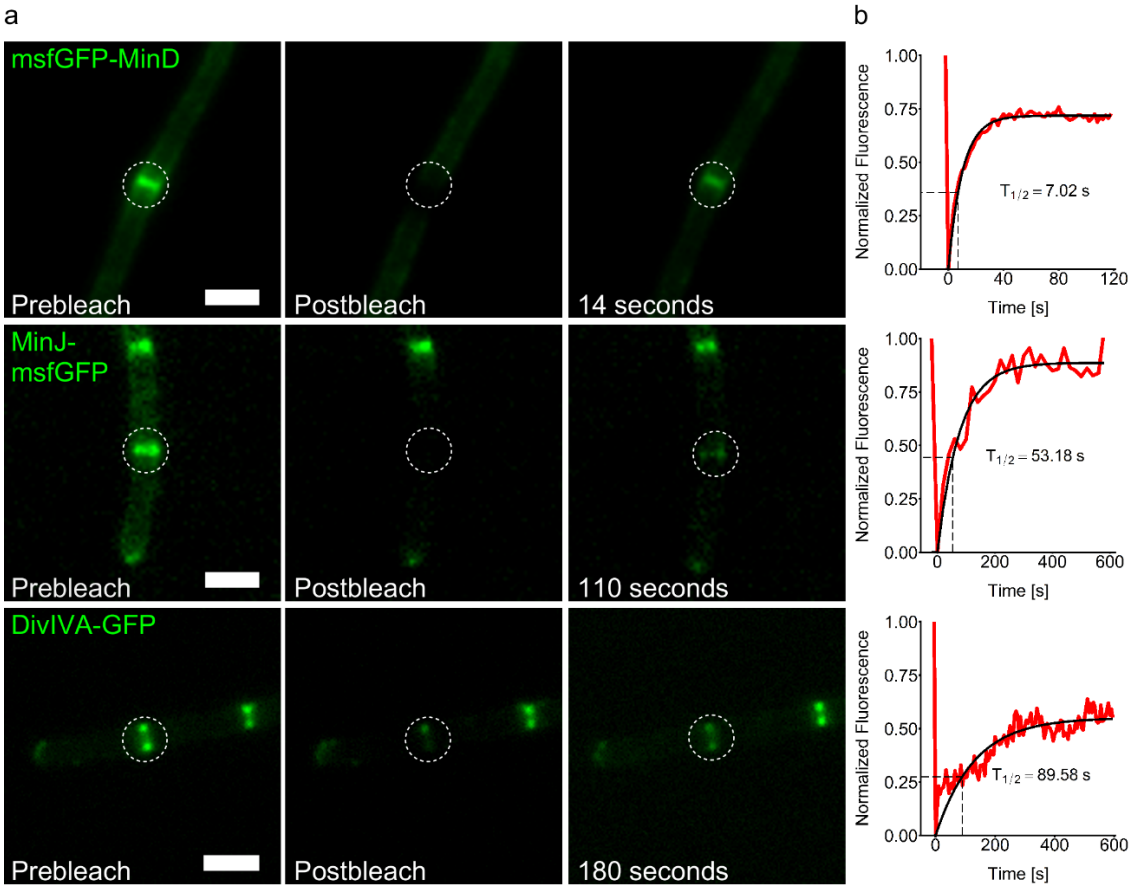

Fig. 2.5: FRAP analysis of *B. subtilis* reveals dynamics of all Min proteins.

(a) Representative microscopy images of strains producing msfGFP-MinD (BHF017), MinJ-msfGFP (BHF007) and DivIVA-GFP (1803), respectively. **From left to right**, images show a prebleached state, the postbleach state right after the bleaching laser pulse (488 nm, 10 ms) was applied to the indicated region (white dotted circle), and a later timepoint where fluorescence recovered. Scale bars 2 µm. **(b)** Representation of the normalized fluorescence recovery in the green channel over time. $T_{1/2}$ = time when fluorescence recovery reaches half height of total recovery, indicated on the graph with a dashed square. The red line represents measured values, black the fitted values. Values were obtained as described in the methods.

The fastest recovery was displayed by msfGFP-MinD (BHF017) ($T_{1/2}$ = 7.55 ± 1.31 s), suggesting a fast exchange of MinD molecules around the division septum (**Fig. 2.5 a**, upper panel; **Table 2.2**), correlating well with previously reported behavior of MinC in *B. subtilis* (Gregory et al. 2008). MinD molecules from the vicinity as well as polar regions appeared to partake in recovery, as the fluorescent signal reduced evenly throughout the cell. Around 79% of the population was found to be mobile (**Table 2.2**). Recovery of a bleached septum in MinJ-msfGFP (BHF007) was significantly slower ($T_{1/2}$ = 62.35 ± 19.71 s, **Table 2.2**), yet still in the expected range for a membrane protein with 6 transmembrane helices (Kumar et al. 2010). Similarly to msfGFP-MinD, the majority of MinJ-msfGFP proteins appeared mobile (77%). Finally yet importantly, DivIVA-GFP (1803) was measured as the slowest recovering Min protein ($T_{1/2}$ = 128.64 ± 30.92 s), with a mobile fraction of roughly two thirds (65%). Therefore, the fraction of immobile protein (35%) was larger for DivIVA compared to MinD and MinJ, which seems logical for a protein that forms relatively large and stable multimers (Oliva et al. 2010). To account for the two copies of *divIVA* that strain 1803 harbors, we also performed FRAP on strain BHF028, producing partial-functioning DivIVA-mNeonGreen at wild type levels (**Fig. 2.6**).

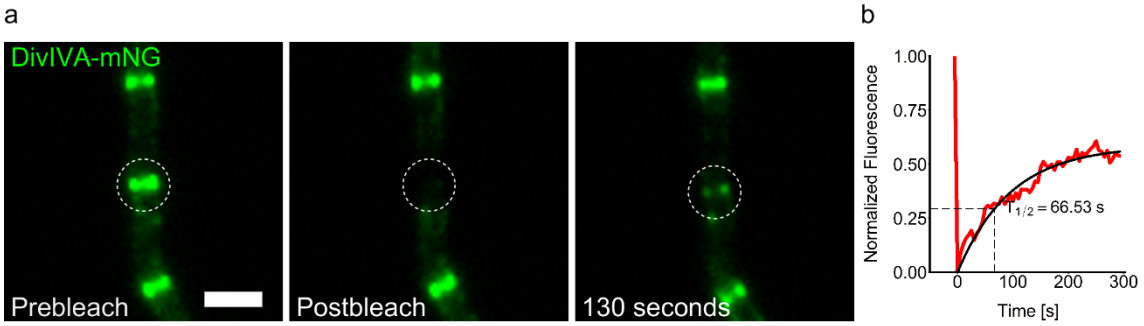

Fig. 2.6: FRAP recovery of DivIVA-mNeonGreen is comparable to DivIVA-GFP.

(a) Representative microscopy images of strain BHF027 producing DivIVA-mNeonGreen. **From left to right**, images show a prebleached state, the postbleach state right after the bleaching laser pulse (488 nm, 10 ms) was applied to the indicated region (white dotted circle), and a later timepoint where fluorescence recovered. Scale bars 2 µm. **(b)** Representation of the normalized fluorescence recovery in the green channel over time. $T_{1/2}$ = time when fluorescence recovery reaches half height of total recovery, indicated on the graph with a dashed square. The red line represents measured values, black the fitted values. Values were obtained as described in the methods.

The recovery speed of DivIVA-mNeonGreen was roughly twice as fast ($T_{1/2}$ = 60.34 ± 16.57 s) when comparing the two strains, which was consistent in different genetic backgrounds (see next chapter). This seems logical, since strain 1803 produces two versions of DivIVA, of which only one is fluorescently labeled. While both protein populations will partake in replacing the bleached fraction after the laser pulse, only one can be quantified, resulting in an apparent slower recovery. DivIVA has been reported as non-mobile before (Eswaramoorthy et al. 2011), however observed in an overexpression strain. In contrast, mobility of DivIVA was inferred in a study from our lab using a merodiploid strain (Bach et al. 2014).

2.1.3. Min components affect each other in their dynamics

Components of the Min system were shown to interact directly before, e.g. through bacterial two-hybrid (B2H) tests (Bramkamp et al. 2008; Patrick and Kearns 2008). These interactions were of hierarchical nature, with DivIVA recruiting MinJ, which in turn recruits MinD and thus MinC. To characterize these interactions and their effect on the mobility and intracellular localization of the respective interactor(s), FRAP was successfully performed on fluorescent fusions expressed in strains with different genetic knockout backgrounds of the Min genes (**Fig. 2.7**). The results of all FRAP experiments are summarized in **Table 2.2**, while the half-time recovery for all strains is visualized in **Fig. 2.8**.

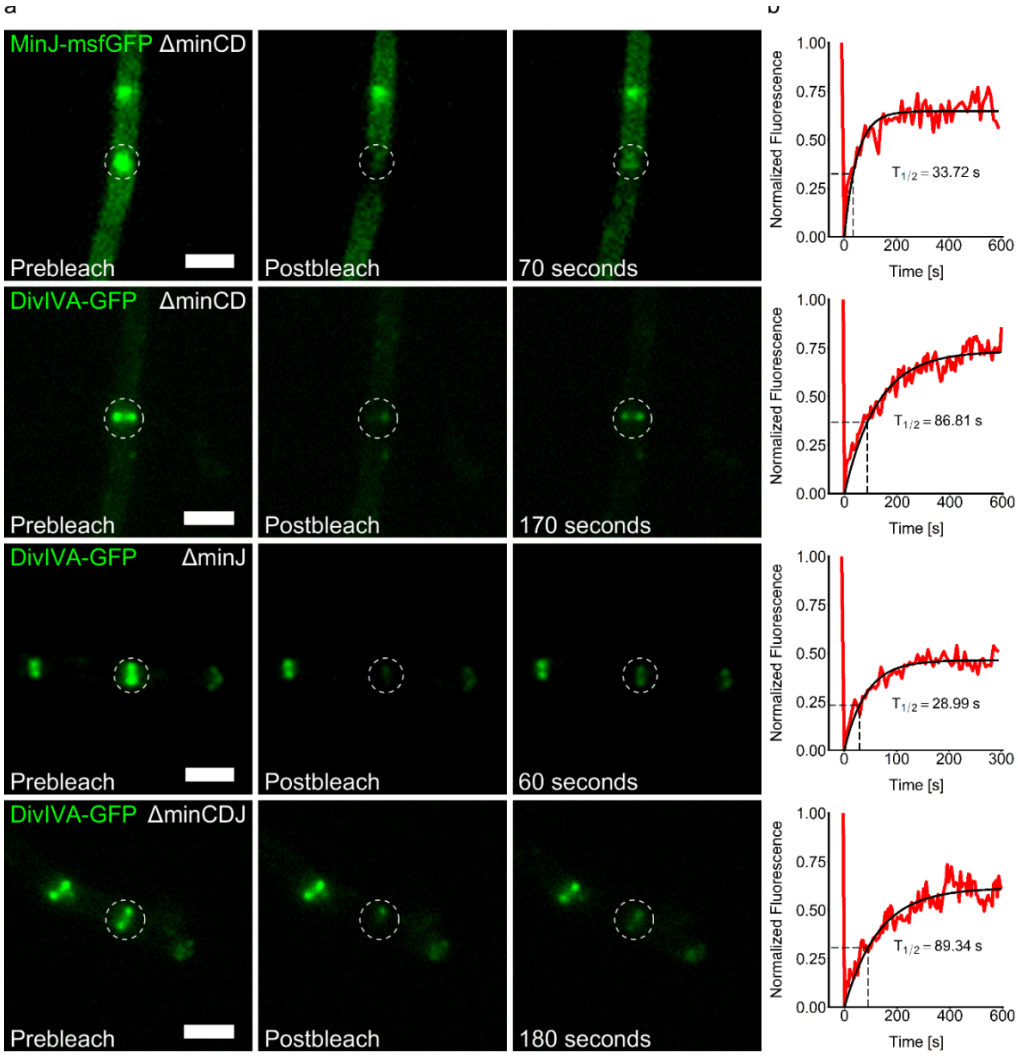

Fig. 2.7: Interaction of Min proteins affects their dynamics in FRAP experiments.

(a) Representative microscopy images of FRAP in strains producing MinJ-msfGFP or DivIVA-GFP in different genetic backgrounds, respectively (see **Table 2.2**). From left to right, images show a prebleached state, the postbleach state right after the bleaching laser pulse (488 nm, 10 ms) was applied to the indicated region (white dotted circle), and a later timepoint where fluorescence recovered. Scale bars 2 µm. **(b)** Representation of the normalized fluorescence recovery in the green channel over time. $T_{1/2}$ = time when fluorescence recovery reaches half height of total recovery, indicated on the graph with a dashed square. The red line represents measured values, black the fitted values. Values were obtained as described in the methods.

Table 2.2: Results of FRAP analysis of Min proteins in different genetic backgrounds.

Protein and genetic background	Fluorophore	Diffusion coefficient [$\mu m^2 * 10^{-3} * s^{-1}$]	Half-Time Recovery [s]	Mobile Fraction [%]
MinD in wild type	msfGFP	57.78 ± 10.05	7.55 ± 1.31	0.79 ± 0.06
MinJ in wild type	msfGFP	7.19 ± 2.27	62.35 ± 19.71	0.77 ± 0.14
MinJ in *ΔminCD*	msfGFP	14.46 ± 9.54	30.18 ± 19.92	0.75 ± 0.07
DivIVA in wild type	GFP	3.39 ± 0.82	128.64 ± 30.92	0.65 ± 0.23
DivIVA in *ΔminCD*	GFP	3.74 ± 1.36	116.79 ± 42.40	0.68 ± 0.26
DivIVA in *ΔminJ*	GFP	8.57 ± 4.43	50.94 ± 26.35	0.49 ± 0.15
DivIVA in *ΔminCDJ*	GFP	4.98 ± 2.93	87.67 ± 51.55	0.61 ± 0.27
DivIVA in wild type	mNeonGreen	7.23 ± 1.99	60.34 ± 16.57	0.64 ± 0.23
DivIVA in *ΔminCD*	mNeonGreen	6.88 ± 2.76	63.43 ± 25.41	0.67 ± 0.20
DivIVA in *ΔminJ*	mNeonGreen	18.01 ± 3.22	24.40 ± 4.33	0.39 ± 0.11
DivIVA in *ΔminCDJ*	mNeonGreen	9.47 ± 4.26	46.07 ± 20.71	0.66 ± 0.23

As expected, msfGFP-MinD completely lost its polar and septal localization when expressed in either *ΔdivIVA* (BHF026) or *ΔminJ* (BHF025; data not shown). The same was observed for MinJ-msfGFP expressed in *ΔdivIVA* (BHF032; data not shown). These strains were not analyzed further, as initial FRAP experiments of the diffuse cytosolic signal of msfGFP-MinD in *ΔdivIVA* (BHF026) indicated random diffusive movement (data not shown), which was too fast to be characterized reliably via FRAP. Since diffusive behavior seemed to dominate in these strains, no valuable information for Min dynamics could be gained. Generally, Min knockout phenotypes of erroneous cell division and consequential increased cell length exacerbate FRAP experiments and analysis, which might be reflected in higher standard variations in the respective strains (**Table 2.2**, **Fig. 2.8**).

When *minCD* was knocked out in a strain expressing MinJ-msfGFP, the recovery speed surprisingly dropped to around half ($T_{1/2}$ = 30.18 ± 19.92 s), indicating higher mobility of MinJ in absence of MinCD. This observation provides more evidence for the direct interaction with MinD, which appears to stabilize MinJ and could physically slow it down when bound. However, the phenotype of *ΔminCD* might contribute to the effect, as cells grow larger and often re-initiate division at one pole after dividing successfully (van Baarle and Bramkamp 2010). In contrast, DivIVA-GFP and DivIVA-mNeonGreen dynamics were not significantly affected in a *ΔminCD* strain compared to a wild type background (**Table 2.2**, **Fig. 2.8**), which was expected due to the lack of direct interaction. Indirect effects through MinJ did not seem to affect DivIVA dynamics is these strains. In opposition, but in line with the hierarchy of the Min

system, DivIVA-GFP and DivIVA-mNeonGreen displayed less than half of the recovery time when comparing the *ΔminJ* with the wild type background (**Table 2.2**, **Fig. 2.8**).

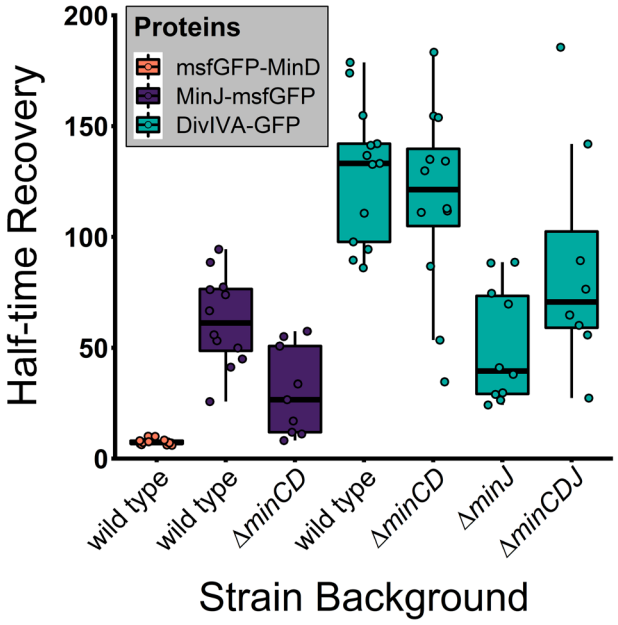

Fig. 2.8: Interactions of the Min proteins affects their dynamics.

Half-time recovery values were plotted as a boxplot with the median indicated by a black bar inside each box. Each box represents a different strain, and every dot represents a single FRAP experiment, with n ≥ 8. Mean values are listed in **Table 2.2**.

This significant increase in mobility is another strong indicator for a direct interaction between MinJ and DivIVA and the stabilizing effect MinJ exerts on DivIVA. Strikingly, the mobile fraction of DivIVA-GFP drastically reduced from 65% to 49% between the wild type and *ΔminJ* (**Table 2.2**). This effect was even more pronounced in DivIVA-mNeonGreen expressing strains (64% to 39%, **Table 2.2**). One possible explanation for this could be a higher tendency of DivIVA to cluster due to increased self-interaction in absence of MinJ. A larger fraction of DivIVA would be located in the center of the larger clusters and therefore be immobilized, while the fraction of free DivIVA could diffuse faster as it is not membrane-tethered through MinJ interaction.

Summed up, Min protein dynamics are modulated through direct interaction and complex formation, thereby mirroring the presumed hierarchy of Min proteins. Stable MinD localization at the division septum can only be achieved in presence of both MinJ and DivIVA as observed in genetic knockout backgrounds of the respective genes. Furthermore, a functional ATPase domain of MinD is vital for this localization, demonstrated by mutations which disrupt either ATP hydrolysis (G12V) or binding (K16A) (Karoui and Errington 2001). DivIVA and thus

MinCDJ only re-locate to midcell in a late state of cell division, i.e. after formation of strong negative curvature subsequent to initiation of septum cross-wall formation. Therefore, we argue that cell geometry dictates stable positioning of MinD and thus MinC at the division septum. This contributes to correct timing of cell division and disassembly of divisome components (Gregory et al. 2008; van Baarle and Bramkamp 2010). Due to aberrant MinD localization when carrying either mutation or in absence of MinJ/DivIVA, it is challenging to investigate this experimentally. Hence, we decided to use mathematical modeling to be able to characterize the observed dynamics and the importance of the MinD ATPase cycle in more detail.

2.1.4. Mathematical model of the *B. subtilis* Min system

The oscillating *E. coli* Min system can be described as intracellular pattern-forming system, and is therefore a reaction-diffusion system in confined intracellular space. The components of the system diffuse at either cell membrane or in the cytosol, which can hence be described as different spatial domains where reactions take place (Halatek and Frey 2018). These reactions characterize changes in state (e.g. active/inactive or membrane-bound/cytosolic), which are induced biochemically (e.g. binding or hydrolysis of ATP by MinD). In *E. coli*, these reactions between MinC, MinD and MinE lead to a pole-to-pole oscillation of the Min components, during which almost the entire mass of MinD and MinE is redistributed, demonstrating that pattern-forming systems could also be described as protein redistribution processes (Halatek and Frey 2012, 2018). Strikingly, this process is intrinsically tied to the cell's geometry (Wu et al. 2016), in this example enabling detection of the cell center as spatial cue. While the *E. coli* Min system has been characterized in-depth both experimentally and theoretically (also see chapter 1.1.4.2), modeling of the Min system in *Bacillus* has rarely been performed. To our knowledge, there is only a single published study examining the mechanism for polar localization of Min in *B. subtilis* theoretically, using quantitative mathematical models (Howard 2004). To understand the implications and to integrate the knowledge gained through the previous experiments into a functional mathematical model, we collaborated with Laeschkir Würthner and Prof. Dr. Erwin Frey (Arnold-Sommerfeld-Center for Theoretical Physics and Center for NanoScience, LMU Munich), who have extensive modeling expertise, e.g. in the *E. coli* Min system (Halatek and Frey 2012; Wu et al. 2016; Denk et al. 2018; Halatek and Frey 2018).

2.1.4.1. Quantification of Min proteins

After obtaining diffusion coefficients and knowledge about the hierarchy of Min components and their interactions (**Table 2.2**, **Fig. 2.8**), we next determined protein quantities. Relative protein amounts in pattern forming self-organizing systems like the Min system can affect localization and interactions greatly (Halatek et al. 2018). To be able to set-up a robust model that can simulate the observed behavior of the individual Min components and how they affect each other realistically, the individual amount of protein is hence one of the key data. To this end, we made of use previously constructed strains expressing fluorescent fusions of Dendra2 and the Min proteins (BHF011, JB38 und JB36, **Table 2.1**). Through relative in-gel fluorescence and with the help of a previous study that quantified MinD via mass spectrometry (Maass et al. 2011), we were able to quantify the Min proteins in mid-exponential phase (**Table 2.3**, **Fig. 2.9**).

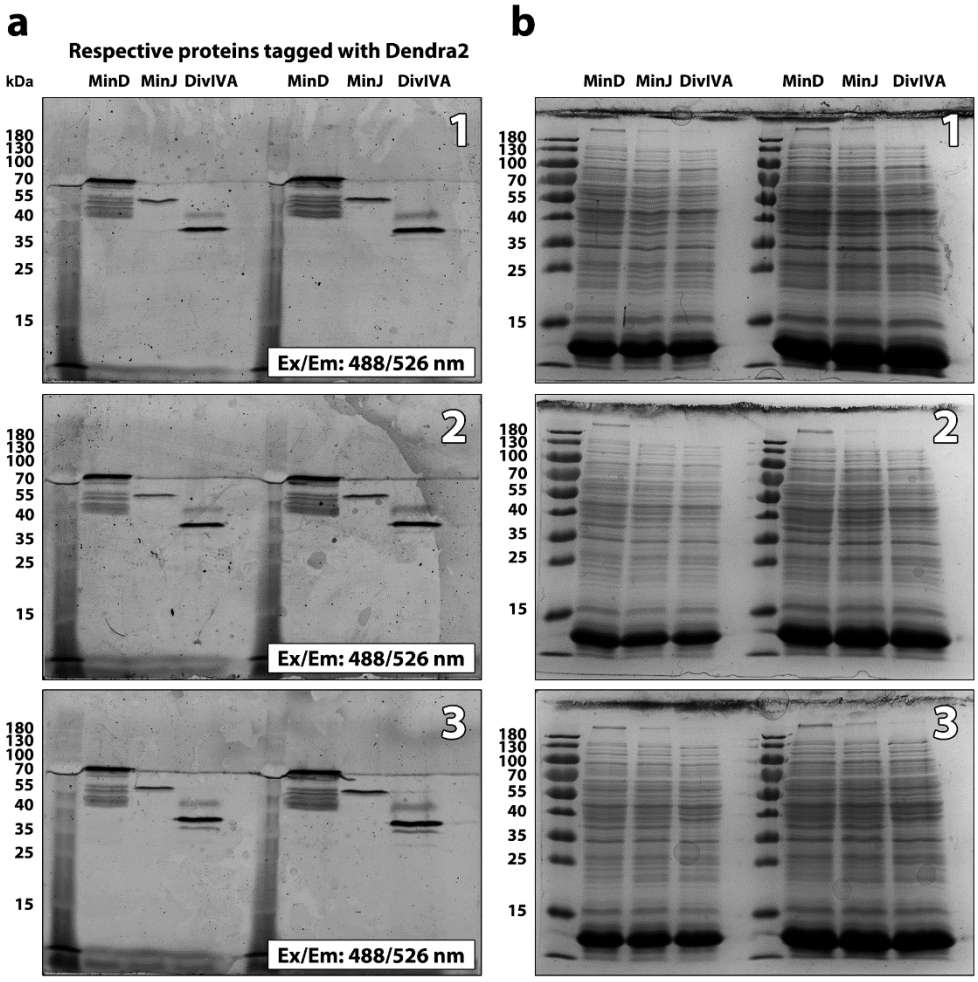

Fig. 2.9: Relative quantification of Min proteins through in-gel fluorescence analysis.

(a) In-gel fluorescence of SDS-PAGE gels, performed with biological triplicates (top right numbers **1 -3**). Cell lysates of mid-exponentially growing *B. subtilis* strains expressing Dendra2 fused to MinD (BHF011), MinJ (JB38) and DivIVA (JB36), respectively, were partially denatured with SDS loading dye at room temperature for 20 min, loaded in different relative amounts (1x left, 2x right) and separated through SDS-PAGE. Visualization was performed in a Typhoon Trio scanner at indicated excitation and emission wavelengths. **(b)** Coomassie stain of the respective gels from (a) as loading control. For results of the quantification, see **Table 2.3**.

Table 2.3: Results of quantification of Min proteins fused to Dendra2.

Relative amounts of protein were obtained through in-gel fluorescence of biological triplicates of cell lysates (see **Fig. 2.9**) and subsequent analysis in ImageJ. Total number of protein copies per cell were determined relative to MinD, which was quantified in comparable conditions in a different study (Maass et al. 2011). Values are displayed with standard deviation.

Protein	Relative amount	Total copies per cell
MinD	100% ± 2.51%	3544 ± 89
MinJ	16.25% ± 4.36%	576 ± 25
DivIVA	47.70 %± 3.51%	1690 ± 59

Quantification of MinD, MinJ and DivIVA mirrored previous observations from fluorescence microscopy experiments: While MinD is abundant in high copy number (3544 ± 89 copies per cell) and therefore emits a strong fluorescent signal when fluorescently tagged (e.g. **Fig. 2.2**, **Fig. 2.5**), MinJ is only lowly expressed (576 ± 25), which reflects in a rather dim signal (**Fig. 2.2**, **Fig. 2.5**). The copy number of DivIVA (1690 ± 59) is around half of MinD, even though fluorescence intensity seems comparable (**Fig. 2.2**, **Fig. 2.5**). This can be explained by DivIVA's strong affinity to negative curvature, concentrating most of the protein at poles and septa, resulting in a strong fluorescence signal when fluorescently tagged, while less of the total copy number of MinD appears to localize to these positions.

2.1.4.2. A reaction-diffusion model of the *Bacillus* Min system

Building on previous approaches for intracellular protein dynamics (Halatek and Frey 2012; Thalmeier et al. 2016; Wu et al. 2016; Denk et al. 2018) and the presented experimental data for Min dynamics and quantities, a mathematical model was built (**Fig. 2.10 a**).

Specifically, the minimal model in **Fig. 2.10 a** and **b** accounts for MinJ-DivIVA dependent MinD recruitment and stabilization and includes a specific set of biochemical reactions for the ATPase MinD (for details and underlying equations, see chapter 4.7, **Table 4.5** and **Fig. 4.1**). In short, MinD-ATP can bind the membrane at rate k_D ($0.068\ \mu m\ s^{-1}$) where it can nonlinearly self-recruit more MinD at rate k_{dD} ($0.04\ \mu m^2\ s^{-1}$). Upon hydrolysis of ATP at rate k_H ($0.1\ s^{-1}$), MinD-ADP detaches from the membrane, and can only rebind after nucleotide exchange from ADP to ATP leading to re-activation of MinD at rate λ ($6\ s^{-1}$). MinD thus cycles between cytosol and membrane and displays different diffusion coefficients when cytosolic ($D_D = 16\ \mu m^2\ s^{-1}$) or membrane-bound ($D_d = 0.06\ \mu m^2\ s^{-1}$). Furthermore, a realistic cellular geometry is accounted for, presented in detail in **Fig. 4.1**. In regions of high negative curvature (poles and septum), the recruitment rate of MinD is increased, while the detachment rate is decreased, accounting for the action of MinJ-DivIVA complexes that recruit and stabilize MinD and are

more prevalent in these regions. At the same time, MinD-ATP can bind to flat membranes (**Fig. 2.10 b**), although less favored due to lower abundance of MinJ-DivIVA complexes.

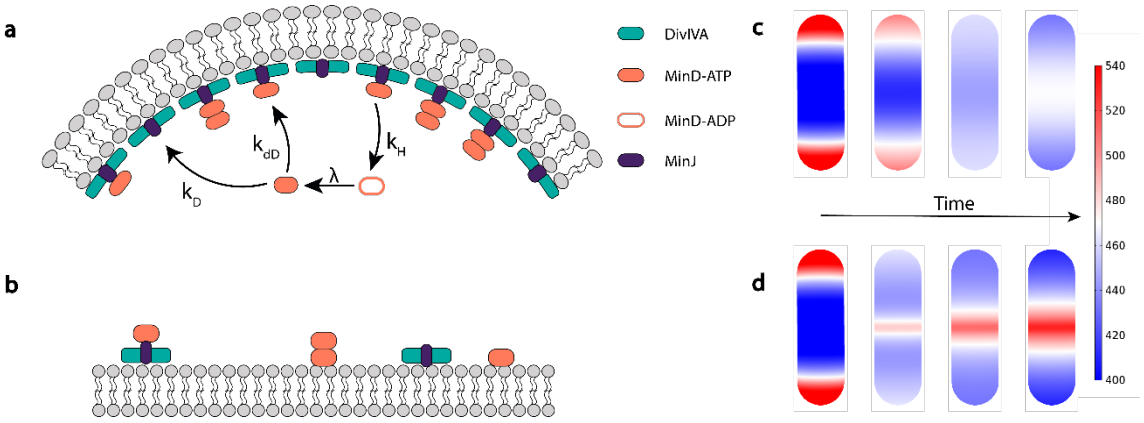

Fig. 2.10: Model and simulation of the Min system.

Min polarization and localization can be established through a highly dynamic process. **(a)** DivIVA (green) can sense a specific geometry (negative curvature) and recruits/stabilizes MinJ (purple) to these regions. Through MinJ, DivIVA scaffolds MinD recruitment of ATP-bound, cytosolic MinD (orange). MinD-ATP membrane binding occurs with a rate k_D, and membrane bound MinD-ATP in turn recruits more MinD-ATP with a recruitment rate k_{dD}. After hydrolysis of ATP at a space-dependent detachment rate k_H, which reflects stabilization through MinJ-DivIVA complexes, MinD-ADP can only rebind the membrane after regenerating ATP at a rate λ. **(b)** MinD can also bind flat membranes and recruit MinD-ATP, although less favored due to lower local abundance of MinJ-DivIVA complexes. **(c)** Simulation of the reaction-diffusion model in a 3D-rod shaped cell (geometry details in **Fig. 4.1**). Blue-to-red (heatmap) indicates MinD density distribution. Starting in a steady-state distribution scenario with polar DivIVA (high polar recruitment and low polar detachment rate, **left**), MinD is most dense at the poles. When polar DivIVA is removed (recruitment and attachment rate uniform on entire membrane), MinD redistributes over time **(left to right)**, with preferred localization around midcell in the final steady-state **(right)**. **(d)** To test for possible recruitment of MinD to midcell by MinJ-DivIVA within our dynamic model, simulations were started **(left)** at the same initial conditions as (c), but with MinJ-DivIVA localized at midcell (enhanced recruitment and decreased detachment). Over time **(left to right)** MinD localizes at the septum, with high density and sharp boundaries in the final steady-state **(right)**. Figure and analysis by Laeschkir Hassan and Erwin Frey (Arnold Sommerfeld Center for theoretical physics, LMU Munich).

Based on the presented reaction-diffusion model, finite-element computational studies were carried out. In a growing *B. subtilis* cell, that has not formed a septum yet, the majority of DivIVA-MinJ is assumed to be concentrated at the polar region of the cell, reflected in increased recruitment and decreased detachment of MinD. Since these conditions are based on experimental observations, characterizing DivIVA as scaffolding protein with high affinity for negative curvature (Lenarcic et al. 2009; Ramamurthi et al. 2009), it was chosen as starting point for the simulations, depicted in **Fig. 2.10 c** and **d** (left). By simulating disappearance of polar MinJ-DivIVA through equalization of MinD recruitment and detachment rates over the whole length of the cell (**Fig. 2.10 c**), polar MinD localization is lost over time (left to right). In the final steady state (**Fig. 2.10** right), MinD localizes preferentially in the center of the cell in a dynamic equilibrium state. The protein is however dispersed and can be found throughout the

whole cell body, in accordance to our experimental observations of fluorescently labeled MinD in *ΔminJ* or *ΔdivIVA* strains (chapter 2.1.3). Based on the same reaction-diffusion model, we next ran a computational study to test if MinD can re-localize to midcell upon septum formation (**Fig. 2.10 d**). Formation of a septum was simulated through DivIVA and MinJ re-localization from poles to midcell, mirrored in the shift of locally increased recruitment and decreased detachment rates of MinD from the poles to the cell center. Over time (**Fig. 2.10 d**, left to right), MinD sharply localizes to the center of the cell, following MinJ-DivIVA complexes, again in a dynamic equilibrium state. In the final steady state (**Fig. 2.10**, right), the width of the MinD distribution was directly dependent on the relationship between membrane diffusion and local recruitment of MinD through MinJ-DivIVA (see chapter 4.7.2 for details).

Hence, the proposed model is in accordance with our experimental observations, and demonstrates how the *B. subtilis* Min system can reach an over-time averaged stable localization of MinD at poles and midcell, despite being very mobile and displaying high protein exchange rates. Interestingly, the relative protein amounts were important for functionality of the system. Upon artificially misbalancing the given protein amounts (**Table 2.3**) during simulations, aberrant MinD localization could be observed, and MinD could no longer stably localize to poles or midcell in a dynamic equilibrium (data not shown), underlining the importance of native protein expression levels for functionality of interdependent systems like the Min systems.

2.1.5. SMLM analysis of the Min system

2.1.5.1. SMLM reveals apparent clustering of Min proteins

The Min system in *B. subtilis* is frequently regarded as stable gradient with highest protein concentrations at poles and midcell (Rowlett and Margolin 2015; Haeusser and Margolin 2016). This assumption is mainly based on diffraction-limited microscopy of fluorescently labeled Min proteins, as it can also be observed in **Fig. 2.2**. In the last chapter, we proposed a new model and mechanism, where Min proteins and especially MinD cycle dynamically between membrane and cytosol and re-localize to midcell upon septum formation, creating a dynamic equilibrium. This would translate into Min proteins being localized along the entire membrane as well as lateral sites in a still image, only displaying a gradient when observed over time. To investigate this with highest possible resolution, we decided to use PALM to reconstruct Min localization in chemically fixed *B. subtilis* cells expressing fluorescently labeled Min proteins. To this end, strains with PALM compatible fluorophores were successfully constructed when not already available (**Table 4.3**). While Dendra2-MinD (BHF011) and DivIVA-PAmCherry (JB37) could be successfully imaged with average precision of 25-30 nm (**Fig. 2.11**, left and

right), MinJ-Dendra2 (JB38) emitted only little and dim signal, leading to unsatisfactory imaging results. Therefore, MinJ-mNeonGreen (JB40), which produces a strong and correctly localized fluorescent signal in conventional fluorescence microscopy (**Table 2.1**, **Fig. 2.1**), was employed and successfully imaged with a localization precision of around 25-30 nm (**Fig. 2.11**, center). In PALM, mNeonGreen presents some challenges compared to conventional PALM fluorophores, which prompted us to optimize PALM sample preparation and imaging of the said fluorophore (Stockmar et al. 2018), which will be discussed in a later chapter (2.3).

Importantly, no distinct gradient could be observed for any of the Min proteins (**Fig. 2.11**). Instead, proteins appear to accumulate mainly in clusters, localized at the membrane (**Fig. 2.11**, MinD, MinJ and DivIVA) and in the cytosol (**Fig. 2.11**, MinD and DivIVA).

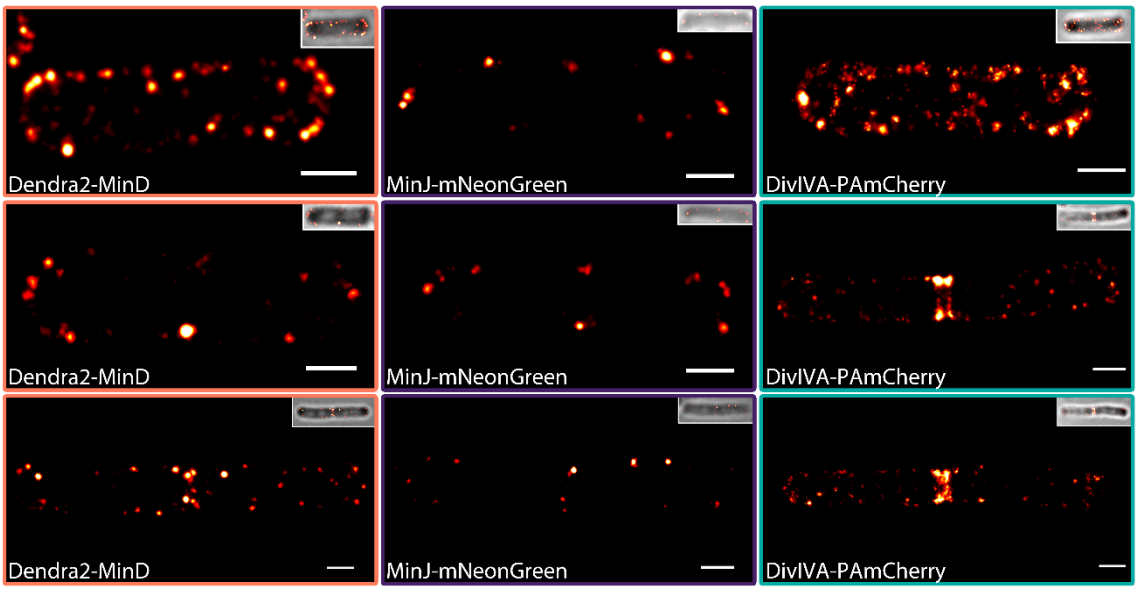

Fig. 2.11: PALM of Min proteins in fixed cells reveals membrane and cytosolic clusters.

Strains expressing Dendra2-MinD (BHF011, **left**), MinJ-mNeonGreen (JB40, **center**) or DivIVA-PAmCherry (JB37, **right**) were grown to mid-exponential phase, chemically fixated with formaldehyde (1.5%) and subsequently imaged via PALM. All shown images are representative images of cells in different divisional states. The top row shows cells before formation of a division septum. Upon formation of a septum (center and bottom row), Min proteins partially re-localize from poles to midcell. Individual top right insets display an overlay of the corresponding widefield image and PALM rendering, respectively. Scale bar 500 nm.

Clustering indicates that DivIVA-MinJ complexes recruit other Min components, resulting in a higher affinity of Min proteins to an existing cluster compared to individual membrane binding, while detachment rates should be lower in comparison, due to stabilizing and crowding effects, a finding support by the mathematical model. Also in agreement with our model, we observed active enrichment of Min proteins at young poles (**Fig. 2.11**, center and bottom panel). This finding supports the hypothesis of a role of the Min system in regulation of cell division and cell size maintenance (van Baarle and Bramkamp 2010; Yu et al. 2020), rather than a role in

positioning of FtsZ or protection of poles from aberrant cell division. Additionally, we observed double-rings around the putative division-site in late divisional cells expressing MinJ and DivIVA (**Fig. 2.11**, center and bottom panel). These rings have been detected before in 3D-SIM images (Eswaramoorthy et al. 2011) and further highlight the importance of increased resolution for structural analysis.

Next, we wanted to understand why diffraction-limited microscopy displays Min proteins as gradients (e.g. **Fig. 2.2**). To make sure that the observed clusters are not fixation artifacts, we first investigated localization and appearance of the fusion proteins in chemically fixed cells in conventional fluorescence microscopy. Some protein fusions like DivIVA-PAmCherry (JB37) cannot be visualized satisfactorily in a conventional microscope due to the need for activation of the fluorophore and rather dim signal. However, disregarding the generally lower fluorescence intensity (which was expected due to quenching), localization and appearance did not drastically change between live and fixed cells for any tested strain, of which two examples can be found in **Fig. 2.12 d** (see **Fig. 2.2** for comparison). At a closer look however, especially Dendra2-MinD gradients appeared more discontinuous in fixed cells (**Fig. 2.12 a** and **d**). The more punctiform appearance of Dendra2-MinD along the lateral membrane in **Fig. 2.12 d** can thus be interpreted as small clusters that were masked before due to the long exposure time (200 ms), considering the fast diffusion of MinD. Since the resolution in a light microscope cannot resolve structures below 200 nm, we further investigated this phenomenon using PALM.

When investigating fixed cells in PALM, the final rendered image represents a still snapshot of the localization of all labeled proteins inside the cells at a certain time point, including very dynamic proteins like MinD. It is thus possible that a superimposition of several images of the same cell recorded at different time points could appear as a gradient. To examine this, Dendra2-MinD (BHF011) was imaged in live-cell PALM for 75 s with very short frames (15 ms), which indeed appears as a gradient when rendered into one image (**Fig. 2.12 b)**. This gradient however displays significantly sharper edges due to the increased resolution when compared to conventional microscopy (**Fig. 2.12 a** and **b**, left and right panel). To simulate a comparable, lower resolution, the image was next rendered with an artificial PSF of 200 nm (**Fig. 2.12 c**), indeed resembling the conventional light microscopy image (**Fig. 2.12 a)**. In summary, the observed gradient of Min components observed in diffraction-limited microscopy can likely be ascribed to its limited acquisition speed and spatial resolution. When resolved with higher localization precision and shorter exposure times, the Min system can be observed to form clusters, further enhanced by the capacity of PALM to detect single molecules.

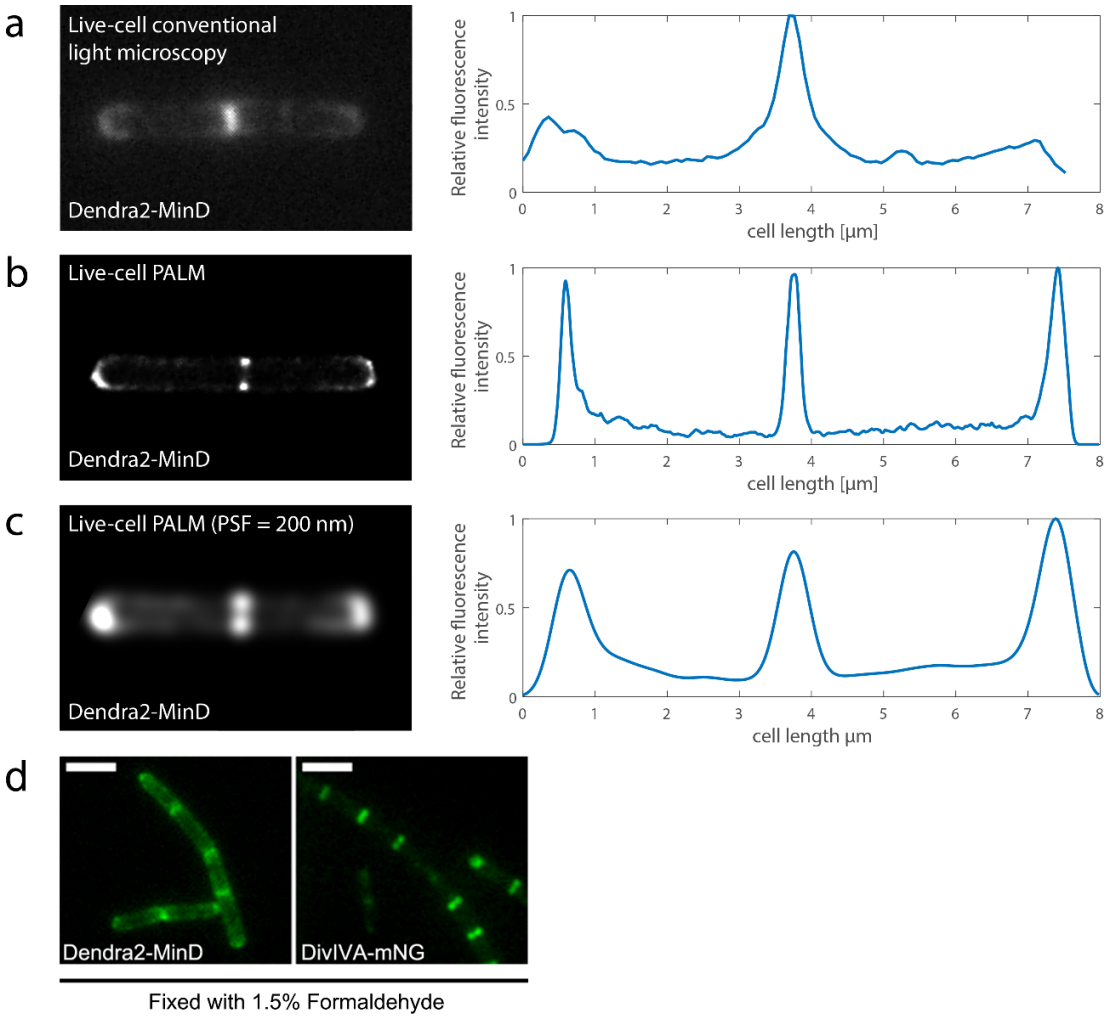

Fig. 2.12: Dendra2-MinD appears as gradient in time-lapse live-cell PALM.

(a-c) Comparison of Dendra2-MinD (BHF011) fluorescent signal (**left**) and longitudinal relative fluorescence intensity (**right**) between **(a)** conventional live-cell light microscopy, **(b)** live-cell PALM and **(c)** live-cell PALM with a rendered point-spread function of 200 nm to resemble conventional light microscopy resolution. While (b) reveals a very sharp gradient with strong peaks at poles and geometric mid-cell, (a) and (c) appear to have a smoother Dendra2-MinD gradient, likely due to lower localization precision (d) Conventional light microscopy of cells chemically fixed with 1.5% formaldehyde expressing Dendra2-MinD (BHF011) and DivIVA-mNeonGreen (BHF028). The labeled proteins still appear as a gradient, especially Dendra2-MinD. Scale bars 3 µm.

2.1.5.2. Cluster analysis of the Min system

To confirm formation of clusters and characterize their structure and distribution, a single-molecule point based cluster analysis utilizing the OPTICS algorithm (Ankerst et al. 1999) was performed next (see chapter 4.6.2.3 for details). While analysis of Dendra2-MinD and DivIVA-PAmCherry PALM data was successful (see **Fig. 2.13**, **c-e**), MinJ-mNeonGreen did not emit enough signal during imaging to be analyzed reliably for its clustering capabilities. It was therefore excluded from the analysis, but from the little data available we assume it to behave similarly to MinD and DivIVA, which naturally needs further experimental confirmation.

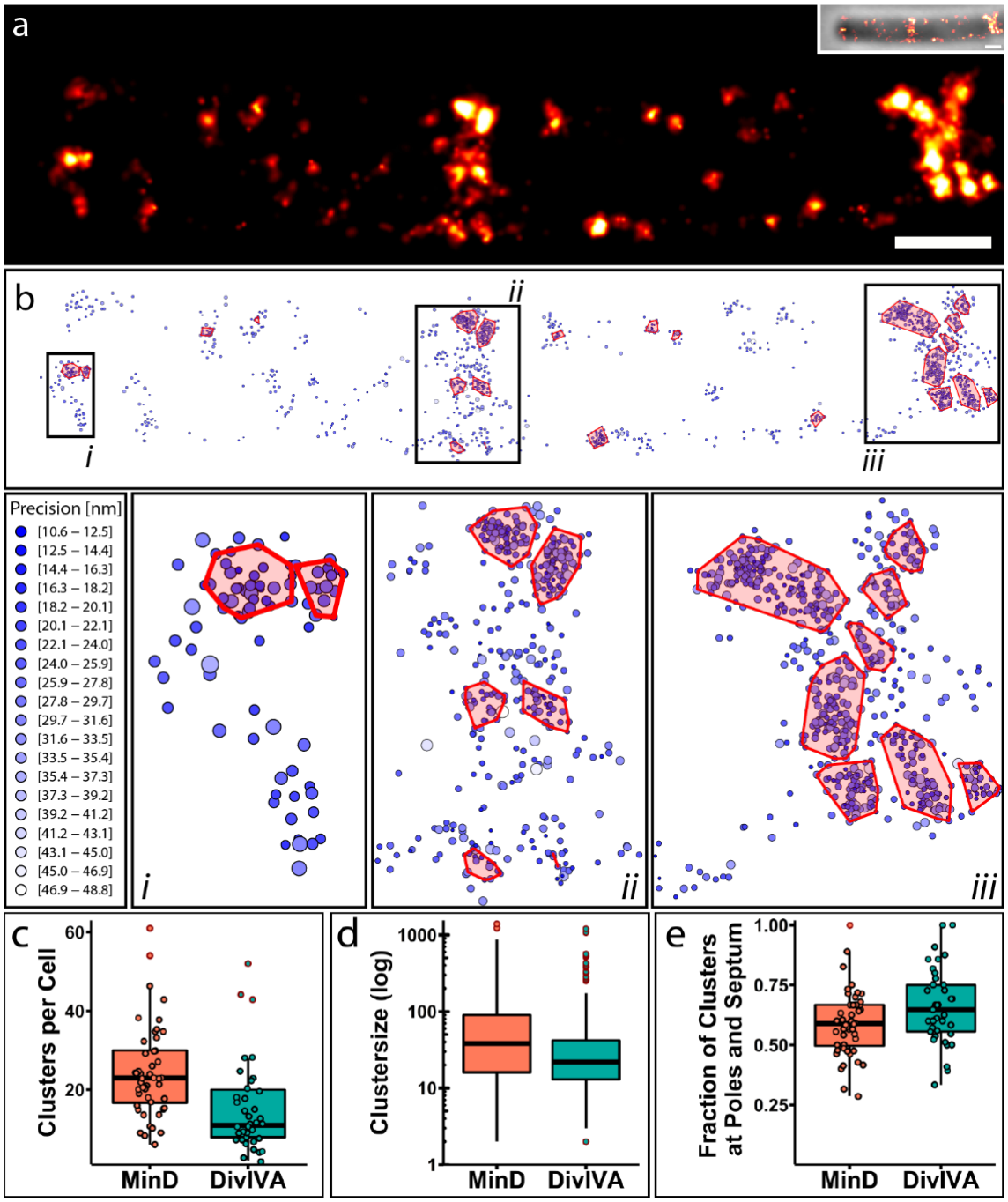

Fig. 2.13: Cluster analysis of MinD and DivIVA reveals large and dense clusters.

MinD and DivIVA frequently form large clusters, of which the majority is localized at poles and septum. **(a)** Representative PALM image of *B. subtilis* expressing DivIVA-PAmCherry (JB37) in a late divisional state. Scale bar 500 nm. **(b)** Representative cluster analysis of (a), displayed as a point pattern with three highlighted regions (***i, ii*** and ***iii***). Clusters are indicated through red-zones, as defined via the OPTICS algorithm (see chapter 4.6.2.3). Point size and color indicate localization precision of every recorded event, defined in the legend. **(c)** Boxplot of the number of clusters of Dendra2-MinD (BHF011) and DivIVA-PAmCherry (JB37) per cell (MinD, n_{cells} = 48, DivIVA, n_{cells} =37). **(d)** Boxplot of the number of proteins per cluster, no jitter is shown due to high sample number (Dendra2-MinD, $n_{clusters}$ = 1171, DivIVA-PAmCherry, $n_{clusters}$ = 586). **(e)** Boxplot of fraction of clusters localized at poles and septa per cell (MinD, n_{cells} = 48, DivIVA, n_{cells} =37). Outliers in boxplots are indicated by red outline.

In total, 151,887 events of Dendra2-MinD (BHF011) were recorded, obtained from 48 different cells, while 52,377 events of DivIVA-PAmCherry (JB37) were recorded in 37 cells. To assign these events to clusters, we used the OPTICS algorithm (Ankerst et al. 1999), and defined the minimum cluster size as 10 events based on the observed density (for details refer to chapter 4.6.2.3). During PALM, fluorophores can spontaneously switch to a dark-state for several frames, before reversing back into the on-state, which makes it difficult to allocate the corresponding different events to the same protein. Due to these blinking events, protein numbers can be slightly overestimated during PALM. This can be corrected for using control experiments and localization- and time-based grouping. Since we were only interested in the relative clustering of the protein population, events and not protein quantities were analyzed here. Under these conditions, 55.61% of Dendra2-MinD (84,470) and 52.27% (27,379) DivIVA-PAmCherry events could be allocated to clusters, indicating a generally strong tendency of the Min proteins to cluster. Next, clusters per cell were counted, which were in average 24 clusters per cell for Dendra2-MinD and 15 clusters per cell for DivIVA-PAmCherry (**Fig. 2.13 c**). Thereby, the size of these clusters varied greatly (**Fig. 2.13 d**), and Dendra2-MinD clusters were found with an average size of 72 events per cluster, while DivIVA-PAmCherry presented an average of 47 events per cluster. Rarely, very large clusters were observed, containing up to 1390 (MinD) and 1198 (DivIVA) events, respectively. When investigating the relative position of clusters (**Fig. 2.13 e**), 59% of Dendra2-MinD and 66% of DivIVA-PAmCherry clusters were found at poles and septa, revealing a high tendency for positions displaying negative curvature. The other clusters were found in the cytosol or along the lateral membrane. The observed clustering is in agreement with our model and the predicted localization of the Min proteins, where DivIVA localizes and nucleates in positions of negative curvature (Poles/Septum) and recruits MinJ and, as a result, most of the available MinD. While MinD can also bind to flat membranes, it is found in much greater numbers at sites of negative curvature (**Fig. 2.13 e**), since it is locally recruited and stabilized through MinJ-DivIVA complexes (**Fig. 2.13 e**). This becomes even more evident when analyzing DivIVA localization, of which around two thirds were found at the former or future division sites. Furthermore, this value might be even higher when observed with a different method, as filtering and post-processing in SMLM is quite challenging for very dense protein like DivIVA. Since we follow a rather conservative approach to avoid oversampling or artifacts (see chapters 4.6.2.3 and 2.3), some true localizations in these dense spots might have been filtered out. Finally, Both MinD and DivIVA were found with a higher tendency to bind to existing clusters, and could not be observed as homogeneous distribution along the lateral membrane. Furthermore, no gradient of any Min protein could be observed when imaging chemically fixed Min proteins in SMLM.

2.2. Establishing of SPT

Even though it seems most imaging in the field of microbiology is still performed on conventional fluorescent microscopes, when scanning recent publications, one microscopy application appears to receive increasing attention: single-particle tracking PALM. This apparent gain in popularity can be explained by its sensitivity and versatility in identifying different protein or DNA/RNA populations and their binding or diffusion dynamics by tracking particles and their trajectories over time, making it a very strong tool. SPT has been used to e.g. determine localization and dynamics of replisome proteins in *B. subtilis* (Li et al. 2019), for diffusion localization of tRNA in *E. coli* (Plochowietz et al. 2017) and for direct measurements of tRNA protein synthesis kinetics (Volkov et al. 2018), to monitor bacterial DNA repair processes (Klein et al. 2019) or DNA gyrase activity (Stracy et al. 2019) or to study CRISPR–Cas/DNA interaction dynamics and quantities in *E. coli* (Turkowyd et al. 2019). Recently, SPT was even shown to be feasible for fast detection of influenza viruses and possibly others (Robb et al. 2019).

Since SPT is ideal to identify and characterize protein populations and can theoretically be performed in our SMLM microscope with some limitations (Zeiss Elyra P.1), I set out to analyze and confirm the previously observed Min dynamics with this independent method. Since this technique is quite complex and must be fine-tuned to produce valid results, a reliable experimental routine had to be established first.

2.2.1. Sample preparation for SPT imaging

Sample preparation in SPT is quite challenging due to its high sensitivity, making it prone for detection of background fluorescence, both intercellular and extracellular (Turkowyd et al. 2019). Compared to PALM or STORM, where samples are often fixed and immobilized by e.g. poly-L-lysine, SPT requires cells to be viable throughout the imaging process. As phototoxicity or cellular stress often result in increased autofluorescence and might even affect the physiology of the organism, the (mounting) medium and imaging process need to be evaluated to ensure reliable experimental results. Since this process is different between organisms or even experimental conditions, there is no universal solution, so different conditions need to be tested. To analyze the *Bacillus* Min system via SPT, I first tested for an adequate mounting medium. Since cells must remain immobile for SPT without affecting their physiology, agar pads (1.5% agar in colorless MD medium) were the first choice, in combination with high precision coverslips (Zeiss High Performance). MD medium was chosen, as it did not produce significant

background when used as liquid medium in PALM samples of fixed cells, which were additionally also grown in MD prior fixing (see chapter 2.1.5).

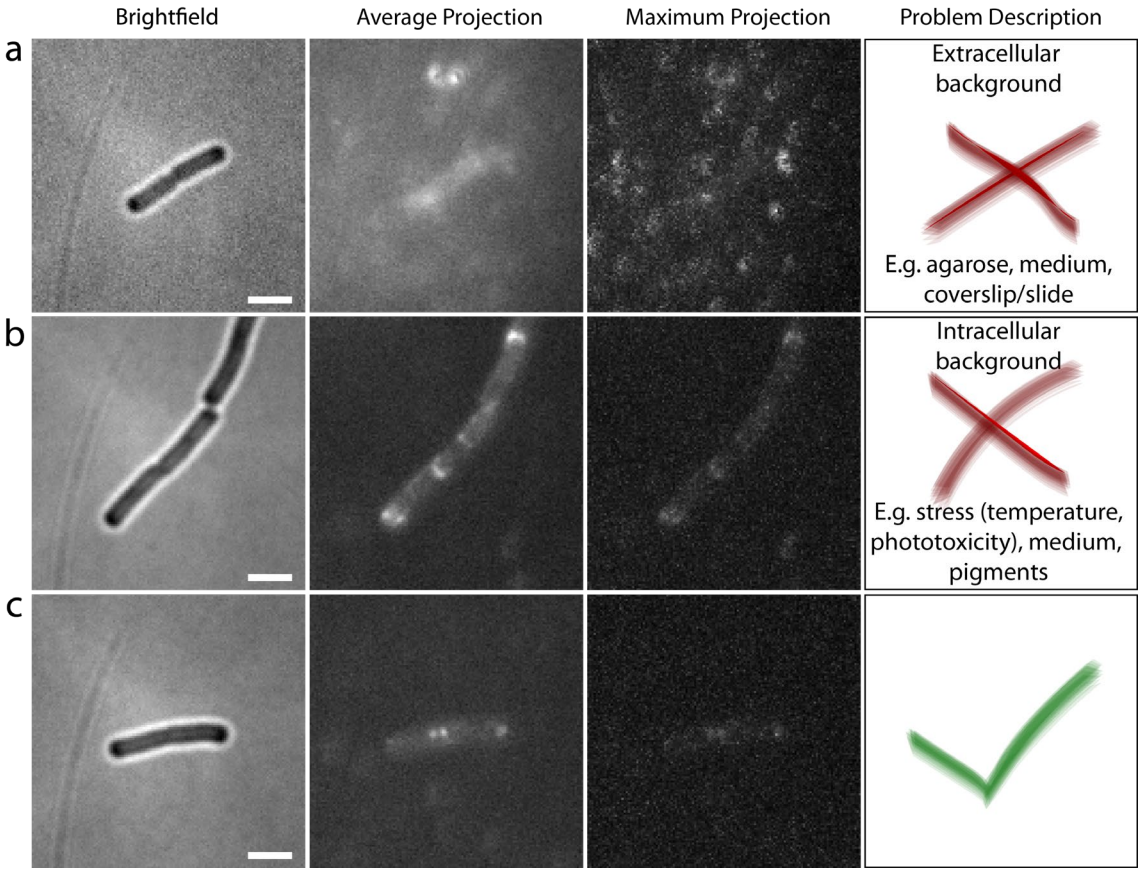

Fig. 2.14: Single particle tracking in SMLM requires careful optimization.

Sample preparation and imaging need to be optimized in SPT to remove background signal. Comparison of widefield fluorescent images of differently prepared samples of growing *B. subtilis* cells expressing Dendra2-MinD (BHF011). Generally, cells were mounted on agarose pads (1.5% in filtered MD medium) and covered with a specifically treated/cleaned coverslip (see chapter 4.6.2.1). **(a)** Example of a sample where the medium was not filtered and coverslips were not treated/cleaned. **(b)** Example of cells that were imaged for a too long duration (15,000 frames instead of 5,000), increasing their autofluorescence over time. **(c)** Example of optimized sample preparation, not creating any excessive background in the final raw data. The first column shows a bright field image of the respective cells taken before fluorescent imaging. The second column displays an average projection of 100 consecutive frames, while the third column shows a maximum projection of the same 100 frames. The last columns describes possible artifact sources during imaging in the respective samples. Samples (a) and (c) were imaged for 5000 frames, sample (b) for 15000 frames, with 15 ms exposure per frame. Dendra2 was converted with a 405 nm laser (0.5 % laser power/~4 W cm^{-2}) and excited with a 562 nm laser (30 % laser power /~400 W cm^{-2}). Scale bars 2 µm.

Unfortunately, the tested samples displayed a strong extracellular background (**Fig. 2.14 a**), interfering with the analysis process. Upon filtering the medium (0.2 µm membrane filter) to remove larger dirt particles, extracellular background was reduced, yet still too high (data not shown). Therefore, different agarose types and melting procedures were tested. When comparing low-melting agarose (Biozym) and regular agarose (Serva), no measureable

difference could be observed (data not shown). Inspired by a previous publication (Uphoff et al. 2013), I next compared two methods of preparing the agarose pad: (1) melting 3% agarose in ultra-pure water and subsequently mixing it with 2x MD medium and (2) melting 1.5% agarose directly in MD medium. Again, I could not measure or observe a significant difference (data not shown). To produce a thinner, flat and more defined agar pad, gene-frames (Thermo Scientific) were used from this point onwards, which led to slightly less background and a very consistent focal plane level, however still not fully satisfactory results. Therefore, I next turned toward different cleaning procedures of the microscopy slides and coverslips. After testing different protocols, I could see a significant decrease in background fluorescence (**Fig. 2.14 c**). Testing included e.g. overnight incubation in 1M KOH (Turkowyd et al. 2017), Plasma cleaning (Lelek et al. 2014), or organic solvents/alkaline concentrate (Rosch et al. 2018a). The best balance between speed, effort and efficiency of the procedure were obtained using a protocol utilizing ultra-sonication and Hellmanex III (Hellma Analytics) (for details see chapter 4.6.2.1, adapted from (Rosch et al. 2018a)). The remaining extracellular background could be filtered or excluded by the spot detection algorithm. To reduce intracellular background, imaging conditions were optimized next.

2.2.2. Optimization of imaging conditions for SPT

Since Min proteins can display a wide spectrum of mobility, spanning immobile protein and membrane-bound diffusive complexes, but also freely diffusive protein (see results 2.1.4), a wide temporal range needs to be covered. To be able to register fast moving molecules with precision, SPT requires the camera to collect photons with high sensitivity, but also very fast, optimally 10 ms or less per frame (Bakshi et al. 2011; Klein et al. 2019), while slowly diffusing or immobile molecules can be imaged at slower frame-times of around 30 ms or more (Turkowyd et al. 2019). To achieve a fast imaging speed with the camera in our system (Andor iXon 897 EM-CCD), the field of view (FOV) needs to be cropped to a smaller size, here corresponding to 12.8 µm * 12.8 µm, limiting the number of cells that can be imaged at a time. Utilizing this, the shortest frames that can be recorded in our system last 13.3 ms, which is unfortunately too slow to record very fast diffusing particles accurately (Bakshi et al. 2011; Turkowyd et al. 2019). Due to these constraints, a single time-scale with a frame length of 15 ms was used as a compromise to obtain the first data sets. In an optimal study however, images are recorded at two or even three different time-scales to obtain reliable data for all protein populations (Turkowyd et al. 2019).

Furthermore, statistically reliable analysis of SPT requires a large number of tracks, which makes it seem attractive to image cells for as long as possible, only limited by cell viability.

Therefore, cells were screened for phototoxicity and survivability on the agar pads. Best results were obtained when samples were used for a maximum of 30 min after preparation, as cells slowly started to produce autofluorescence past this point, comparable to the cell in **Fig. 2.14 b**. Next, adequate laser intensities for imaging were determined. The acceptable power of the activation laser directly depends on density and quantity of the labeled protein. This was determined manually for each sample by visually inspecting images acquired with increasing laser powers, and furthermore compared to a wild type strain to indicate possible autofluorescence. Optimally, the camera records exactly one event per cell and frame to avoid overlapping particles while still collecting as much information as possible. In our system, best results were obtained with laser intensities varying between ~1 – ~ 8 W cm^{-2}. It can be beneficial to increase the laser power stepwise over the course of the experiment, which is however relatively hard to reliably perform manually due to the short experiments (75 s), while automated increase is not satisfactory configurable in the proprietary imaging software (ZEN 2.3, black edition, Zeiss). To create reproducible results, ~4 W cm^{-2} were used hereafter. Since excitation laser (561 nm) intensities had been optimized for static imaging of Dendra2 and PAmCherry before (see chapters 4.6.2.2 and 2.3), ~200 W cm^{-2} were applied first. Localization precision was poor when using a frame length of 15 ms due to an insufficient amount of photons emitted, likely caused by the shorter frame length (15 instead of 50 ms). Hence, the laser power was increased stepwise up to ~ 800 W cm^{-2}, with ~400 W cm^{-2} representing the "sweet-spot" between localization precision and fluorophore bleaching/phototoxicity, which was henceforth used. Cell viability was tested by screening visible cell growth 30 min after imaging, using different total numbers of frames. At 15 ms frame length and ~4 and ~400 W cm^{-2} laser intensities for the 405 nm and 561 nm lasers, respectively, all 20 tested cells were still growing after 5,000 frames, while most cells stopped growing when being imaged for 10,000 frames (16 out of 20). Upon doubling the frame length to 30 ms, the 561 nm laser intensity was halved to ~200 W cm^{-2}, and even though 5,000 frames correspond to an also doubled time-span, cells were still growing after imaging, prompting me to use a maximum of 5,000 frames for both acquisition speeds.

2.2.3. Choosing the data analysis method for particle tracking

After establishing appropriate and reliable methods for sample preparation and SPT imaging, initial data of Dendra2-MinD (BHF011) were collected. To identify and analyze molecule trajectories, several algorithms and tools have been developed, of which some popular examples can be found in the following publications: (Jaqaman et al. 2008; Tinevez et al. 2017; Hansen et al. 2018; Rosch et al. 2018b; Herbert 2019). Since the applications of SPT cover a broad spectrum, the choice of tracking algorithm is situational and depends on the type of data and analysis,

which often manifests in hand-tailored/home-built applications and analysis scripts, developed individually, e.g. (Plochowietz et al. 2017; Li et al. 2019; Stracy et al. 2019). Generally, the SPT workflow includes several imaging analysis processes that can encompass background noise reduction, spatial localization of particles, connection and reconstruction of the particles trajectories, analysis and classification of the particles mode of movement and subcategorization of different protein populations. This process was recently reviewed by (Ma et al. 2019).

To establish a functional and fast routine for SPT, three different tracking softwares were tested and compared, namely GDSC SMLM (Herbert 2019), Trackmate 3.8 (Tinevez et al. 2017) and u-Track 2 (Jaqaman et al. 2008). Important criteria in the comparison were (1) quality of the trajectories and available correction methods, (2) relative duration of spot detection and subsequent trajectory reconstruction, (3) automatization capabilities and (4) trajectory analysis features, of which the results are summarized in **Fig. 2.15**. Naturally, it was desirable to obtain high quality trajectories quickly, with the option to filter, e.g. falsely connected tracks from neighboring cells or artifacts, and the possibility to automatize the process to analyze several experiments in one run. Furthermore, features that allow direct analysis of trajectories were positively connoted, as well as free availability of the software package and its accessories.

All three software packages use different localization and tracking algorithms. I first tested GDSC SMLM (Herbert 2019) (**Fig. 2.15 a**), a free plugin collection for ImageJ2 (Rueden et al. 2017) that is included in the Fiji distribution (Schindelin et al. 2012) and localizes particles through a 2D Gaussian fit utilizing either a non-linear least squares Levenberg-Marquardt method or Maximum Likelihood fitting, followed by a tracking algorithm that is based on the work of (Coltharp et al. 2012). While the plugin can be customized to great detail for every kind of optical system, doing so is extremely complex and requires testing, calibration and detailed knowledge about physical parameters of the system. The fitting algorithm (PeakFit), however, has been described as one of the most powerful in a side-by-side comparison study (Sage et al. 2019). To obtain high quality trajectories, it is nevertheless necessary to filter out artefacts or falsely connected trajectories, which is the biggest drawback of GDSC SMLM. Even though it is theoretically possible to filter tracks by exporting the results and doing it manually, this is not feasible when working with large datasets or aiming for a large number of trajectories ($n \geq 5000$). Batch analysis is possible through the ImageJ macro language, and performs very fast: generation of trajectories from raw data was possible in less than 30 seconds when using least squares fitting. The plugin includes the most important types of analysis, comprising mean squared displacement (MSD) and jump distance (JD) analysis based on (Weimann et al. 2013), which allow to calculate diffusion coefficients and to identify protein populations of different mobility.

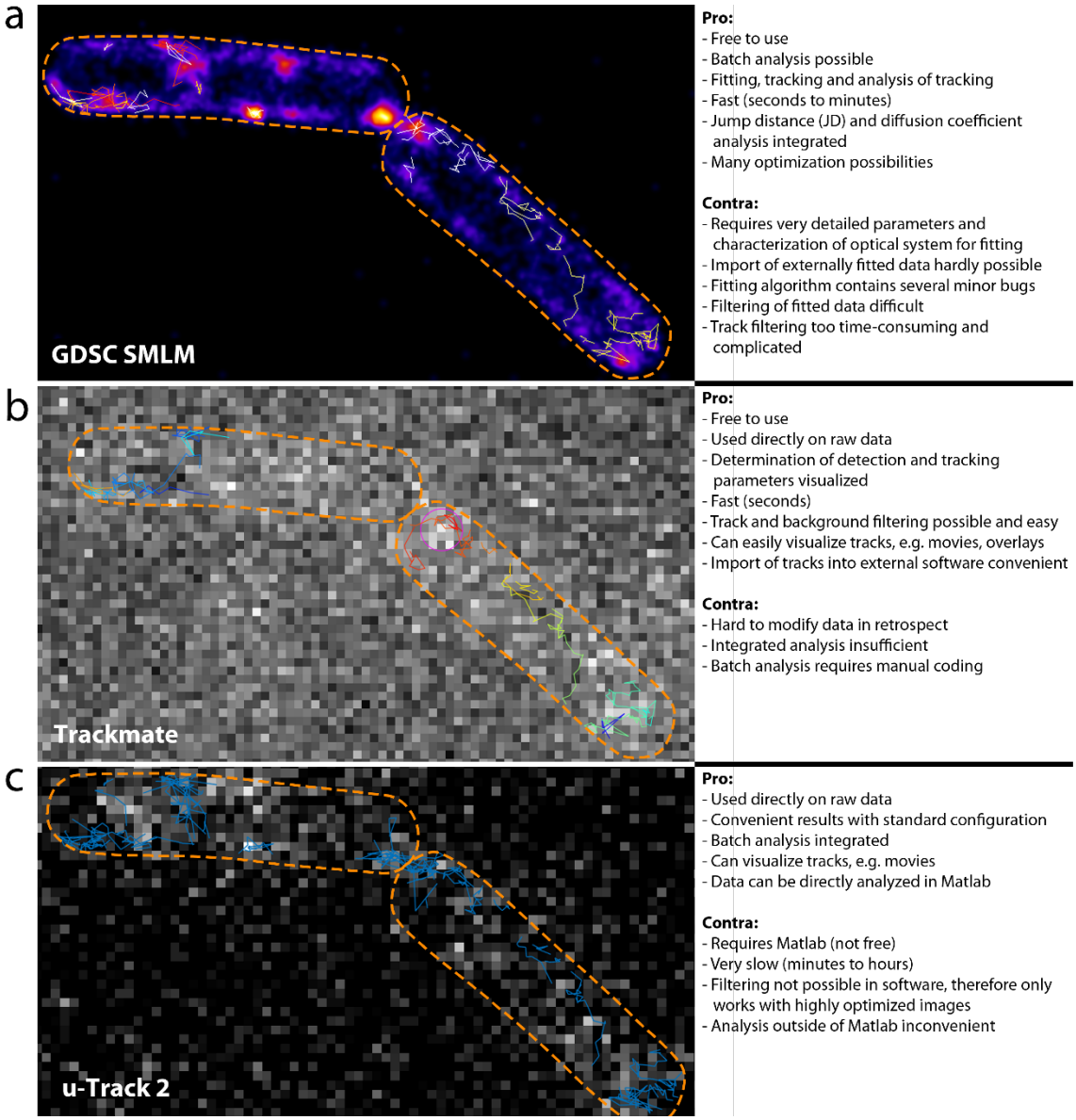

Fig. 2.15: Comparison of three tracking software packages for SPT analysis.

As analysis of SPT data is very time consuming, an initial choice for a suited tracking software had to be made before analysis of data from the Min system. Using a SMLM SPT dataset of *B. subtilis* Dendra2-MinD (BHF011) obtained as described in 2.2.2, three different software packages ((**a**) GDSC SMLM; (**b**) Trackmate and (**c**) u-Track 2) for particle tracking were tested and compared. The most important findings are described in the right column, sorted by pro and contra.

Next, Trackmate (Tinevez et al. 2017), a plugin for ImageJ2 (Rueden et al. 2017) that is likewise included in the Fiji distribution (Schindelin et al. 2012), was tested (**Fig. 2.15 b**). Trackmate is also directly applied to raw data. It first identifies spots through either of four relatively simple detection algorithms, which are all based on Laplacian of Gaussian filtering (Tinevez et al. 2017), but also allows for manual spot identification. Configuration via an estimated signal diameter and a detection threshold value is straightforward and can directly be visually tested on any open image with the chosen settings. Proceeding, spots can be conveniently filtered by several

parameters like signal-to-noise ratio (SNR), intensity or quality, before a tracking algorithm is applied to the remaining spots. Tracking can be executed by either of different implementations of Linear Assignment Problem (LAP) trackers, which are stripped down versions of the algorithm developed by (Jaqaman et al. 2008) for u-Track 2 and well suited for particles undergoing Brownian motion (Tinevez et al. 2017), but also include a Kalman filter (Kalman 1960) based algorithm and a simple nearest-neighbor tracker. Due to the multitude of available parameters whose effects are directly visualized, filtering of tracks is easy and straightforward. Furthermore, the direct visualization is very helpful, since the human eye is still best at detecting artifacts and erroneous tracks. Spot detection and tracking could again be executed below 30 seconds in the used test data. Analysis of the tracks is unfortunately very limited inside the plugin. The output consist of detailed statistics for every spot, track and link, but offers no way to analyze or visualize the data. Fortunately, Trackmate data can be exported with ease, and the format is widely supported by most analysis software packages, e.g. Spot-On (Hansen et al. 2018) or SMTracker (Rosch et al. 2018b), and furthermore supplies tools to export the data directly to other software like Matlab (The MathWorks, Inc). Finally, automatized batch analysis was possible, but only through manual coding in the Python programming language (Python Software Foundation, https://www.python.org/) and not as an included feature of the plugin.

The last tracking algorithm tested was u-Track 2 (Jaqaman et al. 2008) (**Fig. 2.15 c**), which is likely the most widely used tracking software package for SPT. It requires Matlab and can therefore not be considered free to use, even though the plugin itself is freely available. The analysis process is divided into detection, tracking and analysis. Detection can be performed with different algorithms, either based on Gaussian local intensity maxima fitting (Jaqaman et al. 2008) or spot extraction via multiscale products of significance thresholded wavelet coefficients (Olivo-Marin 2002). The standard parameters for spot detection thereby produce quite reliable results, but can be refined according to the data and optical system used, which requires some training. For analysis of *B. subtilis* SPT data, Gaussian fitting was chosen to detect particles. Once detection is complete, tracking can be performed. The tracking algorithm uses one afore mentioned mathematical framework, the LAP. First, detected particles between consecutive frames are linked, which generates track segments. These segments are linked in the second step, which simultaneously closes gaps and captures particle merge and split events, while using temporally global optimization to assign the track segments (Jaqaman et al. 2008). This process allows robust tracking of particles, even in very dense datasets. The cost of this robust tracking however, is the computing time, which is considerably higher than in the other two tested software packages. A single image with dense tracks regularly took 20 min or more for a full run, with some specific data sets running for more than 2 h. Even though batch analysis is implemented so that analysis can be ran over-night, testing parameters should be performed

on smaller datasets. Filtering of the data is not possible in the software itself, and has to be done manually in the resulting data in Matlab, which is additionally time consuming. Some analysis is offered by the program itself, namely motion analysis and microtubule plus-end classification, of which only the former was tested, producing a histogram of linking distances similar to JD analysis. However, since the analysis results (particles, tracks, segments etc.) are already stored in Matlab, they can readily be analyzed more in-depth, although requiring proficiency in the Matlab programming language and environment and the respective analysis algorithms.

After testing these software plugins, all three produced comparable and convenient tracking results. Trackmate was chosen for further data analysis, as it was the most time efficient plugin tested, while still producing appropriate tracking results. It furthermore allows easy filtering of data to exclude artifacts, and resulting data can be analyzed by a variety of third-party software packages. For further analysis of these tracking data, the SMTracker 1.5 software package was used (Rosch et al. 2018b), as it offers most of the common analysis methods, while it can be used without programming skills, producing statistically solid and visually appealing results.

2.2.4. SPT of the *B. subtilis* Min system

After establishing an experimental routine and means to analyze the data accordingly, SPT datasets for the Min systems were recorded. To analyze and confirm dynamics of Min proteins through this independent method, strains expressing Dendra2-MinD (BHF011), MinJ-Dendra (JB38) and DivIVA-PAmCherry (JB37) were imaged and analyzed according to the previously established method (also see chapter 4.6.2). Similar to the cluster analysis, MinJ-Dendra2 did unfortunately not produce enough signal or an appropriate SNR to be analyzed robustly, and was therefore excluded from the analysis, while the results for Dendra2-MinD and DivIVA-PAmCherry are summarized in **Fig. 2.16** and **Fig. 2.17**.

2.2.4.1. Analysis of Min dynamics through MSD analysis

Firstly, the expected mobility of Dendra2-MinD (BHF011) and DivIVA-PAmCherry (JB37) could be confirmed by the SPT experiments (**Fig. 2.16**). Thereby, trajectories could be observed and recorded throughout the length of the cell, summarized in a normalized cell in **Fig. 2.16 a, *ii*** (blue trajectories), with most trajectories being located at poles and septa where Min activity is expected, exemplary shown in **Fig. 2.16 a, *i***. Consequently, the same was true for the localization of all recorded signals, of which a mirrored heat map is shown in **Fig. 2.16 a, *iii***.

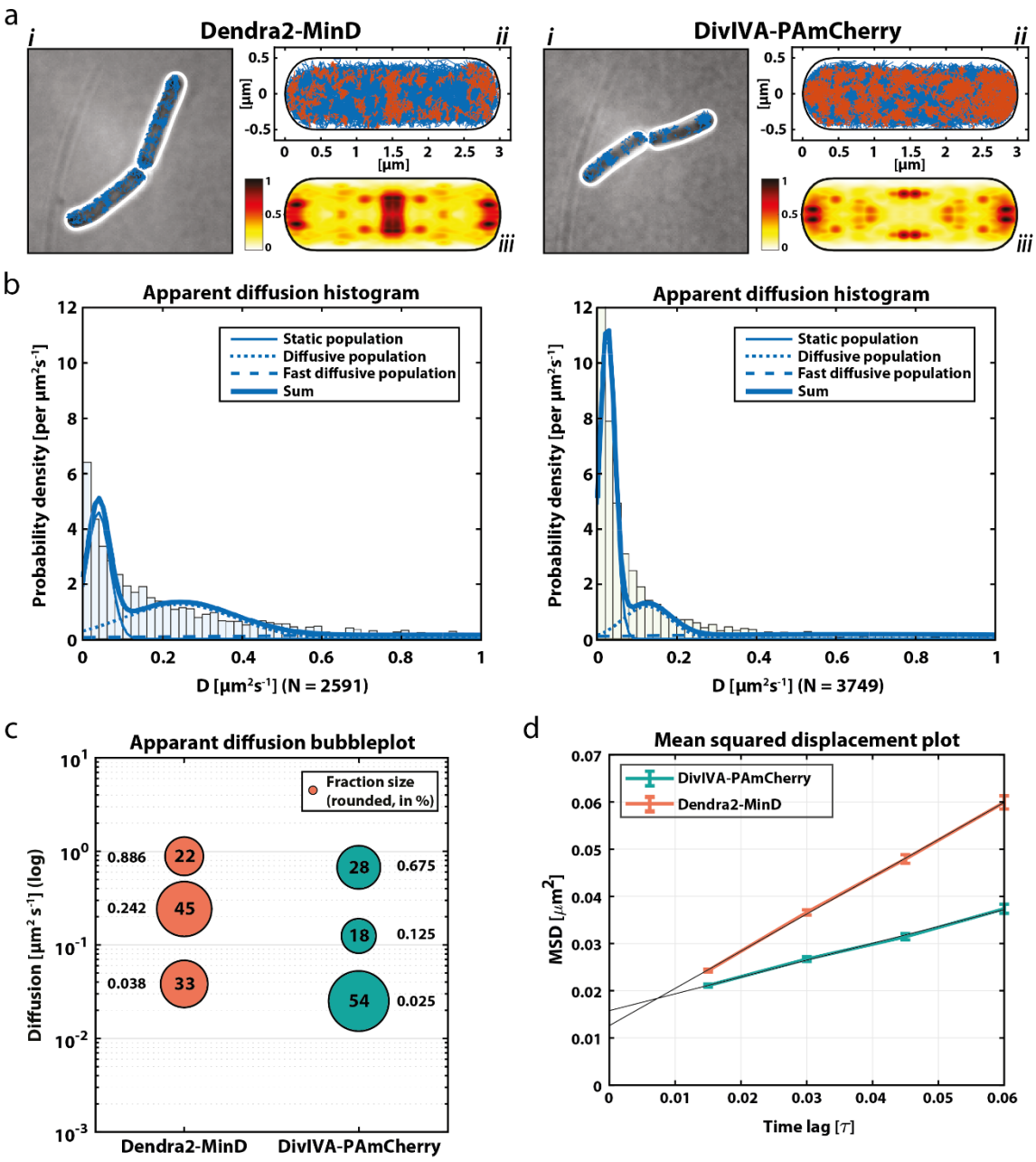

Fig. 2.16: SPT of Dendra2-MinD and DivIVA-PAmCherry confirms mobility.

(a, *i*) Exemplary image of an SPT experiment for Dendra2-MinD **(left)** and DivIVA-PAmCherry **(right)**. **(a, *ii*)** Plots of all tracks on normalized cells, respectively. Confined tracks that only moved within a radius of 130 nm are highlighted in orange, most frequently recorded at poles, septum and the membrane. For DivIVA-PAmCherry, a higher number of confined tracks can be observed. **(a, *iii*)** Heatmaps displaying normalized localization of all recorded signal, mirrored in both axes. Regions with many signals are mainly the poles and the cell center (septum) **(b)** Apparent diffusion probability distribution histograms of Dendra2-MinD **(left)** and DivIVA-PAmCherry **(right)**, respectively. Diffusion coefficients *D* were obtained from per track MSD analysis, with three different populations indicated as described in the legend. Populations were determined through multi-fitting and the best fit was selected via R^2 comparison. DivIVA-PAmCherry populations were found to be slower and more static compared to Dendra2-MinD. 5000 Frames per experiment, 15ms integration time, min. track length 5 frames, with no gaps allowed, n indicated below graph, bin size = 0.02. **(c)** Apparent diffusion bubbleplot according to data from (b). **(d)** Mean squared displacement analysis of all recorded tracks of Dendra2-MinD and DivIVA-PAmCherry, respectively. The averaged MSDs of all tracks are plotted against a timelag (τ, 5 frames) and linearly fitted. For simple Brownian motion, the slope of the fitted line is proportional to the diffusion coefficient (Dendra2-MinD 0.197 µm² s^{-1}, DivIVA-PAmCherry 0.089 µm² s^{-1}). All images were created with SMTracker (Rosch et al. 2018b) and subsequently modified.

While *B. subtilis* cells that did not contain any fluorophore (wild type) did not show significant autofluorescence, strains expressing a freely diffusive fluorophore (free PAmCherry, JB70) did not display a (similar) pattern in control experiments (data not shown), validating the obtained data for MinD and DivIVA. Quantification of mobility and identification of protein populations following different mobility modes can be performed in various ways (Weimann et al. 2013). The most commonly used type of SPT analysis to characterize the free diffusion of particles is the mean-squared displacement (MSD) analysis. To obtain diffusion coefficients (from here on referred to as "*D*"), the MSD for a particle during a given timelag (τ) is plotted against this timelag (τ) (Barak and Webb 1982), here 5 frames (**Fig. 2.16 d**). The gradient of the resulting curve is proportional to the respective *D* if the particles undergo simple Brownian motion. When averaging and plotting the MSDs of all tracks (**Fig. 2.16 d**), Dendra2-MinD (BHF011) displayed a much faster average *D* (0.197 $\mu m^2 s^{-1}$) compared to DivIVA-PAmCherry (0.089 $\mu m^2 s^{-1}$), which was expected from the previous FRAP experiments (see **Fig. 2.5**). As a control, DivIVA-PAmCherry was imaged under the same conditions after fixing it with 1.5% formaldehyde, resulting in a *D* of 0.003 $\mu m^2 s^{-1}$ (see **Fig. 3.2** in discussion). Considering that both MinD and DivIVA can freely diffuse, but also bind membrane, more than one subpopulation was expected for each of both proteins, which cannot by identified through an MSD plot. Therefore, an apparent diffusion histogram was utilized (**Fig. 2.16 b**), allowing identification of different subpopulations and the respective underlying *D*, also displayed in a bubbleplot (**Fig. 2.16 c**). For both MinD and DivIVA, the best fit was achieved for three different populations (stable/immobile, slow diffusive and fast diffusive). Again, DivIVA-PAmCherry subpopulations were generally observed with slower diffusion when compared to Dendra2-MinD (**Fig. 2.16 c**).

The baseline for the apparent diffusion of an immobile fraction in particle tracking is the finite localization precision, which leads to a localization measurement error (Qian et al. 1991), prohibiting immobile particles from appearing truly immobile in the analysis. For DivIVA-PAmCherry, 54% of all proteins appeared immobile (D = 0.025 $\mu m^2 s^{-1}$), while this subpopulation was smaller for Dendra2-MinD (33%, D = 0.038 $\mu m^2 s^{-1}$), a tendency that was also observed in FRAP experiments (**Fig. 2.5**, **Table 2.2**). When highlighting trajectories that are confined and do not leave a certain radius (here 130 nm, **Fig. 2.16 a, *ii,*** orange tracks), most of these tracks are found at poles and septum, especially for Dendra2-MinD. The slow diffusive population made up the largest fraction for Dendra2-MinD (45%, D = 0.242 $\mu m^2 s^{-1}$), being roughly twice as fast as the much smaller fraction of slow diffusive DivIVA-PAmCherry (18%, D = 0.125 $\mu m^2 s^{-1}$).

This population could comprise protein in different binding states (membrane or protein bound), e.g. mobile protein clusters and/or membrane associated protein, as well as trajectories from protein that display a transition between different types of motion (e.g. free diffusive

protein that binds a stable cluster). Since MinD is expected to actively cycle between cytosol and membrane/clusters due to its ATPase activity (see chapter 2.1.4.2), the large size of this subpopulation seems plausible. Finally, both proteins showed a small population of fast diffusive protein (**Fig. 2.16 c**). While Dendra2-MinD was observed with a higher diffusion coefficient (22%, D = 0.886 μm² s^{-1}), the fast diffusive population of DivIVA-PAmCherry was larger in comparison (28%, D = 0.675 μm² s^{-1}). It is possible that the D of freely diffusing particles in this analysis is generally underestimated due to technical reasons, which is debated in the discussion section (chapter 3.2.2).

2.2.4.2. Analysis of Min dynamics through jump distance analysis

Even though widely used to analyze SPT data, MSD analysis by itself is limited in its significance for several reasons, specifically in bacterial SPT. The per-track MSD and the resulting D is usually calculated as the average of the various displacements within a trajectory for the given timelag. For a particle that was tracked for 7 continuous frames and a τ of 5 frames, this would result in 3 different MSD values, that would be averaged for a final value. While this method reduces statistical scatter, it obscures changes in mobility, e.g. if a protein binds a membrane ligand during tracking after freely diffusing in the cytosol (Weimann et al. 2013). Furthermore, the resulting D does not equal an accurate diffusion coefficient because of cell confinement, motion blurring, and localization error (Uphoff et al. 2013; Stracy et al. 2014; Stracy et al. 2015), which are more pronounced in bacterial cells compared to eukaryotes. To account for these factors, Monte Carlo diffusion simulations have been employed before by the Kapanidis lab (Stracy et al. 2015), which is however not included in this study. Instead, a second type of analysis was chosen to confirm the observed data, jump distance (JD) analysis (**Fig. 2.17**). While MSD analysis for short trajectories (<32 steps) often results in wide distributions of D and thus inaccurate results (Saxton 1997), JD analysis performs better when analyzing short trajectories or particles that undergo changes in motion, with increasing precision in larger data sets above 750 trajectories (Weimann et al. 2013; Turkowyd et al. 2019). Since SPT data from fluorescent proteins usually results in relatively short tracks due to photobleaching, and MinD is expected to change motion frequently, JD analysis is appropriate to analyze diffusion of the Min proteins. Furthermore, it is less sensitive to incompletely connected trajectories, as long as connections made are correct (Weimann et al. 2013). In JD analysis, a probability distribution is created by counting the jump distances that single particles travel within a set time-interval (Δt) (Weimann et al. 2013). By fitting the data with a Rayleigh distribution, D can be estimated, with the possibility to extend the analytical expression to fit different subpopulations and determine their distinct D and fraction size (Weimann et al. 2013). The minimal number of necessary

subpopulations to describe the data can thereby be predicted quite reliably by comparing residuals of the fit of models with increasing complexity, starting with one population, up until no systematic deviation occurs (Weimann et al. 2013). Utilizing JD analysis, the previously analyzed data was re-investigated to confirm the number of populations and their respective fraction size and *D*. Again, a fit with three populations produced the best results compared to one or two populations (**Fig. 2.17**).

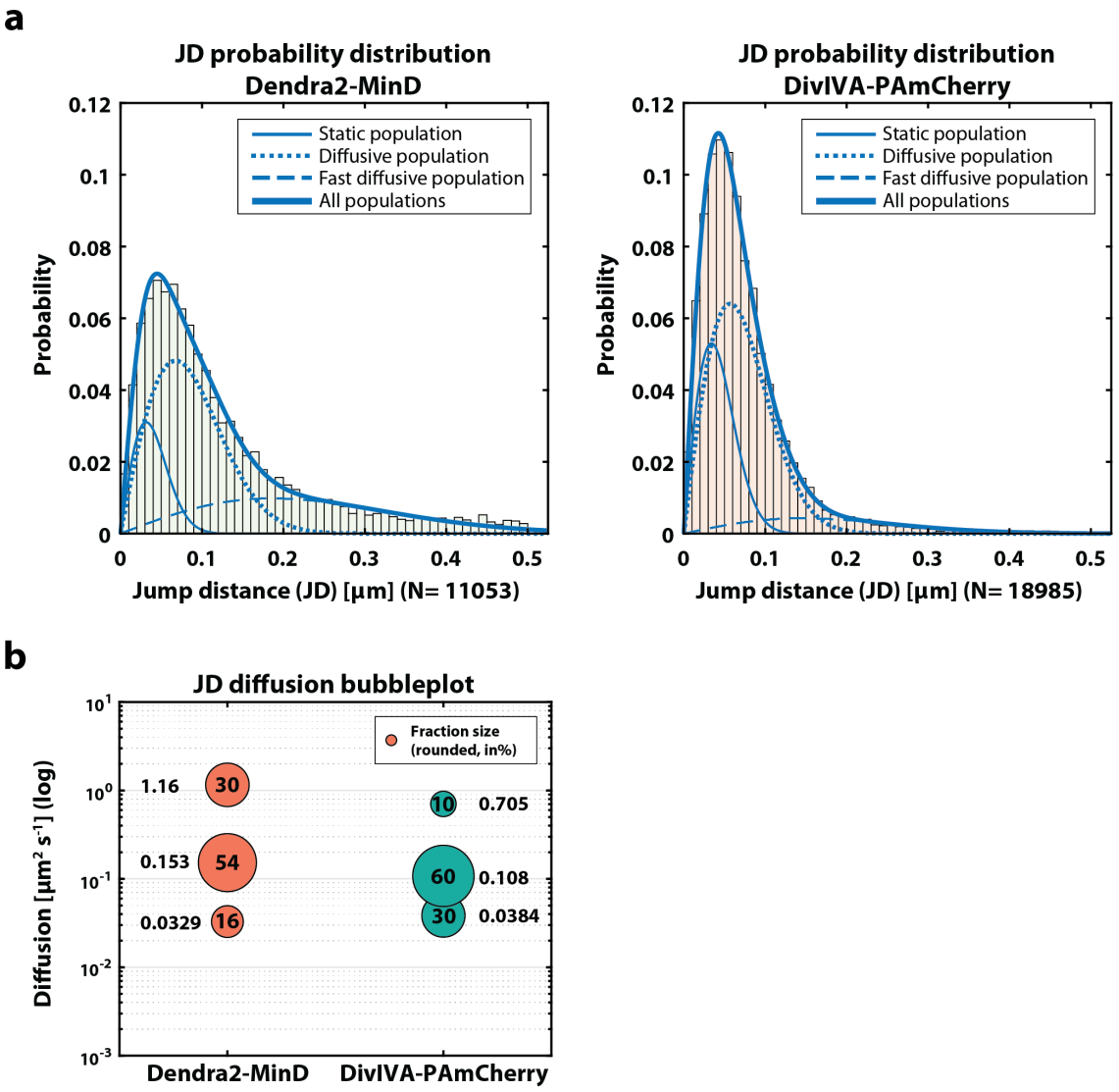

Fig. 2.17: JD analysis suggests three subpopulations for MinD and DivIVA.

(a) Probability density function (PDF) histogram of tracking data described in **Fig. 2.16** (**MinD left, DivIVA right**), with Δt 1 frame (15 ms) and bin size = 10 nm. The number of populations was automatically selected by SMTracker via p-value comparison between models with 1, 2 and 3 populations, separated by their mobility. The different population fractions and diffusion coefficients were determined by fitting the PDF with Rayleigh distributions. **(b)** Diffusion coefficient bubbleplot of the respective populations from (a) determined via JD analysis. All images were created with SMTracker (Rosch et al. 2018b) and subsequently modified for enhanced visualization of the data.

Generally, the JD results confirmed MSD analysis, with some deviations. The immobile fraction is smaller for both Dendra2-MinD (16%, D = 0.0329 $\mu m^2 s^{-1}$) and DivIVA-PAmCherry (30%, D = 0.0384 $\mu m^2 s^{-1}$), albeit still being significantly higher for DivIVA compared to MinD, similar to the FRAP results (see **Fig. 2.5**). The slower diffusive populations of Dendra2-MinD (54%, D = 0.153 $\mu m^2 s^{-1}$) and DivIVA-PAmCherry (60%, D = 0.108 $\mu m^2 s^{-1}$) were the largest subpopulations observed for both proteins. For Dendra2-MinD (see 2.2.4.1) this was expected and correlates well with the results from MSD analysis (**Fig. 2.16 b** left and **c**). For DivIVA-PAmCherry, the *D* of this subpopulation is more similar to the immobile subpopulation in comparison, and both populations are not well separated in the probability distribution (**Fig. 2.17 a**, right). The fast diffusive subpopulations of both Dendra2-MinD (30%, D = 1.16 $\mu m^2 s^{-1}$) and DivIVA-PAmCherry (10%, D = 0.75 $\mu m^2 s^{-1}$) confirm a higher mobility of MinD when compared to DivIVA. While the fast diffusive population of MinD increased in size and speed when comparing JD to MSD analysis, the respective subpopulation of DivIVA decreased significantly, indicating that it might have been overestimated in MSD analysis. A lower number of cytosolic and thus fast diffusing DivIVA proteins correlates well with FRAP results, where MinD recovered around 10-fold faster, (see **Fig. 2.5**). Possible reasons for the discrepancy between the SPT analysis method results as well as FRAP data will be debated in the discussion (see chapter 3.2.2).

In summary, I could confirm the mobility of both MinD and DivIVA via SMLM analysis. Both protein populations were observed to consist of several subpopulations, of which some are immobile and found in clusters, while others are diffusing freely or associated with the membrane/a cluster, which is consistent with the previous FRAP analysis (2.1.2 and 2.1.5) and our proposed mathematical model (2.1.4). All these notions provide evidence for a dynamic steady state of the Min system, which was previously rather described as a stationary gradient (Rowlett and Margolin 2015; Haeusser and Margolin 2016). Our group previously reported on re-localization of Min proteins from the poles to active division sites upon septum formation (Bach et al. 2014). These results conflict with the idea of a division-site selection system, as membrane invagination and thus negative curvature at the septum is the basis for re-localization of DivIVA and hence MinCDJ, an event downstream of division-site selection. Instead, we propose a role of the *B. subtilis* Min system in cell cycle regulation and disassembly of the division apparatus, a finding indicated in an earlier publication from our group (van Baarle and Bramkamp 2010) and also supported by other research groups (Rodrigues and Harry 2012; Yu et al. 2020). The observed and described steady state dynamics of the Min components are thereby necessary to continuously scan the cell for a division-site (negative curvature) and relocate upon detection to act downstream of division. The exact functions and relevance in this regard have to be further determined in the future. Additionally, the role of the Min system during sporulation should be further investigated. Since the asymmetric division also includes

formation of negative curvature, the Min system and its dynamic steady state should be affected, although RNA transcription of Min components is considerably tuned down during sporulation (Nicolas et al. 2012).

2.3. Optimization of mNeonGreen PALM imaging

The choice of the right FP is one of the most consequential decisions when designing fluorescence microscopy based experiments. This decision depends on various factors, including the structure of the target protein, the maturation time, oligomerization state, compatibilities with other fluorophores during multi-color imaging, available microscope filters and the organism of interest. PALM furthermore requires a specific type of genetically incorporated FP that is capable of photoactivation, photoswitching or photoconversion (for details see chapter 1.3.1.1). Therefore, the choice of FP for PALM is quite limited when imaging bacterial cells with short generation times like *E. coli* or *B. subtilis*. This problem amplifies when performing dual-color PALM, as it requires compatible, spectrally distinct fluorophores and specific imaging/analysis strategies (Subach et al. 2009; Ishitsuka et al. 2014; Rosenbloom et al. 2014). A common combination of FPs in dual-color PALM is green and orange, where the choice of compatible combinations is rather limited, especially for compatible green FPs (Gahlmann et al. 2013; Foo et al. 2015; Bach et al. 2017). One of these FPs is mNeonGreen, distinguished by its excellent photo-characteristics (brightness and stability), short maturation time and truly monomeric behavior (Shaner et al. 2013). Originally derived from the lancelet *Branchiostoma lanceolatum*, it is widely used in diffraction limited fluorescence microscopy (Barykina et al. 2016; Heppert et al. 2016; Bach et al. 2017; Bisson-Filho et al. 2017; Hostettler et al. 2017; Mastop et al. 2017; Schubert et al. 2017), but has also been shown to be PALM compatible by its developers due to its innate ability to switch between a bright and dark state (Shaner et al. 2013). Similar to eYFP, its photoswitching behavior is still not fully understood on a molecular level (Dickson et al. 1997; Biteen et al. 2008). On the one hand, this makes mNeonGreen hard to control during PALM imaging. On the other hand, however, it is an advantage, that activation and excitation are performed by a single laser (488 nm) while most PA-FPs (e.g. Dronpa or mGeos-M) require two different wavelengths for activation and excitation (see 1.3.1.1).

When we first tried to utilize mNeonGreen in a PALM experiment to image DivIVA, a protein with known structure and localization, we obtained unsatisfactory results due to many simultaneous emissions of neighboring molecules, leading to overlapping PSFs. Since these emitters could not be fitted correctly, resulting localizations appeared too large and distant from their actual position, creating artifacts and a blurry appearance (data not shown). Since the

choices for fast maturing, monomeric and bright green PA-FPs are very limited in bacterial PALM and many labs already utilize mNeonGreen in conventional microscopy, we decided to optimize PALM imaging of mNeonGreen in bacterial cells. To this end, we characterized the properties of mNeonGreen, and optimized sample preparation, imaging conditions and post-processing, creating a solid and reproducible workflow.

2.3.1. Finding the optimal laser intensity for mNeonGreen imaging

Similar to our first impression of mNeonGreen PALM imaging, our collaboration partner Jae Yen Shin (MPI of Biochemistry, Munich) compared results of PALM experiments of *B. subtilis* expressing ParB fused to either mNeonGreen (BSG2204) or mEos3.2 (BSG2205) (Stockmar et al. 2018). She found a discrepancy between both strains, where only mEos3.2 was able to resolve the expected sub-clusters that ParB forms in *B. subtilis* (Marbouty et al. 2015; Stockmar et al. 2018). When investigating the properties of the recorded localizations that are the basis for the final image, it became obvious that the distribution of localization widths was different between the respective fluorophores (**Fig. 2.18**, **a** and **b**). The localization width is the radius around the localization center of an event, at which the fitted Gaussian function drops to e^{-1} of its maximum (note, that the reported width here is $\sqrt{2\sigma}$, where σ is the Gaussian standard deviation).While mEos3.2 localization widths revealed the expected Gaussian normal distribution (**Fig. 2.18 b)**, the distribution of localization widths of mNeonGreen showed a large tail and was generally wider in average (**Fig. 2.18 a**). The subpopulation of events with a large localization width thereby most likely corresponded to the previously observed neighboring emitters that could not be fitted correctly due to overlapping PSFs. Accordingly, most localizations with a wide localization width were recorded in the beginning of the experiment (**Fig. 2.18 c**), where the number of photon-emitters is the highest and thus increasing the chance for overlaps.

Since photoswitching behavior is controlled by the illumination power, we tested the effect of various different laser powers on DivIVA-mNeonGreen localization widths. With increasing laser powers, the mean localization width decreased from ~260 nm to 190 nm, reaching a plateau at moderate laser powers (**Fig. 2.18 d**). Even though the localization width slightly decreased further when increasing the laser power above 15%, bleaching of mNeonGreen occurred faster, resulting in less total signal (data not shown). We could however reduce simultaneous photo-activation with this laser power, which is why we settled on a moderate intensity (15%).

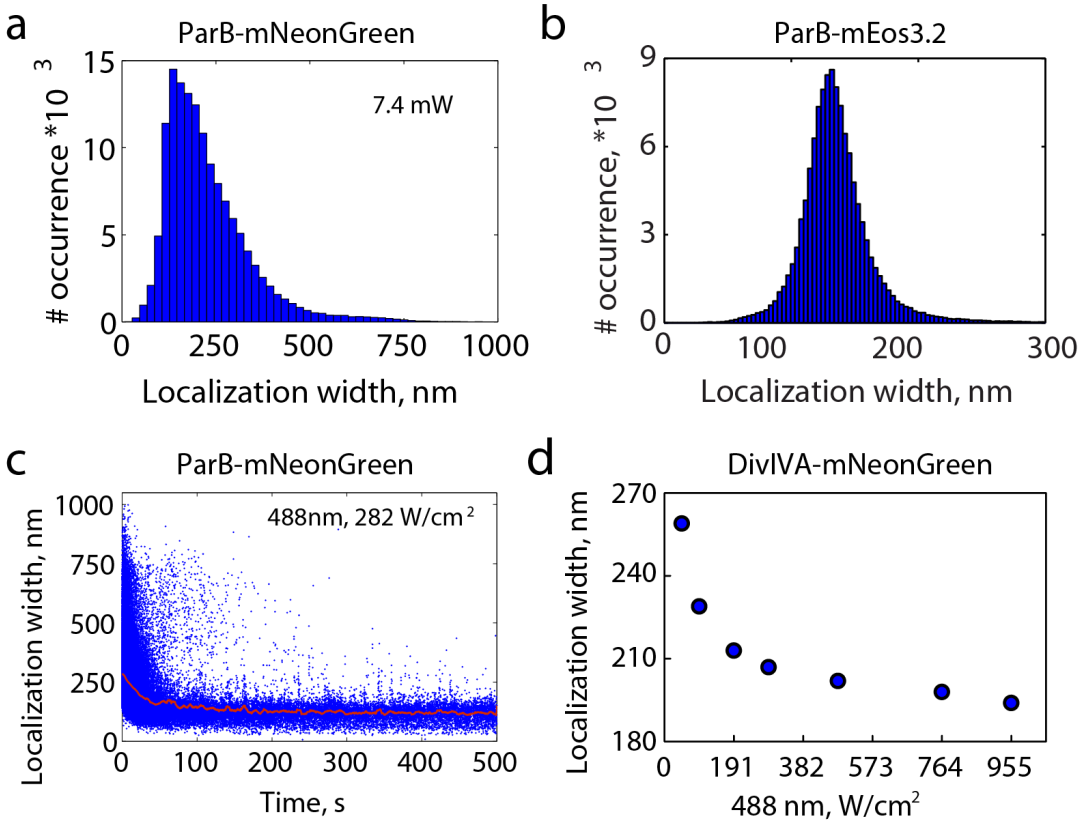

Fig. 2.18: Effect of the 488 nm laser intensity on localization width.

The localization width of recorded events of mNeonGreen and mEos3.2 in PALM imaging was investigated. **(a)** Histogram of the ParB-mNeonGreen (BSG2204) localization width at 7.4 mW (15%) of 488 nm power and **(b)** histogram of the ParB-mEos3.2 (BSG2205) localizations width. ParB-mNeonGreen expressing cells were imaged with pseudo-TIRF illumination with moderate 488 nm laser power. ParB-mEos3.2 expressing cells were imaged with pseudo-TIRF illumination with 405 nm and 561 nm laser. Data were analyzed using the Zen software (Zeiss Black 2012). **(c)** Individual mNeonGreen localization width over time with underlying data of (a). Red line is a moving window average of 100 frames. **(d)** Plot of the mean localization widths of mNeonGreen at various 488 nm laser power (46, 91, 191, 282, 458, 764 and 955 W cm^{-2}, corresponding to 2.5, 5, 10, 15, 25, 40 and 50% in the Zen software). Each data point represents the mean value from hundreds of localizations at the given laser power. Localization width is the radius at which the fitted Gaussian drops to e^{-1} of its maximum. Image modified from (Stockmar et al. 2018), data and figure for (a), (b) and (c) were prepared by Jae Yen Shin (MPI of Biochemistry, Munich), data and figure for (d) were prepared by me.

2.3.2. Characterization of mNeonGreen and comparison to Dronpa

To obtain a better understanding of mNeonGreen and its behavior during PALM imaging, we wanted to establish important photo-characteristics such as the photon budget and on- and off-switching rates. Furthermore, we wanted to compare these to the properties of other commonly used green PA-FPs, especially Dronpa (Ando et al. 2004) and mGeosM (Chang et al. 2012). To obtain results appropriate for comparison and to enable realistic conditions for bacterial PALM, I first constructed strains that express DivIVA fused to either mNeonGreen (BHF028), Dronpa (BHF057) or mGeosM (BHF058) from their native locus (see **Table 2.1** and **Fig. 2.3**). As already described earlier (see chapter 2.1.1), all three constructs indicated varying degrees of DivIVA

functionality, judged by their phenotype in diffraction-limited microscopy (**Fig. 2.3**). Since the mGeosM fusion displayed the highest degree of mislocalization, it was not analyzed further.

We then compared the photon budget detected per localization of mNeonGreen and Dronpa during a typical PALM experiment, shown as distributions in **Fig. 2.19 a**.

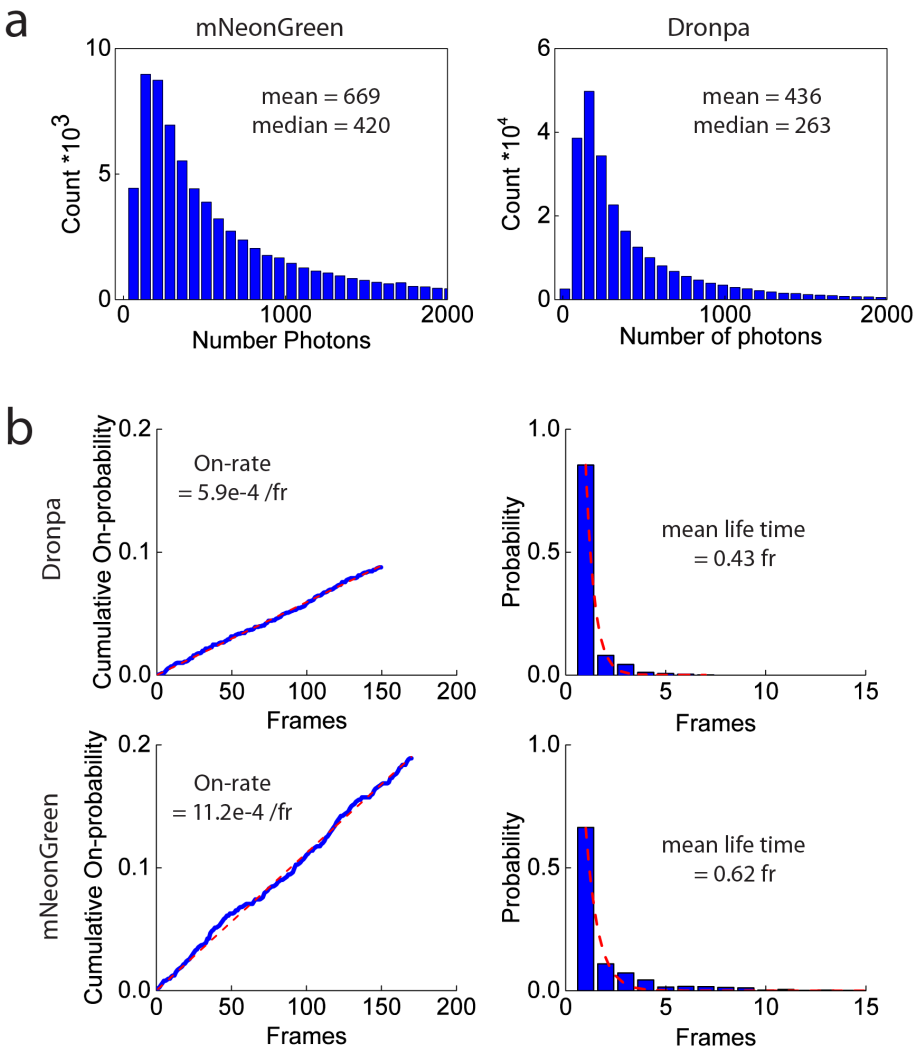

Fig. 2.19: Comparison of photo-physical properties of mNeonGreen and Dronpa.

Comparison of mNeonGreen and Dronpa revealed a higher photon count, on-rate and photo stability of mNeonGreen. **(a)** Histograms of photon numbers per recorded event from unfiltered PALM data of mNeonGreen (**left**, BHF028) and Dronpa (**right**, BHF057) fused to DivIVA and expressed in *B. subtilis* (see materials and methods 4.6.2.3). **(b, left)** Initial linear section of the relative cumulative on-switching probability vs time was fitted (red dotted line) linearly to obtain the on-switching rate. **(b, right)** Distribution of the on-state lifetime was fitted to an exponential decay function (red dotted line) to obtain the mean lifetime, the inverse of which yields the off-switching rate. One frame corresponds to 20 ms. (See also **Table 2.4**). Image modified from (Stockmar et al. 2018). All data was obtained by me, figure (a, b) and analysis (b) done by Jae Yen Shin (MPI of Biochemistry, Munich).

Table 2.4: Photo-physical properties of Dronpa and mNeonGreen.

Obtained from PALM images of *B. subtilis* expressing Dronpa (BHF057) and mNeonGreen (BHF028) fused to DivIVA.

PA-FP	On-switching rate, s^{-1}	Mean life time, s	On-off switching rate ratio
Dronpa	0.029 ($5e^{-5}$)	0.009 ($6e^{-4}$)	$2.5 * 10^4$
mNeonGreen	0.056 ($1.3e^{-4}$)	0.012 ($3.4e^{-4}$)	$6.9 * 10^4$

Reported errors in parenthesis are standard errors of the fitted parameters. For details, see materials and methods (4.6.2.3) and **Fig. 2.19**.

Similar to earlier studies (Shaner et al. 2013; Wang et al. 2014), the mean number of photons per localization for mNeonGreen (669) was higher when compared to Dronpa (436). This was expected, as mNeonGreen is one of the brightest FPs available (Shaner et al. 2013). Next, we measured and the on-switching rate and lifetime of both fluorophores (**Fig. 2.19 b** and **Table 2.4**), according to an established protocol (Wang et al. 2014) (also see chapter 4.6.2.3). The mean lifetime that was obtained for Dronpa (9 ms) is in good agreement with what was previously reported (9.6 ms, (Wang et al. 2014)), and shorter when compared to mNeonGreen (12 ms). The on-switching rate we determined for Dronpa was, however, only around half (29 ms^{-1}) of what was reported previously (60 ms^{-1}, (Wang et al. 2014)). An explanation for this difference could be the different environment. While Dronpa was previously expressed and investigated in mammalian cells (Wang et al. 2014), our approach characterized it in the bacterial background of *B. subtilis*. To our surprise, the on-switching rate of mNeonGreen was significantly higher (56 ms^{-1}) in comparison. This increased switching frequency could provide an explanation for the frequently observed and hard to control overlapping signals in regions of the cell where DivIVA-mNeonGreen is found in high densities (poles and septum), which was also observed in **Fig. 2.18 a**.

2.3.3. Post-processing steps increase mNeonGreen PALM image fidelity

Even though optimization of imaging conditions decreased the problem of overlapping emitters of mNeonGreen, it could not eliminate the problem. Large localization widths still obscured the expected localization patterns of DivIVA. As it can be observed in **Fig. 2.11**, **right panel**, and as it has been described before (Eswaramoorthy et al. 2011), DivIVA accumulates into structures that resemble double rings at mature septa, where membrane invagination has already proceeded. As these rings are in close proximity of each other, they can only be visually separated when using superresolution-imaging techniques (Eswaramoorthy et al. 2011; Stockmar et al. 2018). Furthermore, they represent areas where DivIVA is present in high

densities. Consequently, when first imaging DivIVA-mNeonGreen expressed in *B. subtilis* (BHF028), these rings could not be visually separated due to their spatial proximity (**Fig. 2.20 c**), obscured by localization artifacts from overlapping PSFs. To eliminate the problem of large localization widths, we hence systematically investigated the effect of selective data filtering on the PALM images of DivIVA-mNeonGreen (**Fig. 2.20**).

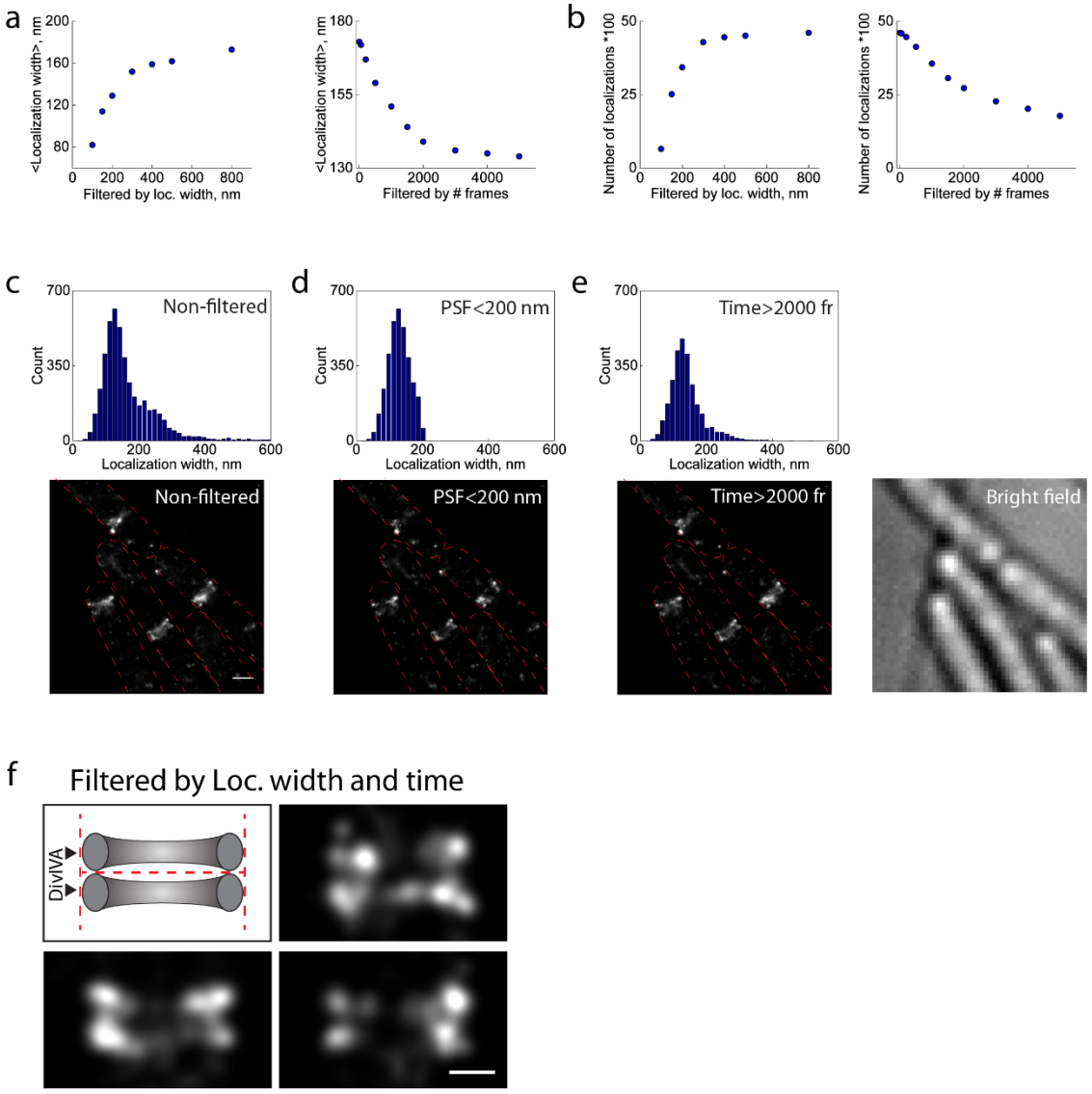

Fig. 2.20: Effects of data filtering on DivIVA-mNeonGreen PALM data.

Based on data from PALM imaging of *B. subtilis* expressing mNeonGreen fused to DivIVA (BHF028), limited to the ROI shown in (c). Data filtering during post-processing effectively removed most overlapping and erroneous localizations. **(a)** Mean widths of unfiltered mNeonGreen localizations vs. filtered by (**left**) localization width or (**right**) number of frames. **(b)** Total number of localizations vs. filtering by (**left**) localization width or (**right**) number of frames. **(c,d** and **e)** Histograms of localization widths (c) before and (d) after filtering out localizations widths larger than 200 nm or (e) all localizations from the first 2000 frames **(f)** Cartoon representation and zoomed-in examples of DivIVA-mNeonGreen double ring after data filtering. Image modified from (Stockmar et al. 2018). All data was collected by me, final figure was prepared by Jae Yen Shin (MPI of Biochemistry, Munich) and analysis was done by Jae Yen Shin and me.

To this effect, we choose a ROI containing several double bands that appeared rather blurred (**Fig. 2.20 c**, bottom) to test different filters. Specifically, we assessed the influence of filtering out localizations above a certain width or localizations that appeared before a defined number of frames (**Fig. 2.20**, **a** and **b**). Accordingly, both mean localization width (**Fig. 2.20 a**) and total number of localizations (**Fig. 2.20 b**) decreased in a direct correlation with stringency of filtering, i.e. allowing only smaller localization widths or removing a higher number of frames. As the stringency of filters and the resulting increase in image fidelity plateaus at a certain point when increased, these parameters have to be evaluated carefully to avoid artifacts or removal of correctly fitted data. As optimization of imaging did not entirely remove simultaneous emission of nearby fluorophores (see above), we investigated the effect of these filters to the PALM image and the histogram of localization widths (**Fig. 2.20 c**-**f**). Without filtering, the histogram reveals a distribution containing two populations, with their peaks located at ~130 nm and ~250 nm, respectively (**Fig. 2.20 c**). Thereby, the second population contains around 30% of localizations, likely corresponding at least partially to emitters with overlapping PSFs during imaging. When removing/reducing this subpopulation by filtering out localizations with a width above 200 nm or localizations that appeared before frame 2000, the two DivIVA rings could be clearly separated in the resulting PALM image (**Fig. 2.20 d** and **e**). When combining both filters (**Fig. 2.20 f**), this effect was even clearer, corresponding to what is obtained when performing PALM with conventional, well-established PA-FPs like PAmCherry (see **Fig. 2.11**, right panel, center). It should be mentioned that the two DivIVA rings, instead of appearing as continuous rings, rather appear as four separated points when being imaged via PALM (**Fig. 2.20 f**). This can be explained by the focal plane being located around midcell and the rather thin section that is illuminated, in contrast to methods like 3D-SIM (Eswaramoorthy et al. 2011).

Since the artifacts in the PALM images were caused by a second population of erroneously fit and thus wider localizations (**Fig. 2.20 c**), we next tested if another fitting algorithm capable of fitting multiple emitters simultaneously could separate the DivIVA bands similarly. To this end, we employed the Fiji plugin ThunderSTORM (Ovesny et al. 2014), utilizing its multi-Gaussian PSF fitting function (**Fig. 2.21**). Even though multi-fitting reduced the problem of overlapping signal (**Fig. 2.21 a**), it was not sufficient to eliminate it. Again, filtering the data by its localization width (here Sigma) or by removing all localizations from the first 2000 frames (**Fig. 2.21 b** and **c**), could eliminate the artifacts obstructing the space between the two rings. Albeit the multi-fit function being a valid option, the algorithm was much slower compared to a single-Gaussian fit due to the increased complexity of the model (hours vs minutes). We thus decided to incorporate the previously presented post-processing as a quick, but solid method into our workflow instead, which allows the use of mNeonGreen in bacterial PALM, even appropriate to analyze dense structures.

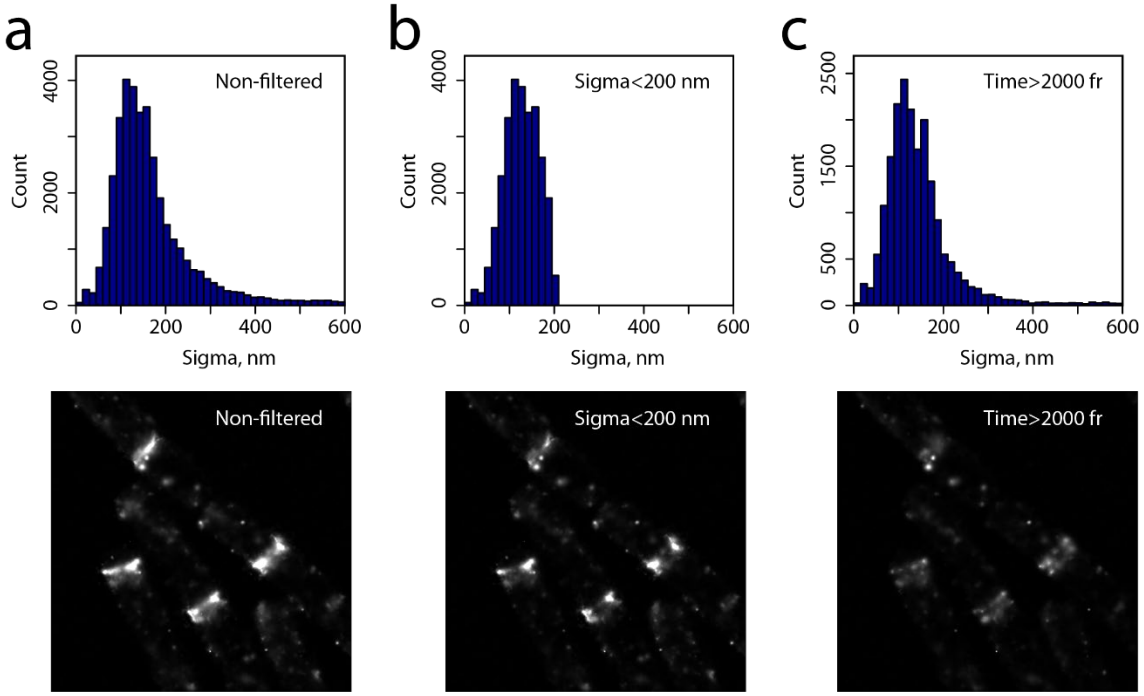

Fig. 2.21: Multi-Gaussian PSF fitting of DivIVA-mNeonGreen PALM data.

To test if a multi-Gaussian PSF fitting function is able to separate dense and thus overlapping localizations of mNeonGreen, DivIVA-mNeonGreen data from **Fig. 2.20** was analyzed with the respective method (maximum likelihood with enabled multi-emitter fitting) of the ThunderSTORM software (Ovesny et al. 2014). Histograms of the reported localization width (sigma) **(a)** before and **(b)** after filtering out localizations with sigma larger than 200 nm or **(c)** all localizations from the first 2,000 frames. The resulting PALM images are shown. Sigma is the standard deviation of the probability density of the fitted 2D Gaussian function of every localization, effectively corresponding to the localization/PSF width of the Zen software.

2.3.4. PALM sample preparation optimization

The preparation of a sample is a crucial step when performing bacterial PALM. To ensure reliable and reproducible conditions, several factors should be determined and tested for every strain or experiment, including the growth and embedding medium, the cell density and the fixation conditions. After optimization of media and final cell density (data not shown), we also tested and compared several concentrations of paraformaldehyde for chemical fixation of *B. subtilis* expressing DivIVA-mNeonGreen (BHF028). Since brightness and thus number of photons directly influences the localization precision in SMLM experiments and as cells have to be fixed for structural analysis of proteins, it is desirable to choose a fixation protocol that preserves as much fluorescent signal as possible. Therefore, we imaged these cells in conventional microscopy and quantified the fluorescence intensity at the DivIVA-mNeonGreen band, including live cells as reference (**Fig. 2.22**).

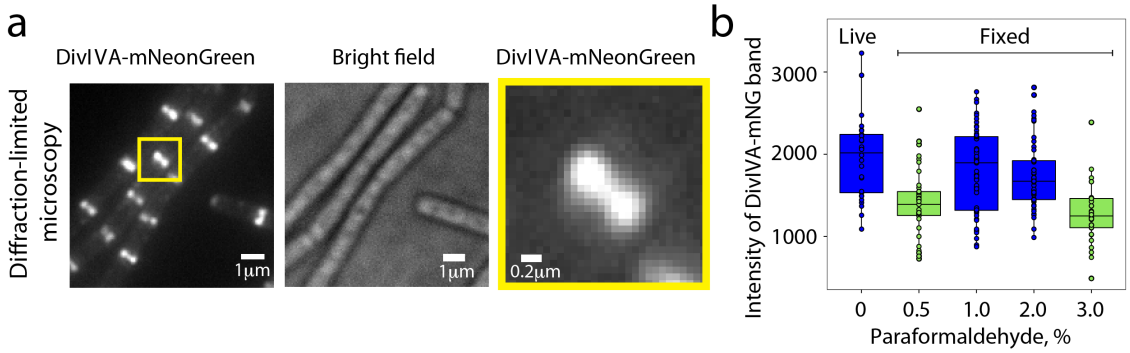

Fig. 2.22: Effect of paraformaldehyde fixation on fluorescence intensity.

Different concentrations of paraformaldehyde were applied to investigate the effect on fluorescence intensity of DivIVA-mNeonGreen **(a)** Exemplary diffraction-limited microscopy images of *B. subtilis* expressing DivIVA-mNeonGreen (BHF028). Cells were grown and prepared according to materials and methods and mounted on agarose pads. **(a, left)** Fluorescence and **(a, center)** bright field microscopy images of the same field of view. **(a, right)** Magnification of yellow inset from (a, left). Scale bar size indicated. **(b)** Boxplot of DivIVA-mNeonGreen fluorescence intensity at different concentrations of paraformaldehyde fixations. Intensity was determined by drawing a line along the fluorescent DivIVA-mNeonGreen bands and extracting the peak value of the intensity profile along the line using the Fiji package. At least 29 bands were measured in five different fields of view per experiment for each condition. Significant differences between the samples were determined using a multiple comparison test (pairwise comparisons adjusted appropriately for multiple comparisons) after Kruskal-Wallis (P value: 0.05). Results are indicated in green or blue, in which conditions in the same color represent no statistical difference. Image modified from (Stockmar et al. 2018).

Generally and as expected, fixation reduced fluorescence intensity (**Fig. 2.22 b**). However, when using one percent paraformaldehyde, the statistical difference to live cells was smallest, prompting us to use this condition for further imaging. It should be mentioned that these conditions have to be evaluated separately for every strain, as they did not provide the best results for other strains that were tested by our collaboration partner, like *B. subtilis* expressing ParB-mNeonGreen (BSG2204) (Stockmar et al. 2018).

3. Discussion

3.1. The *B. subtilis* Min system

The Min reaction network and similar systems of division-site placement have been described and investigated at length for various prokaryotes (Rowlett and Margolin 2015; Eswara and Ramamurthi 2017). This includes the positive division site selection systems SsgB in *S. coelicolor* (Willemse et al. 2011), PomXYZ in *M. xanthus* (Treuner-Lange et al. 2013; Schumacher et al. 2017) and MapZ(LocZ) in *S. pneumonia* (Fleurie et al. 2014; Holeckova et al. 2014), as well as the negative division site selection systems MipZ in *C. crescentus* (Thanbichler and Shapiro 2006; Kiekebusch et al. 2012), FlhG in *C. jejuni* (Balaban and Hendrixson 2011) and the Min system in *E. coli* (Hu and Lutkenhaus 1999, 2000, 2001, 2003; Park et al. 2011; Denk et al. 2018; Halatek and Frey 2018) and *B. subtilis* (Marston et al. 1998; Marston and Errington 1999; Bramkamp et al. 2008; van Baarle and Bramkamp 2010). The system presumably best understood is the Min system of *E. coli*. It is a highly dynamic and self-organizing reaction network (Ramm et al. 2019). Through a remarkable pole-to-pole oscillation of MinCD, FtsZ is only able to polymerize into a ring like structure around midcell (Hu and Lutkenhaus 1999), thereby defining the divisional plane in this prime example of intracellular protein pattern formation (Denk et al. 2018). Since MinC and MinD in *B. subtilis* are well conserved compared to *E. coli*, it was unexpected that the *B. subtilis* Min system was described as a rather static bipolar gradient, with increasing concentration of MinC from poles to midcell. In *E. coli*, MinE stimulates ATP-hydrolysis of MinD, which subsequently detaches from the membrane, resulting in MinCD oscillation. In contrast, no MinE homologue was found in *B. subtilis*. Instead, the curvature sensing DivIVA was found to recruit MinCD to poles and septa, bridged by the transmembrane protein MinJ. Even though the Min system is still described as a rather static gradient in recent reviews (Rowlett and Margolin 2015; Haeusser and Margolin 2016), dynamic behavior and relocalization of MinC to active septa was observed in fluorescence microscopy (Gregory et al. 2008). A similar dynamic relocalization from poles to septa was observed for MinJ (Bramkamp et al. 2008; van Baarle and Bramkamp 2010). Furthermore, earlier studies from our lab suggested dynamic relocalization of DivIVA in dividing cells (Bach et al. 2014). Combined with the findings that Min in *Bacillus* might act downstream of Z-ring formation (Bramkamp et al. 2008; Patrick and Kearns 2008; van Baarle and Bramkamp 2010), we were prompted to re-characterize dynamics and intracellular localization of the Min components, to finally understand how dynamic behavior and relocalization is conformable with the observation of a static gradient.

3.1.1. Construction of functional fluorescent fusions

Prior to this work, *B. subtilis* Min proteins were analyzed and characterized in several experimental studies, e.g. the following important milestones: (Marston et al. 1998; Marston and Errington 1999; Thomaides et al. 2001; Bramkamp et al. 2008; Gregory et al. 2008; Patrick and Kearns 2008; Eswaramoorthy et al. 2011; van Baarle et al. 2013). However, whenever microscopy was employed, most of these studies mainly utilized strains, which either overexpress fluorescent fusions of Min proteins from ectopic loci like *amyE* or *aprE*, or produce the protein at approximate wild type levels in these ectopic loci through their native promoter, while a wild type copy is expressed in the native locus. To my knowledge, the only studies using functional fluorescent fusions expressed from their native locus are (Patrick and Kearns 2008; Eswaramoorthy et al. 2011) (MinJ-YFP) and (Gregory et al. 2008) (MinC4-GFP), while the only native fusion of MinD (MinD4-GFP, strain JAG118 from (Gregory et al. 2008)) was described as non-functional. In contrast, no fully functional fluorescent fusion of DivIVA could be obtained to date. As already described in (Gregory et al. 2008), overexpression of protein can create to static populations, of which a minority can already mask dynamic populations during conventional fluorescence microscopy, which prompted us to create fluorescent fusions expressed from the native locus. In this work, I therefore first constructed and tested functional fluorescent fusions of Min components in their native locus fused to various FPs (**Table 2.1** and **Fig. 2.2**).

For MinD, only one functional fusion could be obtained here (Dendra2-MinD, BHF011), while other constructs introduced a mild phenotype of cell elongation and minicells production (msfGFP-MinD, BHF017), sometimes accompanied by localization artifacts (mCherry2-MinD, BHF016; mKate2-MinD, BHF059). This underlines the importance of carefully testing different fluorophores for fluorescent fusions, which was the only difference between some of these strains. Even though many fluorophore characteristics like maturation time or specific influence on protein folding or oligomerization have been experimentally determined and can be checked through public databases (e.g. https://www.fpbase.org/), certain cross-reactions or interactions remain enigmatic and need to be tested experimentally. Furthermore, the structure and localization of the protein of interest itself remains the most important determinant to create a functional fluorescent fusion.

MinJ remained functional when C-terminally fused to a variety of different fluorophores, respectively (see **Table 2.1**), judging from the phenotypic comparison with wild type and Δ*minJ*. This had been observed with other fluorescent fusions in the past (Bramkamp et al. 2008; van Baarle and Bramkamp 2010), which were however overexpression constructs in ectopic loci. The fusion constructs created here are, however, the first functional fusions expressed from the

native locus, ensuring native protein levels. Therefore, folding or interaction domains of MinJ do not seem to be affected by the fluorescent tag.

In contrast, DivIVA was tested with far more options throughout several studies (also see **Table 2.1**), without success. One possible explanation for this is the structure of DivIVA: it can be divided in two functional domains, located at the Nt and Ct and likely connected via a flexible linker sequence (**Fig. 1.5**) (Lenarcic et al. 2009; Oliva et al. 2010). While the Nt enables membrane binding through positively charged hydrophobic residues located in the outward facing loops and multimerization via its coiled-coil region, the Ct was found to be involved in tetramerization of the protein, also displayed in **Fig. 1.5** (Oliva et al. 2010). Therefore, fusing a fluorescent protein to either side of the protein likely interferes at least partially with either of these functions, which both seem vital for the proteins purpose and thus the Min system.

In actinomycetes like *C. glutamicum*, DivIVA was shown to be an essential protein for polar growth and thus elongation (Letek et al. 2008), but is also vital for polar chromosome tethering through direct interaction with ParB (Donovan et al. 2012). In these bacteria, a Ct fusions of DivIVA to mCherry did not produce a detectable phenotype and was thus considered fully functional (Donovan et al. 2012). The amino acid sequence of actinobacterial DivIVA shows however significant differences when compared to DivIVA in Firmicutes, which is shorter and does not contain the central insertion which was shown to be indispensable for interaction with ParB in *C. glutamicum* (Donovan et al. 2012).

One approach to overcome this challenge could be a sandwich fusion, where the fluorescent tag is expressed in a more central position of the protein, flanked by the Nt and Ct. Finding the right position for such a fusion can be difficult and laborious due to the need for extensive screening. It could however be achieved with certain strategies, e.g. transposon insertion, that was already employed for MinC (successful) and MinD (unsuccessful) (Gregory et al. 2008), first described in (Sheridan et al. 2002). On the other hand, a sandwich fusion could interfere with the general protein shape of DivIVA. The shape was deemed important for its ability to sense negative curvature through molecular bridging (Lenarcic et al. 2009), making DivIVA a difficult target protein for a functional fluorescent fusion in *B. subtilis*. Furthermore, DivIVA was identified as a scaffold protein for a multitude of proteins besides MinJ, e.g. the chromosome anchor RacA that acts during sporulation (Ben-Yehuda et al. 2003; Wu and Errington 2003), SpoIIE, which is involved in formation of the asymmetric septum (Eswaramoorthy et al. 2014), the transcriptional regulator ComN (dos Santos et al. 2012) or the division inhibitor Maf (Briley et al. 2011), whose binding sites could be unpredictably perturbed in such a construct. Therefore, creating a functional DivIVA fusion in *B. subtilis* remains a challenge to be solved.

3.1.2. *B. subtilis* Min proteins are dynamic and form clusters

Even though the Min system is described to form a rather stable gradient (Rowlett and Margolin 2015; Haeusser and Margolin 2016), studies about the dynamics of individual Min proteins are sparse. MinC was shown to be rather mobile when observed in time-lapse and TIRF microscopy (Gregory et al. 2008), suggesting a similar behavior of MinD, which appears to recruit MinC solely and thus dictates its mobility. Without a functional fluorescent fusion of MinD, this mobility could however not be demonstrated in *B. subtilis*. Furthermore, DivIVA mobility was previously investigated through FRAP experiments of overexpressed DivIVA-GFP with approximately 75-fold increased production (Eswaramoorthy et al. 2011), where it did not show any substantial recovery when an existing DivIVA-ring was bleached. In contrast, a later study from our lab could demonstrate mobility of DivIVA through time-lapse microscopy, FRAP and photoconversion, utilizing merodiploid strains expressing DivIVA-Dendra2, DivIVA-GFP or DivIVA-PA-GFP, respectively (Bach et al. 2014). To our knowledge, no study previously investigated the mobility of MinJ. Therefore, this study was carried out to characterize the mobility of all relevant Min components in *B. subtilis*.

3.1.2.1. FRAP and quantification of the Min proteins

After observing MinD mobility during time-lapse and photoconversion microscopy (**Fig. 2.4**), a FRAP analysis of all Min components expressed from their native promoters was performed, which were all found to be dynamic (**Fig. 2.5**). Furthermore, the Min components were quantified through relative in-gel fluorescence (**Fig. 2.9**).

MinD displayed the fastest recovery of the three proteins analyzed, while MinJ and DivIVA were significantly slower in recovery, however still in a similar range when compared. The diffusion coefficients of the three proteins thereby ranged between 0.057 $\mu m^2 s^{-1}$ and 0.0034 $\mu m^2 s^{-1}$ (see **Table 2.2**), which is in an expected spectrum for bacterial membrane (-associating) proteins (Kumar et al. 2010). The mobile subpopulations varied between the three components: while around 79% of MinD and 77% of MinJ proteins took part in recovery, only 65% of DivIVA proteins did participate in fluorescence recovery at bleached septa (**Table 2.2**). Considering the nature of DivIVA, the generally slower diffusion and smaller mobile population are to be expected. The structure of DivIVA does not only favor oligomerization (Oliva et al. 2010), it also leads to extensive clustering in regions of negative curvature, where it 'bridges' the two neighboring membranes in a mechanisms phrased 'molecular bridging' (Lenarcic et al. 2009), in turn stabilizing it for further interactions. Furthermore, the role of DivIVA as protein scaffold for a variety of proteins places it at the center of protein clusters (Stahlberg et al. 2004; Lenarcic

et al. 2009; Oliva et al. 2010), where it is then rather immobile. Furthermore, DivIVA-mNeonGreen (BHF028) fluorescence recovered around twice as fast during FRAP when compared to DivIVA-GFP (1803), irrespective of the genetic background (**Table 2.2**). Since strain 1803 expresses a second, native version of untagged DivIVA under control of the same promoter, only half of the respective total DivIVA population should be fluorescently tagged and thus be able to produce fluorescence recovery. If there is no cooperativity in binding, this correlation hints toward a limitation in DivIVA binding sites at the septum, where FRAP recovery was measured, resulting in the consistent slower recovery of strain 1803. MinJ, the transmembrane protein scaffolding DivIVA and MinD showed similar diffusion coefficients as DivIVA, while MinD recovered around 10-fold faster. Considering the larger size of the fast diffusive mobile population of MinD and the generally higher protein quantities (**Table 2.3**), this difference might suggest a frequent protein exchange of membrane-bound MinD at the septum. However, analyzing different subpopulations of diffusive proteins in bacterial FRAP is technically inept. For this purpose, SPT is a more suitable method, as it produces more distinctive and detailed results due to the higher spatiotemporal resolution. The results of SPT analysis of MinD and DivIVA and their comparison to FRAP results will be discussed in a later chapter (see 3.2.2).

Generally, measured protein quantities of MinD, MinJ or DivIVA fused to Dendra2, respectively (**Table 2.3**, **Fig. 2.9**), reflected observations previously made during fluorescence microscopy concerning intensity and appearance of the different constructs (see e.g. **Fig. 2.2** or **Fig. 2.5**). While MinD was the most abundant Min protein in exponential growing cells, DivIVA levels corresponded to roughly half as many molecules. MinJ on the other hand was significantly less abundant (16% of MinD abundance), making FRAP, PALM or SPT analysis more challenging concerning MinJ fluorescence intensity.

Furthermore, interaction between Min proteins and their hierarchical recruitment was reflected in the data, when FRAP was performed on fluorescent fusions of Min proteins in different genetic knockout backgrounds of other Min proteins (**Fig. 2.7**, **Fig. 2.8** and **Table 2.2**). In accordance with previous genetic studies (Bramkamp et al. 2008; Patrick and Kearns 2008), absence of the upstream recruiting factor abolished septal and polar localization of the respective downstream element(s) (DivIVA > MinJ > MinD). While a decrease in recovery time of DivIVA in a *ΔminJ* strain seems logical due to the absence of the direct interaction partner, it is not clear why DivIVA recovers slower in a *ΔminCDJ* background. Cells with this genetic background did however grow rather heterogeneous compared to the other genotypes. Furthermore, septal recovery varied strongly between cells, reflected in a large standard deviation (87.67 ± 51.55 s). Furthermore, aberrant growth patterns and a frequent lack of regular

division septa made it technical difficult to obtain reliable data, leading to a relative small sample size for this specific strain (n=8).

Since msfGFP-MinD mislocalized in genetic backgrounds of *ΔminJ* (BHF025) or *ΔdivIVA* (BHF026) and could not be measured adequately (see chapter 2.1.3), the direct effect of MinJ or DivIVA on the membrane binding dynamics of MinD could not be characterized. Mutations in the ATPase domain of MinD drastically alter its localization (Karoui and Errington 2001) and thus, similar to *E. coli*, ATPase activity it is expected to control membrane binding. It would therefore be interesting to investigate effects of different mutants on the dynamics of MinD and the other Min proteins. Replacement of the native gene of *minD* with mutated versions did however either not produce viable cells (G12V, ATP hydrolysis mutant; D40A, trapped dimer) or only produced diffuse cytosolic signal similar to *ΔminJ/ΔdivIVA* (K16A, ATP binding mutant) and could therefore not be satisfactorily analyzed via FRAP. In addition, it would be interesting to alter the MTS of MinD or the lipid-binding region of DivIVA and test how this affects the respective FRAP recovery rates, to determine the importance of membrane binding for functionality and inter-dependence of the system.

3.1.2.2. SMLM analysis and a model for the *B. subtilis* Min proteins

The *B. subtilis* Min proteins have not been analyzed in single-molecule resolution prior to this study. Using conventional microscopy, MinD, MinJ and DivIVA all appear as polar gradients with rather static localization (see **Fig. 2.12**). When it became evident that Min proteins relocalize from poles to newly formed septa (Gregory et al. 2008; van Baarle and Bramkamp 2010), it was unclear how a rather stable gradient achieves this fast shift upon septum formation. To get a more detailed picture of the individual Min proteins, their localization in chemically fixed cells during division was determined with nanometer precision (**Fig. 2.11**). Additionally, based on our experimental results and with the help of previously gained information from the *E. coli* Min system, a minimal reaction-diffusion model was built, correctly reproducing qualitative attributes of MinD localization in *B. subtilis* (**Fig. 2.10**). While this chapter will discuss the biological implications, a later chapter (see 3.3) will debate technical aspects of the SMLM analysis.

MinD, MinJ and DivIVA were frequently observed to form clusters of variable sizes (**Fig. 2.11**, **Fig. 2.13**), where more than 50% of all recorded events for MinD and DivIVA could be allocated to a cluster. Furthermore, many of these clusters were observed in the cytosol or along the lateral cell wall instead of the expected polar and septal regions. While around 66% of DivIVA clusters were found at poles and septa, roughly 59% of MinD assemblies localized in these

regions. Clusters localized at the lateral cell wall and the cytosol likely reflect the dynamic behavior of Min proteins observed during FRAP and SPT.

Furthermore, the fast FRAP recovery rates give reason to speculate about the protein exchange rates inside existing clusters or protein accumulations. Likely, the edges of existing clusters are more unstable and allow for more frequent binding and unbinding of Min proteins. Due to its fast recovery in FRAP, turnover of MinD likely proceeds at fastest rates of all Min proteins. Therefore, we expect generally rapid recruitment and detachment of MinD. Further, we assume that recruitment dominates in zones of DivIVA-MinJ stabilization and detachment dominates in the rest of the cell, which was utilized as a base assumption in the mathematical model (see 4.7 in materials and methods).

Multiple models to mathematically reproduce the Min reaction-diffusion network in *E. coli* have been presented and refined (Huang et al. 2003; Fange and Elf 2006; Halatek and Frey 2012; Wu et al. 2016; Halatek and Frey 2018). However, we could only find a single study that employs a reaction-diffusion based model to simulate the polar localization of Min proteins in *B. subtilis* (Howard 2004). Nevertheless, this model was created with rather limited underlying information, i.e. before discovery of MinJ in 2008 (Bramkamp et al. 2008; Patrick and Kearns 2008) or refinement of data about DivIVA structure and function (Lenarcic et al. 2009; Oliva et al. 2010). Therefore, some of the basic assumptions of this model are outdated, as they have been experimentally rebutted. Generally, binding of MinCD to the membrane is suspected, however with a reduced rate at cell poles (Howard 2004). In the next step, the author assumes binding of DivIVA to the edges of the polar MinCD, stabilizing it to form clusters, while membrane bound MinCD from non-polar regions will be quickly released from the membrane, finally leading to a mainly polar localization of MinCD (Howard 2004). Additionally, it was assumed that DivIVA is an intrinsically cytoplasmic protein that only binds the membrane through MinD (Howard 2004), which was disproven later (Lenarcic et al. 2009). With the experimental data available at the time, the model sufficiently reproduces polar localization of MinCD, and is therefore a valuable first step towards a more refined model. The reaction-diffusion model presented in this study (**Fig. 2.10 a** and **b**) is therefore built on experimental data extracted from my own work (diffusion coefficients and protein quantities, **Table 2.2** and **Table 2.3**) and previous theoretical studies of intracellular protein dynamics (Huang et al. 2003; Halatek and Frey 2012; Thalmeier et al. 2016; Denk et al. 2018), summarized in **Table 4.5**. Since the model and corresponding simulations were created by Laeschkir Würthner and Erwin Frey (Arnold Sommerfeld center for theoretical physics, LMU Munich), they will only be discussed briefly.

The underlying assumption of this model is spatial recruitment of MinD through DivIVA-MinJ complexes. Recruitment of MinD to regions of negative curvature is simulated through space-

dependent recruitment and detachment rates, which are increased and decreased, respectively, at poles and septum, to mimic recruitment and stabilization of MinD by DivIVA and MinJ (for details see chapter 4.7). In computational analysis of this minimal-model (FEM simulations, depicted in **Fig. 2.10 c** and **d**), localization of MinD to poles and septum could be achieved and corresponds to a dynamic equilibrium state of the reaction-diffusion equation. Furthermore, the model provides evidence that protein (re-)localization can be induced solely through (changes in) geometry, here shown through relocalization of MinD to sites of division (**Fig. 2.10 d**). Moreover, the model can be extended to account for DivIVA and MinJ dynamics.

The experiments in combination with the mathematical model presented in this study now allow careful follow-up investigations in the future, especially to validate some rather speculative parts of the analysis. Simulations of the model, represented by **Fig. 2.10 c** and **d**, reproduce observations of general MinD localization through DivIVA and MinJ. Important parameters of the mathematical model, like relative protein quantities, appeared to influence the outcome of simulations extended for DivIVA and MinJ substantially (data not shown). Validation and analysis of these observations could be performed by artificially in- or decreasing the respective protein levels through an inducible promoter. As already discussed in the last chapter, more information also needs to be gained about the ATPase activity and its function in MinD. We predict MinD in *B. subtilis* to function similarly to the closely related *E. coli* MinD, which is stimulated to hydrolyze ATP by MinE (Hu and Lutkenhaus 2001; Loose et al. 2008). In the mathematical model, a yet unknown protein or mechanism stimulates MinD-ATP hydrolysis at a similar rate (k_H, **Table 4.5**) as MinE does in *E. coli*, which in turn triggers membrane detachment. The responsible protein or mechanisms has, however, not been identified yet. Since the ATP domain of MinD is well conserved (Karoui and Errington 2001), and both membrane bound and cytosolic MinD populations can be observed (e.g. in **Fig. 2.2**, **Fig. 2.5** or **Fig. 2.11**) and separated in their dynamics (see SPT chapter 2.2.4), its existence is most probable. Moreover, future MinD characterization should include modifications of the MinD MTS. While membrane binding appears to be ATP driven, recruitment via DivIVA-MinJ stabilizes MinD in septal and polar locations. Besides the previously mentioned possible influence on MinD dynamics, it is questionable if removal of the MTS would abolish MinD clustering or only affect membrane localization. Similarly, it would be important to observe the effects of mutations abolishing MinD:MinD or MinD:MinC interactions. To challenge the reaction-diffusion model, these modifications could be predicted through its extension or alteration and then later experimentally validated. Similarly, mutation of DivIVA oligomerization domains could provide valuable information about the effect of accumulation in regions of negative curvature, also considering effects on MinCDJ proteins. Finally, multi-

color PALM with two or even three different Min components could provide essential data on the interaction surfaces and actual stochastics of clusters or accumulations of Min proteins.

Combining all shown data, we here present a new, modified model for dynamics of the Min system in *B. subtilis* (**Fig. 3.1**):

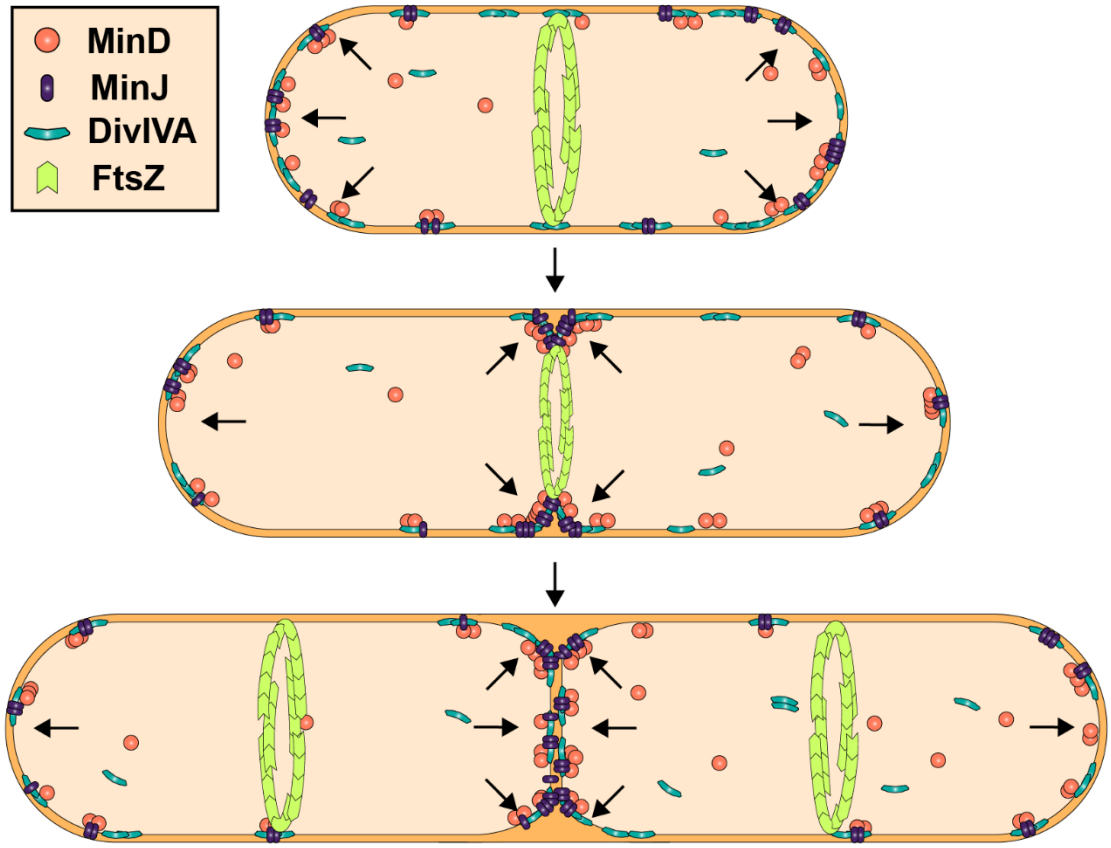

Fig. 3.1: Model of dynamic localization of Min proteins in *B. subtilis*.

Before cell division **(top)**, a large fraction of Min proteins is stabilized in polar clusters, while a smaller fraction probes the cell for negative curvature, which stabilizes clusters due to molecular bridging of DivIVA. Upon formation of a division septum **(center)**, strong negative curvature leads to stabilization of more clusters in the center of the cell. Towards the end of division **(bottom)**, Min proteins aid in disassembly of the divisome, and daughter cells will contain Min cluster in majority located at the poles, probing again for sites of high negative curvature. **Arrows** indicate regions of highest negative curvature, where clusters are stabilized.

We postulate that many Min proteins reside in larger clusters around poles and septa that are relatively stable. In those accumulations, proteins typically show less dynamic behavior, further diminishing towards the center (**Fig. 3.1**, indicated by **arrows**), which is characteristic for protein clusters (Sieber et al. 2007). Compared to spontaneous membrane binding, we expect non-membrane-bound MinD to bind an existing cluster with higher affinity due to recruitment by DivIVA-MinJ, which then also stabilizes it and therefore lowers the detachment rate in comparison, an assumption included in our mathematical model (chapter 2.1.4). At the same time, a fraction of freely diffusive protein will probe different regions of the cell (e.g. lateral

membrane), where it can nucleate into novel clusters. If the negative curvature is high enough, these clusters will persist due to molecular bridging of DivIVA (Lenarcic et al. 2009), which will in turn recruit and stabilize MinJ and MinD. Without negative curvature, these clusters will vanish or re-localize more quickly, resulting in a dynamic steady-state of the Min system in *B. subtilis*. This dynamic equilibrium appears as septal-polar gradient, represented in (**Fig. 3.1**), but was revealed to manifest in dynamic clusters when observed with SMLM.

Finally, it should be noted that the observed dynamics of Min proteins in *B. subtilis* are not compatible with a division-site selection system, as ongoing division and the consequential negative curvature at midcell is a requirement for correct localization of the Min proteins. Indications for this conclusion were already found a decade ago in a study from our lab, where MinJ was shown to contribute to divisome disassembly, downstream of FtsZ positioning (van Baarle and Bramkamp 2010). Thereby, MinJ appeared to protect poles from re-initiation of division by the still assembled division machinery, leading to minicell production in genetic knockout strains, where cells also displayed multiple Z-rings (van Baarle and Bramkamp 2010). In agreement, a very recent study also displayed an essential role of the Min system in disassembly of the Z-ring, utilizing microscopy and microfluidic systems (Yu et al. 2020). The same study suggested the Min system to be involved in PG remodeling by inhibiting PG turnover, especially at the poles. Additionally, data from Elizabeth Harry's lab demonstrated that FtsZ is able to identify the central divisional plane in absence of both Min system and nucleoid occlusion (Rodrigues and Harry 2012). Therefore, identifying the mechanisms that defines the divisional plane and ensures correct positioning of FtsZ remains a major task in the characterization of cell division in *B. subtilis*.

3.2. SPT analysis of MinD and DivIVA

Tracking of individual molecules has increasingly been used in life sciences to describe and characterize individual protein dynamics and kinetics, reviewed by (Manzo and Garcia-Parajo 2015) and more recently by (Shen et al. 2017a). Due to the small size and the rather low copy number of proteins, SPT remains challenging in bacteria. The technical progress in microscopy techniques and associated development of fluorophores towards the end of the last decade however allowed imaging of single molecules in combination with tracking (Manley et al. 2008), even in bacterial cells (Xie et al. 2008). Although technically challenging, bacterial proteins have been investigated numerously using SPT since then, recently reviewed by (Kapanidis et al. 2018), allowing to gain information on protein dynamics in unmatched detail. In this work, a SPT analysis routine was established and optimized (chapters 2.2.1 - 2.2.3) and finally used to investigate dynamics of the Min system in living *B. subtilis* cells (chapter 2.2.4).

3.2.1. Technical aspects of SPT in bacterial cells

SPT in PALM has the advantage of being extremely sensitive, as it allows tracking of many individual molecules in a single cell, thereby drastically reducing the total amount of cells required for a solid statistical analysis (Manley et al. 2008). As described by (Turkowyd et al. 2019), the downside of this sensitivity is the need for careful sample preparation to avoid intra- and extracellular background. Therefore, sample preparation was first optimized to ensure reliable and reproducible conditions to image fluorophore-tagged proteins in *B. subtilis* (see chapter 2.2.1 and **Fig. 2.14**). These steps included choice of growth and mounting medium, the agarose type and preparation of agarose pads and cleaning procedures of the microscopy slides and coverslips. Next, imaging conditions were optimized individually (chapter 2.2.2), followed by the choice and finally establishment of an analysis workflow (chapter 2.2.3 and **Fig. 2.15**).

Cellular autofluorescence, caused by certain metabolites and cellular structural components that act as endogenous fluorophores, has been investigated and discussed in-depth before, reviewed e.g. in (Billinton and Knight 2001) or (Croce and Bottiroli 2014). While cytosolic autofluorescence is caused almost exclusively by NAD(P)H and flavins (Aubin 1979; Croce and Bottiroli 2014), other components like aromatic amino acids, collagen/elastin, fatty acids, vitamins or cytokeratins have been exploited as autofluorescent intrinsic biomarkers (Croce and Bottiroli 2014). Therefore, growth medium and temperature can have an impact on autofluorescence, which needs to be individually tested, similar to the mounting medium. Fortunately, our established minimal growth medium (MD) did not produce considerable

autofluorescence in *B. subtilis* during SPT experiments. An increase in autofluorescence could however be observed when cells were imaged for an extended amount of time, or when increasing laser powers (see chapter 2.2.2). This effect has been linked to increased expression of genes from the flavin biosynthesis pathways as a reaction to cellular stress, indicating a struggle for survival (Surre et al. 2018). When carefully observed, this effect can be utilized as an internal control, since it can help in identifying overexposure during live-cell SMLM imaging.

While choice of agarose or its preparation did not make a measurable difference here, cleaning of glass slides and coverslips was indispensable to remove extracellular autofluorescence (**Fig. 2.14 c**), likely caused by impurities or dirt particles. Thereby, all tested cleaning procedures, e.g. overnight incubation in 1M KOH (Turkowyd et al. 2017), Plasma cleaning (Lelek et al. 2014) or the use of organic solvents/alkaline concentrate (Rosch et al. 2018a) decreased the extracellular fluorescence to a satisfactorily amount. Consequently, the cleaning procedure was adjusted for time-effectiveness (see protocol in 4.6.2.1), while still removing most background particles.

Regarding cell viability, adjustment of laser powers and total exposure time during SPT could be controlled for, as diminished cell growth and increased autofluorescence indicated overexposure (see chapter 2.2.2). These tests were coupled and compared to a negative control, i.e. data from wild type cells that do not express a fluorophore, to be able to identify autofluorescence. Further controls were performed, including a strain expressing cytosolic, free diffusive fluorophore. This is important to test performance of the respective fluorophore, but also to determine the maximum velocity of a freely diffusing particle that does not interact with cellular compounds. Unfortunately, the relatively slow camera speed (15 ms) in our set-up did not allow satisfactorily quantification, which will be discussed later. Another important control is an immobile fluorescent marker, e.g. a fixed strain expressing a fluorescent fusion. Even though the fluorescent marker does not move physically, acquired trajectories will display residual vibrations in the range of the localization precision. This control, exemplary shown for DivIVA-PAmCherry (JB37) in **Fig. 3.2**, serves as a reference for immobile protein populations and can help to identify artifacts during trajectory reconstruction. Here, only 2% of tracks were identified as mobile, which is an acceptable background. These tracks presumably stem from falsely connected trajectories. Since DivIVA localizes in dense clusters and accumulations (**Fig. 2.13**), this artifact is difficult to avoid, which was also noted during regular SMLM (**Fig. 2.20**). Although these tracks could be filtered in a dataset where mobile populations can be excluded, this is not possible for proteins with unknown mobility. They could also be reduced by using less activation power, resulting in lower chances of overlapping molecules, but also significantly less total tracks per experiment. Another popular method to decrease overlap of signal during SPT of dense protein is pulsed or stroboscopic activation of fluorophores (Hansen et al. 2018).

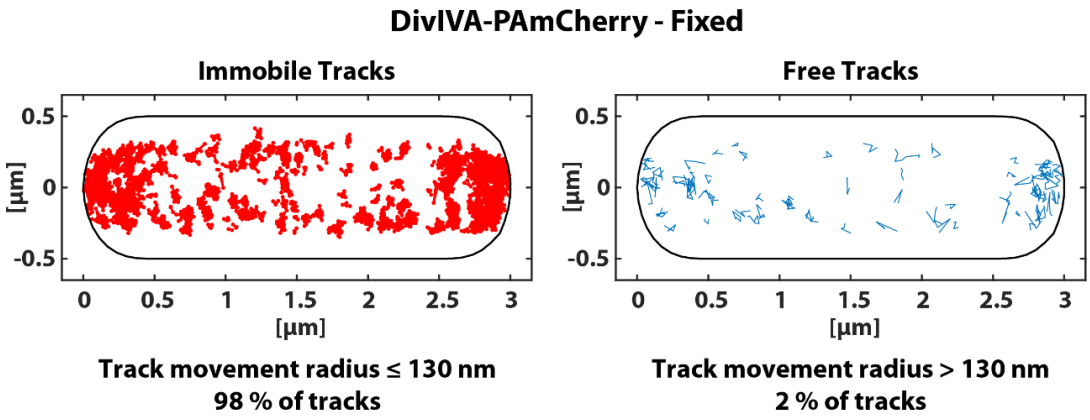

Fig. 3.2: Example of a control for immobile populations during SPT.

B. subtilis expressing DivIVA-PAmCherry (JB37) was grown in MD until mid-exponential phase and subsequently chemically fixated with 1.5% paraformaldehyde before being imaged and analyzed according to Materials and Methods (see 4.6.2.2 and 4.6.2.3). Immobile **(left)** and free **(right)** tracks from multiple cells were separated via a confinement radius of 130 nm, the same conditions used in **Fig. 2.16** and **Fig. 2.17**, and plotted on a normalized cell, respectively. Total number of tracks (n) = 734. The apparent distance of tracks from the lateral cell walls is an effect of the cell selection mask, which was chosen larger than the actual cells, to not exclude any valid tracks.

Thereby, only small protein fractions are activated during periodic pulses (~100 – 200 ms) of activation laser illumination. This does not only help in separation of molecules during trajectory reconstruction, but also reduces phototoxicity due to reduction of total illumination time by the high-energy activation laser (typically 405 nm). Unfortunately, the proprietary imaging software (Zen Black 2012, Zeiss) did not allow for such illumination modes, as it only offers constant or linearly increasing laser intensity.

Finally, data analysis was tested with different analysis and tracking software packages. Since all tested software packages for trajectory reconstruction produced a reasonably similar output when tested (see e.g. **Fig. 2.15**), the choice mostly depends on the specific experiment and its requirements, as well as the quality of the imaging data. Trackmate (Tinevez et al. 2017) and u-Track 2 (Jaqaman et al. 2008) are widely used and accepted in the field and generated data is supported by other analysis software like Spot-On (Hansen et al. 2018) or SMTracker (Rosch et al. 2018b). Therefore, the overall SPT workflow was established with a focus on time-efficiency while maintaining enough flexibility and detail in the analysis, producing solid SPT data for the Min system that will be discussed in the next chapter. It should however be mentioned that some research groups that are specialized in SMLM related microscopy techniques, e.g. the group around Ulrike Endesfelder, write their own software to reconstruct and filter trajectories and analyze their data individually (Balinovic et al. 2019; Wimmi et al. 2019). This allows for hand-tailored implementation of desired features and regard for individual optical systems. While this is not generally feasible due to time restrictions and lack of programming expertise in many groups that perform microscopy, it allows for very specific types of analysis, which is often sought after when performing SPT.

3.2.2. Subpopulations of MinD and DivIVA in SPT

With the help of the SPT workflow established in the previous chapter, mobility of MinD and DivIVA was analyzed (**Fig. 2.16** and **Fig. 2.17**). Thereby, localization of mobile and immobile trajectories correlated well with the previously established idea of stable clusters at poles and septum and more dynamic protein along lateral cell wall and cytosol (**Fig. 2.16 a)**. Furthermore, MinD was found to be faster than DivIVA in both MSD (**Fig. 2.16 b and c**) and JD analysis (**Fig. 2.17**), again displaying a similar tendency when compared to FRAP results (**Fig. 2.8**).

The immobile fraction of DivIVA in SPT data analyzed via MSD (54%; **Fig. 2.16 c**) and JD (30 %; **Fig. 2.17**) was considerably larger when compared to MinD (33% and 16%, respectively). A similar trend was observed during FRAP experiments (**Fig. 2.5** and **Fig. 2.6**) and could be explained by the rather stable and large clusters DivIVA forms, also observed in SMLM (**Fig. 2.11**, right panel and **Fig. 2.13**). Most proteins in these clusters are expected to be slow or immobile, increasing toward the center, as it is typically observed in clusters (Sieber et al. 2007). The majority of DivIVA (>50%) was found in clusters, with relatively few clusters per cell (15 per cell in average), indicating very high density in these clusters. This density could explain the discrepancy between results of MSD and JD analysis: While MSD analysis identified a relatively small slow diffusive population of DivIVA (18%, D = 0.125 $\mu m^2 s^{-1}$) in combination with a large immobile population (54%, D = 0.025 $\mu m^2 s^{-1}$), JD analysis indicated a much larger slow diffusive population (60%, D = 0.108 $\mu m^2 s^{-1}$) and a therefore smaller immobile population (30%, D = 0.0384 $\mu m^2 s^{-1}$), in combination with a reduced mobile fraction. The previously mentioned densities of DivIVA assemblies possibly lead to technical difficulties during SPT imaging, as dense structures often produce artifacts due to simultaneous activation of spatially proximal molecules (Hansen et al. 2018). Even though this can be tuned through the activation laser power, it cannot be fully avoided that signals from neighboring DivIVA-PAmCherry molecules in a dense cluster are recorded in succession and falsely connected into one track. Even though it is problematic to differentiate between slow diffusive and immobile DivIVA molecules, these subpopulations make up the largest fraction of DivIVA molecules in either type of analysis, a tendency already observed during FRAP (see 2.1.2), and are likely just differently pronounced due to the differences between MSD and JD analysis (Weimann et al. 2013). In this type of data, JD analysis should theoretically provide a more realistic idea of the different protein populations and their mean diffusion coefficients (Weimann et al. 2013), since MSD analysis was shown to perform poorly in simulations when large fraction of protein are simulated to be membrane or protein associated and therefore slowly diffusive or immobile (Hansen et al. 2018).

Finally, the fast diffusive subpopulations of both Dendra2-MinD (30%, D = 1.16 $\mu m^2 s^{-1}$) and DivIVA-PAmCherry (10%, D = 0.75 $\mu m^2 s^{-1}$) were determined. While they again confirm a higher mobility of MinD when compared to DivIVA, there are several reasons why these fractions are likely underestimated in size and speed: First, the camera speed was limited to 15 ms, which is too slow to accurately and reliably record fast diffusing particles without causing motion-blur artifacts (Berglund 2010; Bakshi et al. 2011; Deschout et al. 2012; Hansen et al. 2018; Turkowyd et al. 2019), while immobile protein will be accurately depicted. Even though the camera can theoretically be used at slightly faster speeds (13.3 ms), this is not feasible when using fluorophores like Dendra2 and PAmCherry, as a significantly shorter frame time also shortens the span of photon collection (integration time), leading to a reduced SNR. This problem can be tackled by using the excitation laser at higher power, which would however increase phototoxicity, or by the use of an even more sensitive camera. Alternatively, chemical dyes can reach an acceptable photon budget to reliably record fast moving particles in the described scenario. Another problem is the calibration of the tracking algorithm, where the maximum distance a particle can travel between two frames has to be defined. When frames are short (5-10 ms), this is not a problem as these distances are relatively small, but frame lengths of 15 ms or more allow a particle to travel increasing distances between frames, which can cause artifacts during trajectory reconstruction by connecting two unrelated and distant signals in successive frames. After testing different parameters, a maximum distance of 500 nm was chosen, a compromise between detection of very fast particles and avoidance of false trajectories.

Anyhow, underestimation of fast populations is a general caveat of SPT due to several reasons (Hansen et al. 2018). Besides the previously mentioned motion blurring artifacts (Berglund 2010; Deschout et al. 2012; Frost et al. 2012) and tracking errors caused by dense localizations (see **Fig. 3.2**), SPT in general describes three-dimensional motion while recording only two dimensions. Once in-focus, a bound or slow particle will rarely slip out-of-focus, allowing frequent recording of long and stable trajectories, while a fast and freely diffusing particle will do so more often. While the length of trajectories can be normalized, e.g. by weighted analysis of jump distances (mean jump distance, MJD) to calculate mean diffusion coefficients of distinct populations (Grunwald et al. 2008), the lower total number of tracks depicting fast populations that exceed the threshold for minimal-track length leads to further underestimation of the respective fraction size.

When comparing the diffusion coefficients of MinD and DivIVA between SPT and FRAP analysis, the numbers are several fold apart, even though they both show significant faster diffusion of MinD compared to DivIVA (see **Table 2.2**). SPT analysis is one of the most precise diffusion measurement techniques in live-cells (Struntz and Weiss 2018), and therefore

considered more precise than FRAP. Additionally, diffusion measurement calculations in FRAP scale directly with the size of the bleaching laser, which is challenging to measure precisely (see chapter 4.6.1.1). Therefore, diffusion coefficients obtained via SPT analysis are likely a better estimation of protein mobility. However, compared to eukaryotes, both FRAP and SPT are generally more difficult to perform in bacteria due to small cell sizes and low protein expression levels, and therefore more error prone. Technical difficulties of SPT can however be encountered through further optimization in the future, which could include data correction by incorporating Monte Carlo simulations (Stracy et al. 2014; Stracy et al. 2015), the use of synthetic dyes instead of fluorescent proteins to obtain longer and more distinct trajectories, the employment of a faster and/or more sensitive camera, and by investigating at-least two different temporal regimes (Turkowyd et al. 2019). Furthermore, it would be necessary to characterize MinD membrane binding regimes in detail, as the currently employed exponential fit to determine halt-time recovery of FRAP experiments (see Materials and Methods, 4.6.1.1) might be inappropriate to describe MinD behavior, as it only accurately describes recovery in diffusion dominated systems opposed to a reaction dominated system (Sprague et al. 2004).

However, the SPT results most probably depict the different mobile populations of MinD and DivIVA more accurately compared to FRAP. While the exact diffusion coefficients did not play a large role in the here presented reaction-diffusion model (**Fig. 2.10**), the observed differences between dynamics of Min proteins seem to be more central. By confirming a significantly higher mobility and smaller immobile fraction when comparing MinD to DivIVA (**Fig. 2.16** and **Fig. 2.17**), this study represents an important first implementation of a functional SPT workflow in our laboratory, and should next be extended for the different Min genetic knockout backgrounds investigated during FRAP (**Fig. 2.8**). Demonstrating the power and versatility of SMLM analysis methods, this study lays the basis for further future analysis of bacterial protein dynamics.

3.3. Bacterial PALM with mNeonGreen

Green fluorescent proteins that are compatible with PALM, as well as bright and monomeric, are sparse, especially when imaging bacterial cells that require fast maturation due to relative short generation times. Consequently, we wanted to establish a routine PALM workflow using mNeonGreen, a FP with excellent photocharacteristics (Shaner et al. 2013). To this end, we identified optimal illumination conditions that minimize the frequently occurring simultaneous emissions of multiple neighboring mNeonGreen molecules (**Fig. 2.18**), likely caused by the high on-switching rate of mNeonGreen, which we discovered when comparing photophysical

properties with Dronpa (**Fig. 2.19**) (Stockmar et al. 2018). Moreover, we established simple and fast post-processing steps to eliminate most remaining overlapping emissions (**Fig. 2.20**). These steps can optionally be combined with multi-emitter fitting (**Fig. 2.21**) (Stockmar et al. 2018). In addition, we tested different conditions during sample preparation and optimized paraformaldehyde fixation of *B. subtilis* samples (**Fig. 2.22**) to produce the most suitable PALM sample. We assume that this simple and optimized workflow can motivate other researchers to utilize mNeonGreen for bacterial PALM imaging as an alternative to other green fluorescent proteins (Stockmar et al. 2018).Similar to eYFP (Dickson et al. 1997; Biteen et al. 2008), the exact physical mechanism of photoswitching/blinking of mNeonGreen is not understood (Shaner et al. 2013). While this renders controlled activation of mNeonGreen during PALM experiments challenging, the advantages of only using a single wavelength (488 nm) for activation and imaging stands out.

As reported in chapter 2.3, we encountered the problem of simultaneous emissions in close proximity when we first tried imaging mNeonGreen fused to DivIVA in PALM, leading to faulty PSF fitting and in turn blurred PALM images. This problem is commonly encountered during PALM of dense structures (Kamiyama and Huang 2012), and often solved by employing pre-bleaching with strong laser intensities to the field of view, driving many molecules to a dark state until fitted PSFs rarely overlap (Betzig et al. 2006; Lee et al. 2012; Shaner et al. 2013). The same procedure was also employed for eYFP, which appears to have a similar (unknown) switching mechanism (Biteen et al. 2008). This process targets the same issue as the post-processing in this study, since most overlapping emissions occur during the first frames of the experiment (**Fig. 2.18 c**), where the entire protein pool can still be activated. We argue that the disadvantage of bleaching is a permanent loss of a large fraction of switchable mNeonGreen and thus a possible loss of information. Pre-bleaching of a whole field of view allows less control over removed localizations, and the "sweet-spot" (**Fig. 2.18 c**, here after ~2000 frames) could be missed, as bleaching is irreversible. Furthermore, only a fraction of mNeonGreen will blink (Shaner et al. 2013). Bacteria express usually lower amounts of protein compared to eukaryotes, so in a structure less dense, pre-bleaching of mNeonGreen might not result in a sufficient total number of localizations. On the other hand, less dense structures would likely induce less problems linked to overlapping PSFs from simultaneously emitting molecules.

In addition, we investigated the impact of laser power on simultaneous overlapping emission, reflected in the width of the (falsely) fitted PSFs (Localization width, **Fig. 2.18 d**), plateauing at medium intensities. Higher laser intensities can help reduce this problem further, by driving molecules faster and in higher quantity towards a dark state, and by increasing the photon budget due to increased fluorophore excitation. At the same time, higher intensities will lead to

much faster depletion of the available pool of mNeonGreen, resulting in less total signal, which is necessary for reconstruction of structures. For this reason, we continued imaging with medium laser intensities, underlining the importance of individually testing these parameters for every fluorophore used in PALM.

Photon budget and switching properties dictate the image quality of the final image in SMLM, since the localization precision is inversely proportional to the square root of the number of collected photons from the fluorescent molecules. The obtained mean number of photons (~669, **Fig. 2.19**) is in good agreement with previously obtained values (300-660, (Shaner et al. 2013)), and the obtained localization precision of 25-30 nm presents a satisfactory range. We could tell apart the known structure of DivIVA double-rings at septa (Eswaramoorthy et al. 2011) when tagged with mNeonGreen (**Fig. 2.20**), also visible in PALM images of DivIVA-PAmCherry (**Fig. 2.11 right** and **Fig. 2.13 a**). However, the density of DivIVA in this structure is lower compared to images obtained with DivIVA-PAmCherry, which can likely be attributed to the smaller population of mNeonGreen that will blink reliably (Shaner et al. 2013). Therefore, using mNeonGreen might result in some loss of information when imaging lowly abundant protein, like MinJ-mNeonGreen in **Fig. 2.11**, which should therefore be repeated with another fluorophore in the future, most optimally a chemical dye.

To test if a multi-Gaussian PSF fitting function can help in solving the problem of overlapping emission, the multiple-emitter fitting analysis of ThunderSTORM was employed, which uses statistical model selection methods to determine the optimal number of molecules to fit (Ovesny et al. 2014; Sage et al. 2019). When this fitting procedure was used, it helped removing some of the faulty fitted PSFs, but did not resolve the problem entirely (**Fig. 2.21 a**), while resulting in a manifold increased computing time for fitting the PSFs. Moreover, it still needed to be coupled to post-processing filtering, which is fast and easy to implement if quality of data allows for it, producing good results and a clear separation of DivIVA double rings here (**Fig. 2.21 b** and **c**). Therefore, we concentrated on optimizing post-processing to remove possible artifacts (**Fig. 2.20**). Post-processing needs to be performed with greatest care to avoid over-filtering of data. This would not only results in a loss of information but might also introduce artifacts or biased results. In an optimal case, baseline filter conditions for a fluorophore should be optimized by imaging a known structure, and different filter settings should be tested. For proteins of unknown localization, a test with different FPs should be employed when possible, ensuring avoidance of misinterpretation through FP induced mislocalization. Mislocalization of fluorescent fusions in bacteria is not uncommon (Margolin 2012), often caused by the tendency of fluorescent proteins to di-/tetramerize (Matz et al. 1999; Ando et al. 2002; Chudakov et al. 2003; Karasawa et al. 2004; Shaner et al. 2005), leading to clustering of the tagged protein, even

induced by supposedly monomeric FPs (Wang et al. 2014). This effect has infamously affected bacterial research in the past, as the bacterial actin homologue MreB had been shown to form fascinating helical structures (Shih et al. 2005; Vats and Rothfield 2007; Vats et al. 2009; Wang et al. 2012), only to be later identified as YFP induced artifacts (Swulius and Jensen 2012). Similarly, DivIVA localization artifacts were observed in this study: while localization was correct when fused to either mNeonGreen (**Fig. 2.20**) or PAmCherry (**Fig. 2.11**), Dronpa and mGeosM induced mislocalization artifacts (**Fig. 2.3**). This emphasizes the necessity for a wider choice of truly monomeric protein for PALM like mNeonGreen, as well as the need for careful testing prior interpretation of localization data obtained from fluorescent fusions.

As already presented for SPT experiments (**Fig. 2.14**), sample preparation should be individually optimized for PALM (**Fig. 2.22**) to enhance the fidelity of rendered PALM images (Whelan and Bell 2015). Growth and embedding medium need to be characterized (**Fig. 2.14**), and cell adhesion and density should be adjusted for reproducible results (Stockmar et al. 2018). Since cells are chemically fixed for structural PALM, optimization of fixation with respect to fluorescence intensity can help to increase the signal even further (**Fig. 2.22**), since fluorophores are often quenched by fixative agents (Joosen et al. 2014). Furthermore, also fixation can lead to mislocalization artifacts, especially in SMLM (Kamiyama and Huang 2012; Whelan and Bell 2015), emphasizing the need for additional controls like live-cells without fixative agent.

In summary, mNeonGreen fused to DivIVA in *B. subtilis* could be imaged with a satisfactorily localization precision in PALM with the relative simple workflow presented here. Especially for multi-color PALM in combination with an orange/red FP like PAmCherry (Subach et al. 2009), mNeonGreen offers a bright alternative to other green FPs when fused to a relative abundant protein, as it can be activated and imaged by using a single laser line. We therefore hope this study presents a good starting point for utilization of mNeonGreen in bacterial PALM.

3.4. Conclusion and outlook

Even though the Min system of *B. subtilis* is partially well conserved when compared to *E. coli*, a fundamentally different role has been brought to light by recent advances in research: While the Min system in *E. coli* is essential for identification of the divisional plane through positioning of the tubulin homologue FtsZ, perception of the *Bacillus* Min system shifted towards a role downstream of FtsZ assembly, where it aids in preventing re-initiation of division via disassembly of the divisome and FtsZ-filaments. In agreement with this role, we here determined individual dynamics of the Min system components, which appear to be essential for re-localization upon septum formation and are affected by their hierarchical, direct

interactions. With the help of modern microscopy methods, we could further reveal the strong tendency of cluster formation exhibited by Min proteins. Combining these data with protein quantities, a mathematical model was built, reproducing our experimental observations during simulations. This model now represents an excellent starting point for further characterization of the Min components and respective implications for the whole system. On the one hand, experimental observations can now be used to challenge, refine and extend the minimal reaction-diffusion model further, while predictions obtained through simulations can be experimentally validated. There are many open questions concerning the Min system, starting with the search for a protein or mechanism stimulating MinD ATP hydrolysis and more details regarding functional details of said ATPase to help understand what induces the fast cycling of MinD molecules. Furthermore, investigating the effect on localization and dynamics from mutations in the MTS of MinD or the membrane-binding domain of DivIVA would help determining the importance of membrane binding and interaction.

In follow-up experiments, I was able to establish a workflow for SPT, allowing further characterization of Min dynamics. Generally, SPT offers a variety of possibilities to investigate and monitor intracellular activities on the single molecule scale. First results indicated different subpopulations of MinD and DivIVA, confirming generally faster diffusion of MinD, already observed during FRAP. In the future, SPT can be used to obtain more information about the binding kinetics and dwell times of the Min proteins, in combination with precise intracellular localization. This should also be extended to genetic knockout backgrounds. Moreover, the role of the Min system during sporulation remains puzzling and should be carefully analyzed via SPT, since this asymmetric mode of division could be the central reason for the existence of different Min systems in *Bacillus* and *E. coli*. In theory, these analyses could be performed or supported by simultaneous multi-color imaging due to the possibility to utilize mNeonGreen reliably in SMLM. Together with PAmCherry or other compatible FPs, protein interactions studies, further cluster analysis or SPT could be performed to gain new insights into the Min system or related structures.

Finally, when thinking about the “bigger picture”, it remains to be identified how FtsZ is able to localize to the cell center in *B. subtilis*. Understanding these fundamental elements of cell division in model organisms like *Bacillus* is not only vital to help identify pathways that could be attacked to inhibit cell division in the form of antibiotics, but could also be used to exploit these pathways for biotechnological use.

4. Materials and Methods

4.1. Reagents

Chemicals used in experiments of this study were obtained from companies Merk (Merk KGaA, Darmstadt, Germany), Roth (Carl Roth GmbH + Co. KG, Karlsruhe, Germany), Serva (SERVA Electrophoresis GmbH, Heidelberg, Germany) and VWR (VWR International, Radnor, PA, USA). For procedures in molecular biology, biochemistry or microscopy, products from companies Genaxxon (Genaxxon Bioscience GmbH, Ulm, Germany), Macherey-Nagel (MACHEREY-NAGEL GmbH & Co. KG, Düren, Germany), NEB (New England Biolabs Inc., Ipswich, USA), Roche (F. Hoffmann-La Roche AG, Basel, Switzerland), Thermo-Fischer (Thermo Fisher Scientific Inc., Waltham, MA, USA) and Zeiss (Carl Zeiss AG, Oberkochen, Germany) were used.

4.2. Oligonucleotides, plasmids and bacterial strains

All oligonucleotides, plasmids and bacterial strains used in this study can be found in **Table 4.1**, **Table 4.2** and **Table 4.3**. Some strains constructed for this study have been published before in (Stockmar et al. 2018), others have been used in a study that is currently in preparation for re-submission (mBio - ASM) and has been previously published on a preprint server (BioRxiv, (Feddersen et al. 2020)). Details of strain construction can be found in the following chapter (4.3). *E. coli* NEB Turbo or NEB 5-Alpha were used to amplify and maintain plasmids.

Table 4.1: Oligonucleotides used for strain construction.

Restriction sites or are indicated by an underline. Golden gate overhangs are highlighted in red, nucleotide modifications resulting in (point) mutations are highlighted in blue.

Name	Description	Sequence 5'-3'
HF0001	mCherry2-GG-f	AATGGTCTCTGGAGGGATGGTCAGCAAGGGAGAG
HF0002	mCherry2-GG-r	TTTGGTCTCGCGAATTAGGATCCTGAGCCGCT
HF0009	MinD-IN-f	CTAGGTCTCTCCGACGTGATGCTGACCGTATTATAG
HF0010	MinD-IN-R	TATGGTCTCCCTCCAGATCTTACTCCGAAAAATG
HF0011	MinD-Down-F	ACGGGTCTCAAATGTGTGATAGAATCAAAGAGAAGA
HF0012	MinD-Down-R	CGGGGTCTCTTAGTGAGAACAAGGCAGGCCGACA
HF0027	pJPR1-SNAP-f	CAGGTCGACATGGACAAAGATTGCGAAATG
HF0028	pJPR1-SNAP-r	GAAGGATCCTCCCAGACCCGGTTTACC
HF0029	msfGFP-GG-f	AATGGTCTCTGGAGGGATGGGTACCCTGCAGATG
HF0030	msfGFP-GG-r	TTTGGTCTCGCGAATTTGTAGAGCTCATCCATGC
HF0037	gg-minD-N-UP-F	TATGGTCTCCCCGAGTTCATTCTATTGACAGTGAAGT

HF0038	gg-minD-N-UP-R	CTAGGTCTCTCTCCTTCACATTCCTCCCTCAAG
HF0039	gg-minD-N-UP-RBS-R	CTAGGTCTCTCTCCTTAGTAGTTTCTCCTCTTTAATTTCACATTCCTCCCTCAAG
HF0040	Spec-N-F	AATGGTCTCTGGAGGGGTGAAAGGATGTACTTA
HF0041	Spec-N-R	TTTGGTCTCGCGAATAATTGAGAGAAGTTTCTATAG
HF0042	Dendra2-N-F	GGAGGTCTCTTTCGATGAACACCCCGGGAATTAAC
HF0043	Dendra2-N-R	CACGGTCTCCCATTCCACACCTGGCTGGGCAGG
HF0044	minD-N-IN-F	ACGGGTCTCAAATGGGTTGGGTGAGGCTATCGTAATAAC
HF0045	minD-N-IN-R	CGGGGTCTCTTAGTCAATATTTTCCTCTTGCTCCAGC
HF0050	mCherry2-N-F	GGAGGTCTCTTTCGATGGTCAGCAAGGGAGAG
HF0051	mCherry2-N-R	CACGGTCTCCCATTGGATCCTGAGCCGC
HF0054	MinDmut-G12V-f	GTAATAACTTCGGGAAAAGTCGGAGTAGGTAAGACAACAAC
HF0055	MinDmut-G12V-r	GTTGTTGTCTTACCTACTCCGACTTTTCCCGAAGTTATTAC
HF0056	MinDmut-K16A-f	GAAAAGGCGGAGTAGGTGCGACAACAACATCTGCG
HF0057	MinDmut-K16A-r	CGCAGATGTTGTTGTCGCACCTACTCCGCCTTTTC
HF0058	minD-N-IN-R2_mut	CACGGTCTCGATTAAGATCTTACTCCGAAAAATGAC
HF0059	minD-N-IN2_DWN-F	GCAGGTCTCTTAATGTGATAGAATCAAAGAGAAG
HF0060	minD-N-IN2_DWN-R	CGGGGTCTCTTAGTCAAAATCATATAAAGCAACATC
HF0061	pUC18_mut-HF-F	GTCGGTCTCAACTAGAATTCGTAATCATGGTCATAGCTG
HF0062	pUC18_mut-HF-R	CTCGGTCTCATCGGAAGCTTGGCACTGGCC
HF0063	pKill-GG-HF-F	CGAGGTCTCAACTATTACCC
HF0064	pKill-GG-HF-R	CACGGTCTCATCGGG
HF0065	msfGFP-N-F	GGAGGTCTCTTTCGATGGGTACCCTGCAGATG
HF0066	msfGFP-N-R	CACGGTCTCCCATTTTTGTAGAGCTCATCCATGC
HF0067	xbaI-SD-mNG/PAmC-BamHI-F	CACTCTAGAGCAGATTAGGAGGATTTAGCATGGTGAGCAAGGGCGAG
HF0068	xbaI-SD-mNG/PAmC-BamHI-R	GTCGGATCCCTTGTACAGCTCGTCCATGCC
HF0071	DivIVA-IN-Link-GG-F	CTAGGTCTCTCCGAGAATTCCTAGCCCAAGTCAG
HF0072	DivIVA-IN-Link-GG-R	TATGGTCTCCCTCCGAATTCGCCAGAACCAGCAGCGGAGCCAGCGGATCCTTCCTTTTCCTCAAATACAGC
HF0073	MinD-KO-ErmR-F	AATGGTCTCTGGAGATGAACGAGAAAAATATAAAAC
HF0074	MinD-KO-ErmR-R	TTTGGTCTCGCGAATTACTTATTAAATAATTTATAGC
HF0075	MinD-KO-Dwn-F	GGAGGTCTCTTTCGGTGATAGAATCAAAGAGAAG
HF0076	MinD-KO-Dwn-R	CACGGTCTCCTAGTCAAAATCATATAAAGCAACATC
HF0077	psmOrange2-GG-F	AATGGTCTCTGGAGGGATGGTGAGCAAGGGCG
HF0078	psmOrange2-GG-R	TTTGGTCTCGCGAATTACTTGTACAGCTCGTCCATG
HF0083	SepF-IN-F	CTAGGTCTCTCCGAATGAAAAATAAACTGAAAAAC
HF0084	SepF-IN-R	TATGGTCTCCCTCCCCACCTCTGATGTTCG
HF0085	SepF-Dwn-F	ACGGGTCTCAAATGAGCGAGATGATCCTTTATC
HF0086	SepF-Dwn-R	CGGGGTCTCTTAGTGCCGCTTTAATCCTATG
HF0087	ZapA-N-IN-F	ACGGGTCTCAAATGGGTTGTCTGACGGCAAAAAAAC
HF0088	ZapA-N-IN-R	CGGGGTCTCTTAGTGTGTATGGTTAATGATCACATTTG

HF0089	ZapA-N-UP-F	TATGGTCTCCCCGACTGGCTCAGCGAATTG
HF0090	ZapA-N-UP-R	CTAGGTCTCTCTCCCGTTTCTCCTCCATTCC
HF0091	psmOrange2-N-F	AATGGTCTCTGGAGATGGTGAGCAAGGGCG
HF0092	psmOrange2-N-R	TTTGGTCTCGCGAACTTGTACAGCTCGTCCATG
HF0093	Cat-N-F	AATGGTCTCTGGAGCTTTAGATAAAAATTTAGGAGGC
HF0094	Cat-N-R	TTTGGTCTCGCGAATTATAAAAGCCAGTCATTAGG
HF0095	Ery-N-F	AATGGTCTCTGGAGATTCATATAACCAAATTAAAG
HF0096	Ery-N-R	TTTGGTCTCGCGAATTACTTATTAAATAATTTATAGC
HF0097	Tet-N-F	AATGGTCTCTGGAGTATTGTTGTATAAGTGATGA
HF0098	Tet-N-R	TTTGGTCTCGCGAATTAGAAATCCCTTTGAGAAT
HF0099	Kan-N-F	AATGGTCTCTGGAGTTGAAATCCCCTCAAAAACCC
HF0100	Kan-N-R	TTTGGTCTCGCGAAGCGCCATGACAGCCATGATAATTA
HF0177	mNG-RBS-pJPR1-N-F	AGCTAAGCTTGCAGATTAGGAGGATTTAGCATGGTGAGCAAGGGCGAG
HF0178	mNG-RBS-pJPR1-N-R	AGCTACTAGTCTTGTACAGCTCGTCCATGCC
HF0181	MinD-pJPR1-N-F	AGCTACTAGTTTGGGTGAGGCTATC
HF0182	MinD-pJPR1-N-R	AGCTGCGGCCGCTTAAGATCTTACTCCGAAAAATG
HF0197	mKate2-GG-N-F	AATGGTCTCTTTCGGTTTCTGAACTTATCAAAG
HF0198	mKate2-GG-N-R	CACGGTCTCCCATTACGATGGCCAAG
G5	Cat-GG-f	GGAGGTCTCTTTCGGGCTTTAGATAAAAATTTAGGAGGC
G6	Cat-GG-r	CACGGTCTCCCATTTTATAAAAGCCAGTC
G20	DendraGG-f	AATGGTCTCTGGAGGGATGAACACCCCGGGAATTAAC
G21	DendraGG-r	TTTGGTCTCGCGAATTACCACACCTGGCT
G26	pamCherry-GG-f	AATGGTCTCTGGAGGGATGGTGAGCAAGGGCGAGGA
G27	pamCherry-GG-r	TTTGGTCTCGCGAATTACTTGTACAGCTC
G32	DivIVADown-GG-F	ACGGGTCTCAAATGGGATTCTCTGATTATCT
G33	DivIVADown-GG-r	CGGGGTCTCTTAGTATCGGGAAATCTGTT
G34	DivIVAIN-GG-f	CTAGGTCTCTCCGAGAATTCCTAGCCCAAGTCAG
G35	DivIVAIN-GG-r	TATGGTCTCCCTCCTTCCTTTTCCTCAAA
G36	Spec-GG-f	GGAGGTCTCTTTCGGGGTGAAAGGATGTACTTA
G37	Spec-GG-r	CACGGTCTCCCATTTAATTGAGAGAAGTT
G40	MinJIn-GG-f	CTAGGTCTCTCCGATGTCGGATTTGGACA
G41	MinJIN-GG-r	TATGGTCTCCCTCCTGATCCCGAAGCGAC
G42	MinJDown-GG-f	ACGGGTCTCAAATGGGAAGGCAGCCCGGCACCGCAGG
G43	MinJDown-GG-r	CGGGGTCTCTTAGTCCATGATGGCTGGTG
G46	SNAP-GG-f	AATGGTCTCTGGAGGGATGGACAAAGATTGC
G47	SNAP-GG-r	TTTGGTCTCGCGAATTATCCCAGACCCGG
G56	mNeonGreen-GG-F	AATGGTCTCTGGAGGGATGGTGAGCAAGGGCGAGGA
G57	mNeonGreen-GG-R	TTTGGTCTCGCGAATTACTTGTACAGCTC
G66	mKateGG-f	AATGGTCTCTGGAGGGGTTTCTGAACTTATC
G67	mKateGG-r	TTTGGTCTCGCGAATTAACGATGGCCAAG
G69	tet-GG-f	GGAGGTCTCTTTCGTATTGTTGTATAAGTGATGA
G70	tet-GG-r	CACGGTCTCCCATTTTAGAAATCCCTTTGAGAAT
G72	Kan-GG-f	GGAGGTCTCTTTCGTTGAAATCCCCTCAAAAACCC
G73	Kan-GG-R	CACGGTCTCCCATTGCGCCATGACAGCCATGATAATTA

Table 4.2: Plasmids utilized in this study.

Plasmid	Characteristic	Reference
pUC18	*lacZα, pMB1 ori, bla*	(Norrander et al. 1983)
pUC18mut	pUC18 with mutated BsaI site in *bla*	(Feddersen et al. 2020)
pKill	pUC18mut with inverted *txpA* (*yqdB*) gene (toxin) for selection against single-crossover	Laboratory collection
pNCS-mNeonGreen	*pUC ori, SV40 ori, bla*	Allele Biotechnology
pDendra2-N	*pUC ori, SV40 ori, PCMVIE, aph3, dendra2* source	Evrogen
pmCherry2	*mCherry2* source plasmid	Laboratory collection, (Shen et al. 2017b)
pmKate2	*mKate2* source plasmid	Laboratory collection
pBAD-PSmOrange2	*PSmOrange2* source plasmid, pBAD	(Subach et al. 2012)
pHJS105	*amyE*-integration vector containing *Pxyl-msfGFP-MCS, aad3, bla*	(Jahn et al. 2015)
pJPR1	*bla amyE3' cat Pxyl amyE5'*	(Bramkamp et al. 2008)
pSNAP-tag (T7)-2	*M13 ori, pMB1 ori, lac-o, P-T7, SNAP26b, bla*	NEB
pMinD-D40A	*minD (D40A)* source plasmid (synthesized)	Eurofins genomics
pHF01	*pUC18mut-minDup-aad9-dendra2-minD*	(Feddersen et al. 2020)
pHF02	*pUC18mut-minDup-aad9-msfGFP-minD*	(Feddersen et al. 2020)
pHF03	*pUC18mut-minJ-msfGFP-aad9-minJdown*	(Feddersen et al. 2020)
pHF04	*pUC18mut-minJ-mNG-aad9-minJdown*	(Feddersen et al. 2020)
pHF05	*pUC18mut-divIVA-mNG-aad9-divIVAdown*	(Feddersen et al. 2020)
pHF06	*pUC18mut-minJ-dendra2-aad9-minJdown*	(Feddersen et al. 2020)
pHF07	*pUC18mut-divIVA-dendra2-aad9-divIVAdown*	(Feddersen et al. 2020)
pHF08	*pUC18mut-minD-mNG-aad9-minDdown*	This study
pHF09	*pUC18mut-minJ-SNAP-aad9-minJdown*	This study
pHF10	*pUC18mut-divIVA-mCherry2-cat-divIVAdown*	This study
pHF11	*pUC18mut-minDup_RBS-aad9-dendra2-minD*	This study
pHF12	*pUC18mut-minDup-aad9-mCherry2-minD*	This study
pHF13	*pUC18mut-divIVA_L-dendra2-cat-divIVAdown*	This study
pHF14	*pUC18mut-divIVA_L-mCherry2-cat-divIVAdown*	This study
pHF15	*pUC18mut-divIVA_L-mNGeonGreen-aad9-divIVAdown*	This study
pHF16	*pKill-minJ-PSmOrange2-aad9-minJdown*	This study
pHF17	*pKill-minDup-aad9-dendra2-minD(G12V)-minDdown*	This study
pHF18	*pKill-minDup-aad9-dendra2-minD(K16A) minDdown*	This study
pHF19	*pKill-minDup-aad9-dendra2-minD(D40A) minDdown*	This study
pHF20	*pKill-sepF-PAmCherry-cat-sepFdown*	This study
pHF21	*pKill-zapAup-cat-PAmCherry2-zapA*	This study
pHF22	*pKill-minDup-aad9-mNG-minD*	This study
pHF23	*pKill-minDup-cat-mKate2-minD*	This study
pHF24	*pKill-minDup-erm-minDdown*	This study
pHF25	*pJPR1-SNAP*	This study
pHF26	*pJPR1-mNeonGreen-minD(G12V)*	This study
pHF27	*pJPR1-mNeonGreen-minD(K16A)*	This study
pHF28	*pJPR1-mNeonGreen-minD(D40A)*	This study

Table 4.3: Bacterial Strains used in this study.

All *B. subtilis* strains are auxotrophic for tryptophan (*trpC2*) and are based on the wild type 168 (BGSC 1A1), except when indicated otherwise.

Strain	Characteristic	Reference
B. subtilis		
168	*trpC2*	Laboratory collection
1803	*divIVA::pSG1612 (P_{divIVA}-GFP divIVA$^+$ cat)*	(Thomaides et al. 2001)
3309	*minCD::aph3*	(Wu and Errington 2004)
4041	*divIVA::tet*	(Bramkamp et al. 2008)
BHF002	*minD::minD-mNeonGreen-aad9*	This study, pHF08 in 168
BHF003	*minJ::minJ-SNAP-aad9*	This study, pHF09 in 168
BHF004	*divIVA::divIVA-mCherry2-cat*	This study, pHF10 in 168
BHF005	*minJ::minJ-SNAP-aad9; divIVA::divIVA-mCherry2-cat*	This study, pHF10 in BHF003
BHF006	*amyE::Pxyl-SNAP-cat*	This study, pHF25 in 168
BHF007	*minJ::minJ-msfGFP-aad9*	(Feddersen et al. 2020)
BHF008	*minJ::minJ-msfGFP-aad9; divIVA::divIVA-mCherry2-cat*	This study, pHF03 in BHF004
BHF010	*divIVA::tet; minCD::aph3; minJ::minJ-msfGFP-aad9*	This study, pHF03 in SB075
BHF011	*minD::aad9-dendra2-minD*	(Feddersen et al. 2020)
BHF012	*minD::RBS-aad9-dendra2-minD*	This study, pHF11 in 168
BHF013	*minD::aad9-dendra2-minD; minJ::tet*	This study, pHF01 in RD021
BHF014	*divIVA::divIVA-mCherry2-cat; minJ::tet*	This study, pHF10 in RD021
BHF015	*minJ::minJ-msfGFP-aad9, minCD::aph3*	(Feddersen et al. 2020)
BHF016	*minD::aad9-mCherry2-minD*	This study, pHF12 in 168
BHF017	*minD::aad9-msfGFP-minD*	(Feddersen et al. 2020)
BHF018	*divIVA::divIVA-linker-dendra2-cat*	This study, pHF13 in 168
BHF019	*divIVA::divIVA-linker-mCherry2-cat*	This study, pHF14 in 168
BHF025	*minD::aad9-msfGFP-minD, minJ::tet*	(Feddersen et al. 2020)
BHF026	*minD::aad9-msfGFP-minD, divIVA::tet*	(Feddersen et al. 2020)
BHF027	*divIVA::divIVA-mNeonGreen-aad9, minJ::tet*	(Feddersen et al. 2020)
BHF028	*divIVA::divIVA-mNeonGreen-aad9*	(Stockmar et al. 2018)
BHF029	*minJ::minJ-PSmOrange2-aad9*	This study, pHF16 in 168
BHF030	*minD::aad9-dendra2-minD(K16A)*	This study, pHF17 in BHF046
BHF032	*minJ::minJ-msfGFP-aad9, divIVA::tet*	(Feddersen et al. 2020)
BHF033	*sepF::sepF-PAmCherry-cat; divIVA::divIVA-mNeonGreen-aad9*	This study, pHF20 in BHF028
BHF034	*zapA::PAmCherry-zapA-cat; divIVA::divIVA-mNeonGreen-aad9*	This study, pHF21 in BHF028
BHF035	*sepF::sepF-PAmCherry-cat*	This study, pHF20 in 168
BHF036	*divIVA::divIVA-mNeonGreen-aad9, minCD::aph3-A3*	(Feddersen et al. 2020)
BHF037	*divIVA::divIVA-mNeonGreen-aad9, minCD::erm, minJ::tet*	(Feddersen et al. 2020)
BHF038	*divIVA::divIVA-dendra2-aad9; minJ::tet*	This study, pHF07 in RD021
BHF039	*divIVA::divIVA-linker-mNeonGreen-aad9*	This study, pHF15 in 168
BHF040	*divIVA::divIVA-GFP-cat, minCD::aph3-A3*	(Feddersen et al. 2020)

BHF041	*divIVA::divIVA-GFP-cat, minJ::tet*	(Feddersen et al. 2020)
BHF042	*divIVA::divIVA-GFP-cat, minCD::erm, minJ::tet*	(Feddersen et al. 2020)
BHF043	*ftsZ::loxP-erm-loxP-mNG-15aa-FtsZ-loxP-cat-loxP; divIVA::tet*	This study, bAB181 gDNA in 4041
BHF044	*ftsZ::loxP-erm-loxP-mNG-15aa-FtsZ-loxP-cat-loxP*	This study, bAB181 gDNA in 168
BHF045	*ftsZ::loxP-erm-loxP-mNG-15aa-FtsZ-loxP-cat-loxP; minJ::tet*	This study, bAB181 gDNA in RD021
BHF046	*minD::erm*	This study, pHF24 in 168
BHF047	*ftsZ::loxP-erm-loxP-mNG-15aa-FtsZ-loxP-cat-loxP; minD::mCherry2-minD-aad9*	This study, bAB181 gDNA in BHF016
BHF048	*minC::minC4-GFP, sacA::tet; minD::mCherry2-minD-aad9*	This study, pHF12 in EBS499
BHF049	*amyE::Pxyl-mNG-minD(G12V)-cat*	This study, pHF26 in 168
BHF050	*amyE::Pxyl-mNG-minD(G12V)-cat; minD::erm*	This study, pHF26 in BHF046
BHF051	*amyE::Pxyl-mNG-minD(K16A)-cat; minD::erm*	This study, pHF27 in BHF046
BHF052	*amyE::Pxyl-mNG-minD(D40A)-cat*	This study, pHF28 in 168
BHF053	*amyE::Pxyl-mNG-minD(D40A)-cat; minD::erm*	This study, pHF28 in BHF046
BHF055	*minD::aad9-mNeonGreen-minD*	This study, pHF22 in 168
BHF057	*divIVA::divIVA-dronpa-aad9*	(Stockmar et al. 2018)
BHF058	*divIVA::divIVA-mGeosM-aad9*	(Stockmar et al. 2018)
BHF059	*minD::cat-mKate2-minD*	This study, pHF23 in 168
BHF060	*minD::cat-mKate2-minD; amyE:: aad9-Pxyl-minJ-GFP*	This study, pHF23 in MB002
BHF061	*minD::cat-mKate2-minD, divIVA::divIVA-mNeonGreen-aad9*	This study, pHF23 in BHF028
BSG2204	*parB::parB-mNeonGreen-aad9*	(Stockmar et al. 2018)
BSG2205	*parB::parB-mEos3.2-aad9*	(Stockmar et al. 2018)
JB36	*divIVA::divIVA-Dendra2-aad9*	(Feddersen et al. 2020)
JB37	*divIVA::divIVA-pamCherry-aad9*	(Stockmar et al. 2018)
JB38	*minJ::minJ-dendra2-aad9*	(Feddersen et al. 2020)
JB40	*minJ::minJ-mNeonGreen-aad9*	(Feddersen et al. 2020)
RD021	*minJ::tet*	(Bramkamp et al. 2008)
MB002	*amyE:: aad9-Pxyl-minJ-GFP*	(Bramkamp et al. 2008)
SB075	*minCD::erm, minJ::tet*	Laboratory collection
EBS499	*minC4-gfp, sacA::tet*	(Gregory et al. 2008)
bAB181 (PY79)	*ftsZ::loxP-erm-loxP-mNG-15aa-FtsZ-loxP-cat-loxP* in wild type PY79	(Bisson-Filho et al. 2017)
E. coli		
BL21(DE3)pLysS	*F–, ompT, hsdS$_B$ (r_B–, m_B–), dcm, gal, λ(DE3), pLysS, cat*	Thermo Fisher Scientific
NEB Turbo	*F' proA+B+ lacIq ΔlacZM15 / fhuA2 Δ(lac-proAB) glnV galK16 galE15 R(zgb-210::Tn10)TetS endA1 thi-1 Δ(hsdS-mcrB)5*	New England Biolabs
NEB 5-alpha	*fhuA2 Δ(argF-lacZ)U169 phoA glnV44 Φ80 Δ(lacZ)M15 gyrA96 recA1 relA1 endA1 thi-1 hsdR17*	New England Biolabs

4.3. Strain construction

4.3.1. Golden Gate assembly

Golden gate cloning was performed according to the established protocol (Engler et al. 2008; Engler et al. 2009). Fragments for Golden Gate assembly were amplified from *B. subtilis* 168 (*trpC2*) genomic DNA or template plasmids via PCR with the respective primers containing directional overhangs (**Table 4.1**). The vectors pUC18mut and pKill were also amplified via PCR to introduce BsaI restriction sites and allow subsequent digestion of circular PCR template with DpnI, which only cuts methylated DNA. For plasmid construction, *E. coli* NEB5-alpha or NEB Turbo were utilized, which were previously made chemically competent (Green and Rogers 2013). Plasmids were verified via individual control digestion and DNA sequencing. Correct plasmids (see **Table 4.2**) were transformed into *B. subtilis* 168 with the respective genetic background to obtain the described strains (**Table 4.3**) and selected for the introduced resistance. Resistant clones were confirmed with PCR and microscopy. Presence of full-length fluorescent fusions was also confirmed via western blot analysis or in-gel fluorescence.

pHF01 [pUC18mut-minDup-aad9-Dendra2-minD] was created by a Golden Gate assembly of 5 fragments: 1) PCR with primers HF0061 and HF0062 using pUC18mut as template (yielding a linear pUC18mut; 2) PCR with primers HF0037 and HF0038 and 168 genomic DNA (containing the region upstream of *minD*); 3) PCR with primers HF0040 and HF0041 and JB40 genomic DNA (containing the spectinomycin adenyltransferase *aad9*); 4) PCR with primers HF0042 and HF0043 and pDendra2-N plasmid DNA (containing the Dendra2 gene); 5) PCR with primers HF0044 and HF0045 and 168 genomic DNA (containing the N-terminal region of *minD*).

pHF02 [pUC18mut-minDup-aad9-msfGFP-minD] was created by a Golden Gate assembly of 5 fragments: 1) PCR with primers HF0061 and HF0062 using pUC18mut as template (yielding a linear pUC18mut; 2) PCR with primers HF0037 and HF0038 and 168 genomic DNA (containing the region upstream of *minD*); 3) PCR with primers HF0040 and HF0041 and JB40 genomic DNA (containing the spectinomycin adenyltransferase *aad9*); 4) PCR with primers HF0065 and HF0066 and pHJS105 plasmid DNA (containing the msfGFP gene); 5) PCR with primers HF0044 and HF0045 and 168 genomic DNA (containing the N-terminal region of *minD*).

pHF03 [pUC18mut-minJ-msfGFP-aad9-minJdown] was created by a Golden Gate assembly of 5 fragments: 1) PCR with primers HF0061 and HF0062 using pUC18mut as template (yielding a linear pUC18mut; 2) PCR with primers G40 and G41 and 168 genomic DNA (containing the C-terminal region of *minJ*); 3) PCR with primers HF0029 and HF0030 and pHJS105 plasmid DNA (containing the msfGFP gene); 4) PCR with primers G36 and G37 and JB40 genomic DNA

(containing the spectinomycin adenyltransferase *aad9*); 5) PCR with primers G42 and G43 and 168 genomic DNA (containing the region downstream of *minJ*).

pHF04 [pUC18mut-minJ-mNG-aad9-minJdown] was created by a Golden Gate assembly of 5 fragments: 1) PCR with primers HF0061 and HF0062 using pUC18mut as template (yielding a linear pUC18mut; 2) PCR with primers G40 and G41 and 168 genomic DNA (containing the C-terminal region of *minJ*); 3) PCR with primers HF0077 and HF0078 and pNCS-mNeonGreen plasmid DNA (containing the mNeonGreen gene); 4) PCR with primers G36 and G37 and JB40 genomic DNA (containing the spectinomycin adenyltransferase *aad9*); 5) PCR with primers G42 and G43 and 168 genomic DNA (containing the region downstream of *minJ*).

pHF05 [pUC18mut-divIVA-mNG-aad9-divIVAdown] was created by a Golden Gate assembly of 5 fragments: 1) PCR with primers HF0061 and HF0062 using pUC18mut as template (yielding a linear pUC18mut; 2) PCR with primers G34 and G35 and 168 genomic DNA (containing the C-terminal region of *divIVA*); 3) PCR with primers HF0077 and HF0078 and pNCS-mNeonGreen plasmid DNA (containing the mNeonGreen gene); 4) PCR with primers G36 and G37 and JB40 genomic DNA (containing the spectinomycin adenyltransferase *aad9*); 5) PCR with primers G32 and G33 and 168 genomic DNA (containing the region downstream of *divIVA*).

pHF06 [pUC18mut-minJ-Dendra2-aad9-minJdown] was created by a Golden Gate assembly of 5 fragments: 1) PCR with primers HF0061 and HF0062 using pUC18mut as template (yielding a linear pUC18mut; 2) PCR with primers G40 and G41 and 168 genomic DNA (containing the C-terminal region of *minJ*); 3) PCR with primers G20 and G21 and pDendra2-N plasmid DNA (containing the Dendra2 gene); 4) PCR with primers G36 and G37 and JB40 genomic DNA (containing the spectinomycin adenyltransferase *aad9*); 5) PCR with primers G42 and G43 and 168 genomic DNA (containing the region downstream of *minJ*).

pHF07 [pUC18mut-divIVA-Dendra2-aad9-divIVAdown] was created by a Golden Gate assembly of 5 fragments: 1) PCR with primers HF0061 and HF0062 using pUC18mut as template (yielding a linear pUC18mut; 2) PCR with primers G34 and G35 and 168 genomic DNA (containing the C-terminal region of *divIVA*); 3) PCR with primers G20 and G21 and pDendra2-N plasmid DNA (containing the Dendra2 gene); 4) PCR with primers G36 and G37 and JB40 genomic DNA (containing the spectinomycin adenyltransferase *aad9*); 5) PCR with primers G32 and G33 and 168 genomic DNA (containing the region downstream of *divIVA*).

pHF08 [pUC18mut-minD-mNG-aad9-minDdown] was created by a Golden Gate assembly of 5 fragments: 1) PCR with primers HF0061 and HF0062 using pUC18mut as template (yielding a linear pUC18mut); PCR with primers HF0009 and HF0010 and 168 genomic DNA (containing the C-terminal region of *minD*); 3) PCR with primers HF0077 and HF0078 and pNCS-

mNeonGreen DNA (containing the mNeonGreen gene); 4) PCR with primers G36 and G37 and JB40 genomic DNA (containing the spectinomycin adenyltransferase *aad9*); 5) PCR with primers HF0012 and HF0013 and 168 genomic DNA (containing the region downstream of *minD*).

pHF09 [pUC18mut-minJ-SNAP-aad9-minJdown] was created by a Golden Gate assembly of 5 fragments: 1) PCR with primers HF0061 and HF0062 using pUC18mut as template (yielding a linear pUC18mut; 2) PCR with primers G40 and G41 and 168 genomic DNA (containing the C-terminal region of *minJ*); 3) PCR with primers G46 and G47 and pSNAP-tag(T7)-2 (containing the SNAP-tag gene); 4) PCR with primers G36 and G37 and JB40 genomic DNA (containing the spectinomycin adenyltransferase *aad9*); 5) PCR with primers G42 and G43 and 168 genomic DNA (containing the region downstream of *minJ*).

pHF10 [pUC18mut-divIVA-mCherry2-cat-divIVAdown] was created by a Golden Gate assembly of 5 fragments: 1) PCR with primers HF0061 and HF0062 using pUC18mut as template (yielding a linear pUC18mut; 2) PCR with primers G34 and G35 and 168 genomic DNA (containing the C-terminal region of *divIVA*); 3) PCR with primers HF0001 and HF0002 and pmCherry2 plasmid DNA (containing the mCherry2 gene); 4) PCR with primers G5 and G6 and 1803 genomic DNA (containing the chloramphenicol acetyltransferase *cat*); 5) PCR with primers G32 and G33 and 168 genomic DNA (containing the region downstream of *divIVA*).

pHF11 [pUC18mut-minDup_RBS-aad9-dendra2-minD] was created by a Golden Gate assembly of 5 fragments: 1) PCR with primers HF0061 and HF0062 using pUC18mut as template (yielding a linear pUC18mut); 2) PCR with primers HF0037 and HF0039 and 168 genomic DNA (containing the region upstream of *minD* and an extra ribosomal binding site); 3) PCR with primers HF0040 and HF0041 and JB40 genomic DNA (containing the spectinomycin adenyltransferase *aad9*); 4) PCR with primers HF0042 and HF0043 and pDendra2-N plasmid DNA (containing the Dendra2 gene); 5) PCR with primers HF0044 and HF0045 and 168 genomic DNA (containing the N-terminal region of *minD*).

pHF12 [pUC18mut-minDup-aad9-mCherry2-minD] was created by a Golden Gate assembly of 5 fragments: 1) PCR with primers HF0061 and HF0062 using pUC18mut as template (yielding a linear pUC18mut); 2) PCR with primers HF0037 and HF0038 and 168 genomic DNA (containing the region upstream of *minD*); 3) PCR with primers HF0040 and HF0041 and JB40 genomic DNA (containing the spectinomycin adenyltransferase *aad9*); 4) PCR with primers HF0050 and HF0051 and pmCherry2 plasmid DNA (containing the mCherry2 gene); 5) PCR with primers HF0044 and HF0045 and 168 genomic DNA (containing the N-terminal region of *minD*).

pHF13 [pUC18mut-divIVA_linker-dendra2-cat-divIVAdown] was created by a Golden Gate assembly of 5 fragments: 1) PCR with primers HF0061 and HF0062 using pUC18mut as template

(yielding a linear pUC18mut; 2) PCR with primers HF0071 and HF0072 and 168 genomic DNA (containing the C-terminal region of *divIVA* and a 15AA linker); 3) PCR with primers G20 and G21 and pDendra2-N plasmid DNA (containing the Dendra2 gene); 4) PCR with primers G5 and G6 and 1803 genomic DNA (containing the chloramphenicol acetyltransferase *cat*); 5) PCR with primers G32 and G33 and 168 genomic DNA (containing the region downstream of *divIVA*).

pHF14 [pUC18mut-divIVA_linker-mCherry2-cat-divIVAdown] was created by a Golden Gate assembly of 5 fragments: 1) PCR with primers HF0061 and HF0062 using pUC18mut as template (yielding a linear pUC18mut; 2) PCR with primers HF0071 and HF0072 and 168 genomic DNA (containing the C-terminal region of *divIVA* and a 15AA linker); 3) PCR with primers HF0001 and HF0002 and pmCherry2 plasmid DNA (containing the mCherry2 gene); 4) PCR with primers G5 and G6 and 1803 genomic DNA (containing the chloramphenicol acetyltransferase *cat*); 5) PCR with primers G32 and G33 and 168 genomic DNA (containing the region downstream of *divIVA*).

pHF15 [pUC18mut-divIVA_linker-mNeonGreen-aad9-divIVAdown] was created by a Golden Gate assembly of 5 fragments: 1) PCR with primers HF0061 and HF0062 using pUC18mut as template (yielding a linear pUC18mut; 2) PCR with primers HF0071 and HF0072 and 168 genomic DNA (containing the C-terminal region of *divIVA* and a 15AA linker); 3) PCR with primers HF0077 and HF0078 and pNCS-mNeonGreen DNA (containing the mNeonGreen gene); 4) PCR with primers G36 and G37 and JB40 genomic DNA (containing the spectinomycin adenyltransferase *aad9*); 5) PCR with primers G32 and G33 and 168 genomic DNA (containing the region downstream of *divIVA*).

pHF16 [pKill-minJ-PSmOrange2-aad9-minJdown] was created by a Golden Gate assembly of 5 fragments: 1) PCR with primers HF0063 and HF0064 using pKill as template (yielding a linear pKill); 2) PCR with primers G40 and G41 and 168 genomic DNA (containing the C-terminal region of *minJ*); 3) PCR with primers HF0077 and HF0078 and pNCS-mNeonGreen DNA (containing the mNeonGreen gene); 4) PCR with primers G36 and G37 and JB40 genomic DNA (containing the spectinomycin adenyltransferase *aad9*); 5) PCR with primers G42 and G43 and 168 genomic DNA (containing the region downstream of *minJ*).

pHF17 [pKill-minDup-aad9-dendra2-minD(G12V)-minDdown] was created by a Golden Gate assembly of 6 fragments: 1) PCR with primers HF0063 and HF0064 using pKill as template (yielding a linear pKill); 2) PCR with primers HF0037 and HF0038 and 168 genomic DNA (containing the region upstream of *minD*); 3) PCR with primers HF0040 and HF0041 and JB40 genomic DNA (containing the spectinomycin adenyltransferase *aad9*); 4) PCR with primers HF0042 and HF0043 and pDendra2-N plasmid DNA (containing the Dendra2 gene); 5) PCR with primers HF0044 and HF0058 and 168 genomic DNA (containing the full-length gene *minD*); 6)

PCR with primers HF0059 and HF0060 and 168 genomic DNA (containing the region downstream of *minD*); To introduce the G12V mutation, an established site-directed mutagenesis protocol was applied after completion of the plasmid (Zheng et al. 2004), using primers HF0054 and HF0055.

pHF18 [pKill-minDup-aad9-dendra2-minD(K16A)-minDdown] was created by a Golden Gate assembly of 6 fragments: 1) PCR with primers HF0063 and HF0064 using pKill as template (yielding a linear pKill); 2) PCR with primers HF0037 and HF0038 and 168 genomic DNA (containing the region upstream of *minD*); 3) PCR with primers HF0040 and HF0041 and JB40 genomic DNA (containing the spectinomycin adenyltransferase *aad9*); 4) PCR with primers HF0042 and HF0043 and pDendra2-N plasmid DNA (containing the Dendra2 gene); 5) PCR with primers HF0044 and HF0058 and 168 genomic DNA (containing the full-length gene *minD*); 6) PCR with primers HF0059 and HF0060 and 168 genomic DNA (containing the region downstream of *minD*). To introduce the K16A mutation, an established site-directed mutagenesis protocol was applied after completion of the plasmid (Zheng et al. 2004), using primers HF0056 and HF0057.

pHF19 [pKill-minDup-aad9-dendra2-minD(D40A)-minDdown] was created by a Golden Gate assembly of 6 fragments: 1) PCR with primers HF0063 and HF0064 using pKill as template (yielding a linear pKill; 2) PCR with primers HF0037 and HF0038 and 168 genomic DNA (containing the region upstream of *minD*); 3) PCR with primers HF0040 and HF0041 and JB40 genomic DNA (containing the spectinomycin adenyltransferase *aad9*); 4) PCR with primers HF0042 and HF0043 and pDendra2-N plasmid DNA (containing the Dendra2 gene); 5) PCR with primers HF0044 and HF0058 and pMinD-D40A plasmid DNA (containing the full-length and mutated gene *minD* (D40A)); 6) PCR with primers HF0059 and HF0060 and 168 genomic DNA (containing the region downstream of *minD*).

pHF20 [pKill-sepF-PAmCherry-cat-sepFdown] was created by a Golden Gate assembly of 5 fragments: 1) PCR with primers HF0063 and HF0064 using pKill as template (yielding a linear pKill; 2) PCR with primers HF0083 and HF0084 and 168 genomic DNA (containing the C-terminal region of *sepF*); 3) PCR with primers G26 and G27 and JB37 genomic DNA (containing the PAmCherry gene); 4) PCR with primers G5 and G6 and 1803 genomic DNA (containing the chloramphenicol acetyltransferase *cat*); 5) PCR with primers HF0085 and HF0086 and 168 genomic DNA (containing the region downstream of *sepF*).

pHF21 [pKill-zapAup-cat-PAmCherry2-zapA] was created by a Golden Gate assembly of 5 fragments: 1) PCR with primers HF0063 and HF0064 using pKill as template (yielding a linear pKill; 2) PCR with primers HF0089 and HF0090 and 168 genomic DNA (containing the region upstream of *zapA*); 3) PCR with primers HF0093 and HF0094 and 1803 genomic DNA

(containing the chloramphenicol acetyltransferase *cat*); 4) PCR with primers HF0091 and HF0092 and JB37 genomic DNA (containing the PAmCherry gene); 5) PCR with primers HF0087 and HF0088 and 168 genomic DNA (containing the N-terminal region of *zapA*).

pHF22 [pKill-minDup-aad9-mNG-minD] was created by a Golden Gate assembly of 5 fragments: 1) PCR with primers HF0063 and HF0064 using pKill as template (yielding a linear pKill; 2) PCR with primers HF0037 and HF0038 and 168 genomic DNA (containing the region upstream of *minD*); 3) PCR with primers HF0040 and HF0041 and JB40 genomic DNA (containing the spectinomycin adenyltransferase *aad9*); 4) PCR with primers HF0091 and HF0092 and pNCS-mNeonGreen plasmid DNA (containing the mNeonGreen gene); 5) PCR with primers HF0044 and HF0045 and 168 genomic DNA (containing the N-terminal region of *minD*).

pHF23 [pKill-minDup-cat-mKate2-minD] was created by a Golden Gate assembly of 5 fragments: 1) PCR with primers HF0063 and HF0064 using pKill as template (yielding a linear pKill; 2) PCR with primers HF0037 and HF0038 and 168 genomic DNA (containing the region upstream of *minD*); 3) PCR with primers HF0093 and HF0094 and 1803 genomic DNA (containing the chloramphenicol acetyltransferase *cat*); 4) PCR with primers HF0197 and HF0198 and pmKate2 plasmid DNA (containing the mKate2 gene); 5) PCR with primers HF0044 and HF0045 and 168 genomic DNA (containing the N-terminal region of *minD*).

pHF24 [pKill-minDup-erm-minDdown] was created by a Golden Gate assembly of 4 fragments: 1) PCR with primers HF0063 and HF0064 using pKill as template (yielding a linear pKill; 2) PCR with primers HF0037 and HF0038 and 168 genomic DNA (containing the region upstream of *minD*); 3) PCR with primers HF0073 and HF0074 and SB075 genomic DNA (containing the erythromycin resistance gene); 4) PCR with primers HF0075 and HF0076 and 168 genomic DNA (containing the region downstream of *minD*).

4.3.2. Classical cloning

Fragments for classical cloning were amplified from *B. subtilis* 168 (*trpC2*) genomic DNA or template plasmids via PCR with the respective primers containing the respective directional restriction sites for pJPR1 insertion (**Table 4.1**). Next, the fragments and pJPR1 were digested with the respective enzymes and ligated. Plasmid construction was verified via individual control digestion and DNA sequencing. Correct plasmids (see **Table 4.2**) were transformed into *B. subtilis* 168 with the respective genetic background to obtain the described strains (**Table 4.3**) and selected for the introduced resistance. Resistant candidates were confirmed with PCR and

microscopy. Presence of full-length fluorescent fusions was also confirmed via western blot analysis or in-gel fluorescence.

For construction of pHF25 [pJPR1-SNAP], primers HF0027 and HF0028 were used to amplify the SNAP-tag from pSNAP-tag(T7)-2 plasmid DNA. The PCR product and pJPR1 were digested with SalI/BamHI and subsequently ligated.

For construction of pHF26, pHF27 and pHF28 [pJPR1-mNeonGreen-minD(G12V), minD(K16A) and minD(D40A), respectively], primers HF0177 and HF0178 were used to amplify mNeonGreen from pNCSmNeonGreen plasmid DNA and digested with HindIII/SpeI, while the mutated variants of *minD* were amplified with primers HF0181 and HF0182 from either pHF17, pHF18 or pHF19, respectively, and subsequently digested with SpeI/NotI, while pJPR1 was digested with HindIII/NotI. Finally, the products were ligated.

4.4. Media and growth conditions

E. coli cells were grown in LB (lysogeny broth) [10 g l^{-1} tryptone, 10 g l^{-1} NaCl and 5 g l^{-1} yeast extract] at 37°C (Bertani 1951), supplied with 100 µg ml^{-1} carbenicillin or ampicillin when appropriate. When plated, *E. coli* cells were grown on LB supplied with 1.5% agar.

B. subtilis was grown on nutrient agar plates using commercial nutrient broth (Oxoid/Thermo-Fischer) and 1.5% (w/v) agar at 37°C overnight. To reduce inhibitory effects, antibiotics were only used for transformations or experiments when indicated, since allelic replacement is stable after integration (chloramphenicol 5 µg ml^{-1}, tetracycline 10 µg ml^{-1}, kanamycin 5 µg ml^{-1}, spectinomycin 100 µg ml^{-1}, erythromycin 1 µg ml^{-1}).

For growth curves, *B. subtilis* was inoculated to an OD_{600} 0.05 from a fresh overnight culture and grown in LB at 37°C with aeration in baffled shaking flasks (200 rpm) to OD_{600} 1. Subsequently, cultures were diluted to OD_{600} 0.1 in fresh LB and measured every hour for at least 6 hours.

For microscopy, *B. subtilis* was inoculated to an OD_{600} 0.05 from a fresh overnight culture and grown in MD medium - a modified version of Spizizen Minimal Medium (Anagnostopoulos and Spizizen 1961) – at 37°C with aeration in baffled shaking flasks (200 rpm) to OD_{600} 1. MD medium contains 10.7 mg ml^{-1} K_2HPO_4, 6 mg ml^{-1} KH_2PO_4, 1 mg ml^{-1} Na_3 citrate, 20 mg ml^{-1} glucose, 20 mg ml^{-1} L-tryptophan, 20 mg ml^{-1} ferric ammonium citrate, 25 mg ml^{-1} L-aspartate and 0.36 mg ml^{-1} $MgSO_4$ and was always supplemented with 1 mg ml^{-1} casamino acids. Subsequently, cultures were diluted to OD_{600} 0.1 in fresh MD medium and grown to OD_{600} 0.3-0.5 (exponential

phase). In PALM experiments described in chapter 2.3, minimal SMG medium was used [15 mM $(NH_4)_2SO_4$, 61 mM K_2HPO_4, 44 mM KH_2PO_4, 3.4 mM sodium citrate $2xH_2O$, 1.7 mM $MgSO_4$, 5.9 mM glutamate and 27 mM glucose] instead of MD medium, and cells were grown to a final OD of ~0.15.

For epifluorescence and time-lapse imaging (e.g. FRAP), *B. subtilis* cells were mounted on pre-warmed 1.5% MD agarose pads, sealed with paraffin and incubated 10 min at 37°C before microscopic analysis. When used, FM4-64 dye was added to the agarose pad before polymerization (1 µM final).

4.5. Molecular biological methods

4.5.1. DNA extraction from *E. coli* and *B. subtilis* cells

Plasmid extraction from *E. coli* was carried out utilizing a NucleoSpin™ Plasmid kit (Macherey-Nagel) according to the supplied protocol. Genomic DNA from *B. subtilis* for cloning or transformation was extracted according to (Ward and Zahler 1973). Briefly, cells were grown to late exponential phase, resuspended in saline-citrate solution and lysed with the addition of lysozyme. After lysis (20 to 30 minutes at 37°C, rocking), 3 M - 4 M NaCl was added, and the lysate was filtered through a sterile Millipore membrane filter (0.45 µm pore size).

4.5.2. DNA amplification

Polymerase chain reactions were carried out using Phusion high fidelity polymerase (NEB) or ReproFast Polymerase (Genaxxon Bioscience) according to the respective manufacturer's protocol.

4.5.3. Separation and purification of nucleic acids

Agarose gel electrophoresis was used to separate and purify PCR products, plasmids or (restriction) fragments. To this end, 1% (w/v) agarose gels were run in TAE buffer [40 mM Tris-HCl pH 8, 1 mM EDTA, 20 mM acetic acid] for 20 – 40 min at 110 V. When required, nucleic acids were extracted and purified using a NucleoSpin (Macherey-Nagel) "Gel and PCR Clean" kit, according to the manufacturer's instructions.

4.5.4. Quantification and sequencing of nucleic acids

Concentrations of nucleic acids were determined using a UV/VIS spectrophotometer (BioDrop µLite, Serva), while sequencing was performed by the in-house sequencing service (Genomics service unit, Genetics, Faculty of Biology, LMU). Submitted samples contained approximately 50 ng of DNA fragment or 150-300 ng of plasmid DNA and the respective sequencing primer, stored in 10 mM Tris-HCL buffer.

4.5.5. Enzymatic modification of nucleic acids

Restriction digests were performed according to the manufacturer's protocols (NEB and Thermo Fisher Scientific), using a total reaction volume of 50 µl.

4.5.6. Transformation of *E. coli* and *B. subtilis* cells

For transformation of *E. coli* cells (NEB Turbo or NEB5-alpha) with plasmid DNA, chemically competent cells were thawed on ice. Next, 0.5 - 5 µl of plasmid DNA was added to 50 µl of cells and incubated for 30 min on ice. Cells were then subjected to a heat-shock (42 °C, 30 s), followed by another 5 min on ice. Subsequently, 800 µl of room-temperature SOC medium [20 g l^{-1} tryptone (2% w/v), 5g l^{-1} yeast extract (0.5% w/v), 0.5 g l^{-1} NaCl (8.56 mM), 0.186 g l^{-1} KCl (2.5 mM), 2.033 g $MgCl_2$ (hexahydrate, 10 mM), 2.465 g l^{-1} $MgSO_4$ (heptahydrate, 10 mM) and 3.603 g l^{-1} glucose (20 mM)] was added and the cells were grown at 37°C while shaking for 1 h. Cells were then plated on LB plates containing the appropriate antibiotic and incubated at 37°C overnight.

For transformation of *B. subtilis* cells with Plasmid or genomic DNA, cells were plated on NA plates and incubated at 37°C overnight. In the morning, cells were inoculated into 10 ml fresh MD medium supplemented with 50 µl of 20% (w/v) casamino acids and incubated at 37°C shaking in 100 ml baffled flasks for 4-5 h until an OD_{600} of 1-1.5 was reached. The cells were then diluted with 10 ml of pre-warmed MD medium without casamino acids and incubated for 1 h at 37°C shaking. Subsequently, 800 µl of cells were transferred to 10 ml pre-warmed plastic tubes and DNA was added to a final concentration of 1 µg ml^{-1}. After 20 min incubation at 37°C shaking, 25 µl of 20% (w/v) casamino acids were added to each transformation tube, followed by 1 h incubation at 37°C, shaking. Finally, cells were plated on NA plates with the appropriate antibiotic and incubated at 37°C overnight.

4.6. Microscopy

4.6.1. Fluorescence microscopy

For strain characterization, microscopy images were taken on a Zeiss Axio Observer Z1 microscope equipped with a Hamamatsu OrcaR² camera using a Plan-Apochromat 100×/1.4 Oil Ph3 objective (Zeiss). Fluorophores emitting green light were visualized with filterset 38 HE eGFP shift free (Zeiss), while red emitting fluorophores and FM4-64 membrane dye were visualized with filterset 63 HE mCherry (Zeiss). The microscope was equipped with an environmental chamber set to 37°C. Digital images were acquired with the Zen software (Zeiss) and analyzed with Fiji (ImageJ2) (Schindelin et al. 2012; Rueden et al. 2017). Furthermore, several figures were prepared using the Fiji plugin ScientiFig (Aigouy and Mirouse 2013).

For FRAP and photoconversion experiments, a Delta Vision Elite (GE Healthcare, Applied Precision) equipped with an Insight SSI™ illumination, an X4 laser module and a CoolSnap HQ2 CCD camera was used. Images were taken with a 100×oil PSF U-Plan S-Apo 1.4 NA objective. A four color standard set InsightSSI unit with following excitation wavelengths (DAPI 390/18 nm FITC 475/28 nm, TRITC 542/27 nm, Cy5 632/22 nm); single band pass emission wavelengths (DAPI 435/48 nm, FITC 525/48 nm, TRITC 597/45 nm, Cy5 679/34 nm) and a suitable polychroic for DAPI/FITC/TRITC/Cy5 were used. For FRAP, GFP, msfGFP and mNeonGreen were visualized using FITC settings and exposure times between 0.1 s (msfGFP, GFP) and 0.2 s (mNeonGreen). Bleaching was performed using a 488 nm laser (50 mW) with 10% power and a 0.005 – 0.01 s pulse. Frequency of acquisition and total amount of images for FRAP were chosen according to the individual recovery times after initial testing with various settings.

For Dendra2 photoconversion experiments, previously converted protein was bleached by imaging with FITC settings for 1-2 s. Subsequently, local photoconversion of Dendra2 was performed using a 405 nm laser (100 mW) with 10% power and a 0.005 s pulse. Converted Dendra2 was visualized every 30s for 10 min using TRITC settings and exposure times of 0.2s. Analysis of images and the kymograph were done in Fiji (ImageJ2) (Schindelin et al. 2012; Rueden et al. 2017).

4.6.1.1. FRAP analysis

Analysis of the images was performed using Fiji (ImageJ2) (Schindelin et al. 2012; Rueden et al. 2017). The corrected total cell fluorescence (CTCF) was calculated according to following formula: CTCF = Integrated Density—(Area of selected cell * Mean fluorescence of unspecific background readings) (Gavet and Pines 2010). For FRAP experiments unspecific background

was subtracted for every ROI (see above). The CTCF of the septa was divided by the CTCF of the whole cell to account for photobleaching during acquisition. The respective quotient of the unbleached spot was always set as 1 for normalization. Since *B. subtilis* keeps growing during time-lapse experiments like FRAP, the bleached spot moves in the field of view as cells elongate. Therefore, a macro in Fiji was created to dynamically follow and center the bleached spot through the frames of acquisition without any bias, which resulted in more precise FRAP curves. To determine half-time recovery and mobile/immobile fractions, the FRAP curve from the normalized recovery values was fitted to an exponential equation:

$$I(t) = A(1 - e^{-\tau t}) \qquad \textbf{Eq. 4.1}$$

where $I(t)$ is the normalized FRAP curve, A the final value of the recovery, τ the fitted parameter and t the time after the bleaching event. After determination of the fitted coefficients, they can be used to determine mobile (A) and immobile (1-A) fractions, while following equation was used to determine halftime recovery:

$$t_{half} = \frac{\ln 0.5}{-\tau} \qquad \textbf{Eq. 4.2}$$

where t_{half} is the halftime recovery and τ the fitted parameter. Diffusion coefficients were then calculated with the following formula:

$$D = (w^2/4\tau_{1/2}) * 0.88 \qquad \textbf{Eq. 4.3}$$

according to (Axelrod et al. 1976) – where D is the diffusion coefficient, w is the radius of the circular laser beam and $\tau_{1/2}$ is the time when fluorescence recovery reaches half height of total recovery. To estimate the bleaching spot radius, cells expressing cytosolic GFP were fixed with 1.5% formaldehyde (v/v) as described above, mounted on agarose pads, bleached at laser powers of 10% to 100% in increments of 10% and imaged right after bleaching. The radius was measured in ImageJ and averaged per triplicate to calculate the function of bleach radius over laser power. Graphs and statistics (Kruskal–Wallis) were created and analyzed in R 3.3.1 (Team 2017) utilizing the packages ggplot2 (Wickham 2009) and nlstools (Baty et al. 2015).

4.6.2. Photoactivated localization microscopy (PALM)

4.6.2.1. Sample preparation

For structural PALM imaging of fixed cells, a 0.5 ml portion of *B. subtilis* cells were fixed by addition of formaldehyde (1.5% (w/v) final concentration when not indicated differently) and incubated for 20 min at 37°C. Subsequently, cells were washed (1 min, 5000 rpm), resuspended in fresh MD supplemented with 10 – 15 mM glycine to stop the crosslinking reaction and incubated for 10 min at 37°C. Then, cells were washed two more times with MD containing 10mM glycine. In a final washing step, the pellet was resuspended in 50 µl of MD with 10 mM glycine to reach higher cell density. Cells were mounted on chambered coverslips (µ-slide 8 well, Ibidi) containing 200 µl MD with 10 mM glycine, which were pretreated for 30-60 min with 0.1% Poly-L-lysine and successively washed 3 times with MD containing 10 mM glycine. Furthermore, TetraSpeck microspheres (100 nm, ThermoFisher) were added in a dilution that results in about 3-10 beads per field of view. To help sedimentation of cells and beads and to reach a uniform attachment to the glass surface, the chambered coverslip was centrifuged at 4000 rpm for 10 min in a bucket-swing rotor (Eppendorf).

For optimization of mNeonGreen PALM imaging (chapter 2.3), minimal SMG medium instead of MD medium was used for the above described procedure.

For SPT experiments, microscope slides and coverslips were specifically cleaned to avoid dirt or durst particles causing background in experiments. To this end, they were first sonicated for 20 min in 2% (v/v) Hellmanex III solution (Hellma), which was rinsed off with Milli-Q purified (MQ) water. This was followed by 5 min sonication in fresh MQ water. Next, slides and coverslips were sonicated in acetone for 15 min and subsequently rinsed twice with MQ water, followed by another 20 min sonication in 1M KOH. Finally, slides and coverslips were rinsed twice with MQ water and dried on filter paper in a desiccator.

To prepare SPT samples, gene-frames (Thermo Fisher Scientific, AB0577) were placed on the clean slides. Next, 1.5% (w/v) agarose was molten in pre-filtered MD medium, carefully pipetted into the gene-frame well and covered with another cleaned slide to solidify with a flat surface, for around 10 minutes. Previously prepared slides were not used when older than 2 h. Slides were pre-warmed for 10 minutes at 37°C before mounting 1-3 µl of cells, subsequently covered with a cleaned coverslip. The final samples were used for a maximum of 30 min except when testing cell viability, to ensure reproducibility.

4.6.2.2. Imaging conditions and individual optimization

PALM imaging was performed with the microscope system ELYRA P.1 (Zeiss) and the accompanied Zen software. It is equipped with a 405 nm Diode-Laser (50 mW), a 488 nm laser (200 mW), a 561 nm laser (200 mW) and a 640 nm laser (150 mW). Furthermore, an alpha Plan-Apochromat 100x/1,46 Oil DIC M27 objective (Zeiss) was used, in combination with a 1.6x Optovar. The filter sets were the following: a 77 HE GFP+mRFP+Alexa 633 shift free (EX TBP 483+564+642, BS TFT 506+582+659, EM TBP 526+601+688), a 49 DAPI shift free (EX G 365, BS FT 395, EM BP 445/50), a BP 420-480 / LP 750, a BP 495-550 / LP 750, a LP 570 and a LP 655 filter set. Images were recorded with the Andor EM-CCD camera iXon DU 897, resulting in an effective pixel size of 100 nm. If not indicated differently, samples expressing mNeonGreen were illuminated with the 488 nm laser at ~7.4 mW. Samples expressing Dendra2 or PAmCherry were illuminated with the excitation laser (561 nm, ~5.3 mW) and activation laser (405 nm). The laser intensities were thereby optimized for each fluorophore as described in chapter 2.3.1. To avoid co-occurrence of multiple events in the same spot, the power of the activation laser was increased stepwise from 0.008 mW to 1.6 mW. DivIVA-Dronpa, DivIVA-mNeonGreen and MinJ-mNeonGreen were illuminated in pseudo-TIRF (total internal reflection fluorescence) mode and recorded at 20 Hz with 200 – 250 camera gain, while Dendra2-MinD and DivIVA-PAmCherry were imaged with the same camera settings in regular wide-field mode.

For acquisition of SPT data, imaging conditions were optimized first, described in detail in chapter 2.2.2. Final images of Dendra2-MinD and DivIVA-PAmCherry were acquired at 15 ms frame length for 5000 frames, ~4 and ~400 W cm^{-2} laser intensities for the 405 and 561 nm lasers, respectively and 250 EM Gain, in a field of view of 12.8 μm^2.

4.6.2.3. Data analysis

Analysis of structural PALM was performed in the Zen Black (Zeiss) software, Fiji (ImageJ2) (Schindelin et al. 2012; Rueden et al. 2017) and R 3.3.1 (Team 2017) . Detection of single emitters was performed with a peak mask size of 9 pixels and a minimum peak intensity to noise ratio of 6.0., except for optimization of mNeonGreen, where a ratio of 7.0 was used. Localization was extrapolated via a 2D Gaussian fitting, and images were drift corrected utilizing a fiducial-based mode with at least three beads in focus. Filtering was used to minimize noise, background, out of focus emitters and to exclude beads from the evaluation, according to **Table 4.4**, except when described otherwise (see chapter 2.3.3). DivIVA-mNeonGreen analysis with a multi Gaussian fit was performed using the ThunderSTORM software (Ovesny et al. 2014), with Camera settings according to our system (pixel size 100 nm, 2.78 electrons per A/D count, 100 base level of A/D

counts, EM gain 230). Fitting was performed with standard settings, except for the fitting method (maximum likelihood) and the enabled multi-emitter fitting analysis, which was performed with a maximum of 5 molecules per fitting region, a model selection threshold p-value of 1.0E-6 and a limited intensity range for photos of 50 to 500.

Table 4.4: Filter parameters for PALM imaging of the different strains.

Filters were chosen according to the fluorophore behavior in PALM to eliminate background and signal of fluorescent beads from the results.

Strain/FP	Filter: PSF width [nm]	Filter: Photon Number
Dendra2-MinD	70 - 160	70 – 250
MinJ-mNeonGreen	70 - 160	70 – 300
DivIVA-PAmCherry	60 - 170	50 – 500

Cluster analysis was performed in R 3.3.1 (Team 2017) utilizing the DBSCAN package (Ester 1996; Hahsler et al. 2019) including OPTICS (Ankerst et al. 1999). Clusters were determined by applying the OPTICS algorithm to the respective molecule tables generated via PALM. The minimal number of points that define a cluster (*minPts*) was defined as 10, reflecting apparent clusters seen in rendered PALM imaging, and a minimum distance between cluster edge points (*epsCl*) of 20 and 30 nm for MinD and DivIVA, respectively, according to the observed density of protein localization, which was analyzed via the OPTICS reachability plot.

SPT raw data was first analyzed using TrackMate 3.8.0 (Tinevez et al. 2017) to reconstruct molecule trajectories. To this end, a python script was programmed to automate trajectory reconstruction with previously optimized settings and automated filters. For spot detection, TrackMate was configured to use the LoG detector and an estimated diameter of 0.5 microns, a threshold of 200 with sub-pixel localization and no median filter. For tracking, the integrated "Simple LAP tracker" was chosen, with a linking max distance of 500 nm and no frame gaps allowed, while the minimum track length was set to 5.

For analysis of data created through TrackMate, the Matlab (The MathWorks, Inc) plugin SMTracker (Rosch et al. 2018b) was used, which also requires the use of Oufti (Paintdakhi et al. 2016), where cell outlines for every field of view were manually created. Analysis was then performed in SMTracker according to the instructions and as described in chapter 2.2.4.

The on-switching rate for Dronpa was measured as described earlier (Wang et al. 2014). Briefly, we started to acquire data on the DivIVA-Dronpa expressing strain in absence of the activation laser (405 nm) and in presence of imaging light (488 nm). Then, data acquisition was continued with simultaneous illumination of activation and imaging light until completion. The slope

obtained from the total number of activation events accumulated in a period of time without activation light divided by the total number of activation events represents the on-switching rate. The off-switching rate was obtained from the inverse of the mean lifetime of the on-state (**Fig. 2.19 b** and **Table 2.4**).

4.7. Mathematical modelling of the Min system

This chapter (4.7) about the details and methods of the mathematic model and simulations of the *B. subtilis* Min system was created by Laeschkir Würthner and Erwin Frey (Arnold Sommerfeld center for theoretical physics, LMU Munich). Details can be found in our preprint (Feddersen et al. 2020).

4.7.1. Reaction-diffusion equations

The setup of the mathematical model is based on previous approaches for intracellular protein dynamics (Halatek and Frey 2012; Thalmeier et al. 2016; Wu et al. 2016; Denk et al. 2018). Specifically, we present a minimal model to account for DivIVA mediated MinD localization. The model includes the following set of biochemical reactions: *(i)* attachment of MinD-ATP (with volume concentration u_{DT}) from the bulk to the membrane with constant rate k_D; *(ii)* recruitment of bulk MinD-ATP to the membrane by membrane-bound MinD (with areal concentration u_d) with rate k_{dD}; *(iii)* hydrolysis and detachment of membrane-bound MinD into bulk MinD-ADP (u_{DD}) with rate k_H; *(iv)* reactivation of bulk MinD-ADP by nucleotide exchange to MinD-ATP with rate λ. The system of ensuing reaction-diffusion equations reads

$$\partial_t u_{DD} = D_D \nabla_c^2 u_{DD} - \lambda u_{DD} \qquad \textbf{Eq. 4.4}$$

$$\partial_t u_{DT} = D_D \nabla_c^2 u_{DT} - \lambda u_{DD} \qquad \textbf{Eq. 4.5}$$

$$\partial_t u_d = D_d \nabla_m^2 u_d + (k_D + k_{dD} u_d) u_{DT} - k_H u_d \qquad \textbf{Eq. 4.6}$$

where the subscript c or m denotes that the nabla operator acts in the bulk or on the membrane, respectively. These equations are coupled through nonlinear reactive boundary conditions at the membrane surface stating that the biochemical reactions involving both membrane-bound and bulk proteins equal the diffusive flux onto and off the membrane:

$$D_D \nabla_n u_{DD}|_m = k_H u_d \qquad \textbf{Eq. 4.7}$$

$$D_D \nabla_n u_{DT}|_m = -(k_D + k_{dD} u_d) u_{DT} \qquad \text{Eq. 4.8}$$

Here, the subscript n denotes that we take the nabla operator acting along the outward normal vector of the boundary (membrane). The set of reaction-diffusion equations conserve the total mass of MinD. Hence, the total particle number N_D of MinD obeys the relation

$$N_D = \int_\Omega (u_{DD} + u_{DT})\, dV + \int_{\partial\Omega} u_d dS \qquad \text{Eq. 4.9}$$

We simulated the set of reaction-diffusion equations in a spherocylindrical geometry in three-dimensional space (3D) using the Finite-Element software *COMSOL Multiphysics v5.4*; for an illustration of the geometry used see **Fig. 4.1**. The length and height were set to typical values known for *B. subtilis* cells, $L = 2.8\,\mu m$ and $h = 0.85\,\mu m$, respectively. The mean total density of MinD was set to $[MinD] = 2450\,\mu m^{-3}$ for all simulations (see **Table 4.5**). We assume that, in addition to MinD self-recruitment, MinJ recruits MinD-ATP from the bulk to the membrane and that membrane-bound MinD is stabilized by DivIVA-MinJ complexes on the membrane. We model the interaction of MinD with MinJ and DivIVA implicitly through space-dependent recruitment and detachment rates.

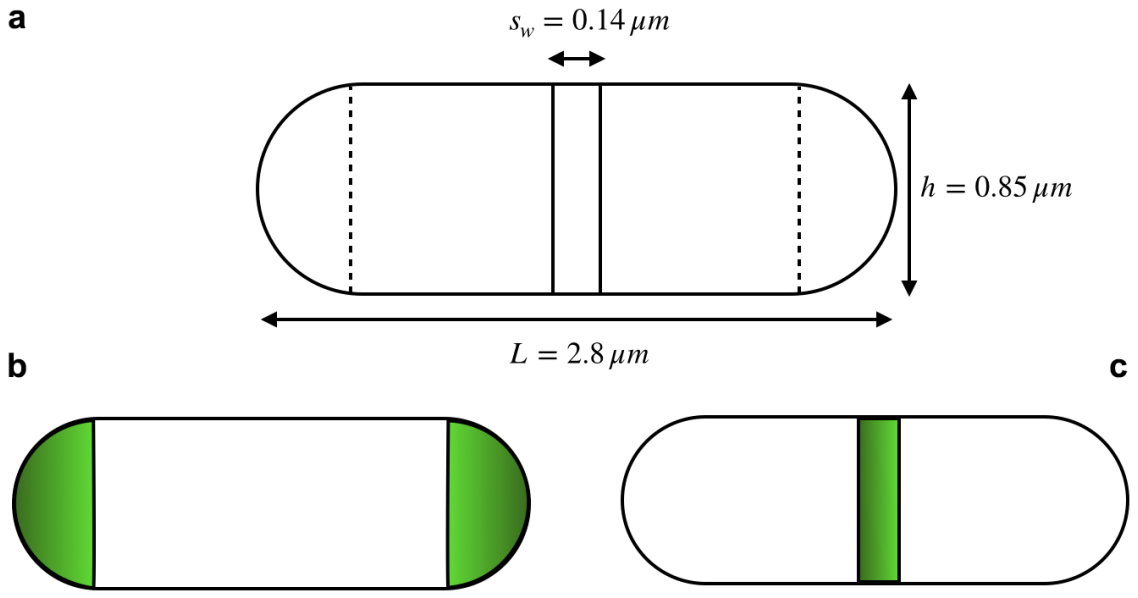

Fig. 4.1: Sketch of *B. subtilis* cell for geometric model of Min system simulations.

(a) Sketch of simulation geometry (spherocylinder) with indicated sizes for septum width (S_w), cell width/height (h) and cell length (L). **(b)** Polar localization was achieved by setting $\alpha = 4$ and $\beta = 3$ at the poles (green area), and $\alpha = \beta = 1$ for the remaining part of the geometry. **(c)** Localization at the septum is achieved by setting $\alpha = 4$ and $\beta = 3$ in a narrow region at mid cell (green) and else $\alpha = \beta = 1$. α = Recruitment rate amplification factor, β = Hydrolysis rate reduction factor, see **Table 4.5**.

To this end, we assume that the recruitment rate is amplified by a factor α and that the detachment rate is reduced by a factor β at regions of high negative curvature (such as the poles or the septum). This assumption is motivated by experiments, which suggest that MinD localization is dependent on MinJ and that DivIVA acts as a scaffold, which stabilizes MinJ and MinD (see results part 2.1.4.2). We therefore set the recruitment and detachment rates to $\tilde{k}_{dD} = \alpha \cdot k_{dD}$ and $\tilde{k}_H = k_H/\beta$, respectively, at regions of high negative curvature (**Fig. 4.1**), where α and β denotes dimensionless amplification and reduction prefactors, respectively. The parameters k_{dD} and k_H denotes the uniform recruitment and hydrolysis rate which one would obtain if interactions between MinD and MinJ-DivIVA complexes are neglected, i.e. if $\alpha = \beta = 1$ (see **Fig. 4.1**).

4.7.2. Simulation of the model

4.7.2.1. Polar localization

In a cell with no pre-existing division apparatus, the Min system localizes at the poles of the bacteria. We modeled this case by setting $\alpha = 4$ and $\beta = 3$ at the polar caps, and $\alpha = \beta = 1$ for the remaining part of the rod-shaped geometry (see **Fig. 4.1 b**). The uniform rates were set to $k_{dD} = 0.04\ \mu m^2\ s^{-1}$ and $k_{dD} = 0.1\ \mu m^2\ s^{-1}$ as given in the results (2.1.4.2). Simulations show that MinD can be pinned to the cell poles for non-uniform kinetic parameters (**Fig. 2.10 c** left).

4.7.2.2. Depletion of MinD at the poles

Next, we tested if the polar distribution of MinD decays to a homogeneous protein distribution along the membrane when the rates are uniform over the whole cell body. To this end, we used the steady state polar distribution of MinD (as obtained above) as initial condition for a simulation with uniform rates in the entire geometry, i.e. $\alpha = 1, \beta = 1$, respectively. We find that for uniform rates MinD proteins preferentially localize near cell center (**Fig. 2.10 c** left to right). The reason for this unexpected inhomogeneous protein distribution is an interplay between reactions, diffusion and cell geometry. In short, this effect can be explained as follows: MinD detaches from the membrane in an inactive MinD-ADP state and can therefore not rebind to the membrane until it exchanges its nucleotide to switch to an active state MinD-ATP. This results in a source degradation process with the decay length set by $l = \sqrt{D_D/\lambda}$. Due to membrane curvature, these reaction volumes overlap near the cell poles, which implies an accumulation of inactive MinD-ADP at the cell poles. For a detailed discussion of this geometric

effect, we refer to (Thalmeier et al. 2016). Note that once DivIVA loses its affinity to the cell poles, this effect alone could explain the switch of MinD localization from the poles to midcell. Hence, 3D simulations were necessary to reveal the influence of cell geometry on the protein dynamics.

4.7.2.3. Localization at septum

The curvature sensing protein DivIVA targets the division-site and guides MinJ and MinD to the septum. Above we showed that MinD localizes to the cell poles if the recruitment and detachment rate of MinD are altered at the poles due to interactions with MinJ and DivIVA. For uniform rates, however, the MinD density distribution is spread around midcell but not sharply localized at the septum as observed in experiments. Sharp localization of MinD at mid cell requires interaction with DivIVA and MinJ and we therefore model this case in the same way as for polar localization: First, we define a narrow region with width $s_w = 0.14\ \mu m$ at midcell, which represents the septum (**Fig. 4.1 c**). We set again $\alpha = 4$ and $\beta = 3$ at this geometric region to model the interactions of MinD with MinJ and DivIVA implicitly through a modified recruitment and detachment rate. Simulations of the model show that MinD localizes sharply at the septum (**Fig. 2.10 d** left to right).

Table 4.5: Kinetic rate constants for MinD dynamics of the mathematic model.

The membrane diffusion coefficient, MinD protein density, cell length and cell width were chosen in accordance to the experiment data. The bulk diffusion coefficient, attachment rate, hydrolysis rate and nucleotide exchange rate were estimated from previous approaches for intracellular protein dynamics (Halatek and Frey 2012; Thalmeier et al. 2016; Wu et al. 2016; Denk et al. 2018).

Parameter	Symbol	Value
Bulk Diffusion	D_D	16 $\mu m^2 \cdot s^{-1}$
Membrane Diffusion	D_d	0.06 $\mu m^2 \cdot s^{-1}$
Mean total density	$[MinD]$	2450 μm^{-3}
Attachment rate	k_D	0.068 $\mu m \cdot s^{-1}$
Uniform recruitment rate	$\tilde{k}_{dD}$	0.04 $\mu^2 \cdot s^{-1}$
Uniform hydrolysis rate	$\tilde{k}_H$	0.1 s^{-1}
Recruitment rate amplification factor	α	4
Hydrolysis rate reduction factor	β	3
Nucleotide exchange rate	λ	6 s^{-1}
Cell length	L	2.8 μm
Cell width	h	0.85 μm

4.8. Protein biochemical methods

4.8.1. Preparation of *B. subtilis* cell lysates

To obtain cell lysates of *B. subtilis*, strains were inoculated from an overnight culture to OD_{600} 0.05 in the morning, and grown to OD_{600} 0.5 in 10 ml LB medium (MD for quantitative studies) at 37°C. Cells were then diluted 1/10 and grown again to mid-exponential phase (OD_{600} 0.5). Cultures were centrifuged at 13.000 rpm for 1 minute, washed once with lysis buffer [10 mM Tris, pH 7.5, 150 mM NaCl, 500 µM EDTA, 1 mM PMSF], and resuspended in lysis buffer with additional 10 mg ml^{-1} lysozyme (Sigma-Aldrich), 10 µg ml^{-1} DNase I (Roche) and 100 µg ml^{-1} RNase A (Roche), concentrating the sample to OD_{600} 30. After incubation at 37°C for 20 minutes, the sample was briefly vortexed to crack remaining intact cells.

4.8.2. Polyacrylamide gel electrophoresis (PAGE)

To separate proteins according to their size, polyacrylamide gel electrophoresis was used (Laemmli 1970). To this end, 30 µl of *B. subtilis* cell lysate was mixed with 10 µl of 4x SDS-PAGE loading buffer [200 mM Tris-HCL pH6.8, 400 mM DTT, 8% SDS, 0.4% bromophenol blue and 40% glycerol (v/v)]. For typhoon imaging and subsequent western blotting, samples were incubated for either 20 min at room temperature, while some samples meant exclusively for western blotting were incubated at 95°C for 10 minutes for full denaturation. 10 or 20 µl of sample were then separated by SDS PAGE in 12% Bis-Tris gels.

4.8.3. In-gel fluorescence and Western blot immunodetection

For visualization of green fluorescent fusions, gels were imaged in a Typhoon Trio (GE Healthcare; PMT 600-800, Excitation 488 nm, Emission 526 SP). For Western blotting, proteins were blotted onto 0.2 µm polyvinylidene difluoride (PVDF) membranes, which were pre-activated in methanol prior to use. Western blots were performed in electrophoretic chambers (Bio-Rad), filled with transfer buffer [25 mM Trsi-HCL pH 8.3, 0.2 M glycine, 20% (v/v) methanol], at 80 mA overnight. Nonspecific binding sites were blocked for 1 h in 5% (w/v) skimmed milk powder in TBS [50 mM Tris-HCl pH 7.5, 150 mM NaCl]. Subsequently membranes were incubated with anti-mCherry (polyclonal, 1:2000, rabbit IgG, BioVision Inc.), anti-mNG (monoclonal, 1:1000, mouse IgG, ChromoTek GmbH) or anti-Dendra (polyclonal, 1:2000, rabbit IgG, OriGene – Thermo Fisher Scientific) primary antibodies, respectively, in 5% skimmed milk powder in TBS for 1h, following three washing steps in TBS for 5 min each.

Secondary antibodies anti-rabbit (polyclonal goat IgG, alkaline phosphatase conjugate, Sigma-Aldrich) or anti-mouse (polyclonal goat IgG, alkaline phosphatase conjugate, Sigma-Aldrich) were applied in 1:10000 dilutions in 5% skimmed milk powder in TBS for 1h. After three more washing steps in TBS for 5 min each, immunodetection was performed using chromogenic alkaline phosphatase substrates 5-bromo-4-chloro-3-indolyl phosphate and nitro blue tetrazolium.

To quantify Dendra2-fusions of MinD, MinJ and DivIVA via in-gel fluorescence, three biological triplicates were prepared and imaged as described above, while avoiding oversaturation. The total number of MinD molecules was taken from a publication that utilized targeted mass spectrometry to determine absolute protein amounts of *B. subtilis* at mid-exponential phase in minimal medium with glucose (Maass et al. 2011). Relative quantification was then performed using Fiji by measuring and comparing intensity of the bands.

5. References

Aarsman, M. E., A. Piette, C. Fraipont, T. M. Vinkenvleugel, M. Nguyen-Disteche, and T. den Blaauwen. 2005. 'Maturation of the *Escherichia coli* divisome occurs in two steps', *Mol Microbiol*, 55: 1631-45.

Abbe, E. 1873. 'Beiträge zur Theorie des Mikroskops und der mikroskopischen Wahrnehmung', *Archiv für Mikroskopische Anatomie*, 9: 413-68.

Adler, H. I., W. D. Fisher, A. Cohen, and A. A. Hardigree. 1967. 'Miniature *Escherichia coli* cells deficient in DNA', *Proc Natl Acad Sci U S A*, 57: 321-6.

Aigouy, B., and V. Mirouse. 2013. 'ScientiFig: a tool to build publication-ready scientific figures', *Nat Methods*, 10: 1048.

Akiyama, T., S. Inouye, and T. Komano. 2003. 'Novel developmental genes, *fruCD*, of *Myxococcus xanthus*: involvement of a cell division protein in multicellular development', *J Bacteriol*, 185: 3317-24.

Anagnostopoulos, C., and J. Spizizen. 1961. 'Requirements for Transformation in *Bacillus subtilis*', *J Bacteriol*, 81: 741-6.

Ando, R., H. Hama, M. Yamamoto-Hino, H. Mizuno, and A. Miyawaki. 2002. 'An optical marker based on the UV-induced green-to-red photoconversion of a fluorescent protein', *Proc Natl Acad Sci U S A*, 99: 12651-6.

Ando, R., H. Mizuno, and A. Miyawaki. 2004. 'Regulated fast nucleocytoplasmic shuttling observed by reversible protein highlighting', *Science*, 306: 1370-3.

Ankerst, M., M. M. Breunig, H. P. Kriegel, and J. Sander. 1999. 'OPTICS: Ordering points to identify the clustering structure', *Sigmod Record*, 28, 2: 49-60.

Annibale, P., S. Vanni, M. Scarselli, U. Rothlisberger, and A. Radenovic. 2011. 'Quantitative photo activated localization microscopy: unraveling the effects of photoblinking', *PLoS One*, 6: e22678.

Aubin, J. E. 1979. 'Autofluorescence of viable cultured mammalian cells', *J Histochem Cytochem*, 27: 36-43.

Autret, S., R. Nair, and J. Errington. 2001. 'Genetic analysis of the chromosome segregation protein Spo0J of *Bacillus subtilis*: evidence for separate domains involved in DNA binding and interactions with Soj protein', *Mol Microbiol*, 41: 743-55.

Axelrod, D., D. E. Koppel, J. Schlessinger, E. Elson, and W. W. Webb. 1976. 'Mobility measurement by analysis of fluorescence photobleaching recovery kinetics', *Biophys J*, 16: 1055-69.

Bach, J. N., N. Albrecht, and M. Bramkamp. 2014. 'Imaging DivIVA dynamics using photo-convertible and activatable fluorophores in *Bacillus subtilis*', *Front Microbiol*, 5: 59.

Bach, J. N., G. Giacomelli, and M. Bramkamp. 2017. 'Sample Preparation and Choice of Fluorophores for Single and Dual Color Photo-Activated Localization Microscopy (PALM) with Bacterial Cells', *Methods Mol Biol*, 1563: 129-41.

Bakshi, S., B. P. Bratton, and J. C. Weisshaar. 2011. 'Subdiffraction-limit study of Kaede diffusion and spatial distribution in live *Escherichia coli*', *Biophys J*, 101: 2535-44.

Balaban, M., and D. R. Hendrixson. 2011. 'Polar flagellar biosynthesis and a regulator of flagellar number influence spatial parameters of cell division in *Campylobacter jejuni*', *PLoS Pathog*, 7: e1002420.

Balinovic, A., D. Albrecht, and U. Endesfelder. 2019. 'Spectrally red-shifted fluorescent fiducial markers for optimal drift correction in localization microscopy', *Journal of Physics D: Applied Physics*, 52.

Barak, L. S., and W. W. Webb. 1982. 'Diffusion of low density lipoprotein-receptor complex on human fibroblasts', *J Cell Biol*, 95: 846-52.

Barykina, N. V., O. M. Subach, D. A. Doronin, V. P. Sotskov, M. A. Roshchina, T. A. Kunitsyna, A. Y. Malyshev, I. V. Smirnov, A. M. Azieva, I. S. Sokolov, K. D. Piatkevich, M. S. Burtsev, A. M. Varizhuk, G. E. Pozmogova, K. V. Anokhin, F. V. Subach, and G. N. Enikolopov. 2016. 'A new design for a green calcium indicator with a smaller size and a reduced number of calcium-binding sites', *Sci Rep*, 6: 34447.

Bates, D., and N. Kleckner. 2005. 'Chromosome and replisome dynamics in *E. coli*: loss of sister cohesion triggers global chromosome movement and mediates chromosome segregation', *Cell*, 121: 899-911.

Baty, F., C. Ritz, S. Charles, M. Brutsche, J. P. Flandrois, and M. L. Delignette-Muller. 2015. 'A Toolbox for Nonlinear Regression in R: The Package nlstools', *J Stat Softw*, 66: 1-21.

Ben-Yehuda, S., and R. Losick. 2002. 'Asymmetric cell division in *B. subtilis* involves a spiral-like intermediate of the cytokinetic protein FtsZ', *Cell*, 109: 257-66.

Ben-Yehuda, S., D. Z. Rudner, and R. Losick. 2003. 'RacA, a bacterial protein that anchors chromosomes to the cell poles', *Science*, 299: 532-6.

Berglund, A. J. 2010. 'Statistics of camera-based single-particle tracking', *Phys Rev E Stat Nonlin Soft Matter Phys*, 82: 011917.

Bernhardt, T. G., and P. A. de Boer. 2005. 'SlmA, a nucleoid-associated, FtsZ binding protein required for blocking septal ring assembly over chromosomes in *E. coli*', *Mol Cell*, 18: 555-64.

Bertani, G. 1951. 'Studies on lysogenesis. I. The mode of phage liberation by lysogenic *Escherichia coli*', *J Bacteriol*, 62: 293-300.

Betzig, E., G. H. Patterson, R. Sougrat, O. W. Lindwasser, S. Olenych, J. S. Bonifacino, M. W. Davidson, J. Lippincott-Schwartz, and H. F. Hess. 2006. 'Imaging intracellular fluorescent proteins at nanometer resolution', *Science*, 313: 1642-5.

Bi, E. F., and J. Lutkenhaus. 1991. 'FtsZ ring structure associated with division in *Escherichia coli*', *Nature*, 354: 161-4.

Billinton, N., and A. W. Knight. 2001. 'Seeing the wood through the trees: a review of techniques for distinguishing green fluorescent protein from endogenous autofluorescence', *Anal Biochem*, 291: 175-97.

Bisicchia, P., D. Noone, E. Lioliou, A. Howell, S. Quigley, T. Jensen, H. Jarmer, and K. M. Devine. 2007. 'The essential YycFG two-component system controls cell wall metabolism in *Bacillus subtilis*', *Mol Microbiol*, 65: 180-200.

Bisson-Filho, A. W., Y. P. Hsu, G. R. Squyres, E. Kuru, F. Wu, C. Jukes, Y. Sun, C. Dekker, S. Holden, M. S. VanNieuwenhze, Y. V. Brun, and E. C. Garner. 2017. 'Treadmilling by FtsZ filaments drives peptidoglycan synthesis and bacterial cell division', *Science*, 355: 739-43.

Biteen, J. S., M. A. Thompson, N. K. Tselentis, G. R. Bowman, L. Shapiro, and W. E. Moerner. 2008. 'Super-resolution imaging in live *Caulobacter crescentus* cells using photoswitchable EYFP', *Nat Methods*, 5: 947-9.

Boersma, M. J., E. Kuru, J. T. Rittichier, M. S. VanNieuwenhze, Y. V. Brun, and M. E. Winkler. 2015. 'Minimal Peptidoglycan (PG) Turnover in Wild-Type and PG Hydrolase and Cell Division Mutants of *Streptococcus pneumoniae* D39 Growing Planktonically and in Host-Relevant Biofilms', *J Bacteriol*, 197: 3472-85.

Booth, S., and R. J. Lewis. 2019. 'Structural basis for the coordination of cell division with the synthesis of the bacterial cell envelope', *Protein Sci*, 28: 2042-54.

Botta, G. A., and J. T. Park. 1981. 'Evidence for involvement of penicillin-binding protein 3 in murein synthesis during septation but not during cell elongation', *J Bacteriol*, 145: 333-40.

Boye, E., and K. Nordstrom. 2003. 'Coupling the cell cycle to cell growth', *EMBO Rep*, 4: 757-60.

Brakemann, T., A. C. Stiel, G. Weber, M. Andresen, I. Testa, T. Grotjohann, M. Leutenegger, U. Plessmann, H. Urlaub, C. Eggeling, M. C. Wahl, S. W. Hell, and S. Jakobs. 2011. 'A reversibly photoswitchable GFP-like protein with fluorescence excitation decoupled from switching', *Nat Biotechnol*, 29: 942-7.

Bramkamp, M., R. Emmins, L. Weston, C. Donovan, R. A. Daniel, and J. Errington. 2008. 'A novel component of the division-site selection system of *Bacillus subtilis* and a new mode of action for the division inhibitor MinCD', *Mol Microbiol*, 70: 1556-69.

Bramkamp, M., and S. van Baarle. 2009. 'Division site selection in rod-shaped bacteria', *Curr Opin Microbiol*, 12: 683-8.

Briley, K., Jr., P. Prepiak, M. J. Dias, J. Hahn, and D. Dubnau. 2011. 'Maf acts downstream of ComGA to arrest cell division in competent cells of *B. subtilis*', *Mol Microbiol*, 81: 23-39.

Burton, B., and D. Dubnau. 2010. 'Membrane-associated DNA transport machines', *Cold Spring Harb Perspect Biol*, 2: a000406.

Buss, J., C. Coltharp, T. Huang, C. Pohlmeyer, S. C. Wang, C. Hatem, and J. Xiao. 2013. 'In vivo organization of the FtsZ-ring by ZapA and ZapB revealed by quantitative super-resolution microscopy', *Mol Microbiol*, 89: 1099-120.

Campos, M., I. V. Surovtsev, S. Kato, A. Paintdakhi, B. Beltran, S. E. Ebmeier, and C. Jacobs-Wagner. 2014. 'A constant size extension drives bacterial cell size homeostasis', *Cell*, 159: 1433-46.

Cha, J. H., and G. C. Stewart. 1997. 'The *divIVA* minicell locus of *Bacillus subtilis*', *J Bacteriol*, 179: 1671-83.

Chalfie, M., Y. Tu, G. Euskirchen, W. W. Ward, and D. C. Prasher. 1994. 'Green fluorescent protein as a marker for gene expression', *Science*, 263: 802-5.

Chang, H., M. Zhang, W. Ji, J. Chen, Y. Zhang, B. Liu, J. Lu, J. Zhang, P. Xu, and T. Xu. 2012. 'A unique series of reversibly switchable fluorescent proteins with beneficial properties for various applications', *Proc Natl Acad Sci U S A*, 109: 4455-60.

Cho, H., and T. G. Bernhardt. 2013. 'Identification of the SlmA active site responsible for blocking bacterial cytokinetic ring assembly over the chromosome', *PLoS Genet*, 9: e1003304.

Chudakov, D. M., V. V. Belousov, A. G. Zaraisky, V. V. Novoselov, D. B. Staroverov, D. B. Zorov, S. Lukyanov, and K. A. Lukyanov. 2003. 'Kindling fluorescent proteins for precise in vivo photolabeling', *Nat Biotechnol*, 21: 191-4.

Clerc, A., C. Manceau, and X. Nesme. 1998. 'Comparison of Randomly Amplified Polymorphic DNA with Amplified Fragment Length Polymorphism To Assess Genetic Diversity and Genetic Relatedness within Genospecies III of *Pseudomonas syringae*', *Appl Environ Microbiol*, 64: 1180-7.

Coltharp, C., R. P. Kessler, and J. Xiao. 2012. 'Accurate construction of photoactivated localization microscopy (PALM) images for quantitative measurements', *PLoS One*, 7: e51725.

Conti, J., M. G. Viola, and J. L. Camberg. 2015. 'The bacterial cell division regulators MinD and MinC form polymers in the presence of nucleotide', *FEBS Lett*, 589: 201-6.

Conti, J., M. G. Viola, and J. L. Camberg. 2018. 'FtsA reshapes membrane architecture and remodels the Z-ring in *Escherichia coli*', *Mol Microbiol*, 107: 558-76.

Cordell, S. C., R. E. Anderson, and J. Löwe. 2001. 'Crystal structure of the bacterial cell division inhibitor MinC', *EMBO J*, 20: 2454-61.

Croce, A. C., and G. Bottiroli. 2014. 'Autofluorescence spectroscopy and imaging: a tool for biomedical research and diagnosis', *Eur J Histochem*, 58: 2461.

Dajkovic, A., G. Lan, S. X. Sun, D. Wirtz, and J. Lutkenhaus. 2008. 'MinC spatially controls bacterial cytokinesis by antagonizing the scaffolding function of FtsZ', *Curr Biol*, 18: 235-44.

de Boer, P. A., R. E. Crossley, A. R. Hand, and L. I. Rothfield. 1991. 'The MinD protein is a membrane ATPase required for the correct placement of the *Escherichia coli* division site', *EMBO J*, 10: 4371-80.

de Boer, P. A., R. E. Crossley, and L. I. Rothfield. 1989. 'A division inhibitor and a topological specificity factor coded for by the minicell locus determine proper placement of the division septum in *E. coli*', *Cell*, 56: 641-9.

de Boer, P., R. Crossley, and L. Rothfield. 1992. 'The essential bacterial cell-division protein FtsZ is a GTPase', *Nature*, 359: 254-6.

Demmerle, J., C. Innocent, A. J. North, G. Ball, M. Muller, E. Miron, A. Matsuda, I. M. Dobbie, Y. Markaki, and L. Schermelleh. 2017. 'Strategic and practical guidelines for successful structured illumination microscopy', *Nat Protoc*, 12: 988-1010.

den Blaauwen, T., L. W. Hamoen, and P. A. Levin. 2017. 'The divisome at 25: the road ahead', *Curr Opin Microbiol*, 36: 85-94.

Denk, J., S. Kretschmer, J. Halatek, C. Hartl, P. Schwille, and E. Frey. 2018. 'MinE conformational switching confers robustness on self-organized Min protein patterns', *Proc Natl Acad Sci U S A*, 115: 4553-58.

Deschout, H., K. Neyts, and K. Braeckmans. 2012. 'The influence of movement on the localization precision of sub-resolution particles in fluorescence microscopy', *J Biophotonics*, 5: 97-109.

Dickson, R. M., A. B. Cubitt, R. Y. Tsien, and W. E. Moerner. 1997. 'On/off blinking and switching behaviour of single molecules of green fluorescent protein', *Nature*, 388: 355-8.

Dominguez-Cuevas, P., I. Porcelli, R. A. Daniel, and J. Errington. 2013. 'Differentiated roles for MreB-actin isologues and autolytic enzymes in *Bacillus subtilis* morphogenesis', *Mol Microbiol*, 89: 1084-98.

Donachie, W. D. 1968. 'Relationship between cell size and time of initiation of DNA replication', *Nature*, 219: 1077-9.

Donovan, C., B. Sieger, R. Kramer, and M. Bramkamp. 2012. 'A synthetic *Escherichia coli* system identifies a conserved origin tethering factor in Actinobacteria', *Mol Microbiol*, 84: 105-16.

dos Santos, V. T., A. W. Bisson-Filho, and F. J. Gueiros-Filho. 2012. 'DivIVA-mediated polar localization of ComN, a posttranscriptional regulator of *Bacillus subtilis*', *J Bacteriol*, 194: 3661-9.

Du, S., and J. Lutkenhaus. 2019. 'At the Heart of Bacterial Cytokinesis: The Z Ring', *Trends Microbiol*, 27: 781-91.

Duman, R., S. Ishikawa, I. Celik, H. Strahl, N. Ogasawara, P. Troc, J. Lowe, and L. W. Hamoen. 2013. 'Structural and genetic analyses reveal the protein SepF as a new membrane anchor for the Z ring', *Proc Natl Acad Sci U S A*, 110: E4601-10.

Ebersbach, G., and K. Gerdes. 2005. 'Plasmid segregation mechanisms', *Annu Rev Genet*, 39: 453-79.

Edwards, D. H., and J. Errington. 1997. 'The *Bacillus subtilis* DivIVA protein targets to the division septum and controls the site specificity of cell division', *Mol Microbiol*, 24: 905-15.

Edwards, D. H., H. B. Thomaides, and J. Errington. 2000. 'Promiscuous targeting of *Bacillus subtilis* cell division protein DivIVA to division sites in *Escherichia coli* and fission yeast', *EMBO J*, 19: 2719-27.

Engler, C., R. Gruetzner, R. Kandzia, and S. Marillonnet. 2009. 'Golden gate shuffling: a one-pot DNA shuffling method based on type IIs restriction enzymes', *PLoS One*, 4: e5553.

Engler, C., R. Kandzia, and S. Marillonnet. 2008. 'A one pot, one step, precision cloning method with high throughput capability', *PLoS One*, 3: e3647.

Erickson, H. P., and M. Osawa. 2010. 'Cell division without FtsZ- a variety of redundant mechanisms', *Mol Microbiol*, 78: 267-70.

Ester, M.; Kriegel, H.P.; Sander, J.; Xu, X. 1996. 'A Density-Based Algorithm for Discovering Clusters in Large Spatial Databases with Noise', *Data Min Knowl Discov*, 96: 226-31.

Eswara, P. J., and K. S. Ramamurthi. 2017. 'Bacterial Cell Division: Nonmodels Poised to Take the Spotlight', *Annu Rev Microbiol*, 71: 393-411.

Eswaramoorthy, P., M. L. Erb, J. A. Gregory, J. Silverman, K. Pogliano, J. Pogliano, and K. S. Ramamurthi. 2011. 'Cellular architecture mediates DivIVA ultrastructure and regulates min activity in *Bacillus subtilis*', *MBio*, 2: e00257-11.

Eswaramoorthy, P., P. W. Winter, P. Wawrzusin, A. G. York, H. Shroff, and K. S. Ramamurthi. 2014. 'Asymmetric division and differential gene expression during a bacterial developmental program requires DivIVA', *PLoS Genet*, 10: e1004526.

Fadda, D., C. Pischedda, F. Caldara, M. B. Whalen, D. Anderluzzi, E. Domenici, and O. Massidda. 2003. 'Characterization of *divIVA* and other genes located in the chromosomal region downstream of the *dcw* cluster in *Streptococcus pneumoniae*', *J Bacteriol*, 185: 6209-14.

Fange, D., and J. Elf. 2006. 'Noise-induced Min phenotypes in *E. coli*', *PLoS Comput Biol*, 2: e80.

Fantes, P. A. 1977. 'Control of cell size and cycle time in *Schizosaccharomyces pombe*', *J Cell Sci*, 24: 51-67.

Feddersen, H., L. Würthner, E. Frey, and M. Bramkamp. 2020. 'Dynamics of the *Bacillus subtilis* Min system', *bioRxiv*: 068676.

Flardh, K. 2003. 'Essential role of DivIVA in polar growth and morphogenesis in *Streptomyces coelicolor* A3(2)', *Mol Microbiol*, 49: 1523-36.

Fleurie, A., C. Lesterlin, S. Manuse, C. Zhao, C. Cluzel, J. P. Lavergne, M. Franz-Wachtel, B. Macek, C. Combet, E. Kuru, M. S. VanNieuwenhze, Y. V. Brun, D. Sherratt, and C. Grangeasse. 2014. 'MapZ marks the division sites and positions FtsZ rings in *Streptococcus pneumoniae*', *Nature*, 516: 259-62.

Foo, Y. H., C. Spahn, H. Zhang, M. Heilemann, and L. J. Kenney. 2015. 'Single cell super-resolution imaging of *E. coli* OmpR during environmental stress', *Integr Biol (Camb)*, 7: 1297-308.

Frost, N. A., H. E. Lu, and T. A. Blanpied. 2012. 'Optimization of cell morphology measurement via single-molecule tracking PALM', *PLoS One*, 7: e36751.

Fujita, M., J. E. Gonzalez-Pastor, and R. Losick. 2005. 'High- and low-threshold genes in the Spo0A regulon of *Bacillus subtilis*', *J Bacteriol*, 187: 1357-68.

Gahlmann, A., J. L. Ptacin, G. Grover, S. Quirin, A. R. von Diezmann, M. K. Lee, M. P. Backlund, L. Shapiro, R. Piestun, and W. E. Moerner. 2013. 'Quantitative multicolor subdiffraction imaging of bacterial protein ultrastructures in three dimensions', *Nano Lett*, 13: 987-93.

Galli, E., M. Poidevin, R. Le Bars, J. M. Desfontaines, L. Muresan, E. Paly, Y. Yamaichi, and F. X. Barre. 2016. 'Cell division licensing in the multi-chromosomal *Vibrio cholerae* bacterium', *Nat Microbiol*, 1: 16094.

Gamba, P., J. W. Veening, N. J. Saunders, L. W. Hamoen, and R. A. Daniel. 2009. 'Two-step assembly dynamics of the *Bacillus subtilis* divisome', *J Bacteriol*, 191: 4186-94.

Garcia, P. S., J. P. Simorre, C. Brochier-Armanet, and C. Grangeasse. 2016. 'Cell division of *Streptococcus pneumoniae*: think positive!', *Curr Opin Microbiol*, 34: 18-23.

Gavet, O., and J. Pines. 2010. 'Activation of cyclin B1-Cdk1 synchronizes events in the nucleus and the cytoplasm at mitosis', *J Cell Biol*, 189: 247-59.

Ghosal, D., D. Trambaiolo, L. A. Amos, and J. Löwe. 2014. 'MinCD cell division proteins form alternating copolymeric cytomotive filaments', *Nat Commun*, 5: 5341.

Gitai, Z. 2006. 'Plasmid segregation: a new class of cytoskeletal proteins emerges', *Curr Biol*, 16: R133-6.

Godin, A. G., B. Lounis, and L. Cognet. 2014. 'Super-resolution microscopy approaches for live cell imaging', *Biophys J*, 107: 1777-84.

Gottfert, F., C. A. Wurm, V. Mueller, S. Berning, V. C. Cordes, A. Honigmann, and S. W. Hell. 2013. 'Coaligned dual-channel STED nanoscopy and molecular diffusion analysis at 20 nm resolution', *Biophys J*, 105: L01-3.

Green, R., and E. J. Rogers. 2013. 'Transformation of chemically competent *E. coli*', *Methods Enzymol*, 529: 329-36.

Gregory, J. A., E. C. Becker, and K. Pogliano. 2008. '*Bacillus subtilis* MinC destabilizes FtsZ-rings at new cell poles and contributes to the timing of cell division', *Genes Dev*, 22: 3475-88.

Gruber, S., and J. Errington. 2009. 'Recruitment of condensin to replication origin regions by ParB/SpoOJ promotes chromosome segregation in *B. subtilis*', *Cell*, 137: 685-96.

Grunwald, D., R. M. Martin, V. Buschmann, D. P. Bazett-Jones, H. Leonhardt, U. Kubitscheck, and M. C. Cardoso. 2008. 'Probing intranuclear environments at the single-molecule level', *Biophys J*, 94: 2847-58.

Gueiros-Filho, F. J., and R. Losick. 2002. 'A widely conserved bacterial cell division protein that promotes assembly of the tubulin-like protein FtsZ', *Genes Dev*, 16: 2544-56.

Gulbronson, C. J., D. A. Ribardo, M. Balaban, C. Knauer, G. Bange, and D. R. Hendrixson. 2016. 'FlhG employs diverse intrinsic domains and influences FlhF GTPase activity to numerically regulate polar flagellar biogenesis in *Campylobacter jejuni*', *Mol Microbiol*, 99: 291-306.

Gunning, P. W., E. C. Hardeman, P. Lappalainen, and D. P. Mulvihill. 2015. 'Tropomyosin - master regulator of actin filament function in the cytoskeleton', *J Cell Sci*, 128: 2965-74.

Gurskaya, N. G., V. V. Verkhusha, A. S. Shcheglov, D. B. Staroverov, T. V. Chepurnykh, A. F. Fradkov, S. Lukyanov, and K. A. Lukyanov. 2006. 'Engineering of a monomeric green-to-red photoactivatable fluorescent protein induced by blue light', *Nat Biotechnol*, 24: 461-5.

Gustafsson, M. G., L. Shao, P. M. Carlton, C. J. Wang, I. N. Golubovskaya, W. Z. Cande, D. A. Agard, and J. W. Sedat. 2008. 'Three-dimensional resolution doubling in wide-field fluorescence microscopy by structured illumination', *Biophys J*, 94: 4957-70.

Guttenplan, S. B., S. Shaw, and D. B. Kearns. 2013. 'The cell biology of peritrichous flagella in *Bacillus subtilis*', *Mol Microbiol*, 87: 211-29.

Haeusser, D. P., and W. Margolin. 2016. 'Splitsville: structural and functional insights into the dynamic bacterial Z ring', *Nat Rev Microbiol*, 14: 305-19.

Hahsler, M., M. Piekenbrock, and D. Doran. 2019. 'dbscan: Fast Density-Based Clustering with R', *Journal of Statistical Software*, 91: 1-30.

Hajduk, I. V., R. Mann, C. D. A. Rodrigues, and E. J. Harry. 2019. 'The ParB homologs, Spo0J and Noc, together prevent premature midcell Z ring assembly when the early stages of replication are blocked in *Bacillus subtilis*', *Mol Microbiol*, 112: 766-84.

Halatek, J., F. Brauns, and E. Frey. 2018. 'Self-organization principles of intracellular pattern formation', *Philos Trans R Soc Lond B Biol Sci*, 373.

Halatek, J., and E. Frey. 2012. 'Highly canalized MinD transfer and MinE sequestration explain the origin of robust MinCDE-protein dynamics', *Cell Rep*, 1: 741-52.

Halatek, J., and E. Frey. 2018. 'Rethinking pattern formation in reaction–diffusion systems', *Nature Physics*, 14: 507-14.

Hamon, M. A., and B. A. Lazazzera. 2001. 'The sporulation transcription factor Spo0A is required for biofilm development in *Bacillus subtilis*', *Mol Microbiol*, 42: 1199-209.

Hansen, A. S., M. Woringer, J. B. Grimm, L. D. Lavis, R. Tjian, and X. Darzacq. 2018. 'Robust model-based analysis of single-particle tracking experiments with Spot-On', *Elife*, 7.

Harry, E. J., J. Rodwell, and R. G. Wake. 1999. 'Co-ordinating DNA replication with cell division in bacteria: a link between the early stages of a round of replication and mid-cell Z ring assembly', *Mol Microbiol*, 33: 33-40.

Heidrich, C., M. F. Templin, A. Ursinus, M. Merdanovic, J. Berger, H. Schwarz, M. A. de Pedro, and J. V. Holtje. 2001. 'Involvement of N-acetylmuramyl-L-alanine amidases in cell separation and antibiotic-induced autolysis of *Escherichia coli*', *Mol Microbiol*, 41: 167-78.

Heilemann, M., S. van de Linde, M. Schuttpelz, R. Kasper, B. Seefeldt, A. Mukherjee, P. Tinnefeld, and M. Sauer. 2008. 'Subdiffraction-resolution fluorescence imaging with conventional fluorescent probes', *Angew Chem Int Ed Engl*, 47: 6172-6.

Heintzmann, R., and C. G. Cremer. 1999. 'Laterally modulated excitation microscopy: improvement of resolution by using a diffraction grating', *Proc. SPIE*, 3568: 185-96.

Hell, S. W., and J. Wichmann. 1994. 'Breaking the diffraction resolution limit by stimulated emission: stimulated-emission-depletion fluorescence microscopy', *Opt Lett*, 19: 780-2.

Heppert, J. K., D. J. Dickinson, A. M. Pani, C. D. Higgins, A. Steward, J. Ahringer, J. R. Kuhn, and B. Goldstein. 2016. 'Comparative assessment of fluorescent proteins for in vivo imaging in an animal model system', *Mol Biol Cell*, 27: 3385-94.

Herbert, A.;. 2019. '*Single Molecule Light Microscopy ImageJ Plugins*', *(http://sussex.ac.uk/gdsc/intranet/microscopy/UserSupport/AnalysisProtocol/imagej/smlm_plugins/)*.

Hoffmann, M., and U. S. Schwarz. 2014. 'Oscillations of Min-proteins in micropatterned environments: a three-dimensional particle-based stochastic simulation approach', *Soft Matter*, 10: 2388-96.

Holden, S. J., T. Pengo, K. L. Meibom, C. Fernandez Fernandez, J. Collier, and S. Manley. 2014. 'High throughput 3D super-resolution microscopy reveals *Caulobacter crescentus* in vivo Z-ring organization', *Proc Natl Acad Sci U S A*, 111: 4566-71.

Holeckova, N., L. Doubravova, O. Massidda, V. Molle, K. Buriankova, O. Benada, O. Kofronova, A. Ulrych, and P. Branny. 2014. 'LocZ is a new cell division protein involved in proper septum placement in *Streptococcus pneumoniae*', *MBio*, 6: e01700-14.

Holtje, J. V. 1998. 'Growth of the stress-bearing and shape-maintaining murein sacculus of *Escherichia coli*', *Microbiol Mol Biol Rev*, 62: 181-203.

Hostettler, L., L. Grundy, S. Kaser-Pebernard, C. Wicky, W. R. Schafer, and D. A. Glauser. 2017. 'The Bright Fluorescent Protein mNeonGreen Facilitates Protein Expression Analysis In Vivo', *G3 (Bethesda)*, 7: 607-15.

Howard, M. 2004. 'A mechanism for polar protein localization in bacteria', *J Mol Biol*, 335: 655-63.

Hu, Z., E. P. Gogol, and J. Lutkenhaus. 2002. 'Dynamic assembly of MinD on phospholipid vesicles regulated by ATP and MinE', *Proc Natl Acad Sci U S A*, 99: 6761-6.

Hu, Z., and J. Lutkenhaus. 1999. 'Topological regulation of cell division in *Escherichia coli* involves rapid pole to pole oscillation of the division inhibitor MinC under the control of MinD and MinE', *Mol Microbiol*, 34: 82-90.

Hu, Z., and J. Lutkenhaus. 2000. 'Analysis of MinC reveals two independent domains involved in interaction with MinD and FtsZ', *J Bacteriol*, 182: 3965-71.

Hu, Z., and J. Lutkenhaus. 2001. 'Topological regulation of cell division in *E. coli*: Spatiotemporal oscillation of MinD requires stimulation of its ATPase by MinE and phospholipid', *Mol Cell*, 7: 1337-43.

Hu, Z., and J. Lutkenhaus. 2003. 'A conserved sequence at the C-terminus of MinD is required for binding to the membrane and targeting MinC to the septum', *Mol Microbiol*, 47: 345-55.

Hu, Z., A. Mukherjee, S. Pichoff, and J. Lutkenhaus. 1999. 'The MinC component of the division site selection system in *Escherichia coli* interacts with FtsZ to prevent polymerization', *Proc Natl Acad Sci U S A*, 96: 14819-24.

Huang, K. C., Y. Meir, and N. S. Wingreen. 2003. 'Dynamic structures in *Escherichia coli*: spontaneous formation of MinE rings and MinD polar zones', *Proc Natl Acad Sci U S A*, 100: 12724-8.

Ireton, K., N. W. th Gunther, and A. D. Grossman. 1994. '*spo0J* is required for normal chromosome segregation as well as the initiation of sporulation in *Bacillus subtilis*', *J Bacteriol*, 176: 5320-9.

Ishitsuka, Y., K. Nienhaus, and G. U. Nienhaus. 2014. 'Photoactivatable fluorescent proteins for super-resolution microscopy', *Methods Mol Biol*, 1148: 239-60.

Jacq, M., V. Adam, D. Bourgeois, C. Moriscot, A. M. Di Guilmi, T. Vernet, and C. Morlot. 2015. 'Remodeling of the Z-Ring Nanostructure during the *Streptococcus pneumoniae* Cell Cycle Revealed by Photoactivated Localization Microscopy', *MBio*, 6: e01108-15.

Jaffe, A., R. D'Ari, and S. Hiraga. 1988. 'Minicell-forming mutants of *Escherichia coli*: production of minicells and anucleate rods', *J Bacteriol*, 170: 3094-101.

Jahn, N., S. Brantl, and H. Strahl. 2015. 'Against the mainstream: the membrane-associated type I toxin BsrG from *Bacillus subtilis* interferes with cell envelope biosynthesis without increasing membrane permeability', *Mol Microbiol*, 98: 651-66.

Jamroskovic, J., N. Pavlendova, K. Muchova, A. J. Wilkinson, and I. Barak. 2012. 'An oscillating Min system in *Bacillus subtilis* influences asymmetrical septation during sporulation', *Microbiology*, 158: 1972-81.

Jaqaman, K., D. Loerke, M. Mettlen, H. Kuwata, S. Grinstein, S. L. Schmid, and G. Danuser. 2008. 'Robust single-particle tracking in live-cell time-lapse sequences', *Nat Methods*, 5: 695-702.

Jemth, P., and S. Gianni. 2007. 'PDZ domains: folding and binding', *Biochemistry*, 46: 8701-8.

Johnson, J. E., L. L. Lackner, C. A. Hale, and P. A. de Boer. 2004. 'ZipA is required for targeting of DMinC/DicB, but not DMinC/MinD, complexes to septal ring assemblies in *Escherichia coli*', *J Bacteriol*, 186: 2418-29.

Johnston, G. C., J. R. Pringle, and L. H. Hartwell. 1977. 'Coordination of growth with cell division in the yeast *Saccharomyces cerevisiae*', *Exp Cell Res*, 105: 79-98.

Joosen, L., M. A. Hink, T. W. Gadella, Jr., and J. Goedhart. 2014. 'Effect of fixation procedures on the fluorescence lifetimes of *Aequorea victoria* derived fluorescent proteins', *J Microsc*, 256: 166-76.

Kalman, R.E. 1960. 'A New Approach to Linear Filtering and Prediction Problems', *Journal of Fluids Engineering*, 82(1): 35-45.

Kamiyama, D., and B. Huang. 2012. 'Development in the STORM', *Dev Cell*, 23: 1103-10.

Kapanidis, A. N., S. Uphoff, and M. Stracy. 2018. 'Understanding Protein Mobility in Bacteria by Tracking Single Molecules', *J Mol Biol*, 430: 4443-55.

Karasawa, S., T. Araki, T. Nagai, H. Mizuno, and A. Miyawaki. 2004. 'Cyan-emitting and orange-emitting fluorescent proteins as a donor/acceptor pair for fluorescence resonance energy transfer', *Biochem J*, 381: 307-12.

Karoui, M. E., and J. Errington. 2001. 'Isolation and characterization of topological specificity mutants of *minD* in *Bacillus subtilis*', *Mol Microbiol*, 42: 1211-21.

Kiekebusch, D., K. A. Michie, L. O. Essen, J. Lowe, and M. Thanbichler. 2012. 'Localized dimerization and nucleoid binding drive gradient formation by the bacterial cell division inhibitor MipZ', *Mol Cell*, 46: 245-59.

Klar, T. A., and S. W. Hell. 1999. 'Subdiffraction resolution in far-field fluorescence microscopy', *Opt Lett*, 24: 954-6.

Klein, H. L., K. K. H. Ang, M. R. Arkin, E. C. Beckwitt, Y. H. Chang, J. Fan, Y. Kwon, M. J. Morten, S. Mukherjee, O. J. Pambos, H. El Sayyed, E. S. Thrall, J. P. Vieira-da-Rocha, Q. Wang, S. Wang, H. Y. Yeh, J. S. Biteen, P. Chi, W. D. Heyer, A. N. Kapanidis, J. J. Loparo, T. R. Strick, P. Sung, B. Van Houten, H. Niu, and E. Rothenberg. 2019. 'Guidelines for DNA recombination and repair studies: Mechanistic assays of DNA repair processes', *Microb Cell*, 6: 65-101.

Kloosterman, T. G., R. Lenarcic, C. R. Willis, D. M. Roberts, L. W. Hamoen, J. Errington, and L. J. Wu. 2016. 'Complex polar machinery required for proper chromosome segregation in vegetative and sporulating cells of *Bacillus subtilis*', *Mol Microbiol*, 101: 333-50.

Krupka, M., and W. Margolin. 2018. 'Unite to divide: Oligomerization of tubulin and actin homologs regulates initiation of bacterial cell division', *F1000Res*, 7: 235.

Krupka, M., M. Sobrinos-Sanguino, M. Jimenez, G. Rivas, and W. Margolin. 2018. '*Escherichia coli* ZipA Organizes FtsZ Polymers into Dynamic Ring-Like Protofilament Structures', *MBio*, 9: e01008-18.

Kumar, M., M. S. Mommer, and V. Sourjik. 2010. 'Mobility of cytoplasmic, membrane, and DNA-binding proteins in *Escherichia coli*', *Biophys J*, 98: 552-9.

Laemmli, U. K. 1970. 'Cleavage of structural proteins during the assembly of the head of bacteriophage T4', *Nature*, 227: 680-5.

Lee, H. J., and J. J. Zheng. 2010. 'PDZ domains and their binding partners: structure, specificity, and modification', *Cell Commun Signal*, 8: 8.

Lee, S. H., J. Y. Shin, A. Lee, and C. Bustamante. 2012. 'Counting single photoactivatable fluorescent molecules by photoactivated localization microscopy (PALM)', *Proc Natl Acad Sci U S A*, 109: 17436-41.

Leisch, N., J. Verheul, N. R. Heindl, H. R. Gruber-Vodicka, N. Pende, T. den Blaauwen, and S. Bulgheresi. 2012. 'Growth in width and FtsZ ring longitudinal positioning in a gammaproteobacterial symbiont', *Curr Biol*, 22: R831-2.

Lelek, M., F. Di Nunzio, and C. Zimmer. 2014. 'FlAsH-PALM: super-resolution pointillist imaging with FlAsH-tetracysteine labeling', *Methods Mol Biol*, 1174: 183-93.

Lenarcic, R., S. Halbedel, L. Visser, M. Shaw, L. J. Wu, J. Errington, D. Marenduzzo, and L. W. Hamoen. 2009. 'Localisation of DivIVA by targeting to negatively curved membranes', *EMBO J*, 28: 2272-82.

Lenhart, J. S., J. W. Schroeder, B. W. Walsh, and L. A. Simmons. 2012. 'DNA Repair and Genome Maintenance in *Bacillus subtilis*', *Microbiol Mol Biol Rev*, 76: 530-64.

Letek, M., E. Ordonez, J. Vaquera, W. Margolin, K. Flardh, L. M. Mateos, and J. A. Gil. 2008. 'DivIVA is required for polar growth in the MreB-lacking rod-shaped actinomycete *Corynebacterium glutamicum*', *J Bacteriol*, 190: 3283-92.

Lewis, P. J., and J. Errington. 1997. 'Direct evidence for active segregation of *oriC* regions of the *Bacillus subtilis* chromosome and co-localization with the SpoOJ partitioning protein', *Mol Microbiol*, 25: 945-54.

Li, Y., Z. Chen, L. A. Matthews, L. A. Simmons, and J. S. Biteen. 2019. 'Dynamic Exchange of Two Essential DNA Polymerases during Replication and after Fork Arrest', *Biophys J*, 116: 684-93.

Loose, M., E. Fischer-Friedrich, C. Herold, K. Kruse, and P. Schwille. 2011. 'Min protein patterns emerge from rapid rebinding and membrane interaction of MinE', *Nat Struct Mol Biol*, 18: 577-83.

Loose, M., E. Fischer-Friedrich, J. Ries, K. Kruse, and P. Schwille. 2008. 'Spatial regulators for bacterial cell division self-organize into surface waves in vitro', *Science*, 320: 789-92.

Löwe, J., and L. A. Amos. 1998. 'Crystal structure of the bacterial cell-division protein FtsZ', *Nature*, 391: 203-6.

Lupas, A., M. Van Dyke, and J. Stock. 1991. 'Predicting coiled coils from protein sequences', *Science*, 252: 1162-4.

Lutkenhaus, J. F., H. Wolf-Watz, and W. D. Donachie. 1980. 'Organization of genes in the *ftsA-envA* region of the *Escherichia coli* genetic map and identification of a new *fts* locus (*ftsZ*)', *J Bacteriol*, 142: 615-20.

Lyu, Z., C. Coltharp, X. Yang, and J. Xiao. 2016. 'Influence of FtsZ GTPase activity and concentration on nanoscale Z-ring structure in vivo revealed by three-dimensional Superresolution imaging', *Biopolymers*, 105: 725-34.

Ma, Y., X. Wang, H. Liu, L. Wei, and L. Xiao. 2019. 'Recent advances in optical microscopic methods for single-particle tracking in biological samples', *Anal Bioanal Chem*, 411: 4445-63.

Maass, S., S. Sievers, D. Zuhlke, J. Kuzinski, P. K. Sappa, J. Muntel, B. Hessling, J. Bernhardt, R. Sietmann, U. Volker, M. Hecker, and D. Becher. 2011. 'Efficient, global-scale quantification of absolute protein amounts by integration of targeted mass spectrometry and two-dimensional gel-based proteomics', *Anal Chem*, 83: 2677-84.

Manley, S., J. M. Gillette, G. H. Patterson, H. Shroff, H. F. Hess, E. Betzig, and J. Lippincott-Schwartz. 2008. 'High-density mapping of single-molecule trajectories with photoactivated localization microscopy', *Nat Methods*, 5: 155-7.

Manuse, S., N. L. Jean, M. Guinot, J. P. Lavergne, C. Laguri, C. M. Bougault, M. S. VanNieuwenhze, C. Grangeasse, and J. P. Simorre. 2016. 'Structure-function analysis of the extracellular domain of the pneumococcal cell division site positioning protein MapZ', *Nat Commun*, 7: 12071.

Manzo, C., and M. F. Garcia-Parajo. 2015. 'A review of progress in single particle tracking: from methods to biophysical insights', *Rep Prog Phys*, 78: 124601.

Marbouty, M., A. Le Gall, D. I. Cattoni, A. Cournac, A. Koh, J. B. Fiche, J. Mozziconacci, H. Murray, R. Koszul, and M. Nollmann. 2015. 'Condensin- and Replication-Mediated Bacterial Chromosome Folding and Origin Condensation Revealed by Hi-C and Super-resolution Imaging', *Mol Cell*, 59: 588-602.

Margolin, W. 2012. 'The price of tags in protein localization studies', *J Bacteriol*, 194: 6369-71.

Marston, A. L., and J. Errington. 1999. 'Selection of the midcell division site in *Bacillus subtilis* through MinD-dependent polar localization and activation of MinC', *Mol Microbiol*, 33: 84-96.

Marston, A. L., H. B. Thomaides, D. H. Edwards, M. E. Sharpe, and J. Errington. 1998. 'Polar localization of the MinD protein of *Bacillus subtilis* and its role in selection of the mid-cell division site', *Genes Dev*, 12: 3419-30.

Mastop, M., D. S. Bindels, N. C. Shaner, M. Postma, T. W. J. Gadella, Jr., and J. Goedhart. 2017. 'Characterization of a spectrally diverse set of fluorescent proteins as FRET acceptors for mTurquoise2', *Sci Rep*, 7: 11999.

Matz, M. V., A. F. Fradkov, Y. A. Labas, A. P. Savitsky, A. G. Zaraisky, M. L. Markelov, and S. A. Lukyanov. 1999. 'Fluorescent proteins from nonbioluminescent Anthozoa species', *Nat Biotechnol*, 17: 969-73.

McCormick, J. R., E. P. Su, A. Driks, and R. Losick. 1994. 'Growth and viability of *Streptomyces coelicolor* mutant for the cell division gene *ftsZ*', *Mol Microbiol*, 14: 243-54.

Meeske, A. J., E. P. Riley, W. P. Robins, T. Uehara, J. J. Mekalanos, D. Kahne, S. Walker, A. C. Kruse, T. G. Bernhardt, and D. Z. Rudner. 2016. 'SEDS proteins are a widespread family of bacterial cell wall polymerases', *Nature*, 537: 634-38.

Mercer, K. L., and D. S. Weiss. 2002. 'The *Escherichia coli* cell division protein FtsW is required to recruit its cognate transpeptidase, FtsI (PBP3), to the division site', *J Bacteriol*, 184: 904-12.

Milner, D. S., L. J. Ray, E. B. Saxon, C. Lambert, R. Till, A. K. Fenton, and R. E. Sockett. 2020. 'DivIVA Controls Progeny Morphology and Diverse ParA Proteins Regulate Cell Division or Gliding Motility in *Bdellovibrio bacteriovorus*', *Front Microbiol*, 11: 542.

Misra, H. S., G. K. Maurya, R. Chaudhary, and C. S. Misra. 2018. 'Interdependence of bacterial cell division and genome segregation and its potential in drug development', *Microbiol Res*, 208: 12-24.

Miyawaki, A., J. Llopis, R. Heim, J. M. McCaffery, J. A. Adams, M. Ikura, and R. Y. Tsien. 1997. 'Fluorescent indicators for Ca2+ based on green fluorescent proteins and calmodulin', *Nature*, 388: 882-7.

Mohammadi, T., V. van Dam, R. Sijbrandi, T. Vernet, A. Zapun, A. Bouhss, M. Diepeveen-de Bruin, M. Nguyen-Disteche, B. de Kruijff, and E. Breukink. 2011. 'Identification of FtsW as a transporter of lipid-linked cell wall precursors across the membrane', *EMBO J*, 30: 1425-32.

Molle, V., M. Fujita, S. T. Jensen, P. Eichenberger, J. E. Gonzalez-Pastor, J. S. Liu, and R. Losick. 2003. 'The Spo0A regulon of *Bacillus subtilis*', *Mol Microbiol*, 50: 1683-701.

Mora, C., D. P. Tittensor, S. Adl, A. G. Simpson, and B. Worm. 2011. 'How many species are there on Earth and in the ocean?', *PLoS Biol*, 9: e1001127.

Moriya, S., R. A. Rashid, C. D. Rodrigues, and E. J. Harry. 2010. 'Influence of the nucleoid and the early stages of DNA replication on positioning the division site in *Bacillus subtilis*', *Mol Microbiol*, 76: 634-47.

Mukherjee, A., and J. Lutkenhaus. 1994. 'Guanine nucleotide-dependent assembly of FtsZ into filaments', *J Bacteriol*, 176: 2754-8.

Mukherjee, A., and J. Lutkenhaus. 1998. 'Dynamic assembly of FtsZ regulated by GTP hydrolysis', *EMBO J*, 17: 462-9.

Nakagawa, J., and M. Matsuhashi. 1982. 'Molecular divergence of a major peptidoglycan synthetase with transglycosylase-transpeptidase activities in *Escherichia coli* - penicillin-binding protein 1Bs', *Biochem Biophys Res Commun*, 105: 1546-53.

Nguyen-Disteche, M., C. Fraipont, N. Buddelmeijer, and N. Nanninga. 1998. 'The structure and function of *Escherichia coli* penicillin-binding protein 3', *Cell Mol Life Sci*, 54: 309-16.

Nicolas, P., U. Mader, E. Dervyn, T. Rochat, A. Leduc, N. Pigeonneau, E. Bidnenko, E. Marchadier, M. Hoebeke, S. Aymerich, D. Becher, P. Bisicchia, E. Botella, O. Delumeau, G. Doherty, E. L. Denham, M. J. Fogg, V. Fromion, A. Goelzer, A. Hansen, E. Hartig, C. R. Harwood, G. Homuth, H. Jarmer, M. Jules, E. Klipp, L. Le Chat, F. Lecointe, P. Lewis, W. Liebermeister, A. March, R. A. Mars, P. Nannapaneni, D. Noone, S. Pohl, B. Rinn, F. Rugheimer, P. K. Sappa, F. Samson, M. Schaffer, B. Schwikowski, L. Steil, J. Stulke, T. Wiegert, K. M. Devine, A. J. Wilkinson, J. M. van Dijl, M. Hecker, U. Volker, P. Bessieres,

and P. Noirot. 2012. 'Condition-dependent transcriptome reveals high-level regulatory architecture in *Bacillus subtilis*', *Science*, 335: 1103-6.

Norrander, J., T. Kempe, and J. Messing. 1983. 'Construction of improved M13 vectors using oligodeoxynucleotide-directed mutagenesis', *Gene*, 26: 101-6.

Oliva, M. A., S. Halbedel, S. M. Freund, P. Dutow, T. A. Leonard, D. B. Veprintsev, L. W. Hamoen, and J. Löwe. 2010. 'Features critical for membrane binding revealed by DivIVA crystal structure', *EMBO J*, 29: 1988-2001.

Olivo-Marin, J. C. 2002. 'Extraction of spots in biological images using multiscale products', *Pattern Recogn*, 35: 1989-96.

Ormo, M., A. B. Cubitt, K. Kallio, L. A. Gross, R. Y. Tsien, and S. J. Remington. 1996. 'Crystal structure of the *Aequorea victoria* green fluorescent protein', *Science*, 273: 1392-5.

Osawa, M., D. E. Anderson, and H. P. Erickson. 2009. 'Curved FtsZ protofilaments generate bending forces on liposome membranes', *EMBO J*, 28: 3476-84.

Osawa, M., and H. P. Erickson. 2013. 'Liposome division by a simple bacterial division machinery', *Proc Natl Acad Sci U S A*, 110: 11000-4.

Ovesny, M., P. Krizek, J. Borkovec, Z. Svindrych, and G. M. Hagen. 2014. 'ThunderSTORM: a comprehensive ImageJ plug-in for PALM and STORM data analysis and super-resolution imaging', *Bioinformatics*, 30: 2389-90.

Paintdakhi, A., B. Parry, M. Campos, I. Irnov, J. Elf, I. Surovtsev, and C. Jacobs-Wagner. 2016. 'Oufti: an integrated software package for high-accuracy, high-throughput quantitative microscopy analysis', *Mol Microbiol*, 99: 767-77.

Park, K. T., A. Dajkovic, M. Wissel, S. Du, and J. Lutkenhaus. 2018. 'MinC and FtsZ mutant analysis provides insight into MinC/MinD-mediated Z Ring disassembly', *J Biol Chem.*

Park, K. T., W. Wu, K. P. Battaile, S. Lovell, T. Holyoak, and J. Lutkenhaus. 2011. 'The Min oscillator uses MinD-dependent conformational changes in MinE to spatially regulate cytokinesis', *Cell*, 146: 396-407.

Patrick, J. E., and D. B. Kearns. 2008. 'MinJ (YvjD) is a topological determinant of cell division in *Bacillus subtilis*', *Mol Microbiol*, 70: 1166-79.

Patterson, G. H., and J. Lippincott-Schwartz. 2002. 'A photoactivatable GFP for selective photolabeling of proteins and cells', *Science*, 297: 1873-7.

Pende, N., N. Leisch, H. R. Gruber-Vodicka, N. R. Heindl, J. Ott, T. den Blaauwen, and S. Bulgheresi. 2014. 'Size-independent symmetric division in extraordinarily long cells', *Nat Commun*, 5: 4803.

Pichoff, S., and J. Lutkenhaus. 2002. 'Unique and overlapping roles for ZipA and FtsA in septal ring assembly in *Escherichia coli*', *EMBO J*, 21: 685-93.

Plochowietz, A., I. Farrell, Z. Smilansky, B. S. Cooperman, and A. N. Kapanidis. 2017. 'In vivo single-RNA tracking shows that most tRNA diffuses freely in live bacteria', *Nucleic Acids Res*, 45: 926-37.

Pogliano, J., K. Pogliano, D. S. Weiss, R. Losick, and J. Beckwith. 1997. 'Inactivation of FtsI inhibits constriction of the FtsZ cytokinetic ring and delays the assembly of FtsZ rings at potential division sites', *Proc Natl Acad Sci U S A*, 94: 559-64.

Ponting, C. P. 1997. 'Evidence for PDZ domains in bacteria, yeast, and plants', *Protein Sci*, 6: 464-8.

Qian, H., M. P. Sheetz, and E. L. Elson. 1991. 'Single particle tracking. Analysis of diffusion and flow in two-dimensional systems', *Biophys J*, 60: 910-21.

Ramamurthi, K. S., S. Lecuyer, H. A. Stone, and R. Losick. 2009. 'Geometric cue for protein localization in a bacterium', *Science*, 323: 1354-7.

Ramirez-Diaz, D. A., D. A. Garcia-Soriano, A. Raso, J. Mucksch, M. Feingold, G. Rivas, and P. Schwille. 2018. 'Treadmilling analysis reveals new insights into dynamic FtsZ ring architecture', *PLoS Biol*, 16: e2004845.

Ramm, B., T. Heermann, and P. Schwille. 2019. 'The *E. coli* MinCDE System in the Regulation of Protein Patterns and Gradients', *Cell Mol Life Sci*, 76: 4245-73.

Rao, C. V., G. D. Glekas, and G. W. Ordal. 2008. 'The three adaptation systems of *Bacillus subtilis* chemotaxis', *Trends Microbiol*, 16: 480-7.

Raskin, D. M., and P. A. de Boer. 1997. 'The MinE ring: an FtsZ-independent cell structure required for selection of the correct division site in *E. coli*', *Cell*, 91: 685-94.

Raskin, D. M., and P. A. de Boer. 1999. 'Rapid pole-to-pole oscillation of a protein required for directing division to the middle of *Escherichia coli*', *Proc Natl Acad Sci U S A*, 96: 4971-6.

Reeve, J. N., N. H. Mendelson, S. I. Coyne, L. L. Hallock, and R. M. Cole. 1973. 'Minicells of *Bacillus subtilis*', *J Bacteriol*, 114: 860-73.

Robb, N. C., J. M. Taylor, A. Kent, O. J. Pambos, B. Gilboa, M. Evangelidou, A. A. Mentis, and A. N. Kapanidis. 2019. 'Rapid functionalisation and detection of viruses via a novel Ca(2+)-mediated virus-DNA interaction', *Sci Rep*, 9: 16219.

Rodrigues, C. D., and E. J. Harry. 2012. 'The Min system and nucleoid occlusion are not required for identifying the division site in *Bacillus subtilis* but ensure its efficient utilization', *PLoS Genet*, 8: e1002561.

Rosch, T. C., S. Altenburger, L. Oviedo-Bocanegra, M. Pediaditakis, N. E. Najjar, G. Fritz, and P. L. Graumann. 2018a. 'Single molecule tracking reveals spatio-temporal dynamics of bacterial DNA repair centres', *Sci Rep*, 8: 16450.

Rosch, T. C., L. M. Oviedo-Bocanegra, G. Fritz, and P. L. Graumann. 2018b. 'SMTracker: a tool for quantitative analysis, exploration and visualization of single-molecule tracking data reveals highly dynamic binding of *B. subtilis* global repressor AbrB throughout the genome', *Sci Rep*, 8: 15747.

Rosenbloom, A. B., S. H. Lee, M. To, A. Lee, J. Y. Shin, and C. Bustamante. 2014. 'Optimized two-color super resolution imaging of Drp1 during mitochondrial fission with a slow-switching Dronpa variant', *Proc Natl Acad Sci U S A*, 111: 13093-8.

Rothfield, L. I., and C. R. Zhao. 1996. 'How do bacteria decide where to divide?', *Cell*, 84: 183-6.

Rowlett, V. W., and W. Margolin. 2013. 'The bacterial Min system', *Curr Biol*, 23: R553-6.

Rowlett, V. W., and W. Margolin. 2015. 'The Min system and other nucleoid-independent regulators of Z ring positioning', *Front Microbiol*, 6: 478.

Rueden, C. T., J. Schindelin, M. C. Hiner, B. E. DeZonia, A. E. Walter, E. T. Arena, and K. W. Eliceiri. 2017. 'ImageJ2: ImageJ for the next generation of scientific image data', *BMC Bioinformatics*, 18: 529.

Rust, M. J., M. Bates, and X. Zhuang. 2006. 'Sub-diffraction-limit imaging by stochastic optical reconstruction microscopy (STORM)', *Nat Methods*, 3: 793-5.

Ryter, A., P. Schaeffer, and H. Ionesco. 1966. 'Cytologic classification, by their blockage stage, of sporulation mutants of *Bacillus subtilis* Marburg', *Ann Inst Pasteur (Paris)*, 110: 305-15.

Sage, D., T. A. Pham, H. Babcock, T. Lukes, T. Pengo, J. Chao, R. Velmurugan, A. Herbert, A. Agrawal, S. Colabrese, A. Wheeler, A. Archetti, B. Rieger, R. Ober, G. M. Hagen, J. B. Sibarita, J. Ries, R. Henriques, M. Unser, and S. Holden. 2019. 'Super-resolution fight club: assessment of 2D and 3D single-molecule localization microscopy software', *Nat Methods*, 16: 387-95.

Saxton, M. J. 1997. 'Single-particle tracking: the distribution of diffusion coefficients', *Biophys J*, 72: 1744-53.

Schindelin, J., I. Arganda-Carreras, E. Frise, V. Kaynig, M. Longair, T. Pietzsch, S. Preibisch, C. Rueden, S. Saalfeld, B. Schmid, J. Y. Tinevez, D. J. White, V. Hartenstein, K. Eliceiri, P. Tomancak, and A. Cardona. 2012. 'Fiji: an open-source platform for biological-image analysis', *Nat Methods*, 9: 676-82.

Schloter, M., M. Lebuhn, T. Heulin, and A. Hartmann. 2000. 'Ecology and evolution of bacterial microdiversity', *FEMS Microbiol Rev*, 24: 647-60.

Schubert, K., B. Sieger, F. Meyer, G. Giacomelli, K. Bohm, A. Rieblinger, L. Lindenthal, N. Sachs, G. Wanner, and M. Bramkamp. 2017. 'The Antituberculosis Drug Ethambutol Selectively Blocks Apical Growth in CMN Group Bacteria', *MBio*, 8: e02213-16.

Schumacher, D., S. Bergeler, A. Harms, J. Vonck, S. Huneke-Vogt, E. Frey, and L. Sogaard-Andersen. 2017. 'The PomXYZ Proteins Self-Organize on the Bacterial Nucleoid to Stimulate Cell Division', *Dev Cell*, 41: 299-314.e13.

Schweizer, J., M. Loose, M. Bonny, K. Kruse, I. Monch, and P. Schwille. 2012. 'Geometry sensing by self-organized protein patterns', *Proc Natl Acad Sci U S A*, 109: 15283-8.

Sengupta, P., and J. Lippincott-Schwartz. 2012. 'Quantitative analysis of photoactivated localization microscopy (PALM) datasets using pair-correlation analysis', *Bioessays*, 34: 396-405.

Shaner, N. C., R. E. Campbell, P. A. Steinbach, B. N. Giepmans, A. E. Palmer, and R. Y. Tsien. 2004. 'Improved monomeric red, orange and yellow fluorescent proteins derived from Discosoma sp. red fluorescent protein', *Nat Biotechnol*, 22: 1567-72.

Shaner, N. C., G. G. Lambert, A. Chammas, Y. Ni, P. J. Cranfill, M. A. Baird, B. R. Sell, J. R. Allen, R. N. Day, M. Israelsson, M. W. Davidson, and J. Wang. 2013. 'A bright monomeric green fluorescent protein derived from *Branchiostoma lanceolatum*', *Nat Methods*, 10: 407-9.

Shaner, N. C., P. A. Steinbach, and R. Y. Tsien. 2005. 'A guide to choosing fluorescent proteins', *Nat Methods*, 2: 905-9.

Shen, B., and J. Lutkenhaus. 2010. 'Examination of the interaction between FtsZ and MinCN in *E. coli* suggests how MinC disrupts Z rings', *Mol Microbiol*, 75: 1285-98.

Shen, H., L. J. Tauzin, R. Baiyasi, W. Wang, N. Moringo, B. Shuang, and C. F. Landes. 2017a. 'Single Particle Tracking: From Theory to Biophysical Applications', *Chem Rev*, 117: 7331-76.

Shen, Y., Y. Chen, J. Wu, N. C. Shaner, and R. E. Campbell. 2017b. 'Engineering of mCherry variants with long Stokes shift, red-shifted fluorescence, and low cytotoxicity', *PLoS One*, 12: e0171257.

Sheridan, D. L., C. H. Berlot, A. Robert, F. M. Inglis, K. B. Jakobsdottir, J. R. Howe, and T. E. Hughes. 2002. 'A new way to rapidly create functional, fluorescent fusion proteins: random insertion of GFP with an in vitro transposition reaction', *BMC Neurosci*, 3: 7.

Shih, Y. L., I. Kawagishi, and L. Rothfield. 2005. 'The MreB and Min cytoskeletal-like systems play independent roles in prokaryotic polar differentiation', *Mol Microbiol*, 58: 917-28.

Shimomura, O., F. H. Johnson, and Y. Saiga. 1962. 'Extraction, purification and properties of aequorin, a bioluminescent protein from the luminous hydromedusan, *Aequorea*', *J Cell Comp Physiol*, 59: 223-39.

Sieber, J. J., K. I. Willig, C. Kutzner, C. Gerding-Reimers, B. Harke, G. Donnert, B. Rammner, C. Eggeling, S. W. Hell, H. Grubmuller, and T. Lang. 2007. 'Anatomy and dynamics of a supramolecular membrane protein cluster', *Science*, 317: 1072-6.

Soderstrom, B., K. Mirzadeh, S. Toddo, G. von Heijne, U. Skoglund, and D. O. Daley. 2016. 'Coordinated disassembly of the divisome complex in *Escherichia coli*', *Mol Microbiol*, 101: 425-38.

Sprague, B. L., R. L. Pego, D. A. Stavreva, and J. G. McNally. 2004. 'Analysis of binding reactions by fluorescence recovery after photobleaching', *Biophys J*, 86: 3473-95.

Spratt, B. G., and A. B. Pardee. 1975. 'Penicillin-binding proteins and cell shape in *E. coli*', *Nature*, 254: 516-7.

Stahlberg, H., E. Kutejova, K. Muchova, M. Gregorini, A. Lustig, S. A. Muller, V. Olivieri, A. Engel, A. J. Wilkinson, and I. Barak. 2004. 'Oligomeric structure of the *Bacillus subtilis* cell division protein DivIVA determined by transmission electron microscopy', *Mol Microbiol*, 52: 1281-90.

Stockmar, I., H. Feddersen, K. Cramer, S. Gruber, K. Jung, M. Bramkamp, and J. Y. Shin. 2018. 'Optimization of sample preparation and green color imaging using the mNeonGreen fluorescent protein in bacterial cells for photoactivated localization microscopy', *Sci Rep*, 8: 10137.

Strack, R. 2015. 'Death by super-resolution imaging', *Nat Methods*, 12: 1111.

Stracy, M., C. Lesterlin, F. Garza de Leon, S. Uphoff, P. Zawadzki, and A. N. Kapanidis. 2015. 'Live-cell superresolution microscopy reveals the organization of RNA polymerase in the bacterial nucleoid', *Proc Natl Acad Sci U S A*, 112: E4390-9.

Stracy, M., S. Uphoff, F. Garza de Leon, and A. N. Kapanidis. 2014. 'In vivo single-molecule imaging of bacterial DNA replication, transcription, and repair', *FEBS Lett*, 588: 3585-94.

Stracy, M., A. J. M. Wollman, E. Kaja, J. Gapinski, J. E. Lee, V. A. Leek, S. J. McKie, L. A. Mitchenall, A. Maxwell, D. J. Sherratt, M. C. Leake, and P. Zawadzki. 2019. 'Single-molecule imaging of DNA gyrase activity in living *Escherichia coli*', *Nucleic Acids Res*, 47: 210-20.

Strauss, M. P., A. T. Liew, L. Turnbull, C. B. Whitchurch, L. G. Monahan, and E. J. Harry. 2012. '3D-SIM super resolution microscopy reveals a bead-like arrangement for FtsZ and the division machinery: implications for triggering cytokinesis', *PLoS Biol*, 10: e1001389.

Struntz, P., and M. Weiss. 2018. 'The hitchhiker's guide to quantitative diffusion measurements', *Phys Chem Chem Phys*, 20: 28910-19.

Strutt, John William. 1879. 'Investigations in optics, with special reference to the spectroscope', *Philosophical Magazine*, Series 6: 8(49):261-74.

Subach, F. V., G. H. Patterson, S. Manley, J. M. Gillette, J. Lippincott-Schwartz, and V. V. Verkhusha. 2009. 'Photoactivatable mCherry for high-resolution two-color fluorescence microscopy', *Nat Methods*, 6: 153-9.

Subach, O. M., D. Entenberg, J. S. Condeelis, and V. V. Verkhusha. 2012. 'A FRET-facilitated photoswitching using an orange fluorescent protein with the fast photoconversion kinetics', *J Am Chem Soc*, 134: 14789-99.

Surre, J., C. Saint-Ruf, V. Collin, S. Orenga, M. Ramjeet, and I. Matic. 2018. 'Strong increase in the autofluorescence of cells signals struggle for survival', *Sci Rep*, 8: 12088.

Sveiczer, A., B. Novak, and J. M. Mitchison. 1996. 'The size control of fission yeast revisited', *J Cell Sci*, 109 (Pt 12): 2947-57.

Swulius, M. T., and G. J. Jensen. 2012. 'The helical MreB cytoskeleton in *Escherichia coli* MC1000/pLE7 is an artifact of the N-Terminal yellow fluorescent protein tag', *J Bacteriol*, 194: 6382-6.

Szeto, T. H., S. L. Rowland, L. I. Rothfield, and G. F. King. 2002. 'Membrane localization of MinD is mediated by a C-terminal motif that is conserved across eubacteria, archaea, and chloroplasts', *Proc Natl Acad Sci U S A*, 99: 15693-8.

Szwedziak, P., Q. Wang, T. A. Bharat, M. Tsim, and J. Löwe. 2014. 'Architecture of the ring formed by the tubulin homologue FtsZ in bacterial cell division', *Elife*, 3: e04601.

Tan, I. S., and K. S. Ramamurthi. 2014. 'Spore formation in *Bacillus subtilis*', *Environ Microbiol Rep*, 6: 212-25.

Team, R Core. 2017. 'R: A Language and Environment for Statistical Computing', *R Foundation for Statistical Computing*: Vienna, Austria. URL https://www.R-project.org/.

Thalmeier, D., J. Halatek, and E. Frey. 2016. 'Geometry-induced protein pattern formation', *Proc Natl Acad Sci U S A*, 113: 548-53.

Thanbichler, M., and L. Shapiro. 2006. 'MipZ, a spatial regulator coordinating chromosome segregation with cell division in *Caulobacter*', *Cell*, 126: 147-62.

Thomaides, H. B., M. Freeman, M. El Karoui, and J. Errington. 2001. 'Division site selection protein DivIVA of *Bacillus subtilis* has a second distinct function in chromosome segregation during sporulation', *Genes Dev*, 15: 1662-73.

Tinevez, J. Y., N. Perry, J. Schindelin, G. M. Hoopes, G. D. Reynolds, E. Laplantine, S. Y. Bednarek, S. L. Shorte, and K. W. Eliceiri. 2017. 'TrackMate: An open and extensible platform for single-particle tracking', *Methods*, 115: 80-90.

Tonthat, N. K., S. T. Arold, B. F. Pickering, M. W. Van Dyke, S. Liang, Y. Lu, T. K. Beuria, W. Margolin, and M. A. Schumacher. 2011. 'Molecular mechanism by which the nucleoid occlusion factor, SlmA, keeps cytokinesis in check', *EMBO J*, 30: 154-64.

Treuner-Lange, A., K. Aguiluz, C. van der Does, N. Gomez-Santos, A. Harms, D. Schumacher, P. Lenz, M. Hoppert, J. Kahnt, J. Munoz-Dorado, and L. Sogaard-Andersen. 2013. 'PomZ, a ParA-like protein, regulates Z-ring formation and cell division in *Myxococcus xanthus*', *Mol Microbiol*, 87: 235-53.

Tsang, M. J., and T. G. Bernhardt. 2015. 'Guiding divisome assembly and controlling its activity', *Curr Opin Microbiol*, 24: 60-5.

Turkowyd, B., A. Balinovic, D. Virant, H. G. G. Carnero, F. Caldana, M. Endesfelder, D. Bourgeois, and U. Endesfelder. 2017. 'A General Mechanism of Photoconversion of

Green-to-Red Fluorescent Proteins Based on Blue and Infrared Light Reduces Phototoxicity in Live-Cell Single-Molecule Imaging', *Angew Chem Int Ed Engl*, 56: 11634-39.

Turkowyd, B., H. Muller-Esparza, V. Climenti, N. Steube, U. Endesfelder, and L. Randau. 2019. 'Live-cell single-particle tracking photoactivated localization microscopy of Cascade-mediated DNA surveillance', *Methods Enzymol*, 616: 133-71.

Turner, J. J., J. C. Ewald, and J. M. Skotheim. 2012. 'Cell size control in yeast', *Curr Biol*, 22: R350-9.

Typas, A., M. Banzhaf, C. A. Gross, and W. Vollmer. 2012. 'From the regulation of peptidoglycan synthesis to bacterial growth and morphology', *Nat Rev Microbiol*, 10: 123-36.

Uehara, T., K. R. Parzych, T. Dinh, and T. G. Bernhardt. 2010. 'Daughter cell separation is controlled by cytokinetic ring-activated cell wall hydrolysis', *EMBO J*, 29: 1412-22.

Uphoff, S., R. Reyes-Lamothe, F. Garza de Leon, D. J. Sherratt, and A. N. Kapanidis. 2013. 'Single-molecule DNA repair in live bacteria', *Proc Natl Acad Sci U S A*, 110: 8063-8.

van Baarle, S., and M. Bramkamp. 2010. 'The MinCDJ system in *Bacillus subtilis* prevents minicell formation by promoting divisome disassembly', *PLoS One*, 5: e9850.

van Baarle, S., I. N. Celik, K. G. Kaval, M. Bramkamp, L. W. Hamoen, and S. Halbedel. 2013. 'Protein-protein interaction domains of *Bacillus subtilis* DivIVA', *J Bacteriol*, 195: 1012-21.

van Raaphorst, R., M. Kjos, and J. W. Veening. 2017. 'Chromosome segregation drives division site selection in *Streptococcus pneumoniae*', *Proc Natl Acad Sci U S A*, 114: E5959-E68.

Vats, P., and L. Rothfield. 2007. 'Duplication and segregation of the actin (MreB) cytoskeleton during the prokaryotic cell cycle', *Proc Natl Acad Sci U S A*, 104: 17795-800.

Vats, P., Y. L. Shih, and L. Rothfield. 2009. 'Assembly of the MreB-associated cytoskeletal ring of *Escherichia coli*', *Mol Microbiol*, 72: 170-82.

Vaughan, S., B. Wickstead, K. Gull, and S. G. Addinall. 2004. 'Molecular evolution of FtsZ protein sequences encoded within the genomes of archaea, bacteria, and eukaryota', *J Mol Evol*, 58: 19-29.

Vermassen, A., S. Leroy, R. Talon, C. Provot, M. Popowska, and M. Desvaux. 2019. 'Cell Wall Hydrolases in Bacteria: Insight on the Diversity of Cell Wall Amidases, Glycosidases and Peptidases Toward Peptidoglycan', *Front Microbiol*, 10: 331.

Vlamakis, H., Y. Chai, P. Beauregard, R. Losick, and R. Kolter. 2013. 'Sticking together: building a biofilm the *Bacillus subtilis* way', *Nat Rev Microbiol*, 11: 157-68.

Volkov, I. L., M. Linden, J. Aguirre Rivera, K. W. Ieong, M. Metelev, J. Elf, and M. Johansson. 2018. 'tRNA tracking for direct measurements of protein synthesis kinetics in live cells', *Nat Chem Biol*, 14: 618-26.

Wang, S., L. Furchtgott, K.C. Huang, and J.W. Shaevitz. 2012. 'Helical Insertion of Peptidoglycan Produces Chiral Ordering of the Bacterial Cell Wall', *Proc Natl Acad Sci U S A*, 109.

Wang, S., J. R. Moffitt, G. T. Dempsey, X. S. Xie, and X. Zhuang. 2014. 'Characterization and development of photoactivatable fluorescent proteins for single-molecule-based superresolution imaging', *Proc Natl Acad Sci U S A*, 111: 8452-7.

Wang, X., and J. Lutkenhaus. 1993. 'The FtsZ protein of *Bacillus subtilis* is localized at the division site and has GTPase activity that is dependent upon FtsZ concentration', *Mol Microbiol*, 9: 435-42.

Ward, J. B., Jr., and S. A. Zahler. 1973. 'Genetic studies of leucine biosynthesis in *Bacillus subtilis*', *J Bacteriol*, 116: 719-26.

Weimann, L., K. A. Ganzinger, J. McColl, K. L. Irvine, S. J. Davis, N. J. Gay, C. E. Bryant, and D. Klenerman. 2013. 'A quantitative comparison of single-dye tracking analysis tools using Monte Carlo simulations', *PLoS One*, 8: e64287.

Weiss, D. S., K. Pogliano, M. Carson, L. M. Guzman, C. Fraipont, M. Nguyen-Disteche, R. Losick, and J. Beckwith. 1997. 'Localization of the *Escherichia coli* cell division protein Ftsl (PBP3) to the division site and cell pole', *Mol Microbiol*, 25: 671-81.

Whelan, D. R., and T. D. Bell. 2015. 'Image artifacts in single molecule localization microscopy: why optimization of sample preparation protocols matters', *Sci Rep*, 5: 7924.

Wickham, H. 2009. 'ggplot2: Elegant Graphics for Data Analysis', *Springer-Verlag New York*: ISBN 978-3-319-24277-4, https://ggplot2.tidyverse.org.

Willemse, J., J. W. Borst, E. de Waal, T. Bisseling, and G. P. van Wezel. 2011. 'Positive control of cell division: FtsZ is recruited by SsgB during sporulation of *Streptomyces*', *Genes Dev*, 25: 89-99.

Wimmi, S., A. Balinovic, H. Jeckel, L. Selinger, D. Lampaki, E. Eisemann, I. Meuskens, D. Linke, K. Drescher, U. Endesfelder, and A. Diepold. 2019. 'Dynamic relocalization of the cytosolic type III secretion system components ensures specific protein secretion', *bioRxiv*: 869214.

Wold, S., K. Skarstad, H. B. Steen, T. Stokke, and E. Boye. 1994. 'The initiation mass for DNA replication in *Escherichia coli* K-12 is dependent on growth rate', *EMBO J*, 13: 2097-102.

Woldringh, C. L., E. Mulder, P. G. Huls, and N. Vischer. 1991. 'Toporegulation of bacterial division according to the nucleoid occlusion model', *Res Microbiol*, 142: 309-20.

Wu, F., J. Halatek, M. Reiter, E. Kingma, E. Frey, and C. Dekker. 2016. 'Multistability and dynamic transitions of intracellular Min protein patterns', *Mol Syst Biol*, 12: 873.

Wu, L. J., and J. Errington. 1994. 'Bacillus subtilis SpoIIIE protein required for DNA segregation during asymmetric cell division', *Science*, 264: 572-5.

Wu, L. J., and J. Errington. 2003. 'RacA and the Soj-Spo0J system combine to effect polar chromosome segregation in sporulating *Bacillus subtilis*', *Mol Microbiol*, 49: 1463-75.

Wu, L. J., and J. Errington. 2004. 'Coordination of cell division and chromosome segregation by a nucleoid occlusion protein in *Bacillus subtilis*', *Cell*, 117: 915-25.

Wu, L. J., S. Ishikawa, Y. Kawai, T. Oshima, N. Ogasawara, and J. Errington. 2009. 'Noc protein binds to specific DNA sequences to coordinate cell division with chromosome segregation', *EMBO J*, 28: 1940-52.

Wu, L. J., S. Lee, S. Park, L. E. Eland, A. Wipat, S. Holden, and J. Errington. 2020. 'Geometric principles underlying the proliferation of a model cell system', *Nat Commun*, 11: 4149.

Xie, X. S., P. J. Choi, G. W. Li, N. K. Lee, and G. Lia. 2008. 'Single-molecule approach to molecular biology in living bacterial cells', *Annu Rev Biophys*, 37: 417-44.

Yang, L., Y. Zhou, S. Zhu, T. Huang, L. Wu, and X. Yan. 2012. 'Detection and quantification of bacterial autofluorescence at the single-cell level by a laboratory-built high-sensitivity flow cytometer', *Anal Chem*, 84: 1526-32.

Yang, X., Z. Lyu, A. Miguel, R. McQuillen, K. C. Huang, and J. Xiao. 2017. 'GTPase activity-coupled treadmilling of the bacterial tubulin FtsZ organizes septal cell wall synthesis', *Science*, 355: 744-47.

Yu, Y., J. Zhou, F. Dempwolff, J. D. Baker, D. B. Kearns, and S. C. Jacobson. 2020. 'The Min System Disassembles FtsZ Foci and Inhibits Polar Peptidoglycan Remodeling in *Bacillus subtilis*', *MBio*, 11: e03197-19.

Zhang, M., H. Chang, Y. Zhang, J. Yu, L. Wu, W. Ji, J. Chen, B. Liu, J. Lu, Y. Liu, J. Zhang, P. Xu, and T. Xu. 2012. 'Rational design of true monomeric and bright photoactivatable fluorescent proteins', *Nat Methods*, 9: 727-9.

Zheng, L., U. Baumann, and J. L. Reymond. 2004. 'An efficient one-step site-directed and site-saturation mutagenesis protocol', *Nucleic Acids Res*, 32: e115.

List of figures

List of tables

Acknowledgements

First, I want to thank my doctoral supervisor Prof. Dr. Marc Bramkamp, who gave me the chance to work on this project in his lab and guided me throughout the years. Even though you have the heaviest workload of all people in our group, you always took the time to discuss scientific or unrelated topics, to give advice or to support us students in any way possible. In addition, your encouragement was very helpful, and I never left a meeting without being motivated to go on with new experiments. For this, I am very grateful; you were a great supervisor, thank you!

Moreover, I thank all members of my thesis committee for their time and the effort, and especially Prof. Dr. Kirsten Jung, who agreed to be the second reviewer of my dissertation.

Furthermore, I would like to thank all people I collaborated with over the years, especially Prof. Dr. Erwin Frey and Laeschkir Würthner, for the productive discussions and meetings, as well as the wonderful data supporting my work.

A big "THANK YOU" goes out to all our former and current lab members and associates, starting with Juri, who helped my discover my love for microscopy, Giacomo, who was always a great friend and a very supportive colleague with great ideas, Kati, who, while always working hard, still took the time to help everyone with everything, Gustavo, for praising the sun and making life more fun, Fabi, for inspiring long walks through the forest, Lijun, who was always giggling about our bad jokes, Abigail, who never complained about our messy office and was always supportive and fun, Nadine, for always helping out and never yelling at me, Karin, for keeping our lab running and being very caring, Manu, for helping me getting started in Kiel and for being a tidy bench neighbor, Derk, the crazy genius with his endless ideas, and of course, all members of the Boshart group, especially Theresa, Kristina and Astrid, for making the time outside the lab so enjoyable and for being great friends. Same goes for all my friends outside of university, thanks for being around and staying in touch, making my life better in every way.

Likewise, I want thank my Family, and especially my parents, for always supporting me throughout my life. Thanks for continually being open-minded and understanding. Without you, I would not have had the opportunity or drive to study and pursue a doctoral degree.

Finally, thank you Janna, for all the support and happiness you brought into my life. I could not image any of this without you. Even though I don't always show it, but I cannot express how much your continuous support and love helped me and means to me. Thank you.

Curriculum vitae